

# NASA Technical Memorandum 100509

## POSTBUCKLING OF LAMINATED ANISOTROPIC PANELS

(NASA-TM-100509) POSTBUCKLING OF LAMINATED  
ANISOTROPIC PANELS (NASA) 183 p CSCL 20K

N88-16011

G3/39      Unclass  
0103611

Glenda L. Jeffrey

October 1987



National Aeronautics and  
Space Administration

Langley Research Center  
Hampton, Virginia 23665

## **Acknowledgements**

Many people at Langley Research Center have been indispensable for their assistance in completing the present work. The author expresses her gratitude first to Dr. Ahmed K. Noor, without whom this work would not have been possible. She would also like to thank the employees of the Structural Mechanics Branch for time spent in many useful discussions. Special thanks is extended to Dr. James H. Starnes, who helped to guide this work, and to Dr. Norman F. Knight, Jr., whose help in running STAGS was invaluable. George Johnson and Jim Kiss, the technicians involved in the experimental work, were excellent; the author could not have asked for better. Gratitude is extended to Jeanne M. Peters for her programming assistance, and to Carl M. Andersen for many useful discussions. The author is also thankful to her supervisors, Brantley R. Hanks and Dr. Jerrold M. Housner, for their tolerance during her first months of employment. Finally, the author is especially grateful for the knowledge, tolerance, moral support, and computational resources volunteered by the personnel of the Computational Structural Mechanics Group.

**PRECEDING PAGE BLANK NOT FILMED**

## Table of Contents

Abstract . . . . .	i
Acknowledgements . . . . .	iii
Table of Contents . . . . .	v
List of Tables . . . . .	ix
List of Figures . . . . .	xi
List of Symbols . . . . .	xv
1. Introduction . . . . .	1
1.1. Overview . . . . .	1
1.2. Review of Previous Pertinent Work . . . . .	3
1.2.1. Global Approximation Function Techniques . . . . .	3
1.2.2. Reduced Basis Work . . . . .	4
1.2.3. Experimental Work . . . . .	5
1.3. Objectives and Scope . . . . .	6
2. Problems Involving Bending-Extensional Coupling and Anisotropy . . . . .	8
2.1. Mechanical Couplings . . . . .	8
2.2. Symmetries Exhibited by Anisotropic Panels . . . . .	13
2.3. Governing Differential Equations of an Anisotropic Plate And Bending-Extensional Coupling . . . . .	16
3. Development of the Modified Rayleigh-Ritz Technique . . . . .	18
3.1. Review of the Rayleigh-Ritz Technique . . . . .	18
3.1.1. Development of the Exact Energy Expression . . . . .	18
3.1.2. Selection and Use of Approximation Functions . . . . .	20
3.1.3. Generation of the Nonlinear Equations in $X_I$ And the Recursion Formulas for the Newton-Raphson Iterative Procedure . . . . .	23
3.1.4. Symmetrization of the Nonlinear Arrays . . . . .	24
3.1.5. Generation of Load Vector $P$ . . . . .	24
3.2. Enforcement of Boundary Conditions Using A Penalty Function Approach . . . . .	25
3.3. Operator Splitting . . . . .	27

3.3.1. Basic Concepts . . . . .	28
3.3.2. Array Symmetrization When Partitioning is Used . . . . .	32
3.4. Application of Reduced Basis Techniques in Conjunction With Operator Splitting . . . . .	34
3.4.1. Generation of Basis Vectors . . . . .	35
3.4.1.a. Linear Problem . . . . .	35
3.4.1.b. Nonlinear Problem . . . . .	37
3.4.2. Generation and Solution of the Reduced Equation System . . . . .	41
3.4.2.a. Linear Problem . . . . .	41
3.4.2.b. Nonlinear Problem . . . . .	41
<b>4. Numerical Studies of Modified Rayleigh-Ritz Technique . . . . .</b>	<b>44</b>
4.1. Comments on Problem Selection . . . . .	44
4.2. Linear Results . . . . .	44
4.2.1. Transversely Loaded Orthotropic Panel . . . . .	47
4.2.2. Transversely Loaded Anisotropic Panel With Bending-Extensional Coupling . . . . .	49
4.2.3. Axially Loaded Orthotropic Panel . . . . .	50
4.2.4. Axially Loaded Anisotropic Panel With Bending-Extensional Coupling . . . . .	52
4.3. Effect of the Penalty Parameter on Accuracy of Linear Results . . . . .	53
4.4. Linear Results Using Reduced Basis Techniques . . . . .	55
4.4.1. Accuracy in Approximating the Full System . . . . .	57
4.4.2. Grammian Results . . . . .	58
4.5. Nonlinear Results . . . . .	59
4.5.1. Orthotropic Panel . . . . .	63
4.5.2. $[\pm 30/90]_5$ Panel . . . . .	64
4.5.3. $[\pm 50/35]_5$ Panel . . . . .	65
<b>5. Experimental and Numerical Studies of   Buckling and Postbuckling Behavior of Panels . . . . .</b>	<b>67</b>
5.1. Characteristics of Test Specimens . . . . .	67
5.2. Description of the Experiment . . . . .	68
5.2.1. Test Setup, Measurement Techniques, and Procedure . . . . .	68
5.2.2. Observations Regarding Experimental Techniques . . . . .	73
5.3. Finite Element Model . . . . .	74
5.3.1. Discretization and Boundary Conditions . . . . .	74
5.3.2. Solution Strategy . . . . .	76
5.4. Comparison of Experimental and Finite Element Results . . . . .	77
5.4.1. Presentation and Discussion of Buckling Load And End Shortening Results . . . . .	77
5.4.1.a. Buckling Load Results and Discussion . . . . .	78
5.4.1.b. Postbuckling Results and Discussion . . . . .	81
5.4.2. Presentation and Discussion of Out-of-Plane Displacement Results . . . . .	84



5.4.3. Presentation and Discussion of Strain Results . . . . .	86
5.5. Failure Initiation and Development . . . . .	89
5.5.1. Qualitative Results . . . . .	89
5.5.2. Quantitative Results . . . . .	91
5.6. Summary of Observations . . . . .	91
 6. Observations and Recommendations . . . . .	 97
6.1. Observations . . . . .	97
6.1.1. Observations Related to the Modified Rayleigh-Ritz Technique . . .	97
6.1.1.a. Observations related to linear results . . . . .	97
6.1.1.b. Observations related to nonlinear results . . . . .	98
6.1.2. Observations Based on Experiments . . . . .	99
6.1.3. Observations Based on Finite Element Modeling Efforts . . . . .	100
6.2. Recommendations . . . . .	102
6.2.1. Recommendations Related to the Modified Rayleigh-Ritz Technique	102
6.2.2. Recommendations Related to Experimental Work . . . . .	102
 References . . . . .	 104
 Appendices	
A. Array Symmetrization Using Only Quadratic Energy Terms . . .	106
B. Experimental Moiré Fringe Photographs . . . . .	108
C. C-Scans of Experimental Panels . . . . .	116
D. STAGSC-1 Runstreams . . . . .	123
 Figures . . . . .	 130

## List of Tables

2.1. Orthotropic Panel Symmetry States . . . . .	15
4.1. Rayleigh-Ritz Analysis Functions . . . . .	46
4.2. Linear Results for $[0_4/90_4]_S$ , Transversely Loaded Panel . . . . .	48
4.3. Linear Results for $[\pm 50/35]_5$ , Transversely Loaded Panel . . . . .	50
4.4. Linear Results for $[0_4/90_4]_S$ , Axially Loaded Panel . . . . .	51
4.5. Linear Results for $[\pm 50/35]_5$ , Axially Loaded Panel . . . . .	52
4.6. Penalty Results – Overall Penalty Parameter . . . . .	54
4.7. Variation of Results with Number of Basis Vectors Used . . . . .	57
4.8. Variation of the Grammian with Number of Basis Vectors Used . . . . .	58
5.1. Material Properties for Hercules AS4-3502 Graphite/Epoxy Tape . . . . .	68
5.2. Constitutive Matrices for $[\pm 50/35]_5$ and $[\pm 30/90]_5$ Panels, Thickness = 0.08 in. . . . .	69
5.3. Measurements of Tested Panels . . . . .	70
5.4. Finite Element Model Discretization . . . . .	74
5.5. Grid Convergence, $[\pm 30/90]_5$ 4-inch-wide Panel . . . . .	75
5.6. Buckling Loads, Pounds . . . . .	79
5.7. Linear Bifurcation Buckling Results, Pounds . . . . .	80
5.8. Slope of Initial Postbuckling Curve . . . . .	81
5.9. Postbuckling Stiffness Degradation . . . . .	82
5.10. Transverse Displacement at Buckling . . . . .	85
5.11. Summary of Twist and Symmetry Results . . . . .	86
5.12. Load and End Shortening at Failure . . . . .	92

PRECEDING PAGE BLANK NOT FILMED

## List of Figures

B.1. Moiré Fringe Photographs for $[\pm 30/90]_5$ 4 Inch-Wide Panel . . . . .	109
B.2. Moiré Fringe Photographs for $[\pm 30/90]_5$ 5.5 Inch-Wide Panel . . . . .	110
B.3. Moiré Fringe Photographs for $[\pm 30/90]_5$ 7 Inch-Wide Panel . . . . .	111
B.4. Moiré Fringe Photographs for $[\pm 50/35]_5$ 4 Inch-Wide Panel . . . . .	112
B.5. Moiré Fringe Photographs Illustrating Mode Change Exhibited by $[\pm 50/35]_5$ 4 Inch-Wide Panel . . . . .	113
B.6. Moiré Fringe Photographs for $[\pm 50/35]_5$ 5.5 Inch-Wide Panel . . . . .	114
B.7. Moiré Fringe Photographs for $[\pm 50/35]_5$ 7 Inch-Wide Panel . . . . .	115
C.1. C-Scan of $[\pm 30/90]_5$ 4 Inch-Wide Panel . . . . .	117
C.2. C-Scan of $[\pm 30/90]_5$ 5.5 Inch-Wide Panel . . . . .	118
C.3. C-Scan of $[\pm 30/90]_5$ 7 Inch-Wide Panel . . . . .	119
C.4. C-Scan of $[\pm 50/35]_5$ 4 Inch-Wide Panel . . . . .	120
C.5. C-Scan of $[\pm 50/35]_5$ 5.5 Inch-Wide Panel . . . . .	121
C.6. C-Scan of $[\pm 50/35]_5$ 7 Inch-Wide Panel . . . . .	122
2.1. Conventions Used in Theoretical Development . . . . .	130
2.2. Effect of Shear-Extensional Coupling on Panel Subject To Uniform Axial Loading . . . . .	131
2.3. Effect of Shear-Extensional Coupling on Postbuckled Shape . . . . .	131
2.4. Method for Observing Twisting Behavior During an Experiment . . . . .	132
4.1. Schematics for Linear Problems . . . . .	133
4.2. Schematic of Mixed Formulation Finite Element Models . . . . .	134
4.3. Linear Results for Simply Supported, Transversely Loaded $[0_4/90_4]_S$ Panel . .	135
4.4. Linear Results for Simply Supported, Transversely Loaded $[\pm 50/35]_5$ Panel .	136
4.5. Linear Results for Clamped/Simply Supported, Axially Loaded $[0_4/90_4]_S$ Panel	137
4.6. Linear Results for Clamped/Simply Supported, Axially Loaded $[\pm 50/35]_5$ Panel	138

4.7. Contour Plots of Linear Solution for Axially Loaded	
Clamped/Simply Supported $[\pm 50/35]_5$ Panel . . . . .	139
4.8. End Shortening Behavior, $[0_4/90_4]_5$ Panel . . . . .	140
4.9. Center Transverse Displacement Behavior, $[0_4/90_4]_5$ Panel . . . . .	141
4.10. Normalized Contour Plots of Transverse Displacement, $[0_4/90_4]_5$ Panel . . . . .	142
4.11. End Shortening Behavior, $[\pm 30/90]_5$ Panel . . . . .	143
4.12. Center Transverse Displacement Behavior, $[\pm 30/90]_5$ Panel . . . . .	144
4.13. Normalized Contour Plots of Transverse Displacement, $[\pm 30/90]_5$ Panel . . . . .	145
4.14. End Shortening Behavior, $[\pm 50/35]_5$ Panel . . . . .	146
4.15. Center Transverse Displacement Behavior, $[\pm 50/35]_5$ Panel . . . . .	147
4.16. Normalized Contour Plots of Transverse Displacement, $[\pm 50/35]_5$ Panel . . . . .	148
5.1. Experiment Schematic and Photograph . . . . .	149
5.2. Support Fixture Schematic . . . . .	150
5.3. Bending as Indicated by Back-to-back Strain Gage Data . . . . .	151
5.4. Sample C-Scan . . . . .	152
5.5. Comparison of Experimental Setup Technique for Isotropic	
And Anisotropic Panels . . . . .	153
5.6. Undeformed Geometry Plot of STAGSC-1 Finite Element Model	
for 5.5-inch-wide $[\pm 50/35]_5$ Panel . . . . .	154
5.7. Typical Panel End-shortening Plot . . . . .	155
5.8. End Shortening Results . . . . .	156
5.9. Estimation of Stiffness Degradation . . . . .	157
5.10. Near-Maximum Transverse Displacement Results . . . . .	158
5.11. Experimental Warping Results . . . . .	159
5.12. STAGSC-1 Warping Results . . . . .	160
5.13. Experimental Symmetry Results . . . . .	161
5.14. STAGSC-1 Symmetry Results . . . . .	162

5.15. Representative Experimental Surface Strain Results . . . . .	163
5.16. Progression of Transverse Displacement Pattern, $[\pm 50/35]_5$ , 7-inch-wide panel	164
5.17. Progression of Transverse Displacement Pattern, $[\pm 30/90]_5$ , 7-inch-wide panel	165
5.18. Progression of Transverse Displacement Pattern, All Panels . . . . .	166
5.19. Failure Locations . . . . .	167
5.20. Strains Across 5.5-inch-wide Panels at Load Near Failure . . . . .	168
5.21. Photograph of Shear Failure, $[\pm 50/35]_5$ 7-inch-wide panel . . . . .	169

## List of Symbols

$a$	Longer panel dimension
$b$	Shorter panel dimension
$A$	Membrane stiffness coefficients
$B$	Bending-extensional coupling stiffness coefficients
$C$	Constitutive matrix
$C$	Transverse shear stiffness coefficients
$D$	Bending stiffness coefficients
$e$	Error measure used in Newton-Raphson iterations
$F_j^i$	Vector of approximation functions representing displacement $i$ and containing $j$ terms
$F$	Vector containing all $F_j^i$ for all displacements
$F$	Symmetrized quadratic stiffness matrix which is cubic in $F_j^i$
$\bar{F}$	Unsymmetrized quadratic stiffness matrix which is cubic in $F_j^i$
$G$	Symmetrized cubic stiffness matrix which is quartic in $F_j^i$
$\bar{G}$	Unsymmetrized cubic stiffness matrix which is quartic in $F_j^i$
$h$	Constraint function; also panel thickness (clear from context)
$\mathcal{I}$	Total number of even state approximation functions
$K$	Symmetrized linear stiffness matrix which is quadratic in $F_j^i$
$\bar{K}$	Unsymmetrized linear stiffness matrix which is quadratic in $F_j^i$
$K$	Reduced linear stiffness matrix
$M$	Moment resultant
$\mathcal{M}$	Total number of odd state approximation functions
$\bar{m}$	Total number of approximation functions
$M$	Gram matrix
$N$	Stress resultant

$n$	Total number of degrees of freedom in nonlinear equation system
$\mathcal{N}$	Number of basis vectors to be used
$P_{cr}$	Panel buckling load
$P$	Load vector
$P$	Reduced load vector
$p$	Load magnitude
$Q$	Shear stress resultants
$R^L$	Matrix containing derivatives of the $F_j^i$ which constitute linear contributions to strain displacement relations
$R^{NL}$	Matrix containing derivatives of the $F_j^i$ which constitute nonlinear contributions to strain displacement relations
$R$	Residual vector
$r$	Penalty parameter
$U$	Total energy of a structure
$U_i$	Strain energy terms involving generalized displacements raised to power $i$
$u_i$	Displacement in direction $i$
$u_{2e}$	Value of $u_2$ at midpoint of long panel edge
$W_{\text{ext}}$	Work of external forces
$w$	Transverse displacement
$w_c$	Center transverse displacement
$x_i$	Spatial coordinate $i$
$X_j^i$	Vector of generalized coordinates representing displacement $i$ and containing $j$ terms
$\mathbf{X}$	Vector containing all $X_j^i$ for all displacements
$\mathbf{X}$	Vector amplitudes associated with basis vectors contained in $\Gamma$
$\delta$	End shortening
$\delta_{ij}$	Krönecker delta, equal to one when $i = j$ and zero otherwise

$\delta U$	Variation of $U$
$\varepsilon$	Strain
$\varepsilon^L$	Linear contribution to strain-displacement relations
$\varepsilon^{NL}$	Nonlinear contribution to strain-displacement relations
$\eta$	Path parameter
$\kappa$	Curvature
$\lambda$	Tracing constant associated with anisotropic stiffness terms
$\phi_1$	Rotation about axis $x_2$
$\phi_2$	Rotation about axis $x_1$
$\sigma$	Stress
$\theta$	Angle principle material axis of orthotropic lamina makes with $x_1$ axis
$\Gamma$	Matrix whose columns are basis vectors
$\Pi$	Penalty function

#### Subscripts

0	Evaluation at $\lambda = 0$
$a, b$	$1, \dots, 8$
$\alpha, \beta$	Dummy indices
$c, d$	$1, \dots, \mathcal{N}$
$I, J, K, L$	$1, \dots, \overline{m}$
$i, j, k, l$	$1, \dots, \mathcal{I}$
$m, n, o, p$	$1, \dots, \mathcal{M}$
$P, Q, R, S, T$	Range is over number of functions approximating $u_1, u_2, \phi_1, \phi_2$ , and $w$ , respectively

All repeated indices denote summation unless otherwise noted.



### Superscripts

O	Orthotropic material stiffness coefficients
A	Anisotropic (nonorthotropic) material stiffness coefficients
$e, o$	Even and odd state functions, respectively

# Chapter 1

## Introduction

### 1.1 Overview

The potential of aeroelastic tailoring methods involving laminated filamentary composite aircraft wing skins has recently been exploited for two primary purposes:

1. Achievement of performance goals by causing changes in wing shape for specified aerodynamic loads.
2. Elimination of instabilities, such as wing divergence, from otherwise desirable designs.

Most tailoring efforts have centered around obtaining desired twisting and bending behavior through careful choice of laminate stacking sequences. Such tailoring is possible because many different mechanical couplings can be induced in a laminate through the use of certain well-defined stacking sequence categories.

Two recent and frequently cited design applications employing aeroelastic tailoring have been the HiMAT remotely piloted vehicle [1] and X-29 fighter plane design efforts. The HiMAT (Highly Maneuverable Aircraft Technology) aircraft, a 0.5 scale research vehicle, is an example of the use of aeroelastic tailoring to achieve a performance goal. In this case, design constraints required that the aircraft's wings attain a certain twist in response to certain operational loads. The X-29, on the other hand, is an example of the use of aeroelastic tailoring to eliminate instabilities from an otherwise feasible design. The wings of the X-29 were tailored in such a way that the divergence inherent in the forward-swept wing was avoided [2].

It is important to note that, even though bending/twisting coupling is the interaction usually desired for aeroelastic tailoring applications, the  $[\pm 50/35]_5$  laminate used in the HiMAT aircraft exhibited all possible types of mechanical couplings. (See Chapter 2 for a discussion of all the different couplings.) Apparently, the analysis only included the effects of bending- and extension-twisting coupling, which might have accounted for some of the

test/analysis discrepancies discussed in [1]. Such an omission is perhaps understandable, in light of the dearth of information regarding the analysis of laminates simultaneously possessing all the couplings present in the  $[\pm 50/35]_5$  laminate. Almost all the literature found by the author deals with laminates in which one or more couplings are not present. It is therefore desirable to compile theoretical and experimental results dealing with such laminates.

A second area which has received much attention is the practical use of laminated filamentary composites in the postbuckling range. Although metallic aircraft substructures having buckling loads within the operational load range of the aircraft have been in use for some time, composite aircraft structures have typically been designed by considering buckling to be synonymous with failure [3]. It has only been fairly recently that investigators have shown that buckling need not be such a limitation, since considerable stiffness is often available at loads equal to many times the buckling load of a composite structure. (See, for example, [4] and [3].) Efficient use of this additional stiffness makes possible the design and construction of structures which are significantly lighter than metal structures of equivalent strength.

The possible future use of lighter, buckled designs in aeroelastically tailored substructures obviates the need for more complete information regarding both the pre- and postbuckling behavior of anisotropic composite laminates with bending-extensional coupling. Although considerable literature exists regarding postbuckling behavior of conventional orthotropic laminates, little is available which examines the postbuckling behavior of laminates like the  $[\pm 50/35]_5$  laminate used in the HiMAT effort.

## 1.2 Review of Previous Pertinent Work

Considerable literature is available which documents analytical and experimental work involving various subsets of the general anisotropic plate with bending-extensional coupling. Leissa has presented a collection of such work [5], both analytical and experimental, and so it will not be discussed here.

### 1.2.1 Global Approximation Function Techniques

First, the work of Ashton and Whitney in the early 1970's is of interest because these two authors both examined the analysis of anisotropic plates (in the bending sense) from the point of view of global approximation functions. Ashton took the classical Rayleigh-Ritz approach, while Whitney worked with a modified Fourier series expansion technique. In both cases, the determining factor in the accuracy of the results was whether or not the natural boundary conditions were satisfied.

Ashton's work [6,7] is limited to the analysis of a few selected problems whose geometric boundary conditions can be satisfied using simple trigonometric functions. In the problems where natural boundary conditions are satisfied by the chosen approximation functions, convergence to accurate solutions is good; however, in those cases where natural boundary conditions are not satisfied, convergence is shown to be unsatisfactory even for gross response quantities such as maximum displacement and buckling load [8]. This limitation is severe in problems where the choice of separable functions of the form  $X(x)Y(y)$  satisfying natural boundary conditions is precluded by coupling between bending and twisting. If coupling between bending and extension is also present, satisfaction of natural boundary conditions becomes even more difficult.

Later work by Whitney [9,10] shows that the use of a modified double Fourier series analysis results in better convergence because functions can be derived which satisfy natural boundary conditions. For the problems studied, the technique works well; however, the method is still not generally applicable in an automated fashion to a wide range of problems,

since new functions must be derived for each set of boundary conditions. Also, if bending-extensional coupling is present, the method as it is presented is not applicable.

The use of the exterior penalty function provides an easily automated way to use global approximation functions for the analysis of a wide range of problems involving complex mechanical couplings and boundary conditions. The penalty function method allows the choice of any set of approximation functions, so long as they are separable and adhere to simple symmetry rules. Boundary conditions are satisfied automatically, freeing the analyst to select approximation functions which represent complicated response quantities more accurately than would functions limited by boundary condition requirements. This freedom from the limitations of boundary conditions should make possible the use of approximation functions chosen for accuracy, making the Rayleigh-Ritz technique a viable alternative to the finite element method for problems having simple shapes.

### 1.2.2 Reduced Basis Work

Considerable work has been devoted to the development of different reduced basis analysis techniques, although this work goes by many different names. Most of the techniques are methods by which large, computationally expensive equation systems describing a discretized structure are approximated by much smaller sets of equations. The techniques are generally based on the approximation of the problem solution by a combination (whether linear or nonlinear) of a set of basis vectors assumed to span the desired solution space.

The different methods are distinguished primarily by the differences in the basis vectors themselves. The modal techniques used in the structural dynamics field are a form of reduced basis analysis, since the problem unknowns are being approximated by a linear combination of modes which are typically selected to be the eigenvectors of the problem at hand [11]. Fairly recently, basis vectors have been developed for use in static nonlinear analysis; these vectors often consist of derivatives of response quantities with respect to some generalized path parameter [12]. More recently, Noor has analyzed anisotropic plates using various order derivatives of response quantities with respect to the anisotropic

material stiffness coefficients as basis vectors [18]. Elements of this last approach will be applied herein.

Noor's work in the area of anisotropic analysis has dealt exclusively with the finite element method, used in conjunction with the symmetry relations published in reference [13]. Taking this approach, he has simplified the process of obtaining a set of basis vectors for an anisotropic problem in three ways. First, the equation systems defining the basis vectors are shown to be approximately half the size of the full equation system; second, only one set of nonlinear equations must be solved to obtain the basis vectors. Finally, many elements of the reduced system are shown to be zero for symmetric or antisymmetric loading.

However, the finite element method is a technique which is best suited to complex geometries not easily characterized analytically. For geometrically simpler structures, a classical Rayleigh-Ritz analysis can take the place of a finite element model. It is particularly interesting to consider such an analysis in the context of the symmetry relations detailed in [13] since these relations can be directly applied in the choice of approximation functions. These simplifications find use in all stages of the analysis, from formation of the full and reduced equation systems, to appropriate choice of approximation functions.

### 1.2.3 Experimental Work

Jensen [14] studied the buckling and postbuckling behavior of fully anisotropic plates with bending-extensional coupling in an experimental context. Square plates of various laminations were tested, and the results compared with both classical Rayleigh-Ritz analysis and finite element analysis results. (Again, the Ritz functions met geometric boundary conditions.) The eleven layup configurations examined ranged from orthotropic to fully anisotropic with bending-extensional coupling.

The work is fairly extensive, but the results do leave room for additional investigation, as noted by the author in his recommendations. The laminates studied in reference [14] were carefully chosen in order isolate several different distinguishing characteristics inherent

in panels with anisotropy and bending-extensional coupling. With this groundwork laid, it is now desirable to study laminates which might be used in the design of actual aircraft. It would also be desirable to test anisotropic laminates using a test setup which has been employed extensively by others (for example, [15]) for two reasons. First, the suitability of such test methods to the testing of anisotropic panels with bending-extensional coupling could be evaluated; second, test results could be qualitatively compared with the results of others.

### 1.3 Objectives and Scope

The overall objective of the present work is to study the effects of anisotropy and bending-extensional coupling on the buckling and postbuckling response of flat panels. The specific objectives of the present work are:

1. To develop a modified Rayleigh-Ritz analysis technique and apply it to the linear and nonlinear analysis of anisotropic panels with bending-extensional coupling. Modifications include, for the linear case:
  - a. Exploiting known symmetries of anisotropic panels in the selection of approximation functions [13].
  - b. Developing and applying a reduced basis technique based on these same symmetries.
  - c. Enforcing the geometric boundary conditions via an exterior penalty function approach, rather than by choosing approximation functions which satisfy the boundary conditions automatically.

For the nonlinear case, only modifications (a) and (c) will be used.

2. To gain insight into the postbuckling response and failure characteristics of panels of various aspect ratios which possess anisotropy and bending-extensional coupling by conducting postbuckling experiments involving such panels. Any

observed phenomena which are not present in the behavior of panels without anisotropy or bending-extensional coupling will be noted.

The scope of the current work includes:

1. Analysis of thin, flat laminated composite panels possessing anisotropy and bending-extensional coupling using both the modified Rayleigh-Ritz technique and readily available finite element analysis tools. The effects of transverse shear deformation are included in the Rayleigh-Ritz analysis, but not in the finite element analysis. Failure criteria will not be considered.
2. Uniaxial loading in all analyses and experiments, with transverse loading being used as a check case in the Rayleigh-Ritz analyses.
3. Use of simple linear and trigonometric approximation functions in the Rayleigh-Ritz analysis.



## Chapter 2

### Problems Involving Bending-Extensional Coupling and Anisotropy

#### 2.1 Mechanical Couplings

The concepts of anisotropy and bending-extensional coupling are most easily explained in terms of the constitutive relations for a laminated panel. The following constitutive equation relates the extensional stress resultants  $N_1$ ,  $N_2$ , and  $N_{12}$ , bending resultants  $M_1$ ,  $M_2$ , and  $M_{12}$ , and transverse shear stress resultants  $Q_1$  and  $Q_2$  to the corresponding strain quantities defined below via the material stiffness matrices  $A$ ,  $B$ ,  $D$ , and  $C$ :

$$\begin{Bmatrix} N_1 \\ N_2 \\ N_{12} \\ - \\ M_1 \\ M_2 \\ M_{12} \\ - \\ Q_2 \\ Q_1 \end{Bmatrix} = \begin{bmatrix} A_{11} & A_{12} & A_{16} & | & B_{11} & B_{12} & B_{16} & | & \cdot & \cdot & \cdot \\ A_{12} & A_{22} & A_{26} & | & B_{12} & B_{22} & B_{26} & | & \cdot & \cdot & \cdot \\ A_{16} & A_{26} & A_{66} & | & B_{16} & B_{26} & B_{66} & | & \cdot & \cdot & \cdot \\ \hline & \text{Symmetric} & & | & D_{11} & D_{12} & D_{16} & | & \cdot & \cdot & \cdot \\ & & & | & D_{12} & D_{22} & D_{26} & | & \cdot & \cdot & \cdot \\ & & & | & D_{16} & D_{26} & D_{66} & | & \cdot & \cdot & \cdot \\ \hline \cdot & \cdot & \cdot & | & \cdot & \cdot & \cdot & | & C_{44} & C_{45} & \cdot \\ \cdot & \cdot & \cdot & | & \cdot & \cdot & \cdot & | & C_{45} & C_{55} & \cdot \end{bmatrix} \begin{Bmatrix} \epsilon_1^0 \\ \epsilon_2^0 \\ 2\epsilon_{12}^0 \\ - \\ \kappa_1 \\ \kappa_2 \\ 2\kappa_{12} \\ - \\ 2\epsilon_{23} \\ 2\epsilon_{13} \end{Bmatrix} \quad (2.1)$$

(Note that for purposes of calculating the material stiffness coefficients shown above, the reference surface is taken to be the middle surface of the panel.) For later reference, the constitutive equation can be written in a more compact form:

$$\begin{Bmatrix} N \\ M \\ Q \end{Bmatrix} = [C] \begin{Bmatrix} \epsilon \\ \kappa \\ \epsilon_s \end{Bmatrix} = \begin{bmatrix} A_{ij} & B_{ij} & \cdot \\ B_{ji} & D_{ij} & \cdot \\ \cdot & \cdot & C_{kl} \end{bmatrix} \begin{Bmatrix} \epsilon \\ \kappa \\ \epsilon_s \end{Bmatrix} \quad \begin{matrix} i, j = 1, 2, 6 \\ k, l = 4, 5 \end{matrix} \quad (2.2)$$

For convenience, the matrix  $C$  is partitioned as shown. The  $A$  coefficients are known as the extensional or membrane stiffnesses of the panel. The  $D$  coefficients are referred to as the bending stiffnesses, and the  $B$  coefficients are called the bending-extensional coupling stiffnesses since they couple bending and extensional behavior. Finally, the  $C$  terms are the transverse shear stiffness coefficients. All these coefficients depend upon the layup

configuration and are derived from basic theory of laminated composites as may be found in any of the standard texts on the subject (See, for example, [8].)

A modified von Kármán type nonlinear plate theory is used with transverse shear strains and bending-extensional coupling included. The strain-displacement relations are:

Extensional Strains	Curvatures
$\varepsilon_1^0 = \partial_1 u_1 + \frac{1}{2}(\partial_1 w)^2$	$\kappa_1 = \partial_1 \phi_1$
$\varepsilon_2^0 = \partial_2 u_2 + \frac{1}{2}(\partial_2 w)^2$	$\kappa_2 = \partial_2 \phi_2$
$2\varepsilon_{12}^0 = \partial_1 u_2 + \partial_2 u_1 + \partial_1 w \partial_2 w$	$2\kappa_{12} = \partial_1 \phi_2 + \partial_2 \phi_1$

(2.3)

Transverse Shear Strains

$$2\varepsilon_{13} = \phi_1 + \partial_1 w$$

$$2\varepsilon_{23} = \phi_2 + \partial_2 w$$

where the symbol  $\partial_i$  indicates differentiation with respect to  $x_i$ . The conventions which are used for the plate geometry, force and moment resultants, loads, and displacements are shown in Figure 2.1.

Three simplified forms of equation 2.1 can be obtained by examining three major types of laminates:

1. Midplane-symmetric orthotropic laminates
2. Unsymmetric orthotropic laminates
3. Anisotropic (nonorthotropic) laminates

The first category, that of midplane-symmetric orthotropic layups, possesses a constitutive matrix of the following form:

$$\begin{Bmatrix} N_1 \\ N_2 \\ N_{12} \\ \text{---} \\ M_1 \\ M_2 \\ M_{12} \\ \text{---} \\ Q_2 \\ Q_1 \end{Bmatrix} = \left[ \begin{array}{ccc|ccc|cc} A_{11} & A_{12} & \cdot & \cdot & \cdot & \cdot & \cdot & \cdot \\ A_{12} & A_{22} & \cdot & \cdot & \cdot & \cdot & \cdot & \cdot \\ \cdot & \cdot & A_{66} & \cdot & \cdot & \cdot & \cdot & \cdot \\ \hline \text{Symmetric} & & & D_{11} & D_{12} & \cdot & \cdot & \cdot \\ & & & D_{12} & D_{22} & \cdot & \cdot & \cdot \\ & & & \cdot & \cdot & D_{66} & \cdot & \cdot \\ \hline \cdot & \cdot & \cdot & \cdot & \cdot & \cdot & C_{44} & \cdot \\ \cdot & \cdot & \cdot & \cdot & \cdot & \cdot & \cdot & C_{55} \end{array} \right] \begin{Bmatrix} \varepsilon_1^0 \\ \varepsilon_2^0 \\ 2\varepsilon_{12}^0 \\ \text{---} \\ \kappa_1 \\ \kappa_2 \\ 2\kappa_{12} \\ \text{---} \\ 2\varepsilon_{23} \\ 2\varepsilon_{13} \end{Bmatrix} \quad (2.4)$$

This form occurs because a midplane-symmetric laminate, by definition, possesses mirror symmetry with respect to the midplane, causing the entire  $B$  matrix to vanish. The only remaining coupling is embodied in the  $A_{12}$  and  $D_{12}$  terms. This coupling is known as the familiar Poisson effect, i.e., the occurrence of lateral strain when an axial load is applied, and vice-versa, as well as the presence of curvature in both directions.

When an orthotropic laminate is not midplane symmetric, the  $B_{ij}$  terms are nonzero and the following relation is obtained:

$$\begin{Bmatrix} N_1 \\ N_2 \\ N_{12} \\ - \\ M_1 \\ M_2 \\ M_{12} \\ - \\ Q_2 \\ Q_1 \end{Bmatrix} = \begin{bmatrix} A_{11} & A_{12} & \cdot & | & B_{11} & B_{12} & \cdot & | & \cdot & \cdot \\ A_{12} & A_{22} & \cdot & | & B_{12} & B_{22} & \cdot & | & \cdot & \cdot \\ \cdot & \cdot & A_{66} & | & \cdot & \cdot & B_{66} & | & \cdot & \cdot \\ \hline & \text{Symmetric} & & | & D_{11} & D_{12} & \cdot & | & \cdot & \cdot \\ & & & | & D_{12} & D_{22} & \cdot & | & \cdot & \cdot \\ & & & | & \cdot & \cdot & D_{66} & | & \cdot & \cdot \\ \hline \cdot & \cdot & \cdot & | & \cdot & \cdot & \cdot & | & C_{44} & \cdot \\ \cdot & \cdot & \cdot & | & \cdot & \cdot & \cdot & | & \cdot & C_{55} \end{bmatrix} \begin{Bmatrix} \varepsilon_1^0 \\ \varepsilon_2^0 \\ 2\varepsilon_{12}^0 \\ - \\ \kappa_1 \\ \kappa_2 \\ 2\kappa_{12} \\ - \\ 2\varepsilon_{23} \\ 2\varepsilon_{13} \end{Bmatrix} \quad (2.5)$$

This relationship, which exhibits coupling between bending and extension, will occur when the layer orientations or thicknesses on one side of the laminate midplane are not identical to orientations or thicknesses on the other side. The presence of the  $B_{ij}$  terms means that when the panel is subjected to inplane forces or displacements, curvatures are observed. Likewise, when bending-type loads or curvatures are applied, extensional strains are observed.

In postbuckling analysis, the effects of bending-extensional coupling must be kept in mind for the following reason. Consider a geometrically symmetric panel with symmetric boundary conditions and bending-extensional coupling. When a symmetric axial load is applied, the prebuckling deformation is symmetric. However, the postbuckled configuration can be such that precise satisfaction of the symmetry conditions described in the next section does not occur. The response is either symmetric or unsymmetric; it is never

antisymmetric. This fact was noted during the finite element analysis of three of the six panels tested and is discussed further in Chapter 5.

Bending-extensional coupling causes one additional difficulty. It means that more information is required in order to evaluate moment and force resultants. In problems where there is no bending-extensional coupling, if only extensional strains are known, then it is a simple matter to obtain force resultants just from the constitutive relations; however, in the presence of bending-extensional coupling, curvatures must also be known to determine inplane force resultants. Similarly, when bending is experienced, moment resultants are easily found using just curvatures and the constitutive relation. When bending-extensional coupling is present, extensional strains are also needed. This additional information requirement can be especially troublesome from an experimental viewpoint, since totally different techniques are used to measure curvatures and strains. An alternative to measurement of curvatures in addition to strains is the calculation of the curvatures and middle surface strains using the assumption that the strain variation is linear in the thickness direction:

$$\left\{ \begin{matrix} \varepsilon_{11} \\ \varepsilon_{22} \\ \varepsilon_{12} \end{matrix} \right\}_{z=z} = \left\{ \begin{matrix} \varepsilon_{11}^0 \\ \varepsilon_{22}^0 \\ \varepsilon_{12}^0 \end{matrix} \right\} + z \left\{ \begin{matrix} \kappa_{11} \\ \kappa_{22} \\ \kappa_{12} \end{matrix} \right\} \quad (2.6)$$

where  $z$  may take on any value from  $-h/2$  to  $h/2$ .

Anisotropic laminates can be distinguished from orthotropic laminates by the presence of any of the following four sets of coupling coefficients:

- 1) Inplane shear-extensional coupling ( $A_{16}$ ,  $A_{26}$  terms)
- 2) Bending-twisting coupling ( $D_{16}$ ,  $D_{26}$  terms)
- 3) Extension-twisting coupling ( $B_{16}$ ,  $B_{26}$  terms)
- 4) Transverse shear coupling ( $C_{45}$  term)

Henceforth, these material stiffness coefficients will be referred to as the anisotropic stiffness coefficients, and are not to be confused with the bending-extensional coupling coefficients for orthotropic laminates, discussed above.

Inplane shear-extensional coupling causes the panel to experience inplane shear deformations when it is subjected to tension or compression. A schematic is shown in Figure 2.2 which exaggerates such deformation for the case of a panel subjected to uniform axial loading. The panels analyzed in the present work are subjected to uniform end shortening, so that the loaded edges are not allowed to shear, as shown in the figure; however, the effects of shear-extensional coupling are still observed. They are particularly obvious in the postbuckling range; the nodal lines of the buckle pattern tend to skew diagonally, as shown in the contour plot of Figure 2.3.

Bending-twisting effects become obvious when the plate begins to exhibit out-of-plane behavior; the plate will then become twisted (nonzero  $\kappa_{12}$ ). During a test, this behavior is easily observed by placing displacement transducers at geometrically symmetric locations and observing the difference between the two displacements. (See Figure 2.4.) This type of coupling also contributes to the overall skewing behavior shown in Figure 2.2.

Extension-twisting coupling can occur only in laminates which are not midplane symmetric, since it is a form of bending-extensional coupling, and, as mentioned above, bending-extensional coupling occurs only when the layup is not midplane symmetric. The result of this type of coupling is that the plate experiences out-of-plane warping or twisting displacements when it is subjected to an inplane load. In the lab, this behavior can be observed in the same way as bending-twisting coupling; however, if both types of coupling are present, their effects cannot be isolated from each other in this way.

The last type of coupling exhibited by anisotropic panels is transverse shear coupling. This coupling, unlike all the others, does not have an obvious, physically observable effect on the panel response. However, it has recently been demonstrated (see [16]) that transverse shear can have a pronounced effect on the postbuckling response of laminated composite panels. Therefore, it is expected that coupling between the two transverse shear quantities can also be important in determining the response.

## 2.2 Symmetries Exhibited by Anisotropic Panels

The symmetry of the response of an isotropic or orthotropic panel is simple: if the panel geometry, loading and boundary conditions have mirror symmetry, then the entire panel response, including displacements, stresses, strains, and force resultants, will exhibit the same mirror symmetry. Similarly, if the loading is perfectly antisymmetric, then the response is also antisymmetric. However, for anisotropic panels, the situation is not so simple; inversion symmetry rather than mirror symmetry is exhibited.

Inversion symmetry, according to [13] and [17], means that if geometry, loading, and boundary conditions are symmetric, then the displacement field will satisfy the following symmetry statements:

$$\begin{aligned} u_\alpha(x_1, x_2) &= -u_\alpha(-x_1, -x_2) \\ w(x_1, x_2) &= w(-x_1, -x_2) \\ \phi_\alpha(x_1, x_2) &= -\phi_\alpha(-x_1, -x_2) \end{aligned} \quad \alpha = 1, 2 \quad (2.7)$$

Symmetry relations for the stress resultants are:

$$\begin{aligned} N_{\alpha\beta}(x_1, x_2) &= N_{\alpha\beta}(-x_1, -x_2) \\ M_{\alpha\beta}(x_1, x_2) &= M_{\alpha\beta}(-x_1, -x_2) \\ Q_{\alpha\beta}(x_1, x_2) &= -Q_{\alpha\beta}(-x_1, -x_2) \end{aligned} \quad \alpha, \beta = 1, 2 \quad (2.8)$$

This kind of symmetry is satisfied for both orthotropic and anisotropic panels. In a post-buckling problem where the out of plane response may be antisymmetric, the same symmetry conditions are obeyed, except that

$$\begin{aligned} w(x_1, x_2) &= -w(-x_1, -x_2) \\ \phi_\alpha(x_1, x_2) &= \phi_\alpha(-x_1, -x_2) \end{aligned}$$

This statement is only true for the case of no bending-extensional coupling. When bending-extensional coupling is present, there are no straightforward symmetry conditions unless the buckle pattern is symmetric (i.e.,  $w$  is symmetric).

Before considering exploiting the aforementioned symmetries in the classical Rayleigh-Ritz technique, one must understand the difference between symmetries exhibited by orthotropic and anisotropic panels. This is most easily done by considering how the problem would be solved when using the Rayleigh-Ritz method. Consider how each displacement degree of freedom might be approximated. Notice that the symmetry conditions on  $u_\alpha$  and  $\phi_\alpha$  are totally satisfied if these displacements are approximated by even functions in one of the coordinate directions and odd functions in the other. In fact, in the solution of orthotropic problems, these are precisely the kinds of functions which are used. The symmetry of the problem requires association of function symmetry with coordinate direction; for symmetric loading and therefore symmetric  $w$ , the symmetry conditions are:

$$\begin{Bmatrix} u_1 \\ u_2 \\ w \\ \phi_1 \\ \phi_2 \end{Bmatrix}_{(x_1, x_2)} = \begin{Bmatrix} -u_1 \\ u_2 \\ w \\ -\phi_1 \\ \phi_2 \end{Bmatrix}_{(-x_1, x_2)} = \begin{Bmatrix} u_1 \\ -u_2 \\ w \\ \phi_1 \\ -\phi_2 \end{Bmatrix}_{(x_1, -x_2)} \quad (2.9)$$

where the subscripts on each vector denote evaluation of the vector at the point shown. If the problem, and therefore  $w$ , is antisymmetric and there is no bending-extensional coupling, then

$$\begin{Bmatrix} u_1 \\ u_2 \\ w \\ \phi_1 \\ \phi_2 \end{Bmatrix}_{(x_1, x_2)} = \begin{Bmatrix} u_1 \\ -u_2 \\ -w \\ \phi_1 \\ -\phi_2 \end{Bmatrix}_{(-x_1, x_2)} = \begin{Bmatrix} -u_1 \\ u_2 \\ -w \\ -\phi_1 \\ \phi_2 \end{Bmatrix}_{(x_1, -x_2)} \quad (2.10)$$

These symmetry relations are the same as the modal symmetry relations cited in [18]. Using these symmetry relations, convenient tables can be formed indicating how the approximation functions should be chosen:

Table 2.1. Orthotropic Panel Symmetry States

	Symmetric $w$		Antisymmetric $w$	
	$x_1$	$x_2$	$x_1$	$x_2$
$w$	even	even	odd	odd
$u_1$ and $\phi_1$	odd	even	even	odd
$u_2$ and $\phi_2$	even	odd	odd	even

Henceforth, the two distinct sets of functions will be referred to as corresponding to an “even state”, where  $w$  is symmetric, or an “odd state”, where  $w$  is antisymmetric.

In the anisotropic case, the displacements still satisfy the inversion symmetry conditions, but they can no longer be approximated by a set of strictly even or strictly odd state functions as delineated for the orthotropic case. Rather, they must be represented by a combination of even and odd function sets since the two states become coupled. This coupling occurs due to the anisotropic material stiffness coefficients; when these terms are zero, the response is decoupled into a symmetric response due to a symmetric load, and an antisymmetric response due to an antisymmetric load. Therefore, as might be expected, the orthotropic problem is a special case of the anisotropic problem as far as symmetries are concerned. This fact will be used in Chapter 3 when operator splitting is introduced as a modification of the classical Rayleigh-Ritz method.

Another consequence of the more complex symmetries exhibited by anisotropic panels is that the finite element model must be larger. For an orthotropic panel, only one quarter of the panel must be analyzed, since the two panel centerlines are lines of response symmetry. However, for an anisotropic panel, the panel diagonal is the only line of response symmetry, and so half the panel must be analyzed. Reference [17] outlines procedures which can be used to analyze half of an anisotropic panel. Furthermore, as noted in later chapters, accurate representation of the more complex response of anisotropic panels requires a higher degree of discretization than for an orthotropic panel.



### 2.3 Governing Differential Equations of an Anisotropic Plate And Bending-Extensional Coupling

A short discussion of the governing differential equations associated with the problems solved herein is presented here. The methods used throughout this thesis are energy methods, but it is also useful to look briefly at the differential equations, since it is frequently helpful to view most problems from different perspectives in order to better understand and solve them.

The static differential equation of an orthotropic plate with no bending-extensional coupling subjected to transverse load is solvable for a fairly large number of cases. Only even-order derivatives of displacements are present in this equation; it can therefore be solved analytically by the method of separation of variables. To effect such a solution, transverse displacement  $w$  is represented by the product of two functions,  $F(x_1)G(x_2)$ , where one of either  $F$  or  $G$  must be a trigonometric function, i.e., a function whose second derivative is a constant times the original function.

However, when bending-twisting terms are included (i.e., terms involving  $D_{16}$  and  $D_{26}$ ), the equation becomes much more complicated due to the presence of odd as well as even-ordered derivatives. In this case, separation of variables will only be effective if either of  $F$  or  $G$  is of the form  $ke^{imx}$ , where  $k$  and  $m$  are constants and  $x$  is either  $x_1$  or  $x_2$ . Even so, the resulting ordinary differential equation is difficult to solve, since it contains imaginary terms. The only known analytical solution to a plate problem involving bending-twisting coupling involves a clamped, elliptical panel under uniform load, which is certainly a very limited case.

For an orthotropic plate subjected to inplane loading, there are three uncoupled differential equations. Two of these equations are simply the plane stress equilibrium equations and are solved first to give the inplane displacement field. The third equation involves only the out-of-plane response and is identically zero if there is no transverse load. However, if there is bending-extensional coupling, then the coupled constitutive relationship

serves to couple all three equations, and the solution becomes commensurately more difficult. If anisotropy is included, the additional difficulty of the odd-order derivatives again presents itself. Of course, if the nonlinear terms are added to the strain-displacement relations, then the inplane and out-of-plane differential equations are coupled even without bending-extensional coupling, since the force resultants will then contain terms involving  $w$ .

Therefore, the differential equations of an anisotropic plate with bending-extensional coupling are sufficiently complex to warrant numerical solution. Available techniques include Galerkin's method and, from an energy standpoint, either the Rayleigh-Ritz technique or its discretized version, the finite element method. Only the two energy methods will be considered herein.

## Chapter 3

### Development of the Modified Rayleigh-Ritz Technique

#### 3.1 Review of the Rayleigh-Ritz Technique

The Rayleigh-Ritz method is a well-known technique for approximating the behavior of engineering structures. It is the forerunner of the finite element method, in that it treats the entire structure as one large finite element. The classical method begins with the potential energy description of the problem, and results in a set of equations to be solved for the amplitudes of chosen approximation functions. This section reviews the technique and introduces the notation which is used in succeeding sections.

##### 3.1.1 Development of the Exact Energy Expression

The first step in the solution of the plate problem which is the topic of this thesis is to write an expression for the energy of the plate, where  $W^{\text{ext}}$  is the work of external forces:

$$U = \frac{1}{2} \int_V (\sigma_{ij} \varepsilon_{ij} + \sigma_{i3} \varepsilon_{i3} + \sigma_{3i} \varepsilon_{3i}) dV - W^{\text{ext}} \quad i, j = 1, \dots, 2 \quad (3.1)$$

Using the strain-displacement relations shown in equation 2.3, the plate strains  $\varepsilon_{ij}$  can be written as the sum of a linear and a nonlinear part as follows:

Linear terms:

$$\begin{Bmatrix} \varepsilon_{11} \\ \varepsilon_{22} \\ 2\varepsilon_{12} \\ 2\varepsilon_{13} \\ 2\varepsilon_{23} \end{Bmatrix}^L = \begin{Bmatrix} \varepsilon_{11}^0 \\ \varepsilon_{22}^0 \\ 2\varepsilon_{12}^0 \\ 2\varepsilon_{13} \\ 2\varepsilon_{23} \end{Bmatrix}^L + x_3 \begin{Bmatrix} \kappa_{11} \\ \kappa_{22} \\ 2\kappa_{12} \\ \cdot \\ \cdot \end{Bmatrix} = \begin{Bmatrix} \partial_1 u_1 + x_3 \partial_1 \phi_1 \\ \partial_2 u_2 + x_3 \partial_2 \phi_2 \\ \partial_1 u_2 + \partial_2 u_1 + x_3 (\partial_1 \phi_2 + \partial_2 \phi_1) \\ \phi_1 + \partial_1 w \\ \phi_2 + \partial_2 w \end{Bmatrix} \quad (3.2)$$

Nonlinear terms:

$$\begin{Bmatrix} \varepsilon_{11} \\ \varepsilon_{22} \\ 2\varepsilon_{12} \end{Bmatrix}^{\text{NL}} = \begin{Bmatrix} \varepsilon_{11}^0 \\ \varepsilon_{22}^0 \\ 2\varepsilon_{12}^0 \end{Bmatrix}^{\text{NL}} = \begin{Bmatrix} \frac{1}{2}(\partial_1 w)^2 \\ \frac{1}{2}(\partial_2 w)^2 \\ \partial_1 w \partial_2 w \end{Bmatrix} \quad (3.3)$$

Substituting these expressions into the strain energy and integrating over  $x_3$  introduces force and moment resultants into the strain energy expression:

$$\begin{aligned}
U = \frac{1}{2} \int & \left( [N_1 \quad N_2 \quad N_{12}] \begin{Bmatrix} \partial_1 u_1 \\ \partial_2 u_2 \\ \partial_1 u_2 + \partial_2 u_1 \end{Bmatrix} \right. \\
& + [M_1 \quad M_2 \quad M_{12}] \begin{Bmatrix} \partial_1 \phi_1 \\ \partial_2 \phi_2 \\ \partial_1 \phi_2 + \partial_2 \phi_1 \end{Bmatrix} \\
& + [N_1 \quad N_2 \quad N_{12}] \begin{Bmatrix} \frac{1}{2}(\partial_1 w)^2 \\ \frac{1}{2}(\partial_2 w)^2 \\ \partial_1 w \partial_2 w \end{Bmatrix} \\
& \left. + [Q_1 \quad Q_2] \begin{Bmatrix} \phi_1 + \partial_1 w \\ \phi_2 + \partial_2 w \end{Bmatrix} \right) dA - W^{\text{ext}}
\end{aligned} \tag{3.4}$$

The following vectors are now defined for ease of notation:

$$\{\varepsilon^L\} = \begin{Bmatrix} \partial_1 u_1 \\ \partial_2 u_2 \\ \partial_1 u_2 + \partial_2 u_1 \\ \partial_1 \phi_1 \\ \partial_2 \phi_2 \\ \partial_2 \phi_1 + \partial_1 \phi_2 \\ \phi_1 + \partial_1 w \\ \phi_2 + \partial_2 w \end{Bmatrix} \quad \{\varepsilon^{\text{NL}}\} = \begin{Bmatrix} \frac{1}{2} \partial_1^2 w \\ \frac{1}{2} \partial_2^2 w \\ \partial_1 w \partial_2 w \\ \cdot \\ \cdot \\ \cdot \\ \cdot \\ \cdot \end{Bmatrix} \tag{3.5}$$

These definitions transform the strain energy into a more manageable form:

$$\begin{aligned}
U = \frac{1}{2} \int & ([N_1 \quad N_2 \quad N_{12} \mid M_1 \quad M_2 \quad M_{12} \mid Q_1 \quad Q_2] \{\varepsilon^L\} \\
& + [N_1 \quad N_2 \quad N_{12}] \{\varepsilon^{\text{NL}}\}) dA - W^{\text{ext}}
\end{aligned} \tag{3.6}$$

The force and moment resultants are related to the strains by the constitutive relations, which are:

$$\begin{Bmatrix} N_1 \\ N_2 \\ N_{12} \\ - \\ M_1 \\ M_2 \\ M_{12} \\ - \\ Q_2 \\ Q_1 \end{Bmatrix} = \begin{bmatrix} A & B & \cdot \\ B^T & D & \cdot \\ \cdot & \cdot & C \end{bmatrix} \begin{Bmatrix} \varepsilon_1^0 \\ \varepsilon_2^0 \\ 2\varepsilon_{12}^0 \\ - \\ \kappa_1 \\ \kappa_2 \\ 2\kappa_{12} \\ - \\ 2\varepsilon_{23} \\ 2\varepsilon_{13} \end{Bmatrix} = [\mathbf{C}] \{ \{\varepsilon^L\} + \{\varepsilon^{\text{NL}}\} \} \tag{3.7}$$

This substitution finally leads to the following concise expression:

$$\begin{aligned}
U &= \frac{1}{2} \int [[\epsilon^L] + [\epsilon^{NL}]] [C] \{ \{\epsilon^L\} + \{\epsilon^{NL}\} \} dA - W^{\text{ext}} \\
&= \frac{1}{2} \int [[\epsilon^L] [C] \{\epsilon^L\} + [\epsilon^L] [C] \{\epsilon^{NL}\} \\
&\quad + [\epsilon^{NL}] [C] \{\epsilon^L\} + [\epsilon^{NL}] [C] \{\epsilon^{NL}\}] dA - W^{\text{ext}}
\end{aligned} \tag{3.8}$$

The energy is now composed of four distinct parts: terms involving either  $\{\epsilon^L\}$  or  $\{\epsilon^{NL}\}$  only, or combinations of  $\{\epsilon^L\}$  and  $\{\epsilon^{NL}\}$ , and the work of external forces. Now the energy can be conveniently subdivided in the following way:

$$U = U_2 + U_3 + U_4 - W^{\text{ext}}$$

where

$$\begin{aligned}
U_2 &= \frac{1}{2} \int [\epsilon^L] [C] \{\epsilon^L\} dA \\
U_3 &= \frac{1}{2} \int [\epsilon^L] [C] \{\epsilon^{NL}\} + [\epsilon^{NL}] [C] \{\epsilon^L\} dA \\
U_4 &= \frac{1}{2} \int [\epsilon^{NL}] [C] \{\epsilon^{NL}\} dA
\end{aligned} \tag{3.9}$$

The numeric subscripts indicate the power to which the generalized displacements are raised in each of the three terms. Notice that, due to the definitions in equation 3.5, the strain energy is now written entirely in terms of the material stiffness coefficients and the five displacement degrees of freedom  $u_1$ ,  $u_2$ ,  $\phi_1$ ,  $\phi_2$ , and  $w$ .

### 3.1.2 Selection and Use of Approximation Functions

At this point, the approximation functions for each of the five displacement degrees of freedom are inserted into the energy expression. In the classical version of the Rayleigh-Ritz method, these functions must be:

1. Capable of satisfying all geometric boundary conditions
2. Linearly independent
3. A subset of a complete set of functions (e.g., Fourier series)

#### 4. Differentiable up to the order present in the strain energy

The chosen set of approximation functions can be written as shown in equation 3.10 below, where  $\mathbf{X}$  is a vector of as yet unknown coefficients of all the approximation functions, and  $\mathbf{F}$  is a vector of the functions themselves. The indices  $P$ ,  $Q$ ,  $R$ ,  $S$ , and  $T$  range over the number of functions chosen to approximate each corresponding displacement; all the ranges may or may not be the same. (After the array multiplication, all repeated subscripts denote summation.)

$$\begin{Bmatrix} u_1 \\ u_2 \\ \phi_1 \\ \phi_2 \\ w \end{Bmatrix} = [\mathbf{F}]\{\mathbf{X}\} = \begin{bmatrix} F_P^{u_1} & F_Q^{u_2} & F_R^{\phi_1} & F_S^{\phi_2} & F_T^w \end{bmatrix} \begin{Bmatrix} X_P^{u_1} \\ X_Q^{u_2} \\ X_R^{\phi_1} \\ X_S^{\phi_2} \\ X_T^w \end{Bmatrix} \quad (3.10)$$

Substitution of these functions into equation 3.5 yields approximate expressions for  $\{\varepsilon^L\}$  and  $\{\varepsilon^{NL}\}$ . The linear strains then become

$$\{\varepsilon^L\} = R_{aI}^L \mathbf{X}_J = \begin{bmatrix} \partial_1 F_P^{u_1} & \cdot & \cdot & \cdot & \cdot \\ \cdot & \partial_2 F_Q^{u_2} & \cdot & \cdot & \cdot \\ \partial_2 F_P^{u_1} & \partial_1 F_Q^{u_2} & \cdot & \cdot & \cdot \\ \cdot & \cdot & \partial_1 F_R^{\phi_1} & \cdot & \cdot \\ \cdot & \cdot & \cdot & \partial_2 F_S^{\phi_2} & \cdot \\ \cdot & \cdot & \partial_2 F_R^{\phi_1} & \partial_1 F_S^{\phi_2} & \cdot \\ \cdot & \cdot & F_R^{\phi_1} & \cdot & \partial_1 F_T^w \\ \cdot & \cdot & \cdot & F_S^{\phi_2} & \partial_2 F_T^w \end{bmatrix}_{8, \overline{m}} \begin{Bmatrix} X_P^{u_1} \\ X_Q^{u_2} \\ X_R^{\phi_1} \\ X_S^{\phi_2} \\ X_T^w \end{Bmatrix} \quad (3.11)$$

where  $\overline{m}$  is the sum of all the ranges of  $P$ ,  $Q$ ,  $R$ ,  $S$ , and  $T$ , i.e., the total number of approximation functions used, and  $a$  ranges from one to eight, the number of strain quantities being used herein. The nonlinear strains are slightly more complicated. Approximation results in the three dimensional array  $R_{aIJ}^{NL}$ , rather than a simple two-dimensional matrix. This array can be thought of as having eight "planes", where each plane corresponds to the index  $a$  taking on a value ranging between one and eight. Therefore, each "plane" of this array corresponds to one element in the nonlinear strain vector shown in equation

3.5. There are only three nonzero planes, since there are only three nonzero nonlinear strain terms. Each plane is a matrix consisting of products of appropriately differentiated approximation functions; for example, the first plane, corresponding to the strain term  $\epsilon_{11}^{\text{NL}} = \frac{1}{2}(\partial_1 w)^2$  is as follows:

[illegible]

where  $T_1$  and  $T_2$  have the same range as  $T$ , i.e., the number of functions approximating  $w$ . All the zero rows and columns are included to maintain compatibility with equation 3.11, so that the indices  $I$  and  $J$  still have the same ranges.

At this point, it becomes more convenient to abandon the matrix notation of equations 3.11 and 3.12 in favor of index notation, so that reference is made to the two  $R$  arrays mentioned above, rather than to the detailed contents of  $\mathbf{F}$ . Using this notation, the two strain vectors become

$$\{\epsilon^L\} \equiv R_{aI}^L \mathbf{X}_I \quad (3.13)$$

$$\{\epsilon^{\text{NL}}\} \equiv R_{aIJ}^{\text{NL}} \mathbf{X}_I \mathbf{X}_J$$

The matrix of material stiffness coefficients is then denoted by  $C_{ab}$ , where  $b$ , like  $a$ , ranges from one to eight. (Recall that when index notation is used, repeated indices denote summation. In the present work, this rule applies only to subscripts.) Furthermore, the arrays  $\overline{K}$ ,  $\overline{F}$ , and  $\overline{G}$  may be introduced as the results of the integration over the area of the panel, excluding the unknowns  $\mathbf{X}_I$ . With these modifications, equation 3.9 becomes:

$$\begin{aligned}
U &= U_2 + U_3 + U_4 - W^{\text{ext}} \\
&= \frac{1}{2} \overline{K}_{IJ} \mathbf{X}_I \mathbf{X}_J + \frac{1}{2} \overline{F}_{IJK} \mathbf{X}_I \mathbf{X}_J \mathbf{X}_K + \frac{1}{2} \overline{G}_{IJKL} \mathbf{X}_I \mathbf{X}_J \mathbf{X}_K \mathbf{X}_L - W^{\text{ext}}
\end{aligned}$$

where

$$\begin{aligned}
U_2 &= \frac{1}{2} \int \mathbf{X}_I R_{Ia}^L \mathbf{C}_{ab} R_{bJ}^L \mathbf{X}_J dA \\
&= \frac{1}{2} \overline{K}_{IJ} \mathbf{X}_I \mathbf{X}_J \\
U_3 &= \frac{1}{2} \int (\mathbf{X}_I R_{Ia}^L \mathbf{C}_{ab} R_{bJK}^{\text{NL}} \mathbf{X}_J \mathbf{X}_K + \mathbf{X}_I \mathbf{X}_J R_{IJa}^{\text{NL}} \mathbf{C}_{ab} R_{bK}^L \mathbf{X}_K) dA \\
&= \frac{1}{2} \overline{F}_{IJK} \mathbf{X}_I \mathbf{X}_J \mathbf{X}_K \\
U_4 &= \frac{1}{2} \int \mathbf{X}_I \mathbf{X}_J R_{IJa}^{\text{NL}} \mathbf{C}_{ab} R_{bKL}^{\text{NL}} \mathbf{X}_K \mathbf{X}_L dA \\
&= \frac{1}{2} \overline{G}_{IJKL} \mathbf{X}_I \mathbf{X}_J \mathbf{X}_K \mathbf{X}_L
\end{aligned} \tag{3.14}$$

### 3.1.3 Generation of the Nonlinear Equations in $\mathbf{X}_I$ And the Recursion Formulas for the Newton-Raphson Iterative Procedure

The next step is to take the variation of the energy with respect to the unknown coefficients and require that the coefficient of the resulting variational quantity  $\delta \mathbf{X}_I$  vanish in order to satisfy the requirement for minimum potential energy. That is,

$$\begin{aligned}
\delta U &= \frac{\partial U}{\partial \mathbf{X}_I} \delta \mathbf{X}_I = 0 \\
\therefore \frac{\partial U}{\partial \mathbf{X}_I} &= 0
\end{aligned} \tag{3.15}$$

A linear set of equations  $\overline{K}_{IJ} \mathbf{X}_J = P_I$  is obtained if the higher order  $U_3$  and  $U_4$  terms are omitted from the energy; otherwise, a nonlinear set of equations in  $\mathbf{X}_I$  is obtained. A typical method of solving such a system of equations is the well-known Newton-Raphson technique, described briefly in Section 4.5. When using the Newton-Raphson technique, one solves a system of linear equations in each iteration. The equations have the form

$$\left[ \frac{\partial}{\partial \mathbf{X}_I} \left( \frac{\partial U}{\partial \mathbf{X}_J} \right) \right] \Delta \mathbf{X}_J = \left\{ P_I - \frac{\partial U}{\partial \mathbf{X}_I} \right\} \tag{3.16}$$

Thus, in order to solve the problem, two partial derivatives of the energy must be taken.



### 3.1.4 Symmetrization of the Nonlinear Arrays

To generate both the linear and nonlinear Newton-Raphson equations correctly requires some care with the index notation. Appendix A describes briefly the correct procedure, referred to as symmetrization, using only the quadratic contribution to the energy.

If the unbarred symbols  $K$ ,  $F$ , and  $G$  are now used to indicate symmetrized arrays as defined in Appendix A, the following nonlinear equations are obtained, along with the corresponding Newton-Raphson recursion formula in  $\mathbf{X}_I$ , where  $P_I$  is the load vector:

Nonlinear equations:

$$K_{IJ}\mathbf{X}_J + \frac{1}{2}F_{IJK}\mathbf{X}_J\mathbf{X}_K + \frac{1}{3}G_{IJKL}\mathbf{X}_J\mathbf{X}_K\mathbf{X}_L - P_I = 0 \quad (3.17)$$

Newton-Raphson recursion formula for iteration  $r + 1$ :

$$\begin{aligned} [K_{IJ} + F_{IJK}\mathbf{X}_K^r + G_{IJKL}\mathbf{X}_K^r\mathbf{X}_L^r]\Delta\mathbf{X}_J^{r+1} \\ = \{P_I - K_{IJ}\mathbf{X}_J^r - F_{IJK}\mathbf{X}_J^r\mathbf{X}_K^r - G_{IJKL}\mathbf{X}_J^r\mathbf{X}_K^r\mathbf{X}_L^r\} \end{aligned} \quad (3.18)$$

### 3.1.5 Generation of Load Vector $P$

The load vector  $P$  was generated from the variation of the work of external forces  $W^{\text{ext}}$  and is therefore dependent upon the particular load system being considered. For the case of a uniform transverse load, the work done is particularly simple; it is simply the product of the load magnitude and the transverse displacement, integrated over the loaded surface:

$$W^{\text{ext}} = \int p w dA = \int p X_T^w F_T^w dA \quad (3.19)$$

Then, the load vector  $P$  shown in equation 3.17 is just the variation of  $W^{\text{ext}}$ :

$$\delta W^{\text{ext}} = P_T \delta X_T^w = p \int F_T^w dA \delta X_T^w \quad (3.20)$$

In the case of an axial load, the situation is only slightly more complex. The work of an axial load is the product of the load magnitude and the axial displacement, integrated

along the loaded edge. If it is assumed that the panel is loaded along the edges  $x_1 = \pm \frac{a}{2}$ , then the work is written

$$\begin{aligned} W^{\text{ext}} &= \int_{-\frac{b}{2}}^{\frac{b}{2}} N_1 u_1(-\frac{a}{2}, x_2) + N_1 u_1(\frac{a}{2}, x_2) dx_2 \\ &= \int_{-\frac{b}{2}}^{\frac{b}{2}} N_1 X_P^{u_1} \left[ F_P^{u_1}(-\frac{a}{2}, x_2) + F_P^{u_1}(\frac{a}{2}, x_2) \right] dx_2 \end{aligned} \quad (3.21)$$

Finally, taking the variation results in the load vector  $P$ :

$$\delta W^{\text{ext}} = P_P \delta X_P^{u_1} = \int_{-\frac{b}{2}}^{\frac{b}{2}} N_1 \left[ F_P^{u_1}(-\frac{a}{2}, x_2) + F_P^{u_1}(\frac{a}{2}, x_2) \right] dx_2 \delta X_P^{u_1} \quad (3.22)$$

### 3.2 Enforcement of Boundary Conditions Using A Penalty Function Approach

In section 3.1.2, it was pointed out that in the classical version of the Rayleigh-Ritz technique, all the approximation functions must satisfy the geometric boundary conditions of the problem at hand. This requirement can be quite limiting, in that first, it is sometimes very difficult to devise functions which satisfy all the geometric boundary conditions, and second, those functions may or may not possess good convergence properties. Therefore, at this point the first deviation from the classical theory is made in the following two ways:

1. Choose functions which do not necessarily satisfy any boundary conditions
2. Enforce the boundary conditions using a penalty function

The penalty function approach consists of adding a penalty term  $\Pi$  to the potential energy expression and then working with the variation of the augmented energy in deriving equations in  $\mathbf{X}_I$ ; that is,

$$\begin{aligned} U_p &= U + \Pi \\ \delta U_p &= \delta U + \delta \Pi = 0 \end{aligned} \quad (3.23)$$

The penalty term represents the degree to which a given constraint (in this case, a boundary condition) is not satisfied. The constraint can be written as

$$\Pi = rh(\mathbf{X}_I) = 0 \quad (3.24)$$

where  $r$  is a penalty parameter and  $h(\mathbf{X}_I)$  is a function of the actual constraint. It is easy to see that if the penalty function is formulated such that it is always positive, then non-satisfaction of the constraint will increase the value of the augmented energy. Therefore, since setting the first variation of  $U_p$  to zero and solving for  $\mathbf{X}_I$  constitutes minimization of  $U_p$ , the penalty term is forced to zero and the constraint is satisfied. Note that the addition of the external penalty function can be viewed as the placement of a very stiff spring at points where constraints are to be imposed. The penalty parameter  $r$  is then analogous to the spring stiffness.

Careful selection of the penalty parameter  $r$  is very important, as noted in reference [19] and confirmed by results presented later. Proper choice of  $r$  strikes a balance between two requirements: the penalty parameter must be large enough to force satisfaction of the constraints, and small enough not to numerically dominate the problem and cause significant loss of precision.

As an example of constraint formulation, take the case of a  $w = 0$  boundary condition along an entire edge  $x_1 = 0$ . An integral constraint for this boundary condition may be written as follows:

$$h = \int_0^b [w(0, x_2)]^2 dx_2 \quad (3.25)$$

The integrand is raised to a power to ensure that the penalty function has a slope of zero when the constraint is satisfied, and so no discontinuity is introduced at the constraint boundary. Obviously, any power of  $w$  will satisfy this requirement; however, the use of an even power ensures that the constraint is positive if it is unsatisfied. Furthermore, an advantage of using the square of the constraint is that its variation is easily added to the linear stiffness matrix  $K$ , as will be shown subsequently.

Noting that  $w$  is represented by a series of approximation functions as described in Section 3.1.2, the constraint may be rewritten as

$$h = \int F_{T_1}^w(0, x_2) F_{T_2}^w(0, x_2) \mathbf{X}_{T_1} \mathbf{X}_{T_2} dx_2 \quad (3.26)$$

where  $T_1$  and  $T_2$  have the same range as  $T$ , i.e., the number of approximation functions representing  $w$ . If the penalty function is included in the derivation of the equilibrium equations as described above, the following term is then obtained:

$$\delta h = \frac{\partial h}{\partial \mathbf{X}_{T_1}} \delta \mathbf{X}_{T_1} = \int F_{T_1}^w(0, x_2) F_{T_2}^w(0, x_2) \mathbf{X}_{T_2} dx_2 \delta \mathbf{X}_{T_1} \quad (3.27)$$

This constraint can be recast in the following form so that it can be added directly to the linear term of the equilibrium equations:

$$\delta h = \begin{bmatrix} \cdot & \cdot & \cdot & \cdot & \cdot & \cdot \\ \cdot & \cdot & \cdot & \cdot & \cdot & \cdot \\ \cdot & \cdot & \cdot & \cdot & \cdot & \cdot \\ \cdot & \cdot & \cdot & \cdot & \cdot & \cdot \\ \cdot & \cdot & \cdot & \cdot & \cdot & \cdot \\ \cdot & \cdot & \cdot & \cdot & \cdot & \cdot \\ \cdot & \cdot & \cdot & \cdot & \cdot & \cdot \\ \cdot & \cdot & \cdot & \cdot & \cdot & \cdot \end{bmatrix} \begin{Bmatrix} X_P^{u_1} \\ X_Q^{u_2} \\ X_R^{\phi_1} \\ X_S^{\phi_2} \\ X_{T_2}^w \end{Bmatrix} \quad (3.28)$$

$[F_{T_1}^w \ F_{T_2}^w]_{T,T} \Big|_{\overline{m}, \overline{m}}$

This integral-type constraint becomes particularly simple if the approximation functions are orthogonal; then, the matrix shown in equation 3.28 is diagonal, since the integral is zero when  $T_1 \neq T_2$ . Notice that all that has been said about the edge constraint can be applied to constraints along a line (or even a curve) anywhere on the panel. Point constraints are even simpler, since they are not integrated; however, the constraint must still involve an even power since it must always be positive.

### 3.3 Operator Splitting

The operator splitting technique used herein allows two modifications to the classical Rayleigh-Ritz technique:

1. Partitioning of the approximation functions into strictly even and strictly odd sets of functions.
2. Splitting of the constitutive matrix into orthotropic and anisotropic parts.

The details and consequences of these modifications will be explained in the current section.

### 3.3.1 Basic Concepts

The justification for partitioning of the approximation functions into even and odd sets lies in the panel symmetry conditions outlined in Section 2.2. There it was noted that orthotropic panels exhibit purely symmetric or antisymmetric responses, depending on the symmetry of the loading and boundary conditions, while for anisotropic panels, coupling between the two types of responses occurs through the anisotropic (nonorthotropic) material stiffness coefficients. Taking these facts into account, it seems reasonable to choose functions for the anisotropic Rayleigh-Ritz analysis which are either strictly even or strictly odd, since it is known that the response can be represented by some combination of the two types of functions. Therefore, a partitioned set of approximation functions is defined, where each partition is of the same form as equation 3.10:

$$\mathbf{F}_I \mathbf{X}_J = F_i^e X_i^e + F_m^o X_m^o = \begin{bmatrix} [F^e]_{\mathcal{I}} & [F^o]_{\mathcal{M}} \end{bmatrix} \begin{Bmatrix} \{X^e\}_{\mathcal{I}} \\ \{X^o\}_{\mathcal{M}} \end{Bmatrix} \quad (3.29)$$

The superscripts  $e$  and  $o$  refer to even or odd symmetry states, respectively. Actually, since indices  $i$  through  $l$  will correspond only to even functions, and indices  $m$  through  $q$  will refer to odd functions, the superscripts are redundant; however, they will enhance readability later on. The uppercase Latin indices range over both sets of functions, while the uppercase script letters  $\mathcal{I}$  and  $\mathcal{M}$  indicate the total number of even and odd state functions, respectively. Recall from Chapter 2 that the term "symmetry state" refers to a set of approximation functions chosen according to the following table, which is repeated here for convenience:

Table 2.1. Orthotropic Panel Symmetry States

	Symmetric $w$		Antisymmetric $w$	
	$x_1$	$x_2$	$x_1$	$x_2$
$w$	even	even	odd	odd
$u_1$ and $\phi_1$	odd	even	even	odd
$u_2$ and $\phi_2$	even	odd	odd	even

At this point, a new convention is introduced for the partitioned arrays. It should be understood that whenever two arrays having indices with different ranges are added together, as in

$$\mathbf{X}_I = \mathbf{X}_i^e + \mathbf{X}_m^o \quad (3.30)$$

each array is to be expanded so as to be conformable for addition. For example, this equation could be rewritten using matrix notation as

$$\{\mathbf{X}\}_{\overline{m}} = \left\{ \frac{\{\mathbf{X}^e\}_{\mathcal{I}}}{\{\mathbf{0}\}_{\mathcal{M}}} \right\}_{\overline{m}} + \left\{ \frac{\{\mathbf{0}\}_{\mathcal{I}}}{\{\mathbf{X}^o\}_{\mathcal{M}}} \right\}_{\overline{m}} \quad (3.31)$$

Utilization of this convention will result in more concise equations, since the zero arrays will not be explicitly written.

It was also stated in Section 2.2 that coupling of even and odd responses occurs due to the presence of nonorthotropic material stiffness terms. In order to more easily understand and use this coupling effect, the problem is separated into two parts: an orthotropic part and a nonorthotropic part. This separation is easily accomplished by writing the constitutive matrix as follows:

$$\mathbf{C}_{ab} = \mathbf{C}_{ab}^O + \lambda \mathbf{C}_{ab}^A \quad (3.32)$$

where the superscripts O and A correspond to orthotropic and anisotropic (nonorthotropic) material stiffness coefficients, respectively. (Recall that the term anisotropic, as defined in Chapter 2, refers to all the constitutive terms with subscripts "16" and "26", as well as

the  $C_{45}$  term.) In this equation,  $\lambda$  is included as a tracing parameter for the anisotropic terms; that is, when those terms are to be included,  $\lambda$  is set to one. Otherwise,  $\lambda$  is zero. As a result of splitting the constitutive matrix, the procedures outlined in section 3.1 will lead to a set of nonlinear equations of the following form:

$$\begin{aligned} \bar{K}_{IJ}^O \mathbf{X}_J + \frac{1}{2} \bar{F}_{IJK}^O \mathbf{X}_J \mathbf{X}_K + \frac{1}{3} \bar{G}_{IJKL}^O \mathbf{X}_J \mathbf{X}_K \mathbf{X}_L \\ + \lambda (\bar{K}_{IJ}^A \mathbf{X}_J + \frac{1}{2} \bar{F}_{IJK}^A \mathbf{X}_J \mathbf{X}_K + \frac{1}{3} \bar{G}_{IJKL}^A \mathbf{X}_J \mathbf{X}_K \mathbf{X}_L) = P_I \end{aligned} \quad (3.33)$$

The combination of the special choice of approximation functions and the splitting of the constitutive matrix results in changes to the equilibrium equations which help to reveal the effects of anisotropy. To illustrate how these changes come about, the linear equations will be examined. Consider first how the linear stiffness array  $\bar{K}_{IJ}$  is formed. The orthotropic part of the  $\bar{K}$  array consists of the sum of the following four terms:

$$\begin{aligned} \bar{K}_{IJ}^O = \int \left( R_{ia}^{L(e)} C_{ab}^O R_{bj}^{L(e)} + R_{ia}^{L(o)} C_{ab}^O R_{bn}^{L(o)} \right. \\ \left. + R_{ma}^{L(o)} C_{ab}^O R_{bj}^{L(e)} + R_{ma}^{L(o)} C_{ab}^O R_{bn}^{L(o)} \right) dA \end{aligned} \quad (3.34)$$

where the parenthetical superscripts indicate the types of functions used to form the  $R$  arrays. The anisotropic part of the  $\bar{K}$  array is similar, except that  $C_{ab}^O$  is replaced by  $C_{ab}^A$ .

When the integration shown above is performed, an interesting thing happens. For the orthotropic array, all those terms formed from a mixture of even and odd functions vanish. In the anisotropic array just the opposite occurs; all terms which do not contain a mixture of terms drop out. Therefore, different combinations of even and odd superscripts also serve to identify whether the arrays are orthotropic or anisotropic. The two linear terms may then be written in a form analogous to equation 3.14:

$$\begin{aligned} \bar{K}_{IJ}^O &= \int \left( R_{ia}^{L(e)} C_{ab}^O R_{bj}^{L(e)} + R_{ma}^{L(o)} C_{ab}^O R_{bn}^{L(o)} \right) dA \\ &= \bar{K}_{ij}^{ee} + \bar{K}_{mn}^{oo} \\ \bar{K}_{IJ}^A &= \int \left( R_{ia}^{L(e)} C_{ab}^A R_{bn}^{L(o)} + R_{ma}^{L(o)} C_{ab}^A R_{bj}^{L(e)} \right) dA \\ &= \bar{K}_{in}^{eo} + \bar{K}_{mj}^{oe} \end{aligned} \quad (3.35)$$

The effect of the splitting process on the linear problem is more easily seen from the matrix form of the full linear set of equations, with the tracing constant included:

$$\left[ \begin{bmatrix} \bar{K}_{ij}^{ee} & \cdot \\ \cdot & \bar{K}_{mn}^{oo} \end{bmatrix} + \lambda \begin{bmatrix} \cdot & \bar{K}_{in}^{eo} \\ \bar{K}_{mj}^{oe} & \cdot \end{bmatrix} \right] \begin{Bmatrix} X_j^e \\ X_n^o \end{Bmatrix} = \begin{Bmatrix} P_i^e \\ P_m^o \end{Bmatrix} \quad (3.36)$$

(After the array multiplication is carried out, repeated indices denote summation.) Here it is easy to see how the even and odd parts of the equations decouple for an orthotropic problem (i.e., where  $\lambda = 0$ ), giving a symmetric response for a symmetric load system and an antisymmetric response for an antisymmetric load system. Conversely, one can also see how the coupling between the symmetric and antisymmetric systems is accomplished when the anisotropic stiffness terms are present.

From the above discussion, it is easy to make the incorrect assumption that whenever a mixture of even and odd functions is used to form the  $\bar{K}$ ,  $\bar{F}$ , or  $\bar{G}$  arrays, the result will be associated with the anisotropic elements of  $\mathbf{C}_{ab}$ . Rather, one way to determine whether terms are orthotropic or anisotropic is to assign a negative one to each odd set of functions comprising a term and a positive one to each even set. Then, take the product of the resulting combination of positive and negative ones. If the result is positive, then the term is orthotropic; otherwise, it is anisotropic. For example, take the two  $F$  terms shown here:

$$(1) \quad \bar{F}_{imj}^{eoe} = \int \left( R_{ia}^{L(e)} C_{ab}^A R_{bmj}^{NL(oe)} + R_{ima}^{NL(eo)} C_{ab}^A R_{bj}^{L(e)} \right) dA$$

$$(2) \quad \bar{F}_{min}^{ooo} = \int \left( R_{ma}^{L(o)} C_{ab}^O R_{bin}^{NL(eo)} + R_{mia}^{NL(oe)} C_{ab}^O R_{bn}^{L(o)} \right) dA$$

Term (1) is anisotropic, since the combination  $(eoe)$  gives  $(1 \cdot -1 \cdot 1) = -1$ , and term (2) is orthotropic, since  $(ooo)$  gives  $(-1 \cdot 1 \cdot -1) = 1$ . These separation properties arise from the form of the partial derivatives involved in the strain-displacement relations; if all the integrals are formed, it is easily seen that terms vanish in the various cases because the integrand is an odd function. This can be mathematically proven using group-theoretic methods; however, the proof is not presented here. Interested readers are referred to [20] for additional material on the subject.



### 3.3.2 Array Symmetrization When Partitioning is Used

As one might imagine, introduction of the partitioning scheme detailed in the previous section complicates derivation of the equations of equilibrium and the Newton-Raphson equations. Some additional bookkeeping is required in forming the various arrays, since there are now four  $\bar{K}$  arrays, eight  $\bar{F}$  arrays, and sixteen  $\bar{G}$  arrays. (These numbers can be reduced by noting that some of the arrays are identical.) In addition, the symmetrization described in Appendix A becomes somewhat more complicated. To illustrate the differences between partitioned and non-partitioned symmetrization, the linear portion of the problem will be re-examined in this section. The following presentation will be analogous to that of Appendix A, so that comparisons are easily made.

First, the energy term  $U_2$ , which involves only  $\bar{K}$ , is modified. This term must now be written to include the four partitions of  $\bar{K}$ , as follows:

$$U_2 = \frac{1}{2} \left[ \bar{K}_{ij}^{ee} X_i^e X_j^e + \bar{K}_{mn}^{oo} X_m^o X_n^o + \lambda (\bar{K}_{in}^{eo} X_i^e X_n^o + \bar{K}_{mj}^{oe} X_m^o X_j^e) \right] \quad (3.37)$$

Again, in order to take the variation of  $U_2$ , dummy indices must be employed, so that

$$\delta U_2 = \frac{\partial U_2}{\partial X_\alpha} \delta X_\alpha + \frac{\partial U_2}{\partial X_\beta} \delta X_\beta \quad (3.38)$$

The index  $\alpha$  has the same range as  $i$ , while  $\beta$  has the same range as  $m$ . Note that since  $U_2$  has been partitioned, its variation is now the sum of two separate variational quantities.

Now, the product rule of differentiation is applied, giving:

$$\begin{aligned} \delta U_2 = \frac{1}{2} \left[ \left[ \bar{K}_{ij}^{ee} \left( \frac{\partial X_i^e}{\partial X_\alpha^e} X_j^e + X_i^e \frac{\partial X_j^e}{\partial X_\alpha^e} \right) + \lambda \left( \bar{K}_{in}^{eo} \frac{\partial X_i^e}{\partial X_\alpha^e} X_n^o + \bar{K}_{mj}^{oe} X_m^o \frac{\partial X_j^e}{\partial X_\alpha^e} \right) \right] \delta X_\alpha^e \right. \\ \left. + \left[ \bar{K}_{mn}^{oo} \left( \frac{\partial X_m^o}{\partial X_\beta^o} X_n^o + X_m^o \frac{\partial X_n^o}{\partial X_\beta^o} \right) + \lambda \left( \bar{K}_{in}^{eo} X_i^e \frac{\partial X_n^o}{\partial X_\beta^o} + \bar{K}_{mj}^{oe} \frac{\partial X_m^o}{\partial X_\beta^o} X_j^e \right) \right] \delta X_\beta^o \right] \end{aligned} \quad (3.39)$$

After conversion of the partial derivatives to Kröneckers deltas, this expression becomes

$$\begin{aligned} \delta U_2 = \frac{1}{2} \left[ \left[ \bar{K}_{ij}^{ee} (\delta_{i\alpha} X_j^e + X_i^e \delta_{j\alpha}) + \lambda (\bar{K}_{in}^{eo} \delta_{i\alpha} X_n^o + \bar{K}_{mj}^{oe} X_m^o \delta_{j\alpha}) \right] \delta X_\alpha^e \right. \\ \left. + \left[ \bar{K}_{mn}^{oo} (\delta_{m\beta} X_n^o + X_m^o \delta_{n\beta}) + \lambda (\bar{K}_{in}^{eo} X_i^e \delta_{n\beta} + \bar{K}_{mj}^{oe} \delta_{m\beta} X_j^e) \right] \delta X_\beta^o \right] \end{aligned} \quad (3.40)$$

Elimination of the Krönecker deltas gives

$$\begin{aligned} \delta U_2 = \frac{1}{2} \left[ \left[ \bar{K}_{\alpha j}^{ee} X_j^e + \bar{K}_{i\alpha}^{ee} X_i^e + \lambda \left( \bar{K}_{\alpha n}^{eo} X_n^o + \bar{K}_{m\alpha}^{oe} X_m^o \right) \right] \delta X_\alpha^e \right. \\ \left. + \left[ \bar{K}_{\beta n}^{oo} X_n^o + \bar{K}_{m\beta}^{oo} X_m^o + \lambda \left( \bar{K}_{i\beta}^{eo} X_i^e + \bar{K}_{\beta j}^{oe} X_j^e \right) \right] \delta X_\beta^o \right] \end{aligned} \quad (3.41)$$

Finally, eliminating the dummy indices gives

$$\begin{aligned} \delta U_2 = \frac{1}{2} \left[ \left( \bar{K}_{ij}^{ee} + \bar{K}_{ji}^{ee} \right) X_j^e + \lambda \left( \bar{K}_{im}^{eo} + \bar{K}_{mi}^{oe} \right) X_m^o \right] \delta X_i^e \\ + \left( \left( \bar{K}_{mn}^{oo} + \bar{K}_{nm}^{oo} \right) X_n^o + \lambda \left( \bar{K}_{im}^{eo} + \bar{K}_{mi}^{oe} \right) X_i^e \right) \delta X_m^o \end{aligned} \quad (3.42)$$

Regrouping terms and adding in the loading terms leads to the complete variational expression of the linear problem:

$$\begin{aligned} \delta U_2 = \frac{1}{2} \left[ \left( \bar{K}_{ij}^{ee} + \bar{K}_{ji}^{ee} \right) X_j^e + \lambda \left( \bar{K}_{im}^{eo} + \bar{K}_{mi}^{oe} \right) X_m^o - P_i^e \right] \delta X_i^e \\ + \frac{1}{2} \left[ \left( \bar{K}_{mn}^{oo} + \bar{K}_{nm}^{oo} \right) X_n^o + \lambda \left( \bar{K}_{im}^{eo} + \bar{K}_{mi}^{oe} \right) X_i^e - P_m^o \right] \delta X_m^o \end{aligned} \quad (3.43)$$

Finally, because coefficients of the two variational quantities must vanish, the following two coupled sets of equations are obtained:

$$\begin{aligned} \frac{1}{2} \left( \bar{K}_{ij}^{ee} + \bar{K}_{ji}^{ee} \right) X_j^e + \frac{1}{2} \lambda \left( \bar{K}_{im}^{eo} + \bar{K}_{mi}^{oe} \right) X_m^o &= P_i^e \\ \frac{1}{2} \left( \bar{K}_{mn}^{oo} + \bar{K}_{nm}^{oo} \right) X_n^o + \frac{1}{2} \lambda \left( \bar{K}_{im}^{eo} + \bar{K}_{mi}^{oe} \right) X_i^e &= P_m^o \end{aligned} \quad (3.44)$$

With this step, symmetrization of the stiffness arrays  $\bar{K}$  has been achieved for a partitioned system. If the unbarred symbol  $K$  is now used to represent the symmetrized arrays, a set of partitioned equations identical to equation 3.36 is obtained:

$$\begin{aligned} K_{ij}^{ee} X_j^e + \lambda K_{im}^{eo} X_m^o &= P_i^e \\ K_{mn}^{oo} X_n^o + \lambda K_{mi}^{oe} X_i^e &= P_m^o \end{aligned} \quad (3.45)$$

Similar operations can be carried out on the  $\bar{F}$  and  $\bar{G}$  arrays in order to arrive at symmetrized arrays. For the same reason that there are only three unique  $K$  arrays ( $\bar{K}_{im}^{eo} = K_{mi}^{oe}$ ), symmetrization results in only four unique  $F$  arrays and five unique  $G$  arrays.

### 3.4 Application of Reduced Basis Techniques in Conjunction With Operator Splitting

Using the information presented in previous sections, one can obtain solutions to many different problems using classical linear and nonlinear equation solution techniques. However, additional information, as well as added computational efficiency, can be obtained by applying reduced basis techniques in conjunction with operator splitting.

Implicit in a reduced basis technique is the assumption that the problem unknowns (in this case, displacements) can be approximated by some linear combination of a set of independent "basis vectors". This assumption amounts to the transformation

$$\{\mathbf{X}\}_{\overline{m}} = [\Gamma]_{\overline{m},\mathcal{N}} \{\mathcal{X}\}_{\mathcal{N}} \quad (3.46)$$

where each column of the matrix  $[\Gamma]$  is a preselected basis vector or assumed mode, the vector  $\{\mathcal{X}\}$  contains an amplitude for each mode,  $\overline{m}$  is the total number of degrees of freedom contained in  $\mathbf{X}$ , and  $\mathcal{N}$  is the number of basis vectors to be used. A common choice for the basis vectors has been derivatives of a nonlinear solution with respect to a generalized path parameter [21]; that is,

$$[\Gamma]_{\overline{m},\mathcal{N}} = [ \{ X \} \quad \left\{ \frac{\partial X}{\partial \eta} \right\} \quad \left\{ \frac{\partial^2 X}{\partial \eta^2} \right\} \quad \dots \quad \left\{ \frac{\partial^{\mathcal{N}-1} X}{\partial \eta^{\mathcal{N}-1}} \right\} ]_{\overline{m},\mathcal{N}} \quad (3.47)$$

where  $\eta$  is the path parameter and  $X$  is the nonlinear solution. These basis vectors are commonly referred to as path derivatives.

The transformation shown above is used to effect a reduction in problem size; thus, a much smaller system of nonlinear equations is obtained. For a finite element problem of some size, solution of reduced equations is of course much less expensive than solution of the full set of equations. The reduced equations are used in place of the full system until a pre-defined error measure dictates that the basis vectors must be regenerated using a new nonlinear solution.

Recently, work has been done in which the basis vectors are derivatives of a finite element solution with respect to a tracing constant  $\lambda$  similar to that introduced in equation 3.32 [18]. The same concept will be used here, so that the transformation matrix  $[\Gamma]$  is defined as

$$[\Gamma]_{\overline{m},\mathcal{N}} = \left[ \{ \mathbf{X} \} |_{\lambda=0} \quad \left\{ \frac{\partial \mathbf{X}}{\partial \lambda} \right\} |_{\lambda=0} \quad \left\{ \frac{\partial^2 \mathbf{X}}{\partial \lambda^2} \right\} |_{\lambda=0} \quad \cdots \quad \left\{ \frac{\partial^{\mathcal{N}-1} \mathbf{X}}{\partial \lambda^{\mathcal{N}-1}} \right\} |_{\lambda=0} \right]_{\overline{m},\mathcal{N}} \quad (3.48)$$

Note that each vector is evaluated at  $\lambda = 0$ . This is because approximation of the problem unknowns in this way amounts to forming a “generalized” Taylor series about  $\lambda = 0$ , in which the normally fixed coefficients of the various series terms are replaced by free parameters [21]. That is, the solution to the anisotropic problem is viewed as a large perturbation from the orthotropic solution.

### 3.4.1 Generation of Basis Vectors

#### 3.4.1.a Linear Problem

A set of recursive equations which define the basis vectors is obtained by successive differentiation of the equilibrium equations and evaluation of the result at  $\lambda = 0$ , regardless of whether a linear or nonlinear problem is being solved. The linear problem will be discussed in the current section in order to introduce the concepts as simply as possible.

First, it is more convenient to deal with one indicial equation, and so the two equations 3.45 are combined to give a single equilibrium equation.

$$K_{ij}^{ee} X_j^e + K_{mn}^{oo} X_n^o + \lambda (K_{in}^{eo} X_n^o + K_{mj}^{oe} X_j^e) = P_i^e + P_m^o \quad (3.49)$$

An equation defining the first basis vector,  $(\mathbf{X}_I)_0 = (X_i^e + X_m^o)_0$ , is obtained by simply evaluating equation 3.49 at  $\lambda = 0$ , giving

$$K_{ij}^{ee} (X_j^e)_0 + K_{mn}^{oo} (X_n^o)_0 = P_i^e + P_m^o \quad (3.50)$$

(The zero subscript is a reminder that all the basis vectors are evaluated at  $\lambda = 0$ .) Notice that this equation can be written as two sets of uncoupled equations in  $X_j^e$  and  $X_n^o$ .

$$\begin{aligned} K_{ij}^{ee} (X_j^e)_0 &= P_i^e \\ K_{mn}^{oo} (X_n^o)_0 &= P_m^o \end{aligned} \quad (3.51)$$

An equation defining the second basis vector is obtained by differentiating equation 3.49 with respect to  $\lambda$  one time and evaluating the result at  $\lambda = 0$ . First, the differentiation:

$$K_{ij}^{ee} \frac{\partial X_j^e}{\partial \lambda} + K_{mn}^{oo} \frac{\partial X_n^o}{\partial \lambda} + (K_{in}^{eo} X_n^o + K_{mj}^{oe} X_j^e) + \lambda \left( K_{in}^{eo} \frac{\partial X_n^o}{\partial \lambda} + K_{mj}^{oe} \frac{\partial X_j^e}{\partial \lambda} \right) = 0 \quad (3.52)$$

Now, evaluation at  $\lambda = 0$  gives:

$$K_{ij}^{ee} \left( \frac{\partial X_j^e}{\partial \lambda} \right)_0 + K_{mn}^{oo} \left( \frac{\partial X_n^o}{\partial \lambda} \right)_0 = -(K_{in}^{eo} (X_n^o)_0 + K_{mj}^{oe} (X_j^e)_0) \quad (3.53)$$

Once again, an uncoupled set of equations is obtained:

$$\begin{aligned} K_{ij}^{ee} \left( \frac{\partial X_j^e}{\partial \lambda} \right)_0 &= -K_{in}^{eo} (X_n^o)_0 \\ K_{mn}^{oo} \left( \frac{\partial X_n^o}{\partial \lambda} \right)_0 &= -K_{mj}^{oe} (X_j^e)_0 \end{aligned} \quad (3.54)$$

These equations can be solved for the second basis vector, which is the first derivative of the problem unknowns with respect to  $\lambda$ . Note that the right hand sides of the above equations contain  $(X_l^o)_0$  and  $(X_j^e)_0$ , which are known from the solution of equations 3.50.

As many basis vectors as are needed can be obtained by continuing this process. The resulting equations are defined by the following recursion formulae:

$$\begin{aligned} K_{ij}^{ee} (X_j^e)_0 + K_{mn}^{oo} (X_n^o)_0 &= P_i^e + P_m^o \\ K_{ij}^{ee} \left( \frac{\partial^c X_j^e}{\partial \lambda^c} \right)_0 + K_{mn}^{oo} \left( \frac{\partial^c X_n^o}{\partial \lambda^c} \right)_0 &= \\ &- c \left( K_{in}^{eo} \left( \frac{\partial^{c-1} X_n^o}{\partial \lambda^{c-1}} \right)_0 + K_{mj}^{oe} \left( \frac{\partial^{c-1} X_j^e}{\partial \lambda^{c-1}} \right)_0 \right) \quad c = 1, 2, \dots, \mathcal{N} \end{aligned} \quad (3.55)$$

Notice that the even and odd partitions will continue to be uncoupled in every set of equations. A large savings in factorization time is therefore obtained, since each partition is generally half the size of the full system of equations, and factorization time is proportional to the cube of the number of equations. Total factorization time is therefore reduced by a factor of four.

An important simplification to the recursive equations can be realized if both the loading and boundary conditions are either purely symmetric or purely antisymmetric. Recall from Chapter 2 that the response symmetry of an orthotropic panel is the same as the symmetry of the load system; that is, if the load is symmetric, then the response is also symmetric, and similarly for an antisymmetric load case. Since equations 3.50 are simply the equilibrium equations for an orthotropic panel, pure symmetry or antisymmetry of the load system gives:

$$\begin{aligned} \text{symmetric loading} &\implies P_m^o = 0 \implies (X_m^o)_0 = 0 \\ \text{antisymmetric loading} &\implies P_i^e = 0 \implies (X_i^e)_0 = 0 \end{aligned}$$

These simplifications propagate through the recursive equations so that in each set of equations, only one matrix, either  $K_{ij}^{ee}$  or  $K_{mn}^{oo}$ , must be factored. For example, if the loading is symmetric, the recursive equations become

$$\begin{aligned} K_{ij}^{ee} (X_j^e)_0 &= P_i^e \\ K_{mn}^{oo} \left( \frac{\partial^c X_n^o}{\partial \lambda^c} \right)_0 &= -c K_{mj}^{oe} \left( \frac{\partial^{c-1} X_j^e}{\partial \lambda^{c-1}} \right)_0 \quad c = 1, 3, 5, \dots \\ K_{ij}^{ee} \left( \frac{\partial^c X_j^e}{\partial \lambda^c} \right)_0 &= -c K_{in}^{eo} \left( \frac{\partial^{c-1} X_n^o}{\partial \lambda^{c-1}} \right)_0 \quad c = 2, 4, 6, \dots \end{aligned} \quad (3.56)$$

The transformation matrix  $[\Gamma]$  also takes on a simpler form when the loading is symmetric or antisymmetric. In the case of load symmetry,  $[\Gamma]$  becomes

$$[\Gamma]_{\overline{m}, \mathcal{N}} = \left[ \left\{ \frac{\{X^e\}_{\mathcal{I}}}{0} \right\}_0 \quad \left\{ \frac{0}{\{\frac{\partial X^o}{\partial \lambda}\}_{\mathcal{M}}} \right\}_0 \quad \left\{ \frac{\{\frac{\partial^2 X^e}{\partial \lambda^2}\}_{\mathcal{I}}}{0} \right\}_0 \quad \dots \right]_{\overline{m}, \mathcal{N}} \quad (3.57)$$

If the load is antisymmetric, then similarly,

$$[\Gamma]_{\overline{m},\mathcal{N}} = \left[ \left\{ \frac{0}{\{X^o\}_{\mathcal{M}}} \right\}_0 \quad \left\{ \frac{\left\{ \frac{\partial X^e}{\partial \lambda} \right\}_{\mathcal{I}}}{0} \right\}_0 \quad \left\{ \frac{0}{\left\{ \frac{\partial^2 X^o}{\partial \lambda^2} \right\}_{\mathcal{M}}} \right\}_0 \quad \dots \right]_{\overline{m},\mathcal{N}} \quad (3.58)$$

### 3.4.1.b Nonlinear Problem

For the nonlinear problem, the procedure for obtaining the recursion equations defining the basis vectors is similar to that used for the linear problem. As with the linear problem, these recursive equations are only half as large as the original set of equations; furthermore, only the first of the equations is nonlinear. As before, equations defining the basis vectors are obtained via successive differentiation of the nonlinear equilibrium equations and evaluation of the result at  $\lambda = 0$ .

Recall first that the nonlinear equations obtained using the method outlined in Appendix A are considerably longer than the linear equations, due to terms involving the three and four dimensional arrays  $F$  and  $G$ . In this section, only the terms involving  $K$  and  $F$  will be included in the explanation of the development, since addition of the  $G$  terms results in extremely long and unwieldy equations which do not significantly add to the understanding of the concepts involved. The reader will find that patterns uncovered in the shorter equations presented here are very similar to those found in the longer equations.

The procedure begins with the following coupled equilibrium equations, which already include the tracing constant  $\lambda$ :

$$\begin{aligned} & K_{ij}^{ee} X_j^e + (F_{ijk}^{eee} + F_{jik}^{eee} + F_{kji}^{eee}) X_j^e X_k^e + 2(F_{mni}^{ooo} + F_{min}^{ooo} + F_{imn}^{ooo}) X_m^o X_n^o \\ & + \lambda [K_{im}^{eo} X_m^o + (F_{ijm}^{eoo} + F_{jim}^{eoo} + F_{imj}^{eoo} + F_{jmi}^{eoo} + F_{mij}^{eoo} + F_{mji}^{eoo}) X_j^e X_m^o] \\ & = P_i^e \\ & \hline & K_{mn}^{oo} X_n^o + (F_{mni}^{ooo} + F_{nmi}^{ooo} + F_{min}^{ooo} + F_{nim}^{ooo} + F_{imn}^{ooo} + F_{inm}^{ooo}) X_i^e X_n^o \\ & + \lambda [(K_{mi}^{oe} X_i^e + (F_{mnp}^{ooo} + F_{nmp}^{ooo} + F_{pnm}^{ooo}) X_n^o X_p^o + 2(F_{ijm}^{eoo} + F_{imj}^{eoo} + F_{mij}^{eoo}) X_i^e X_j^e] \\ & = P_m^o \end{aligned} \quad (3.59)$$

An equation defining the first basis vector,  $(X_I)_0 = (X_i^e + X_m^o)_0$ , is obtained by simply evaluating equations 3.59 at  $\lambda = 0$ , giving

$$K_{ij}^{ee} (X_j^e)_0 + (F_{ijk}^{eee} + F_{jik}^{eee} + F_{kji}^{eee}) (X_j^e)_0 (X_k^e)_0 \\ + 2(F_{mni}^{ooo} + F_{min}^{ooo} + F_{imn}^{ooo}) (X_m^o)_0 (X_n^o)_0 = P_i^e$$


---

$$K_{mn}^{oo} (X_n^o)_0 + (F_{mni}^{ooe} + F_{nmi}^{ooe} + F_{min}^{ooe} \\ + F_{nim}^{oeo} + F_{imn}^{oeo} + F_{inm}^{oeo}) (X_i^e)_0 (X_n^o)_0 = P_m^o \quad (3.60)$$

(The zero subscript is a reminder that all the basis vectors are evaluated at  $\lambda = 0$ .) These two equations are slightly more difficult to uncouple than the corresponding linear equations were, in that assumptions must first be made about the load and boundary condition symmetry. Take the case of perfectly symmetric loading and boundary conditions, in which case the vector  $P_m^o$  is identically zero. To see the result of this, rewrite the second of equations 3.60 as follows:

$$\{K_{mn}^{oo} + (F_{mni}^{ooe} + F_{nmi}^{ooe} + F_{min}^{ooe} + F_{nim}^{oeo} + F_{imn}^{oeo} + F_{inm}^{oeo}) (X_i^e)_0\} (X_n^o)_0 = P_m^o \quad (3.61)$$

If  $P_m^o$  is zero, then either the term in brackets is zero or  $(X_n^o)_0$  is zero. If  $(X_n^o)_0$  is zero, then the first of the recursive equations is just the equilibrium equation for the corresponding orthotropic problem:

$$K_{ij}^{ee} (X_j^e)_0 + (F_{ijk}^{eee} + F_{jik}^{eee} + F_{kji}^{eee}) (X_j^e)_0 (X_k^e)_0 = P_i^e \quad (3.62)$$

This equation completely defines the first basis vector. Note that it is nonlinear; however, it is also half the size of the original full system of equations.



A set of equations defining the second basis vector is obtained by differentiating 3.59 with respect to  $\lambda$  one time and evaluating the result at  $\lambda = 0$ . First, the differentiation:

$$\begin{aligned}
& K_{ij}^{ee} \frac{\partial X_j^e}{\partial \lambda} + (F_{ijk}^{eee} + F_{jik}^{eee} + F_{kji}^{eee}) \left( \frac{\partial X_j^e}{\partial \lambda} X_k^e + X_j^e \frac{\partial X_k^e}{\partial \lambda} \right) \\
& + 2(F_{mni}^{ooo} + F_{min}^{ooo} + F_{imn}^{ooo}) \left( \frac{\partial X_m^o}{\partial \lambda} X_n^o + X_m^o \frac{\partial X_n^o}{\partial \lambda} \right) \\
& + \lambda \left[ (K_{im}^{eo} \frac{\partial X_m^o}{\partial \lambda} + (F_{ijm}^{eeo} + F_{jim}^{eeo} + F_{imj}^{eeo} \right. \\
& \quad \left. + F_{jmi}^{eoe} + F_{mij}^{eoe} + F_{mji}^{eoe}) \left( \frac{\partial X_j^e}{\partial \lambda} X_m^o + X_j^e \frac{\partial X_m^o}{\partial \lambda} \right) \right] \\
& = -(K_{im}^{eo} X_m^o + (F_{ijm}^{eeo} + F_{jim}^{eeo} + F_{imj}^{eeo} + F_{jmi}^{eoe} + F_{mij}^{eoe} + F_{mji}^{eoe}) X_j^e X_m^o) \\
& K_{mn}^{oo} \frac{\partial X_n^o}{\partial \lambda} + (F_{mni}^{ooo} + F_{nmi}^{ooo} + F_{min}^{ooo} + F_{nim}^{ooo} + F_{imn}^{ooo} + F_{inm}^{ooo}) \left( \frac{\partial X_i^e}{\partial \lambda} X_n^o + X_i^e \frac{\partial X_n^o}{\partial \lambda} \right) \\
& + \lambda \left[ (K_{mi}^{oe} \frac{\partial X_i^e}{\partial \lambda} + (F_{mnp}^{ooo} + F_{nmp}^{ooo} + F_{pnm}^{ooo}) \left( \frac{\partial X_n^o}{\partial \lambda} X_p^o + X_n^o \frac{\partial X_p^o}{\partial \lambda} \right) \right. \\
& \quad \left. + 2(F_{ijm}^{eeo} + F_{imj}^{eeo} + F_{mij}^{eeo}) \left( \frac{\partial X_i^e}{\partial \lambda} X_j^e + X_i^e \frac{\partial X_j^e}{\partial \lambda} \right) \right] \\
& = -(K_{mi}^{oe} X_i^e + (F_{mnp}^{ooo} + F_{nmp}^{ooo} + F_{pnm}^{ooo}) X_n^o X_p^o \\
& \quad + 2(F_{ijm}^{eeo} + F_{imj}^{eeo} + F_{mij}^{eeo}) X_i^e X_j^e)
\end{aligned} \tag{3.63}$$

Now, evaluation at  $\lambda = 0$  gives:

$$\begin{aligned}
& K_{ij}^{ee} \left( \frac{\partial X_j^e}{\partial \lambda} \right)_0 + (F_{ijk}^{eee} + F_{jik}^{eee} + F_{kji}^{eee}) \left[ \left( \frac{\partial X_j^e}{\partial \lambda} \right)_0 (X_k^e)_0 + (X_j^e)_0 \left( \frac{\partial X_k^e}{\partial \lambda} \right)_0 \right] \\
& + 2(F_{mni}^{ooo} + F_{min}^{ooo} + F_{imn}^{ooo}) \left[ \left( \frac{\partial X_m^o}{\partial \lambda} \right)_0 (X_n^o)_0 + (X_m^o)_0 \left( \frac{\partial X_n^o}{\partial \lambda} \right)_0 \right] \\
& = -K_{im}^{eo} (X_m^o)_0 \\
& \quad - (F_{ijm}^{eeo} + F_{jim}^{eeo} + F_{imj}^{eeo} + F_{jmi}^{eoe} + F_{mij}^{eoe} + F_{mji}^{eoe}) (X_j^e)_0 (X_m^o)_0 \\
& K_{mn}^{oo} \left( \frac{\partial X_n^o}{\partial \lambda} \right)_0 + (F_{mni}^{ooo} + F_{nmi}^{ooo} + F_{min}^{ooo} \\
& \quad + F_{nim}^{ooo} + F_{imn}^{ooo} + F_{inm}^{ooo}) \left[ \left( \frac{\partial X_i^e}{\partial \lambda} \right)_0 (X_n^o)_0 + (X_i^e)_0 \left( \frac{\partial X_n^o}{\partial \lambda} \right)_0 \right] \\
& = -K_{mi}^{oe} (X_i^e)_0 - (F_{mnp}^{ooo} + F_{nmp}^{ooo} + F_{pnm}^{ooo}) (X_n^o)_0 (X_p^o)_0 \\
& \quad - 2(F_{ijm}^{eeo} + F_{imj}^{eeo} + F_{mij}^{eeo}) (X_i^e)_0 (X_j^e)_0
\end{aligned} \tag{3.64}$$

For a symmetric problem where  $(X_n^o)_0$  is zero, these equations become:

$$K_{ij}^{ee} \left( \frac{\partial X_j^e}{\partial \lambda} \right)_0 + (F_{ijk}^{eee} + F_{jik}^{eee} + F_{kji}^{eee}) \left[ \left( \frac{\partial X_j^e}{\partial \lambda} \right)_0 (X_k^e)_0 + (X_j^e)_0 \left( \frac{\partial X_k^e}{\partial \lambda} \right)_0 \right] = 0$$

---


$$\begin{aligned} K_{mn}^{oo} \left( \frac{\partial X_n^o}{\partial \lambda} \right)_0 + (F_{mni}^{ooo} + F_{nmi}^{ooo} + F_{min}^{ooo} + F_{nim}^{ooo} + F_{imn}^{ooo} + F_{inm}^{ooo}) \left[ (X_i^e)_0 \left( \frac{\partial X_n^o}{\partial \lambda} \right)_0 \right] \\ = - \left[ K_{mi}^{oe} (X_i^e)_0 + 2(F_{ijm}^{eeo} + F_{imj}^{eeo} + F_{mij}^{eeo}) (X_i^e)_0 (X_j^e)_0 \right] \end{aligned} \quad (3.65)$$

The first of these equations says that  $\left( \frac{\partial X_i^e}{\partial \lambda} \right)_0$  vanishes, while the second equation defines the second basis vector  $\left( \frac{\partial X_m^o}{\partial \lambda} \right)_0$ . Notice that both equations are linear, since both  $(X_i^e)_0$  and  $(X_m^o)_0$  are known quantities. Also note that the same pattern of alternation between derivatives of even and odd parts of  $\mathbf{X}_I$  is occurring, as was shown for the linear problem in equation 3.57. As before, as many basis vectors as are needed can be obtained by continuing this process.

### 3.4.2 Generation and Solution of the Reduced Equation System

#### **3.4.2.a Linear Problem**

Once the desired basis vectors have been obtained, the reduction of the original system of equations can be done. Before beginning, it is convenient to rewrite the transformation matrix using the more compact index notation, as well as the superscripts  $e$  and  $o$  to indicate even and odd partitions as before.

$$[\Gamma]_{\overline{m}, \mathcal{N}} = \left[ \frac{[\Gamma^e]_{\mathcal{I}, \mathcal{N}}}{[\Gamma^o]_{\mathcal{M}, \mathcal{N}}} \right]_{\overline{m}, \mathcal{N}} = \Gamma_{ic}^e + \Gamma_{mc}^o \quad (3.66)$$

Using this notation, equation 3.46 can be written in greater detail as

$$X_i^e + X_m^o = (\Gamma_{ic}^e + \Gamma_{mc}^o) \mathcal{X}_c \quad (3.67)$$

Application of the transformation is a fairly simple two step procedure. First, the displacement degrees of freedom in the original equilibrium equation 3.49 are replaced by

the transformation equation; then, the resulting equation is premultiplied by the transformation matrix so that the resulting system is symmetric.

$$\begin{aligned}
 &(\Gamma_{di}^e K_{ij}^{ee} \Gamma_{jc}^e + \Gamma_{dm}^o K_{mn}^{oo} \Gamma_{nc}^o \\
 &+ \Gamma_{di}^e K_{in}^{eo} \Gamma_{nc}^o + \Gamma_{dm}^o K_{mj}^{oe} \Gamma_{jc}^e) \mathcal{X}_c = \Gamma_{dj}^e P_j^e + \Gamma_{dn}^o P_n^o
 \end{aligned} \tag{3.68}$$

This equation is a symmetric system of  $\mathcal{N}$  equations whose solution gives the participation coefficients  $\mathcal{X}_c$ , and can be rewritten as

$$\mathcal{K}_{dc} \mathcal{X}_c = \mathcal{P}_d \tag{3.69}$$

Once the participation coefficients are obtained, the full solution  $\mathbf{X}_I$  can be recovered using equation 3.46, and solution of the linear problem is complete.

### 3.4.2.b Nonlinear Problem

The basis vectors generated by the procedure outlined in Section 3.4.1.b can be used to greatly reduce the computational effort involved in the static nonlinear analysis of an anisotropic panel. More precisely, the effort required for solution of an anisotropic problem can be reduced to slightly more than the effort required for the corresponding orthotropic problem, provided that the loading and boundary conditions are symmetric. The sequence of steps for the simplest possible application of the reduction technique to nonlinear problems is as follows:

1. Given a load factor  $p$ , solve for the  $\mathcal{N}$  nonlinear basis vectors corresponding to that load level. Obtaining the basis vectors involves solution of one nonlinear set of equations (equation 3.62) and  $\mathcal{N} - 1$  linear equations (similar to equation 3.65). All these equation systems are half the size of the corresponding equations for the anisotropic structure.
2. Compute the reduced nonlinear equations using these basis vectors. The resulting system will be much smaller than the original set of equations. Usually no more than fifteen basis vectors are needed. Also, since there is a definite pattern

defining the basis vectors which are zero, the computational effort required to generate the reduced equation system can be reduced by judicious use of this pattern.

3. Solve the reduced system of nonlinear equations to get the participation coefficients  $\mathcal{X}_c$  for each of the basis vectors.
4. Recover the full anisotropic solution by taking  $\mathbf{X}_I = \Gamma_{Ic}\mathcal{X}_c$ .
5. Choose the next load factor and repeat the process until the maximum desired load factor is attained.

The nonlinear equation solutions delineated above can of course be performed using any suitable nonlinear equation solution technique, of which the classical Newton-Raphson method is an example.

Computationally faster techniques have been developed which can be used in place of the above procedure; these techniques are outlined in [18]. There are two basic methods, one of which uses two successive single-parameter reductions, while the other applies only one two-parameter reduction. In both cases, one of the parameters is the anisotropic tracing constant used herein, and the other parameter is the load factor. Both techniques offer advantages over the modified classical Newton-Raphson technique described above, with the two-parameter reduction technique being the most efficient. The procedure described above has the advantage of requiring only one single-parameter reduction and is therefore somewhat easier to develop; from a computer programming standpoint, it should be used as a starting point from which to implement the techniques described in the references.

## Chapter 4

### Numerical Studies of Modified Rayleigh-Ritz Technique

#### 4.1 Comments on Problem Selection

The purpose of the present chapter is to present numerical results, both linear and nonlinear, obtained using the modified Rayleigh-Ritz technique of the previous chapter. Several different physical problems have been chosen for this purpose. In those problems involving anisotropic panels, the laminates, loading, and boundary conditions have been chosen to correspond as closely as possible to the two seven inch-wide experimental panels described in Chapter 5. Further comments regarding the detailed characteristics of each laminate may be found in Chapter 5. The only difference between the anisotropic panels presented in the present chapter and those of Chapter 5 is that in implementing the Ritz technique, some compromises had to be made in modeling the boundary conditions; these are discussed in greater detail later in the current chapter. As a result, quantitative comparison is not made between the Rayleigh-Ritz and experimental results; however, qualitative discussion is presented. Problems presented in this chapter which do not correspond to the panels of Chapter 5 are for comparison purposes only.

#### 4.2 Linear Results

In Rayleigh-Ritz analysis, quality of results depends greatly on the suitability of the displacement approximation functions  $X_i$  to the problem at hand. The present section will determine the suitability of a very simple set of functions by presenting solutions to four problems involving various support/loading conditions and various layup configurations.

The software written to implement the modified Rayleigh-Ritz technique allows the use of any set of functions satisfying the following two criteria:

1. Separability: all functions must be of the form  $f(x)g(y)$ .
2. Symmetry: functions must be such that sets of functions can be formed which adhere to the symmetries shown in Table 2.1.

The fairly simple set of functions shown in Table 4.1 satisfies these two requirements and is composed only of trigonometric functions such as sine and cosine, as well as simple linear polynomials. Various subsets of those functions were used to generate all the results presented in this section.

To determine the suitability of these functions, two sets of symmetric support/loading conditions will be examined:

1. Uniform transverse loading, with simple support boundary conditions.
2. Uniform axial loading, with clamped/simple support boundary conditions.

Schematics of these two problems may be found in Figure 4.1.

Before proceeding, the term "simple support" for the case of a panel with bending-extensional coupling needs clarification. The classical definition of a simply supported boundary is that transverse displacement ( $w$ ) and normal moment ( $M_n$ ) must vanish along the boundary. However, in the presence of bending-extensional coupling, inplane behavior must also be considered, since it will occur even if the load is strictly transverse. According to [5], four different constraint cases involving various combinations of in-plane and out-of-plane displacement constraints and force resultant constraints can imply a simple support boundary condition; the condition used for the linear test problems solved herein is as follows:

$$w = M_n = N_n = N_{nt} = 0$$

where  $n$  and  $t$  are used to designate directions normal and tangent to a boundary, respectively. For a formulation which excludes transverse shear deformation, the only condition to be imposed is the  $w = 0$  requirement, since the constraints on moment and force resultants are considered natural boundary conditions and are therefore not enforceable in a Rayleigh-Ritz formulation. For a formulation which includes transverse shear deformation, the rotational quantity  $\phi_n$  is also constrained for a simply supported edge; in the notation of the present work, for an edge where  $x_1 = \text{constant}$ ,  $\phi_2 = 0$ , and conversely for an edge where  $x_2 = \text{constant}$ ,  $\phi_1 = 0$ .

Table 4.1. Rayleigh-Ritz Analysis Functions

a. Linear Polynomial Functions

	$x_1$ Direction		$x_2$ Direction	
	Even	Odd	Even	Odd
$w$	None	$\frac{2x_1}{a} - 1$	None	$\frac{2x_2}{b} - 1$
$u_1$ and $\phi_1$	$\frac{2x_1}{a} - 1$	1	1	$\frac{2x_2}{b} - 1$
$u_2$ and $\phi_2$	1	$\frac{2x_2}{b} - 1$	$\frac{2x_1}{a} - 1$	1

b. Trigonometric Functions

	$x_1$ Direction			$x_2$ Direction		
	Function	Indices ( $m$ )		Function	Indices ( $n$ )	
		Even	Odd		Even	Odd
$w$	$\sin(\frac{m\pi x_1}{a})$ $\cos(\frac{m\pi x_1}{a})$	1, 3, 5... 0, 2, 4...	2, 4, 6... 1, 3, 5...	$\sin(\frac{n\pi x_2}{b})$ $\cos(\frac{n\pi x_2}{b})$	1, 3, 5... 0, 2, 4...	2, 4, 6... 1, 3, 5...
$u_1$ and $\phi_1$	$\sin(\frac{m\pi x_1}{a})$ $\cos(\frac{m\pi x_1}{a})$	2, 4, 6... 1, 3, 5...	1, 3, 5... 2, 4, 6...	$\cos(\frac{n\pi x_2}{b})$ $\sin(\frac{n\pi x_2}{b})$	2, 4, 6... 1, 3, 5...	1, 3, 5... 2, 4, 6...
$u_2$ and $\phi_1$	$\sin(\frac{m\pi x_1}{a})$ $\cos(\frac{m\pi x_1}{a})$	1, 3, 5... 2, 4, 6...	2, 4, 6... 1, 3, 5...	$\cos(\frac{n\pi x_2}{b})$ $\sin(\frac{n\pi x_2}{b})$	1, 3, 5... 2, 4, 6...	2, 4, 6... 1, 3, 5...

Note: The terms "even" and "odd" refer to symmetry states as defined in Table 2.1.

The following two layup configurations can be combined with the two support/loading conditions to obtain four test problems:

1. Orthotropic  $[0_4/90_4]_S$ , layer thickness = .005 in., size 20 in. by 9 in.
2. Anisotropic with bending-extensional coupling:  
 $[\pm 50/35]_5$ , layer thickness = .00520087 in., size 19.25 in. by 6.5 in.

For all four problems, comparisons were made with an in-house finite element code which included the effects of transverse shear deformation and employed mixed formulation finite elements [22]. For the orthotropic panels, a 12 by 8 grid of MD9-4 elements was used; these elements employ biquadratic shape functions in the approximation of the generalized displacements, and bilinear shape functions in the approximation of the stress resultants. For the anisotropic panels, a 12 by 6 grid of MD16-9 elements was used; these elements employ bicubic shape functions in the approximation of the generalized displacements, and biquadratic shape functions in the approximation of the stress resultants. The finite element model used is shown in Figure 4.2.

To verify the correctness of the Rayleigh-Ritz solution, total strain energy and maximum displacement were compared with the mixed formulation finite element solution, which is taken as the standard for comparison. Also, detailed examinations of the nonzero displacements were made by plotting each displacement at several points along the panel's centerlines.

#### 4.2.1 Transversely Loaded Orthotropic Panel

The transversely loaded orthotropic panel was used because it permits several simplifications which greatly reduce problem size and complexity. First, approximation functions can be chosen which satisfy the boundary conditions; therefore, no penalty function is needed to enforce them. Second, solution of such a problem involves the use of a set of even symmetry state functions only; no odd symmetry state functions are needed, since the load and boundary conditions are symmetric. Also, since there is no bending-extensional



coupling, no functions are needed to represent  $u_1$  and  $u_2$ . Taking these simplifications into account, the functions chosen to represent each displacement are:

$$\begin{aligned}
 u_1 &: 0 \\
 u_2 &: 0 \\
 \phi_1 &: \cos\left(\frac{m\pi x_1}{a}\right) \sin\left(\frac{n\pi x_2}{b}\right) \quad m, n = 1, 3, 5... \\
 \phi_2 &: \sin\left(\frac{m\pi x_1}{a}\right) \cos\left(\frac{n\pi x_2}{b}\right) \quad m, n = 1, 3, 5... \\
 w &: \sin\left(\frac{m\pi x_1}{a}\right) \sin\left(\frac{n\pi x_2}{b}\right) \quad m, n = 1, 3, 5...
 \end{aligned} \tag{4.1}$$

Energy and center transverse displacement results are shown in Table 4.2. The column reporting number of terms refers to the number of terms representing each of the three displacements. Therefore, the total size of the linear system is three times the number of terms shown in Table 4.2.

Table 4.2. Linear Results for  $[0_4/90_4]_s$ , Transversely Loaded Panel

Number Of Terms	Energy		$w_c$ , in.	
	Value	% Error	Value	% Error
1	0.1751	1.16	$4.799 \times 10^{-2}$	2.97
5	0.1770	0.08	$4.651 \times 10^{-2}$	0.22
9	0.1771	0	$4.662 \times 10^{-2}$	0.03
16	0.1771	0	$4.660 \times 10^{-2}$	0.02
25	0.1771	0	$4.661 \times 10^{-2}$	0
FEM	0.1771	—	$4.661 \times 10^{-2}$	—

From the displacements shown in Table 4.2, the solution is essentially converged when five series terms are used. Examination of the plots shown in Figure 4.3 proves this assessment to be correct, since four of the five solutions are indistinguishable. Strain energy, however, reflects a slightly slower convergence, as well as a slight oscillation about the finite element solution as more terms are used. This behavior has proved typical of modified Rayleigh-Ritz technique.

#### 4.2.2 Transversely Loaded Anisotropic Panel With Bending-Extensional Coupling

The transversely loaded anisotropic panel was used because, unlike the orthotropic panel, it admits no simplifications, except that for a small enough load, it is a linear problem. The presence of bending-extensional coupling means that approximation functions must be included for both  $u_1$  and  $u_2$ . Also, for the types of functions used, boundary conditions must be enforced using the penalty function method. Furthermore, both even and odd symmetry state functions must be included, since coupling between the two states is present.

The full set of functions shown in Table 4.1 is used to approximate the response in this problem. Each displacement is approximated by a set of functions composed of the same number of even and odd symmetry state terms. For example, if 102 terms are used to approximate  $u_1$ , then the 51 even state functions consist of one linear term, 25  $\sin(\frac{m\pi x}{a})\cos(\frac{n\pi y}{b})$  terms, and 25  $\cos(\frac{m\pi x}{a})\sin(\frac{n\pi y}{b})$  terms, while the 51 odd state functions are of similar composition. Note that, according to Table 4.1.a, the functions representing  $w$  are an exception. In that case, since there is no even state linear term, only a total of 101 functions would be used. (If the even state linear term were included, then the  $\cos(0)\cos(0)$  term would have to be omitted, since it is also linear. The presence of both terms would introduce redundancy into the system, and the stiffness matrix would become singular and therefore unfactorable.) Also, because both inplane degrees of freedom are completely free, the odd state linear term representing  $u_2$  is omitted.

Energy and center transverse displacement results for the transversely loaded anisotropic panel are shown in Table 4.3. The column reporting number of terms refers to the number of terms representing each of the five displacements, with  $w$  and  $u_2$  being represented by one less function, as discussed above. Therefore, the total size of the linear system is five times the number of terms shown in Table 4.3, minus two.

Table 4.3. Linear Results for  $[\pm 50/35]_5$ , Transversely Loaded Panel

Number Of Terms	Energy		$w_c$ , in.	
	Value	% Error	Value	% Error
18	$2.072 \times 10^{-2}$	0.99	$7.325 \times 10^{-3}$	1.16
38	$2.083 \times 10^{-2}$	0.46	$7.407 \times 10^{-3}$	0.05
66	$2.087 \times 10^{-2}$	0.28	$7.403 \times 10^{-3}$	0.01
102	$2.089 \times 10^{-2}$	0.19	$7.405 \times 10^{-3}$	0.01
FEM	$2.093 \times 10^{-2}$	—	$7.411 \times 10^{-3}$	—

From Table 4.3, the energy and transverse displacement are converged to three digits when 66 terms are used. Examination of the plots shown in Figure 4.4 confirms that using 66 functions per displacement does indeed provide an acceptable solution, in that the 66 term solution is nearly indistinguishable from the 102 term solution and from the finite element solution for the three larger displacements. Also, notice that good agreement is also obtained using the 38 term representation. (The finite element solution displays erratic results for displacements  $u_1$  and  $u_2$  because they are much smaller than the maximum displacement in the panel.)

#### 4.2.3 Axially Loaded Orthotropic Panel

The axially loaded orthotropic panel is another problem which permits several simplifications. First, since there is no out-of-plane behavior when the load is purely axial (and buckling has not occurred) no functions are needed to approximate  $w$ . Also, since the loading is symmetric, no odd state functions are needed. Therefore, the function set to be used consists of all the even state functions shown in Table 4.1, except that no functions are included to represent  $w$  or either of the two rotations  $\phi_1$  and  $\phi_2$ .

Boundary conditions for this problem are slightly more complicated than those for the transversely loaded panels. Because this panel, like all the rest, will exhibit coupling between axial and lateral behavior (i.e., Poisson effect), uniform displacement will not occur along the loaded edges. To prevent bowing of the loaded edges, the first derivative

of  $u_1$  along those edges must be constrained to zero; therefore, the additional penalty term, consistent with the conventions of Section 3.2, is

$$\delta h = \int \frac{\partial F_{t_1}^{u_1}}{\partial x_2} \bigg|_{(0,x_2)} \frac{\partial F_{t_2}^{u_1}}{\partial x_2} \bigg|_{(0,x_2)} \mathbf{X}_{t_2} dx_2 \delta \mathbf{X}_{t_1} \quad (4.2)$$

Table 4.4. Linear Results for  $[0_4/90_4]_S$ , Axially Loaded Panel

Number Of Terms	Energy		$\delta$ , in.		$u_{2_e}$ , in.	
	Value	% Error	Value	% Error	Value	% Error
9	0.2776	0.02	$6.170 \times 10^{-4}$	0.02	$1.433 \times 10^{-5}$	13.1
19	0.2777	0	$6.170 \times 10^{-4}$	0.01	$1.624 \times 10^{-5}$	3.9
33	0.2777	0	$6.171 \times 10^{-4}$	0	$1.501 \times 10^{-5}$	4.0
51	0.2777	0	$6.171 \times 10^{-4}$	0	$1.582 \times 10^{-5}$	1.2
FEM	0.2777	—	$6.171 \times 10^{-4}$	—	$1.564 \times 10^{-5}$	—

Values of energy, loaded edge axial displacement  $\delta$ , and lateral displacement  $u_{2_e}$  along the simply supported edge are compiled in Table 4.4. The column reporting number of terms refers to the number of terms representing each of the two displacements; therefore, the total size of the linear system is twice the number of terms shown in Table 4.4.

From Table 4.4, both the energy and loaded edge displacement are converged to three digits when only 9 terms are used. However,  $u_{2_e}$  never really converges, even when the full 51 terms are used. This behavior is due to the clamped boundary conditions along the loaded edge. Since  $u_1$  is free on all four edges of the panel, a simple linear distribution is obtained, as shown in Figure 4.5.a. However, since  $u_2$  is constrained along the loaded edge, the Poisson effect which would normally cause a lateral expansion along that edge is inhibited. Therefore, since  $u_2$  is not constrained along the unloaded edges of the panel, a look at the short centerline of the panel reveals a slightly more complicated nonlinear distribution for  $u_2$ , as shown in Figure 4.5.b.

#### 4.2.4 Axially Loaded Anisotropic Panel With Bending-Extensional Coupling

The function set used for this problem is identical to that used for the transversely loaded orthotropic panel, except that the odd state linear term is included in the representation of  $u_2$ . The "straight edge boundary condition" introduced for the axially loaded orthotropic panel is also used here, and prevents not only bowing due to the Poisson effect, but also edge shearing due to shear-extensional coupling, as shown in Figure 2.2.

Results for the axially loaded anisotropic panel problem are shown in Table 4.5. Since the full set of functions shown in Table 4.1 must be used to approximate the response, the number of terms reported in Table 4.5 must be multiplied by five, and then one subtracted, to obtain the size of the full linear system.

Table 4.5. Linear Results for  $[\pm 50/35]_5$ , Axially Loaded Panel

Number Of Terms	Energy		$\delta$ , in.	
	Value	% Error	Value	% Error
18	.5474	5.41	$1.684 \times 10^{-3}$	5.34
38	.5613	3.01	$1.727 \times 10^{-3}$	2.92
66	.5670	2.04	$1.745 \times 10^{-3}$	1.91
102	.5700	1.51	$1.754 \times 10^{-3}$	1.41
FEM	.5787	—	$1.779 \times 10^{-3}$	—

From Table 4.5, it is evident that this problem is the most demanding of the four, in terms of the number of functions needed to obtain an accurate solution. Three-digit accuracy is never obtained in any of the solutions shown. Examination of Figure 4.6 indicates that a 102 term approximation provides a good estimate of the finite element solution, while a 66 term approximation gives results very nearly as good. Note that in-plane behavior is predicted well using only a few terms, while the out-of-plane quantities are more difficult to model. (The finite element solution displays erratic results for displacements  $\phi_1$  and  $\phi_2$  because they are much smaller than the maximum displacement in the panel.)

### 4.3 Effect of the Penalty Parameter on Accuracy of Linear Results

For the results just presented, no mention was made of the penalty parameter; however, choice of this parameter can have a profound effect on the accuracy of the solutions. Too large a penalty parameter can result in an ill-conditioned equation system, while a choice at the other extreme can mean that boundary conditions are not adequately satisfied. In this section, results of parametric studies of the penalty parameter are presented to give the reader some appreciation of the effect of this parameter. In this chapter, an overall penalty parameter of  $10^8$  was used, unless otherwise noted.

First, examine Table 4.6. This table presents results from solution of the axially loaded anisotropic panel of Section 4.2.4 for different values of the penalty parameter  $r$ . Several different parameters are presented; the following list defines each one:

$r$  = Penalty parameter

$U$  = Strain energy

$|R|$  = Magnitude of the residual vector  $R$ , calculated by substituting the Ritz coefficients back into the linear equilibrium equation  $K_{ij}X_j - P_i$ .

$\delta$  = End shortening at the center of the panel's loaded edges

$\delta$  BC = Number of digits to which the loaded edges are straight

$w_c$  = Center transverse displacement

$w$  BC = Order of magnitude satisfaction of the  $w = 0$  constraints along the panel's four edges

$u_2$  BC = Order of magnitude satisfaction of the  $u_2 = 0$  constraints along the panel's four edges

It is evident from these results that all three of the response variables,  $U$ ,  $\delta$ , and  $w_c$ , are essentially insensitive to variation of the penalty parameter when the penalty parameter is at least  $10^8$ , and the residual is at an acceptable level regardless of the value of  $r$ . However, boundary condition satisfaction is much more sensitive to variations in the penalty parameter.

It seems that the easiest boundary condition to satisfy is the  $w = 0$  condition; this condition is at an acceptable level for any value of  $r$  greater than  $10^7$ . The most difficult condition to satisfy appears to be the  $u_2 = 0$  condition along the loaded edge; this condition

Table 4.6. Penalty Results – Overall Penalty Parameter\*

$r$	$U$	$ R $	$\delta \times 10^{-2}$	$\delta$ BC	$w_c \times 10^{-2}$	$w$ BC	$u_2$ BC ( $u_2^{\max} \sim 10^{-4}$ )
$10^5$	.6011	$10^{-15}$	.1884	1	-.1131	$10^{-6}$	$10^{-4}$
$10^6$	.5810	$10^{-15}$	.1803	1	-.1086	$10^{-7}$	$10^{-5}$
$10^7$	.5707	$10^{-14}$	.1758	2	-.1059	$10^{-8}$	$10^{-5}$
$10^8$	.5670	$10^{-13}$	.1745	3	-.1053	$10^{-9}$	$10^{-6}$
$10^9$	.5662	$10^{-12}$	.1742	4	-.1052	$10^{-10}$	$10^{-7}$
$10^{10}$	.5661	$10^{-11}$	.1742	5	-.1052	$10^{-11}$	$10^{-8}$
$10^{11}$	.5661	$10^{-10}$	.1742	6	-.1052	$10^{-12}$	$10^{-9}$

\* See text for definitions of variables presented in this table

does not become sufficiently small until  $r$  reaches  $10^{11}$ . (Sufficiently small is defined as six orders of magnitude smaller than the largest displacement in the panel, which is  $\delta$ , at  $10^{-3}$ .) Furthermore, it is also difficult to obtain a constant  $\delta$  condition along the loaded edge; this is not accomplished to six digits until  $r$  reaches  $10^{11}$ .

More insight into these difficulties are gained by examining the contour plots shown in Figure 4.7. Look first at the contour of  $u_1$ ; from this plot, it is evident that the effect of an unsatisfied straight edge condition is that the edge is slightly bowed. Note that the skewing caused by the presence of shear-extension coupling is successfully prevented along the loaded edge; however, one cannot blame this coupling for the difficulty in satisfying the straight edge condition, since similar problems were encountered in working with the  $[\pm 30/90]_5$  panel, which has no extension-shear coupling.

Rather, as is evident from the  $u_2$  contour plot, the cause of the difficulty is the requirement that  $u_2$  be zero along the loaded edge. Notice that steep  $u_2$  gradients are present in the corners of the panel; since  $u_1$  and  $u_2$  are very strongly coupled via the well-known Poisson effect, there is a strong tendency for the loaded edge to bow inward, and for the corners to also move inward. Therefore, much higher penalty parameters are required in order to satisfy both the constant  $\delta$  and  $u_2 = 0$  conditions.

In order to put these difficulties in perspective, it is important to note that, even though the boundary conditions are not satisfied to as many digits as might be desirable, the desired character of the response is obtained. That is, the gradients in  $u_2$  at the corners are in fact present, as is evident from the contour plots, and skewing caused by shear-extensional coupling is totally prevented along the loaded edges.

In addition, experience with nonlinear analysis of these problems indicates that it is unwise to impose overly stringent precision requirements on boundary conditions. For example, orthotropic problems were solved in which an overall penalty parameter of  $10^9$  was used, with a penalty parameter of  $10^{11}$  being used to enforce the straight edge boundary condition. When this problem was run on a VAX 11/785, which carries sixteen significant digits in all calculations (in double precision), acceptable results were obtained. However, the same problem with the same penalty parameter was then solved on a Cray-2, which carries only fourteen significant figures (in single precision); in that case, convergence was not obtained even on the first load step, due to the ill-conditioning caused by the large penalty parameters. Conversely, when the penalty parameter for the entire panel was decreased to  $10^8$ , converged solutions were easily obtained on both machines. Furthermore, note that since only half as many functions were required to solve this orthotropic problem than are needed for an anisotropic problem, ill-conditioning due to the size of the penalty parameter can only get worse for anisotropic problems. Therefore, even though Table 4.6 indicates that acceptable linear solutions can be obtained using high penalty parameters, care must be exercised when choosing penalty parameters for nonlinear problems.

#### **4.4 Linear Results Using Reduced Basis Techniques**

From the results of the previous sections, it is evident that acceptable solutions can be obtained using subsets of the functions shown in Table 4.1. However, as indicated by results for the axially loaded anisotropic panel, the system of linear equations required for an accurate solution can become quite large; in that case, 509 equations were required. The



reduced basis technique described in Section 3.4 is one way to reduce the size of the equation system. Recall that this technique involves approximating the solution using a set of basis vectors which were essentially sensitivity derivatives of the response with respect to the anisotropic material coefficients, evaluated at the point where the anisotropic coefficients are zero.

In this section, solutions obtained using this reduced basis technique will be examined for the axially loaded anisotropic panels of Section 4.2.4. In particular, two details of these results are of interest. First, it is of course important to determine how well the chosen basis vectors approximate the full system. This determination is easily made by examining local and global quantities for the panel being analyzed. Secondly, the basis vectors themselves should be examined in order to determine whether they are linearly independent.

In order to measure the linear independence of a given set of vectors, the Gramian may be used. As explained in [23], the Gramian is the determinant of the Gram matrix, which is formed as follows:

$$\mathcal{M}_{cd} = \Gamma_{cI} \Gamma_{Id} \quad (4.3)$$

That is, elements of the Gram matrix are formed by taking appropriate dot products involving the basis vectors. If the basis vectors are normalized beforehand so that the length of each vector is one, then the Gramian will range between zero and one. If the Gramian vanishes, then the basis vectors can be shown to be linearly dependent, while a Gramian of one indicates complete linear independence. Note that, as will be shown herein, the Gramian can be used to determine the required number of basis vectors, thus eliminating the need for detailed studies of response quantities.

#### 4.4.1 Accuracy in Approximating the Full System

Shown in Table 4.7 are several key quantities calculated using reduced systems ranging in size from one to fifteen basis vectors. These results are for the axially loaded anisotropic plate, whose full model involves 329 equations. From this table, both the strain energy and the end shortening of the panel converge very rapidly; only four basis vectors are required for accurate representation of both quantities. However, in order to obtain a negligible residual vector, at least eight basis vectors are required. The effect of this last result is seen when smaller displacements, such as the maximum transverse displacement  $w_c$ , are calculated; at least seven basis vectors are required before  $w_c$  is converged to six digits. Therefore, accurate solution of this problem requires the use of at least eight basis vectors.

Table 4.7. Variation of Results with Number of Basis Vectors Used

$\mathcal{N}$	$\delta$	$U$	$w_c$	$ R $
1	$.161227 \times 10^{-2}$	0.523919	$-9.29727 \times 10^{-4}$	$10^0$
2	$.174011 \times 10^{-2}$	0.565462	$-1.00345 \times 10^{-3}$	$10^{-1}$
3	$.174465 \times 10^{-2}$	0.566938	$-1.04855 \times 10^{-3}$	$10^{-2}$
4	$.174469 \times 10^{-2}$	0.566950	$-1.04893 \times 10^{-3}$	$10^{-2}$
5	(converged)	(converged)	$-1.05267 \times 10^{-3}$	$10^{-3}$
6	.	.	$-1.05276 \times 10^{-3}$	$10^{-4}$
7	.	.	$-1.05268 \times 10^{-3}$	$10^{-5}$
8	.	.	(converged)	$10^{-6}$
9	.	.	.	$10^{-6}$
10	.	.	.	$10^{-7}$
11	.	.	.	$10^{-8}$
12	.	.	.	$10^{-9}$
13	.	.	.	$10^{-10}$
14	.	.	.	$10^{-10}$
15	.	.	.	$10^{-11}$

#### 4.4.2 Grammian Results

Table 4.8 lists values of the Grammian for different numbers of basis vectors. Again, these results are for the anisotropic axially loaded panel, and 329 functions were used in the full model. These results are consistent with those of the previous subsection since calculation of more than eight basis vectors causes the Grammian to essentially vanish. Furthermore, the results of Table 4.8 indicate that, for this class of problems, the Grammian provides a good prediction of the number of basis vectors required, and therefore alleviates the need to examine detailed results in order to select an appropriate reduced system size.

#### 4.8. Variation of the Grammian with Number of Basis Vectors Used

a. 509 Functions

Number Of Basis Vectors	Grammian
1	1.
2	1.
3	0.50
4	0.45
5	0.23
6	$1.1 \times 10^{-2}$
7	$6.6 \times 10^{-4}$
8	$1.6 \times 10^{-5}$
9	$1.7 \times 10^{-7}$
10	$1.1 \times 10^{-9}$
11	$2.8 \times 10^{-12}$
12	$4.2 \times 10^{-15}$
13	$2.5 \times 10^{-18}$
14	0.
15	0.

b. 89 Functions

Number Of Basis Vectors	Grammian
1	1.
2	1.
3	0.45
4	0.24
5	$4.7 \times 10^{-03}$
6	$1.1 \times 10^{-03}$
7	$1.8 \times 10^{-06}$
8	$2.8 \times 10^{-08}$
9	$9.6 \times 10^{-12}$
10	$1.2 \times 10^{-14}$

Other numerical experiments have shown that, as one might expect, when fewer approximation functions are used and the number of unknowns is therefore smaller, fewer basis vectors are needed to approximate the reduced number of unknowns. This is because the space defined by the smaller set of unknowns is of lower dimension, and so fewer basis vectors are needed to span it. Shown in Table 4.8.b are values of the Grammian calculated for the 89 function model; in that case, only seven basis vectors are needed.

#### 4.5 Nonlinear Results

The problems for which nonlinear results are presented involve axially loaded orthotropic and anisotropic panels similar to those presented in the previous sections, as well as a 6.5 inch wide, axially loaded  $[\pm 30/90]_5$  panel similar to that described in Chapter 5. Note that the dimensions of the orthotropic panel are different from those of the anisotropic panels; this was done in order to obtain a control specimen which, like the two anisotropic panels, buckled into a w-symmetric configuration with respect to the short centerline of the panel.

The two nonorthotropic panels are identical to the corresponding panels discussed in Chapter 5 in both lamination and thickness; however, their widths and lengths have been modified to compensate for the slight difference in the way boundary conditions must be modeled in the Ritz and finite element analyses. In the finite element models of Chapter 5, an extra ring of elements was added to simulate the finite-width supports used to impose boundary conditions in the experiments. However, in the Ritz analysis, the supports are modeled by simply shortening both the panels' dimensions by amounts corresponding to the extra ring of elements added in the finite element model. All five degrees of freedom are constrained along the loaded edges, while only  $w$  is constrained along the other two edges. (In the linear problems presented earlier, both  $w$  and  $\phi_1$  were constrained along the long panel edges.) Note that there is no reason that the exterior penalty function approach presented earlier could not be used to enforce the more complex boundary conditions;

however, it was decided that for purposes of this work, the additional complexity was unnecessary. As a result, quantitative comparison is not made between the experimental results and the other results presented in this section; however, qualitative results are discussed.

Also, in Chapter 5, load was introduced at one end of the panel while the other end remained motionless; for the problems of the present section, load is introduced at both ends of the panel. The two loadings are functionally identical; the latter was used in order to obtain a symmetric loading condition, which is required by the Rayleigh-Ritz formulation. Schematics of the Rayleigh-Ritz analysis models are presented in Figure 4.1.

Three other sets of results are presented for comparison with the Ritz results; these are: STAGS results, results from the mixed formulation finite element model used previously for comparison with the linear results, and the experimental results presented in Chapter 5. The STAGS results presented in the following sections were obtained using models which correspond in geometry, boundary conditions, and lamination with the Ritz models, and so will be slightly different from the results presented in Chapter 5. Results obtained from the mixed formulation finite element analysis also correspond to the Ritz models in geometry, lamination and boundary conditions. (For all three analyses, the mixed formulation analyses employed the MD9-4 finite element described in Section 4.2.) Also, recall that both the Rayleigh-Ritz results and the mixed formulation results include the effects of transverse shear deformation, while the STAGS results do not.

The solution strategy chosen for the Rayleigh-Ritz analysis of the nonlinear post-buckling problem is the well-known Newton-Raphson technique. This technique, although computationally expensive compared with most transformation-type methods, is simple to implement and gives accurate results. The particular solution procedure used herein consists of the following steps:

1. Obtain an approximation for the buckling load of the panel being analyzed. This was accomplished using the finite element code STAGSC-1, since no eigenvalue capability

was included in the Rayleigh-Ritz code. (See Chapter 5 for further discussion of STAGSC-1.)

2. Solve the linear problem at an initial load of 70% to 90% of the buckling load; this solution is an initial estimate for the first nonlinear load step.
3. Form the nonlinear Newton-Raphson equations as described in Chapter 3; the solution from the previous iteration (or the linear problem if this is the first load step) is used in the formation of these equations.
4. Solve this linear set of equations for a correction  $\Delta \mathbf{X}_i$  to the previous solution  $\mathbf{X}_{i-1}$ .
5. Form the new solution vector  $\mathbf{X}_i = \mathbf{X}_{i-1} + \Delta \mathbf{X}_i$ .
6. Calculate an error measure

$$e = \frac{1}{n} \frac{|\Delta \mathbf{X}_i|}{\mathbf{X}_i}$$

where  $n$  is the total number of degrees of freedom. When this error is less than  $10^{-6}$ , the solution is considered converged. If the solution is not converged, return to step 3.

7. When a converged solution has been obtained at the current load step, the load may be incremented. The size of this incrementation depends on the proximity of the current load to the buckling load. If the load is within five to ten percent of  $P_{cr}$ , then incrementation proceeds very slowly. At other points in the solution procedure, the load may be incremented at larger intervals.

Throughout this procedure, an imperfection must be imposed in order to trigger buckling; without it, no branching to the stable secondary path will occur. The imperfection is achieved by applying a sinusoidal transverse load with the same number of half-sine waves in both directions as the first buckling mode shape. (It happens that in all the cases presented, the desired response corresponds to the first buckling mode.) In the case of the STAGS analyses, imperfections of exactly the same shape as the buckling mode shape were used, just as in Chapter 5, and in the case of the mixed formulation results, no imperfection was needed. Therefore, considerable differences between the three sets of results will be

seen in the immediate neighborhood of buckling; however, imperfection related differences will disappear as the load or displacement is increased beyond buckling. For a more general discussion of the use of imperfections to trigger buckling, as well as the entire nonlinear solution procedure, refer to Chapter 5.

For the Rayleigh-Ritz analyses, the same sets of functions are used to solve the post-buckling problems as were used for the linear problems, with only one exception: all five degrees of freedom ( $u_1$ ,  $u_2$ ,  $\phi_1$ ,  $\phi_2$ , and  $w$ ) must be represented for all problems, regardless of the laminate, since both inplane and out-of-plane deformations occur. Results are presented for two problem sizes: 38 and 66 terms per displacement degree of freedom, resulting in full systems of 189 and 329 equations, respectively (since  $w$  is represented by one less function than are the other four displacements). Larger problems would have been desirable, but problem size was limited by the computer hardware. In the case of the orthotropic problem, half as many functions are used, since only the even function set is required, resulting in full systems of 94 and 164 equations.

In the case of the STAGS analyses, the same 411-type elements that were used for the analyses of Chapter 5 were used here. In all three problems, a uniform grid was used, with the loading and boundary conditions applied as described in Chapter 5. For the orthotropic problem, a discretization resulting in 10 by 12 elements per half-wave of the buckling mode shape was used, for a total of 360 elements, while for the orthotropic problems, the discretization gave 10 by 10 elements per half-wave, resulting in a total of 300 elements. Studies were made to assure that these levels of discretization provided converged solutions.

Data presented in the plots of the following sections has all been normalized with respect to the panel buckling load. In the case of the STAGS, Rayleigh-Ritz, and mixed formulation finite element results, this means normalization with respect to the buckling loads obtained via a STAGS bifurcation buckling analysis. The experimental results shown were normalized with respect to the buckling loads presented in Table 5.6.

It is important to note that all the Ritz solutions presented in the following sections were solved on a Cray-2 supercomputer. Because Cray-2 single precision is slightly less accurate than the double precision available on a VAX 11/785, careful choice of an appropriate penalty parameter becomes more important, as was noted earlier. In all three problems, the penalty parameter was set to  $10^8$ .

#### 4.5.1 Orthotropic Panel

The orthotropic panel analysis was taken to a load equal to about three times the buckling load, as determined by bifurcation buckling analyses done with STAGSC-1. Shown in Figure 4.8 is a plot of load versus end-shortening for this panel which includes four of the five sets of results described in the previous section, since no experimental results were available for the orthotropic panel. (For reference, the buckling load for this panel was 1452 lb.)

Aside from the expected differences between the results in the immediate neighborhood of buckling, the primary differences between the three sets of results are seen late in postbuckling. The STAGS results are slightly stiffer than the other three sets of results, which agree well during the early portion of postbuckling. Since the 33 term Ritz solution agrees well with results from the mixed formulation finite element analysis, that solution is considered converged. The 19 term solution, while not in total agreement with the mixed formulation finite element solution, still provides an accurate solution early in postbuckling.

Since the only real difference between the STAGS and Ritz analysis is the presence of transverse shear flexibility in the Ritz analysis, this difference in stiffness late in postbuckling could be attributed to transverse shear deformation. Since agreement is good between the mixed formulation results and the Ritz analysis, the claim that transverse shear deformation is the cause of the disparities in stiffness appears to be well supported. However, note that the degradation in stiffness, as defined in Chapter 5, is essentially identical for the two solutions, due to slight differences in initial postbuckling stiffness.



ORIGINAL PAGE IS  
OF POOR QUALITY

The agreement between the 33 term Ritz solution and the mixed formulation finite element solution is also seen on a pointwise basis, as shown in Figure 4.9, a plot of center transverse displacement. However, the 19 term Ritz solution is evidently not a good estimate of the behavior, and similarly for the STAGS solution. The extreme disagreement between STAGS and the other results in the immediate neighborhood of buckling is due to the larger imperfection imposed in the STAGS analysis, as noted earlier.

Finally, examining the two contour plots shown in Figure 4.10 (one from the Ritz analysis and one from the STAGS analysis), it is also evident that overall qualitative agreement between the two analyses is good for this problem.

#### 4.5.2 $[\pm 30/90]_5$ Panel

The analysis of the  $[\pm 30/90]_5$  panel was also taken to a load equal to about three times the buckling load. Shown in Figure 4.11 is a plot of load versus end-shortening for this panel which includes all five sets of results described earlier. From this plot, it is evident that for the Ritz analysis, 38 functions per displacement degree of freedom is an inadequate representation of the problem; however, agreement is considerably better for the 66 function case. Even so, this higher level of approximation is still not sufficient, since agreement with the mixed formulation solution is not attained. (The fact that the Ritz solution agrees well with the experiment is not taken as proof of convergence, since boundary conditions were not modeled precisely.)

The plot of center transverse displacement, shown in Figure 4.12, displays a very different character from the end shortening results. Apparently, pointwise agreement between the different solutions is not attained for this panel. The analysis which comes closest to the experiment is the STAGS analysis; then, being next in order of agreement, both the mixed formulation results and the Ritz analysis are less stiff than both the experiment and the STAGS results. One might suspect that the large imperfection used in the Ritz analysis is the cause of the disparity for that set of results; however, runs were made to ensure that the postbuckling solution did not vary significantly when the imperfection was made

an order of magnitude larger, thus eliminating imperfection from consideration. Rather, the most likely cause of the disparity between the mixed formulation results and the Ritz results is simply a lack of convergence on the part of the Ritz analysis. Further discussion of the differences between the experimental results and the STAGS analysis may be found in Chapter 5.

Finally, examining the two contour plots shown in Figure 4.13 (one from the Ritz analysis and one from the STAGS analysis), qualitative agreement between the two analyses is attained for this problem in that both analyses display a three half-sine-wave postbuckled shape. However, the Ritz analysis, presumably due to its lack of convergence, displays some distortion near the center of each half wave.

#### 4.5.3 $[\pm 50/35]_5$ Panel

The analysis of the  $[\pm 50/35]_5$  panel was taken to a load equal to about two and one-half times the buckling load. Shown in Figure 4.14 is a plot of load versus end-shortening for this panel which again includes all five sets of results described earlier. From this plot, it is again evident that for the Ritz analysis, 38 functions per displacement degree of freedom is an inadequate representation of the problem, while the 66 function approximation exhibits better agreement with the other solutions, but still is not adequate. Excluding the Ritz solutions and examining the three remaining solutions late in postbuckling, the stiffness degradation seen in the experiment is not predicted by either the STAGS analysis or the mixed formulation results. Therefore, one cannot conclude that transverse shear deformation is responsible for postbuckling stiffness degradation in this problem.

The plot of center transverse displacement, shown in Figure 4.15, displays a character much different from that seen for the  $[\pm 30/90]_5$  panel, in that better agreement is obtained for all results except the 38 term Ritz solution. Obviously, the 38 term approximation is totally inadequate. The disparity between the 66 term Ritz solution and the other curves again indicates the lack of convergence in the Ritz solution.

Finally, examining contour plots for this panel, shown in Figure 4.16, qualitative agreement between the Ritz and STAGS analyses is attained for this problem, since both solutions exhibit a three half-sine-wave postbuckled shape, as well as the skewing of the entire pattern which is characteristic of panels with shear-extensional coupling. As with the  $[\pm 30/90]_5$  panel, the Ritz solution displays some distortion near the centers of the three half-waves. This is particularly true for the center half-wave, where the oblong shape predicted by the STAGS analysis is rotated ninety degrees in the Ritz analysis.

## Chapter 5

### Experimental and Numerical Studies Of Buckling and Postbuckling Behavior of Panels

#### 5.1 Characteristics of Test Specimens

Two of the primary aims of the present study are:

- To investigate the buckling and postbuckling responses of rectangular laminated composite panels possessing anisotropy and bending-extensional coupling
- To use readily available finite element modeling techniques for the analysis of such panels

In order to collect experimental data which quantifies the response of realistic laminates possessing both anisotropy and bending-extensional coupling, six graphite-epoxy panels were constructed; three of the panels were made using a  $[\pm 50/35]_5$  layup configuration, and the other three were constructed using a  $[\pm 30/90]_5$  layup. The  $[\pm 50/35]_5$  laminate has been used in the design of a prototype aircraft known as the HiMAT (Highly Maneuverable Aircraft Technology) vehicle, while the  $[\pm 30/90]_5$  laminate was chosen as a control specimen, since it has no membrane anisotropy. Note that both of these layups are unsymmetric and have a total of fifteen layers. The two sets of panels exhibit all the various couplings described in Chapter 2 to differing degrees.

The first layup,  $[\pm 50/35]_5$ , possesses all the different couplings; its constitutive matrix, which corresponds exactly to the matrix **C** defined in Chapter 2, is shown in Table 5.2.a. The second layup,  $[\pm 30/90]_5$ , exhibits no extension-shear or transverse shear coupling, a lower degree of bending-twisting coupling, and a higher degree of bending-extensional coupling. The constitutive matrix for this laminate is shown in Table 5.2.b. All the panels were made from Hercules AS4-3502 graphite-epoxy unidirectional preimpregnated tape. Properties of this material system are listed in Table 5.1. (Note that the matrices shown in Table 5.2 were calculated using a panel thickness of 0.08 inches. The actual panels

Table 5.1. Material Properties for Hercules AS4-3502 Graphite/Epoxy Tape

$E_{11}^c$	$18.5 \times 10^6$
$E_{22}^c$	$1.64 \times 10^6$
$G_{12}$	$0.832 \times 10^6$
$\nu_{12}$	0.35

had thicknesses slightly different from this nominal value, and so the constitutive matrices used in the analyses were slightly different from those shown in the table; the purpose of presenting the nominal matrices is to show the approximate magnitude of the coupling involved.)

One other parameter, the aspect ratio, was also varied. Three panels in each of the two layup sets were cut to widths of 4, 5.5, and 7 inches, with all lengths being a constant 20 inches. Average thicknesses were calculated for each panel based on eight measurements taken over each panel's surface. These average thicknesses have been used in all analyses presented herein. Widths and thicknesses of each panel are summarized in Table 5.3.

The six panels were all tested to failure, and each test was modeled using the finite element code STAGSC-1 (hereafter referred to as STAGS and described fully in reference [24]). Among other features, STAGS possesses a well-tested set of nonlinear solution algorithms, as well as a linear bifurcation buckling analysis capability, both of which were useful in the present study. The plate bending elements included in STAGS do not permit transverse shear deformation. Correlation between experimental and finite element results is examined in detail.

## 5.2 Description of the Experiment

### 5.2.1 Test Setup, Measurement Techniques, and Procedure

A schematic and photograph of the overall test setup is shown in Figure 5.1; this setup is essentially the same for all the tests conducted in the present study. Tests were conducted using a 120 kip hydraulic test machine. The loading was axial compression in

Table 5.2.a. Constitutive Matrix for  $[\pm 50/35]_5$  Panels, Thickness = 0.08"

$$\begin{aligned}
 & \mathbf{C}_{ij} \quad i, j = 1, 2, \dots, 6 \\
 & \begin{bmatrix}
 .480977 \times 10^6 & .322167 \times 10^6 & .132166 \times 10^6 & -.593526 \times 10^3 & .430193 \times 10^2 & -.219893 \times 10^3 \\
 & .483230 \times 10^6 & .684693 \times 10^5 & .430193 \times 10^2 & .507488 \times 10^3 & .268056 \times 10^3 \\
 & & .342118 \times 10^6 & -.219893 \times 10^3 & .268056 \times 10^3 & .430193 \times 10^2 \\
 & & & .226447 \times 10^3 & .150944 \times 10^3 & .652591 \times 10^2 \\
 \text{Sym.} & & & & .225668 \times 10^3 & .357176 \times 10^2 \\
 & & & & & .160296 \times 10^3
 \end{bmatrix} \\
 & \mathbf{C}_{ij} = \begin{bmatrix} .536847 \times 10^5 & .272511 \times 10^4 \\ .272511 \times 10^4 & .537153 \times 10^5 \end{bmatrix} \quad i, j = 7, 8
 \end{aligned}$$

Table 5.2.b. Constitutive Matrix for  $[\pm 30/90]_5$  Panels, Thickness = 0.08"

$$\begin{aligned}
 & \mathbf{C}_{ij} \quad i, j = 1, 2, \dots, 6 \\
 & \begin{bmatrix}
 .613178 \times 10^6 & .191093 \times 10^6 & 0. & .122973 \times 10^4 & .371607 \times 10^3 & .676815 \times 10^3 \\
 & .613178 \times 10^6 & 0. & .371607 \times 10^3 & -.197295 \times 10^4 & .247720 \times 10^3 \\
 & & .211043 \times 10^6 & .676815 \times 10^3 & .247720 \times 10^3 & .371607 \times 10^3 \\
 & & & .285378 \times 10^3 & .889553 \times 10^2 & .338407 \times 10^1 \\
 \text{Sym.} & & & & .290716 \times 10^3 & .123860 \times 10^1 \\
 & & & & & .983070 \times 10^2
 \end{bmatrix} \\
 & \mathbf{C}_{ij} = \begin{bmatrix} 0.537000 \times 10^5 & 0. \\ 0. & 0.537000 \times 10^5 \end{bmatrix} \quad i, j = 7, 8
 \end{aligned}$$

the long panel direction, and consists of an applied displacement at the bottom edge of the panel.

The boundary conditions were imposed by steel supports attached to the panels along all edges. (See Figure 5.2.) The panels' short edges were clamped along their entire length; each clamping fixture covered an area along the panels' short edge extending from that edge to a line 0.375 inches into the interior of the panel, for a total clamped area of  $w$  by .375 inches, where  $w$  is the panel width. From a modeling standpoint, these clamping

Table 5.3. Measurements of Tested Panels

Layup	Width, in.†	Average Thickness, in $\times 10^{-3}$
[ $\pm 30/90$ ] <sub>5</sub>	4	76.788
	5.5	77.488
	7	78.763
[ $\pm 50/35$ ] <sub>5</sub>	4	77.313
	5.5	77.150
	7	78.013

† All panels are 20 inches long.

supports imply, in the ideal case, that all displacements and rotations are constrained to zero in the area covered by the supports.

The long edges of the panel were constrained using steel knife-edge supports, as shown in Figure 5.2. These supports extended only .25 inches into the interior of the panel. They constrained the out-of-plane displacement ( $w$ ) to zero along their line of contact .25 inches inside the panel edge; however, rotations, as well as inplane displacements  $u_1$  and  $u_2$ , were free, since these supports did not contact the clamping supports.

Five kinds of measurements were made during the tests: load magnitude, out-of-plane displacement, displacement of the loaded edge (or head), strain magnitudes, and qualitative characterization of the overall buckle pattern. Load was measured by the test machine load cell, and was displayed throughout the test on a properly calibrated voltmeter. Strain measurements were made using foil-resistance strain gages placed at various locations on the panel. Out-of-plane displacement was measured using induction-type spring/plunger transducers known as direct current differential transducers, or DCDT's. Displacement of the loading head was also measured using a DCDT, and the overall buckle pattern was displayed using the moiré fringe technique. Strain gage and DCDT voltages were recorded on magnetic tape using an automated data acquisition system and were translated to strain

units and inches, respectively, by postprocessing software. Load data was also recorded in this way.

The strain gage/DCDT layout was decided on the basis of a preliminary STAGSC-1 linear bifurcation-buckling finite element analysis. This analysis provides a good estimate of buckling load and a reliable general indication of the buckle patterns to be expected, and has proven to be accurate enough for final buckling load calculations. The level of accuracy exemplified by these buckling load predictions indicates that the prebuckling behavior for the panels studied was not appreciably nonlinear. Bifurcation analyses have also been helpful in indicating closely spaced modes so that panels may be gaged in case either the first or the second mode is observed. (Closely spaced modes occurred in three of the six panels tested.)

Once the buckle pattern is known from the bifurcation analysis, gages are placed to record the maximum expected strains and displacements in the panel (e.g., in the middle of a half-wave) and also at the center of the panel, as a point of reference. (On two of the panels, strain gages were also placed on nodal lines to investigate suspected failure mechanisms.) The same strain gage pattern is used for both sides of the panel, so that there are pairs of gages mounted back-to-back over the surface of the plate. This arrangement is useful since bending behavior is easily observed by the divergence of back-to-back strains. Divergence occurs because when the panel bends, one of the gages undergoes compression while the other experiences tension. (See Figure 5.3.) In the case of a perfect panel with little or no bending-extensional coupling, the point of divergence is coincident with buckling, whereas a panel with a high degree of bending-extensional coupling or imperfection exhibits divergence at loads far below buckling.

In order to observe the buckle pattern as the test progresses, the moiré fringe technique is used. This technique consists of first painting one side of the panel white so that it is highly reflective. A piece of transparent plastic film covered with very thin vertical lines (50 per inch) is placed in front of the panel's painted side. Then, a high-intensity light source



is directed at the panel throughout the test. The variation in out-of-plane displacement over the panel surface during buckling and postbuckling makes it possible for the observer to see a contour plot of the panel's out-of-plane displacement during the entire test. This technique is extremely helpful to the engineer both during and after the test in determining the overall behavior of the plate without taking reams of data. For example, the effect of anisotropy (in particular, extension/shear coupling) is very obvious, since one can actually see the buckle pattern skewing during the test.

To study various failure characteristics of the six panels, each panel was tested twice; the only difference between the two separate runs was the stopping point of the test. The stopping point of the first test is determined by sounds the panel makes as it is loaded. For the material tested, impending failure is easily detected as a series of cracking or popping sounds; the first audible crack was then used as the stopping point for the first run. Although admittedly an imprecise technique, this method generally allows one to examine the area of failure initiation long before the panel is totally destroyed.

The point of crack initiation is located using a nondestructive test technique known as the C-scan. The C-scan is an ultrasonic technique, in which the panel is submerged in water, sound waves are passed through the panel, and their attenuation is recorded at several thousand points over the panel's surface. Maximum attenuation is seen as a white area on the C-scan, while minimum attenuation is indicated by black areas. At points where the panel has become delaminated, sound does not penetrate the panel, and so the initial failure is identified as a white area on the C-scan, while black areas indicate that the material is still structurally sound. (See Figure 5.4 for a sample C-scan; the remaining C-scans are collected in Appendix C.) Unfortunately, the C-scans also show the strain gages and their associated wiring, since the gages had to be left intact for the second test; however, failure initiation is still clearly visible in most of the C-scans. After C-scanning, the second test run was conducted, in which the panel was allowed to fail totally, so that the final failure location, load, and other data could be recorded.

### 5.2.2 Observations Regarding Experimental Techniques

During this study, important differences between the test methods for orthotropic and anisotropic panels were noted. In tests involving orthotropic panels, two strain symmetry conditions can be used to ensure that the loading head is level. The first symmetry condition is that back-to-back gages must register equal strains at some low load prior to buckling (about 700 lbs. for these panels). The assumption is that if the loading head is level in the plane perpendicular to the plate, then the load is purely axial and there is no transverse component and therefore no bending. Secondly, gages in symmetric locations with respect to the horizontal centerline should show equal strain; this indicates that the loading head is level in the plane of the plate. (Refer to Figure 5.5.) For panels with bending-extensional coupling, the first requirement is never satisfied except at zero load, since bending is experienced whenever an axial load is applied. Furthermore, the symmetry conditions for anisotropic panels are not the same as those for isotropic panels. For anisotropic panels, inversion symmetry rather than mirror symmetry is observed, as described in Chapter 2.

Before these differences were realized, very poor prebuckling stiffness agreement was obtained (30 to 40% error); however, once different methods were used to ensure a level loading head, error was reduced to 2% or less. To level the loading head, a very simple procedure is used. The loading head and platen are brought together and an extremely high load (50,000 – 60,000 pounds) is applied to the loading head. Then, all the leveling screws are tightened. After performing these simple steps, the loading head and platen are parallel.

## 5.3 Finite Element Model

### 5.3.1 Discretization and Boundary Conditions

All the experiments were modeled using the STAGSC-1 finite element code. Sample runstreams for both linear bifurcation buckling and nonlinear analyses are shown in Appendix D. Figure 5.6 is a plot of the undeformed model geometry for the 5.5 inch wide plates, with boundary conditions as noted. In addition to the edge boundary conditions shown, additional constraints were placed on interior nodes to facilitate modeling of the supports described in Section 5.2.1. These constraints, depicted in Figure 5.6, are applied using STAGS load definition cards. Also, although the experiments are conducted using an applied displacement at one edge of the plate, the problem is modeled using an applied load at one point on the loaded edge, in conjunction with multi-point constraints to ensure that the loaded edge remains straight. This technique is easier than formally applying a displacement, since it makes postprocessing for equilibrium forces unnecessary. All the analyses were done using the STAGS 411 plate element.

As can be seen from Figure 5.6, the grid is fairly fine and is nonuniform but mirror-symmetric about the panel centerlines. The nonuniformity arises from the need to compare STAGS displacements with experiment data at certain points on the panels. Symmetric grids were used because deviation from a symmetric pattern adversely affects results unless exceptionally fine grids are used. The grids used for final results are as shown in Table 5.4.

Table 5.4. Finite Element Model Discretization

Panel Width, in.	Total Number Of Elements	Elements per Half-Wave	
		X	Y
4.0	620	12	8
5.5	528	10/12	8
7.0	456	10.5	10

A good starting point for grid evaluation is the bifurcation buckling analysis, since by examining convergence of the critical buckling load, one can get at least a preliminary estimate of the grid required. Shown in Table 5.5 are buckling loads obtained using several different grids in the analysis of the 4 inch-wide,  $[\pm 30/90]_5$  panel. (The support elements around the edges of the model are omitted in the tabulation since they do not contribute to approximation of out-of-plane displacement.) Results shown in this table appear to be more sensitive to the number of elements used in the  $y$  direction than in the  $x$  direction; this is due to the fact that in the  $y$ -direction, the minimum number of elements used (4) is inadequate to approximate the out-of-plane behavior. For final results, the 12 by 8 element model was chosen; however, based on limited experience with coarser grids, adequate results could be obtained with a somewhat lower level of discretization.

Table 5.5. Grid Convergence,  $[\pm 30/90]_5$  4-inch-wide Panel

Elements/Half-Wave $x$ -direction	Elements/Half-Wave $y$ -direction	Total Elements	$P_{cr}^1$
6	4	192	4142
8		252	4160
12		372	4174
6	8	320	4247
8		420	4272
12		620	4290
6	12	448	4278
8		588	4303
12		868	4322

### 5.3.2 Solution Strategy

The details of the nonlinear analysis procedure used herein are explained in terms of a typical end shortening curve for this type of problem, shown in Figure 5.7. The general idea is to allow STAGS to increment the load so that solutions are obtained at various points along the end shortening curve. The analysis is begun at a load below buckling, such as the point labeled one, and is continued far into postbuckling to a load several times the buckling load, such as point three. Since the analysis will be compared with test data, the final load is determined primarily by the panel's exhibited failure load.

The only difficulty is that, for the perfect case, the tangent stiffness matrix becomes singular and therefore unfactorable at buckling (point two in Figure 5.7). To overcome this problem, an imperfection is imposed on the panel in order to remove the singularity. The shape of the imperfection is obtained from a linear bifurcation buckling analysis, which generates the eigenvalue and mode shape and saves them on disk. Then, the user specifies that the nonlinear analysis will use the saved mode shape, multiplied by some constant. The result of this procedure is that, if the imperfection is not too large, the response is almost identical to that of the perfect case, except that the curve is differentiable at buckling, as shown by the solid line in Figure 5.7. The imperfection must not be too large, or the response will be grossly different from the perfect case. For the problems solved herein, the magnitude of the imperfection was about one percent of the total panel thickness, although a larger two percent imperfection was needed in the case of the seven inch wide,  $[\pm 50/35]_5$  panel. One might think that for panels with bending-extensional coupling, the out-of-plane behavior would be enough to trigger buckling without use of an imperfection, but such was not found to be the case. Without the imperfection, the analysis remains on the unstable primary path instead of branching to the stable secondary path, because the level of bending-extensional coupling present in the panels tested does not cause sufficient out-of-plane displacement to trigger buckling.

One more constraint is needed when the buckling analysis shows that the structure has two nearly coincident eigenvalues. In such a case, specifying the proper imperfection shape is not enough to cause the analysis to choose the correct secondary path; convergence difficulties arise and the analysis cannot get past buckling. In order to force the analysis to choose one of the two possible secondary paths, a single Lagrangian constraint can be applied to force the buckled shape to adhere to the symmetry of the desired mode shape. For example, if the desired mode is symmetric (meaning an odd number of half-waves), then the analyst specifies that two appropriate points on either side of the shorter centerline must have the same out-of-plane displacement; if the desired mode is antisymmetric, then the displacements at the two points must be negatives of one another. Of course, points must be chosen which represent the larger displacements in the panel, and the different types of symmetry exhibited by anisotropic panels (described in Chapter 2) must be kept in mind.

The user must also choose the nonlinear solution strategy to be employed. STAGS provides essentially three solution techniques: the classical Newton-Raphson technique, a computationally less expensive modified Newton-Raphson technique, and an option in which the step size is controlled automatically using a path-length parameter as an independent parameter [24]. The path-length technique is used herein and was preferred over the two more classical Newton-Raphson techniques because they are not as effective in the neighborhood of buckling, when the tangent stiffness matrix is ill-conditioned [25].

## **5.4 Comparison of Experimental and Finite Element Results**

### **5.4.1 Presentation and Discussion of Buckling Load And End Shortening Results**

There are many aspects of the experiments which can be compared with computational results; perhaps the most informative of these in terms of global response is panel end shortening. This is because end shortening plots provide a simple measure of overall panel stiffness throughout the test, as well as a good estimate of the buckling load. There are

essentially three regions of interest in examining an end shortening curve. The first is the prebuckling range. It is important that agreement be obtained between model and experiment within this range, since agreement indicates that material stiffness coefficients and boundary conditions used in the analysis are correct. Secondly, one would like to predict the buckling load accurately. Finally, if the prebuckling and buckling responses are accurate, then loading, boundary conditions, and material properties have probably been modeled correctly; therefore, any discrepancies in the postbuckling response cannot be due to improper modeling of these aspects of the problem unless they change as more load is applied.

#### 5.4.1.a Buckling Load Results and Discussion

A few comments are in order concerning the definition of the term "buckling load". For a perfect panel with no bending-extensional coupling, the buckling load is very easy to determine, since buckling can be discerned as a sharp knee in the end shortening curve or the precise point at which back-to-back strain gages diverge. However, in the presence of initial imperfections or bending-extensional coupling, buckling is not well defined; in fact, some say that, to be precise, one should not even use the term "buckling" in such cases. This is because the transition from a prebuckled to a postbuckled configuration is no longer sudden; the phenomenon becomes gradual, and so the previously sharp bifurcation point in the end shortening and back-to-back strain gage curves becomes a gradual curve. However, in the interests of brevity, the term will be used herein, and will indicate that load at which a perfect system without bending-extensional coupling would buckle.

The method used to estimate the buckling load is very simple and is depicted in Figure 5.7; on the end shortening curve, one draws two straight lines, one along the linear prebuckling portion of the curve, and one along the initial part of the postbuckling curve. The intersection of the two lines is then the buckling load, since an end shortening curve for the corresponding perfect system has been constructed. If desired, this estimated load can be confirmed by examining back-to-back strain data, as was shown in Figure

5.3. To evaluate this data, one examines the area of divergence of the two strains; the latter portions of the two curves are then extrapolated backward until they cross at some point within the region of divergence, as shown in Figure 5.3. This point is then taken as buckling.

With this item of terminology defined, results may now be discussed. First, once the loading head leveling procedure described in Section 5.2.2 was used, excellent agreement was obtained for prebuckling stiffnesses, which were taken to be the slope of the end shortening curve in the linear prebuckling range. In all cases, the slope was predicted to within two percent or less. Secondly, buckling load results are shown in Table 5.6, where it is seen that average agreement between experiment and analysis was 14.4%. Both the experimental buckling loads,  $P_{cr}^{exp}$ , and the STAGS buckling loads,  $P_{cr}^{fem}$ , were obtained from the end shortening curves shown in Figure 5.8. The most likely explanation for the difference in experimental and analysis buckling loads is the presence of fairly large initial imperfections. Measurements indicated that imperfections of the order of 1.5 times the panel thickness were not uncommon. It should also be noted that the panel exhibiting the largest difference between analysis and experiment, the  $[\pm 50/35]_5$ , 4 inch-wide panel, also underwent a mode change, suggesting that the two phenomena might be related.

Table 5.6. Buckling Loads, Pounds

Panel Width, inches	Panel Layup	Number Of Half-Waves	$P_{cr}^{exp}$ , lbs.	$P_{cr}^{fem}$ , lbs.	Percent Difference
4.0	$[\pm 30/90]_5$	5	3750	4300	14.7
4.0†	$[\pm 50/35]_5$	5→6	4200	5300	26.2
5.5	$[\pm 30/90]_5$	4	2750	3100	12.7
5.5	$[\pm 50/35]_5$	4	3100	3500	12.9
7.0	$[\pm 30/90]_5$	3	2200	2500	12.0
7.0‡	$[\pm 50/35]_5$	3	2460	2670	7.9

† Experienced mode change

‡ Required 2% imperfection



Linear bifurcation buckling analyses were also conducted for all the experiments discussed; in all these analyses, the first two eigenvalues and mode shapes were calculated. In all but one case, the first mode determined by the analysis was also the mode exhibited by the panel. As shown in Table 5.7, the panel which was the exception underwent a mode change, with the second mode occurring first. This panel also had the smallest percent separation between its buckling loads, as well as the largest percent difference between experimental and analysis buckling loads. As is obvious from the table, very close eigenvalues were frequent, but no trends suggest themselves regarding this phenomenon. It is also worth noting that all the panels exhibit the same trend that one would expect for isotropic or orthotropic panels: a higher aspect ratio means more half-waves in the buckling mode shape.

Table 5.7. Linear Bifurcation Buckling Results, Pounds

Width, inches	Layup	Mode 1		Mode 2		% Sep.†
		Load, lbs.	Half-Waves	Load, lbs.	Half-Waves	
4.0	$[\pm 30/90]_5$	4290	5	4311	6	0.5
4.0†	$[\pm 50/35]_5$	5248	6	5265	5	0.3
5.5	$[\pm 30/90]_5$	3016	4	3028	3	0.4
5.5	$[\pm 50/35]_5$	3468	4	3559	3	2.6
7.0	$[\pm 30/90]_5$	2397	3	2458	2	2.5
7.0	$[\pm 50/35]_5$	2678	3	2839	2	5.7

† Experiment exhibited mode change, with second mode occurring first; next eigenvalue is 5401 lbs.

‡ Indicates the percentage by which the buckling loads for the first two modes are separated.

It is interesting to note that for these panels, comparison of Tables 5.6 and 5.7 indicates that the buckling loads obtained from the linear bifurcation buckling analyses are excellent estimates for the buckling loads obtained from the nonlinear analyses. The average percent difference is only 1.5%. This result indicates that the prebuckling behavior is

not significantly nonlinear, since buckling loads are not appreciably affected by the use of nonlinear theory.

#### 5.4.1.b Postbuckling Results and Discussion

The third and final portion of the end shortening curve depicts global postbuckling response. The end shortening curves shown in Figure 5.8 indicate varying degrees of agreement between experiment and analysis at two distinguishable stages of postbuckling. The first stage is a range of nearly linear behavior immediately after buckling. In this region, the slope of the end shortening curve suggests itself as a simple basis for comparison. Table 5.8 summarizes the slope values for the experiment and analysis curves, and indicates that agreement between analysis and experiment is good in this range, except in the case of the  $[\pm 50/35]_5$ , 4 inch-wide panel. Also, note that agreement is slightly better for the  $[\pm 30/90]_5$  panels, regardless of aspect ratio.

Table 5.8. Slope of Initial Postbuckling Curve

Layup	Width, in.	STAGS Slope $\frac{\text{lbs}}{\text{in}^2} \times 10^4$	Experiment Slope $\frac{\text{lbs}}{\text{in}^2} \times 10^4$	Percent Error
$[\pm 30/90]_5$	4.0	5.89	5.48	7.5
	5.5	7.47	7.19	3.9
	7.0	9.43	9.21	2.4
$[\pm 50/35]_5$	4.0	2.77	2.44	13.5
	5.5	3.69	3.51	5.1
	7.0	4.93	4.58	7.6

The second discernible stage of postbuckling is marked by a gradual but noticeable degradation of the panel's stiffness. Agreement between analysis and experiment also deteriorates markedly in this range, with better correlation being obtained for the  $[\pm 30/90]_5$  panels. By simply examining the end shortening plots, one can obtain a subjective estimate of the stiffness degradation of each panel; however, it is possible to obtain a numerical estimate which more clearly delineates the observed trends. Shown in Figure 5.9 is the

method used to obtain this estimate. In the figure, the early portion of the postbuckling curve is linearly extrapolated to a point having the same end shortening value as that of the experiment curve at a point far into postbuckling. Then, the difference between the extrapolated load and the actual load is taken as the stiffness degradation. The same procedure can be followed for the analysis data, and results can be compared; however, care must be taken to account for the differences in buckling load between experiment and analysis. To accomplish this, points on a set of experimental and analytical curves are chosen to correspond to the same load, nondimensionalized by the estimated buckling load  $P_{cr}$  for the particular curve being examined.

Results of these comparisons are shown in Table 5.9. Although comparisons are easily made between analysis and experiment, it is important to note that panel-to-panel comparisons should not be made, since calculations were done at different values of  $P/P_{cr}$  for each panel. Different values of  $P/P_{cr}$  had to be chosen in order to obtain results which represented the stiffness degradation over the entire postbuckling range. Heeding this admonition, two trends are nevertheless apparent. First, the percent differences between analysis and experiment are always significantly greater for the  $[\pm 50/35]_5$  panels. Secondly, for both layups, percent difference is largest for the 5.5 inch-wide panel, which was the only panel of the three to exhibit an antisymmetric buckling mode shape.

Table 5.9. Postbuckling Stiffness Degradation

Layup	Width, in.	$P/P_{cr}$	STAGS, lb/in	Experiment, lb/in	Percent Difference
$[\pm 30/90]_5$	4.0	2.0	333	400	16.8
	5.5	3.0	800	1267	36.9
	7.0	4.0	2000	2233	10.4
$[\pm 50/35]_5$	4.0	1.4	233	333	30.0
	5.5	2.0	333	867	61.6
	7.0	2.5	767	1533	50.0

The end shortening results presented here appear to be very similar to those presented in [16]. In [16], the effect of transverse shear on the various response quantities of rectangular aluminum and  $[\pm 45]$  graphite-epoxy panels is studied. It is important to note that the laminates and boundary conditions used in [16] are different from those described herein; thus definite conclusions are difficult to draw based on comparison with the present work. Nonetheless, some observations can still be made.

The end shortening curves presented in [16] show that, for the cases studied, transverse shear theory predicts a slightly less stiff postbuckling response than does classical theory. These results are similar to those shown in Figure 5.8, in that the experimental results are less stiff than the finite element results obtained without shear deformation. Thus, it is tempting to attribute the lack of test/analysis correlation during postbuckling to the lack of a transverse shear flexible finite element formulation. However, it is important to note that, in [16], the differences between the classical and transverse shear results begin immediately at buckling; there is no postbuckling region in which the stiffness remains nearly constant and the slopes of the two curves agree, as is the case with the results presented in Table 5.8. Furthermore, the results presented in Table 5.9 differ greatly from those observed in the graphs of [16]. There is no significant disparity in the stiffness degradation predicted by the shear deformation and classical theories in [16], while the disparity is quite large for the panels examined in the present work. For these two reasons, it is difficult to attribute all the differences between experiment and finite element analysis to a lack of transverse shear flexibility in the finite element model; however, the role of transverse shear in the response of anisotropic laminates with bending-extensional coupling should not be discounted, and merits further study.

A second explanation for the degradation of postbuckling stiffness in all the experiments is that a material failure of the type described in [26] has occurred. In [26], the point is made that because of the form of the stress transformation relations for an all- $\pm 45$  laminate, large shear stresses are encountered in the principal material directions and therefore

at the matrix/fiber interface of each lamina. These shear stresses tend to break the bond between the fiber and matrix, resulting in an inplane matrix shearing failure. This failure mechanism seems a likely cause for the more severe postbuckling stiffness degradation observed in the  $[\pm 50/35]_5$  laminate, as well as for the larger disparity between predicted and observed stiffness degradation, since this laminate is very similar to an all- $\pm 45$  laminate. Also, some of the C-scans shown in Appendix C support the existence of matrix shearing, since there does appear to be some damage which runs in the fiber direction.

#### 5.4.2 Presentation and Discussion of Out-of-Plane Displacement Results

Out-of-plane (or transverse) displacement data was collected at seven to eight different points on each of the panels tested. Data obtained at the point of maximum transverse displacement is of interest, since it allows determination of the relative magnitude of out-of-plane behavior at the different stages of the experiment. Also, as mentioned previously, comparison of transverse displacement at reflectionally symmetric points indicates the amount of twist occurring throughout the experiment. Lastly, satisfaction of the anisotropic symmetry conditions described in Chapter 2 can be checked by comparing results at inversionally symmetric points.

Shown in Figure 5.10 are plots of maximum transverse displacement for all six panels. From these plots, three facts can be noted. First, the maximum transverse displacements occurring in these experiments range between one and four times the panel thickness of approximately 0.08 inches. Second, the transverse displacement present at buckling amounts to less than 40% of the panel thickness, decreases with increasing aspect ratio, and is generally larger for the  $[\pm 30/90]_5$  panels, as summarized in Table 5.10. Finally, the STAGS curves and the experimental curves have almost exactly the same curvature in postbuckling, indicating that if one adjusts for the error in buckling load, the transverse displacements are modeled accurately.

The plots of Figure 5.11 indicate the amount of twisting occurring in each of the panels. The two curves appearing in each plot are the absolute values of transverse displacements

Table 5.10. Transverse Displacement at Buckling

Layup	Width, in.	Displacement, in.	$\frac{\text{Displacement}}{\text{Thickness}}$
$[\pm 30/90]_5$	4.0	0.020	26
	5.5	0.025	32
	7.0	0.029	37
$[\pm 50/35]_5$	4.0	0.006	8
	5.5	0.017	22
	7.0	0.016	21

at two reflectionally symmetric points on either side of the short centerline, as shown in the figure legend. If the two lines are coincident, then no twisting has occurred; the distance between the two lines is then the amount of twist. In the case of the  $[\pm 50/35]_5$ , 4 inch-wide panel, a mode change prevents meaningful comparison of the two displacements; therefore, discussion is presented here for the remaining five plots.

Overall, there is no pattern to the presence or absence of twisting behavior. Notice that for the  $[\pm 30/90]_5$  panels, little or no twist is observed when the buckling mode is symmetric (i.e., for the 4 and 7 inch-wide panels), but a significant amount of twist occurs in the 5.5 inch panel, which experienced an antisymmetric buckling mode. From these results, one might be tempted to assert that twisting occurs only when the buckling mode is antisymmetric. However, for the remaining two  $[\pm 50/35]_5$  panels, the amount of twist is non-negligible regardless of mode shape, thus destroying the correlation between twist and mode shape symmetry. Shown in Figure 5.12 are corresponding twist plots generated from the finite element analysis results. These plots are consistent with Figure 5.11.

The plots shown in Figure 5.13 are similar to the twist plots, except that they are displacement plots at inversionally symmetric points, and so indicate the degree of symmetry satisfaction. As was explained in Chapter 2, no precise type of symmetry is expected when an antisymmetric buckling mode is exhibited, and this is confirmed in the plots for

both 5.5 inch-wide panels. For the  $[\pm 30/90]_5$ , 4 inch-wide panel, the symmetry violation is of the same magnitude as the twist, i.e., very small, while for the 7 inch-wide panels, the symmetry conditions are fairly well satisfied early in postbuckling, but become badly violated as the experiment proceeds. Shown in Figure 5.14 are similar plots made from the STAGS results; these plots confirm all the symmetry conditions stated in Chapter two, including the fact that there is no symmetry when the buckling mode is antisymmetric, as in the case of the 5.5 inch-wide panels.

To summarize the twist and symmetry results, the following table is presented:

Table 5.11. Summary of Twist and Symmetry Results

Layup	Width, inches	Symmetry Of Mode Shape	Twist Magnitude		Symmetries Satisfied?	
			Experiment	STAGS	Experiment	STAGS
[±30/90] <sub>5</sub>	4	Symmetric	Negligible	Zero	Yes	Yes
	7				No	
	5.5	Antisymmetric	Large	Large	None Expected or Observed	
[±50/35] <sub>5</sub>	4	—	—	—	—	—
	7	Symmetric	Large	Large	No	Yes
	5.5	Antisymmetric	Large	Large	None Expected or Observed	

#### 5.4.3 Presentation and Discussion of Strain Results

Back-to-back strain gage rosettes and axial strain gages were placed at between nine and fifteen locations on the tested panels. Attempts were made in all cases to record maximum or near-maximum strains, and in two cases, strains were recorded near failure locations.

Shown in Figure 5.15 are plots of strain at those points on each panel which underwent maximum and near maximum strains. In the case of the 5.5 inch-wide panels, the maximum strain, which occurred in the center of the second of four half-waves, was not recorded; instead, strain in the center of the first half-wave was measured. For the other four panels, center strains were the maximums, since an odd number of half-waves were observed in

those cases. Also shown in Figure 5.15 are the estimated buckling loads for each of the panels, which are confirmed by the plotted strains.

The most notable characteristic of these six strain plots is the unusual shape of most of the curves. Look first at plot (b), the center strains for the  $[\pm 50/35]_5$ , 4 inch-wide panel. The discontinuities late in postbuckling are easily explained; they indicate an observed mode change from a five to a six half-wave buckle pattern, and so are not unexpected.

Plots (c) and (d), the near-maximum strains for both 5.5 inch-wide panels, are very similar to other published back-to-back strain curves [15], in that the two strain curves grow smoothly apart and do not curve back toward each other at any point. Since the distance between the curves is essentially twice the local curvature in the axial direction, such behavior simply indicates that the initial buckled shape is becoming more pronounced; i.e., the curvature is steadily increasing. Now compare these plots to plot (f). There, some curvature is developed immediately after buckling, and then about one-third to one-half of the way through postbuckling, the curvature decreases. Such behavior is often taken to indicate an overall mode change; however, this seems peculiar since the plot of maximum transverse displacement indicates that the maximum out-of-plane deformation increases smoothly throughout postbuckling. Also, no mode change was observed in the moiré fringe photographs. At most other points of non-negligible strain on the same panel, the back-to-back strain curves are either very similar to those shown in Figure 5.15, or the two strain curves actually cross over each other, indicating that the curvature has changed sign.

The most obvious explanation which accounts for both the displacement and strain behavior is that, in a gross sense, the initial buckled shape is retained throughout postbuckling, while some of the details of the deformation pattern change. Figure 5.16, a plot of transverse displacement down the long centerline of the  $[\pm 50/35]_5$ , 7 inch-wide panel, displays just such behavior. (This plot was generated using STAGS results, and the



shown strains are actual test data.) Initially, the deformed shape appears nearly sinusoidal. However, at  $P = 5733$  pounds, the following changes have taken place:

- The center half-wave has flattened, causing a decrease in curvature as shown in plot (b) of the figure, while the outer two half-waves have become more pointed, explaining the increase in curvature displayed in plot (a).
- The points of zero deflection (commonly referred to as the nodal lines) have shifted substantially. This explains the curvature sign change seen in plot (c); this set of gages was placed near enough to the nodal line for the line to have shifted from a position above the strain gages to a point below them. No sign change occurred for gages placed far away from a nodal line.
- The inflection points, denoted by the different symbols, have shifted, indicating that the entire deflection pattern has shifted off the load axis. For brevity, this phenomenon will henceforth be referred to as pattern eccentricity. (The inflection points were determined using cubic spline interpolation of the STAGS displacement data.)

Finally, when the load has increased to 8000 lb, curvature at the center of the panel has increased slightly, thus explaining the "hourglass" shape of plot (b).

Similar plots made for the other two  $[\pm 50/35]_5$  panels display all the same trends as Figure 5.16, except that for the 4 inch-wide panel, pattern eccentricity is negligible. (See Figure 5.18 for comparison.) On the other hand, plots produced from the  $[\pm 30/90]_5$  panel analysis data behave somewhat differently, as shown in Figure 5.17. Comparison of this figure and Figure 5.16 indicate that the flattening effect is much more severe in the  $[\pm 50/35]_5$  panel; in the  $[\pm 30/90]_5$  panel, only enough flattening occurs to cause a barely noticeable curvature change in strain plot (b). A shift in the location of the nodal lines is still observed for this panel, causing a curvature sign change in plot (c); also, the outer half-waves become progressively more pointed with load, again causing the steady increase in curvature depicted in plot (a). Pattern eccentricity is not seen in this figure.

Further examination of all the plots shown in Figure 5.18 reveals that one generalization is possible: the flattening effect is consistently more exaggerated in the  $[\pm 50/35]_5$  panels. For the  $[\pm 30/90]_5$  panels, curvature at points of maximum displacement either remains nearly constant after a certain load, or it increases. The other two characteristics, shift of nodal lines and pattern eccentricity, occur with no particular pattern; that is, no real generalizations regarding these phenomena can be made. Furthermore, both phenomena can be observed in orthotropic panels.

It is apparent from this discussion that decreases in curvature partway through post-buckling do not necessarily indicate a mode change, at least not in the classical sense of a shift from one deformation pattern to another, dramatically different pattern because of a newly encountered instability. Rather, such curvature changes can point to subtle changes in the deformation pattern which can best be described as changes in the overall character of the buckled mode shape.

It was suggested by Jensen [14] that such curvature changes represent a localized dimpling, indicating the onset of a classical mode change which actually did occur for his panels. Such a phenomenon is possible and could account for the localized presence of unusual strain patterns; however, the presence of such patterns at many points on the plate, as well as the consistent analysis and test displacement data presented here suggest that dimpling is not causing the decreases in curvature; rather, gradual flattening of central portions of the pattern is at fault.

## **5.5 Failure Initiation and Development**

### **5.5.1 Qualitative Results**

From the combination of the moiré fringe photographs (shown in Appendix B), the C-scan results (shown in Appendix C), and the failed panels themselves, a good qualitative picture of the failure characteristics of each panel is obtained. Shown in Figure 5.19 are sketches, drawn to scale, of all six panels. Three things are indicated on each sketch: area

of failure initiation as detected by C-scans, area of final failure, and final position of the nodal lines as indicated by the moiré fringe photographs. No measurements are shown, since the photographs do not allow precise measurement. Determining the locations of the nodal lines is particularly difficult, since it is hard to ascertain the exact locations of lines of zero displacement by measuring the photographs.

In any case, a few observations are possible. First, note that failure always initiates either on or very close to a nodal line. This fact is consistent with [15]. There, the explanation is advanced that "the higher strains near the specimen edges couple with the out-of-plane deflection gradients at the nodal line to induce sufficient transverse shearing loads to fail the specimen in shear before the large bending strains at the points of maximum displacement become critical". The facts embodied in this statement can for the most part be confirmed by information presented in various parts of this chapter, as will be explained in the following paragraph.

First, it is easy to confirm that strains near the edges of the panel are higher than those along the centerline. Shown in Figure 5.20 are plots of strain data collected at five closely spaced points near the short edges of both 5.5 inch-wide panels. This data allows comparison of strains over the width of both panels. The magnitudes of the middle surface strains, indicated by open circles, are always higher near the edges of the panels. (Note, however, that this is not always true of the surface strains; near the bottom of the  $[\pm 30/90]_5$  panel, one of the center surface strains is actually slightly larger than the two edge strains.) Secondly, strain data collected near the nodal lines of the 7 inch-wide panels confirms that the strains are much higher along the specimen nodal lines, as shown in Figures 5.16 and 5.17. (Whether strain is higher at the edge of the nodal line than at its center cannot be determined here, since no data was taken at the center of a nodal line.) Third, it is obvious from these same two figures that the gradient of transverse displacement is also high at the nodal line. Finally, that the panels fail in shear is suggested by the photograph shown in Figure 5.21. To obtain this photograph, the  $[\pm 50/35]_5$ , 7 inch-wide panel was sectioned so

that the area where the C-scan indicated failure initiation could be examined. A diagonal crack through the thickness is evident, with delaminations propagating in both directions away from the crack.

A second observation involves the relationship between initial and final failure locations. In four of the six panels, the initial delamination and the final failure were nowhere near each other. This is especially true for the 7 inch-wide panels, where the C-scans indicated failure initiation at the top nodal line, while the final failure occurred at the bottom nodal line. Evidently, some redistribution of load occurs after the initial damage is sustained, causing the final failure to frequently occur in a totally different location from the initial damage.

#### **5.5.2 Quantitative Results**

Table 5.12 presents a summary of pertinent quantitative data collected at the failure load of each panel. From this data, the following facts are apparent:

- Normalized loads increase steadily with decreasing aspect ratio, as expected. However, absolute failure loads are nearly the same for the 4 and 5.5 inch-wide panels of each layup, while the load withstood by the 7 inch-wide panels is somewhat higher for both layups.
- Loads carried by the  $[\pm 30/90]_5$  panels are much higher, both in absolute and relative terms, than those carried by the  $[\pm 50/35]_5$  panels.
- Normalized end shortening increases with decreasing aspect ratio, while absolute end shortening does just the opposite.

### **5.6 Summary of Observations**

The following is a short summary of observations made in this chapter. Refer to Chapter 6 for discussion of conclusions, as well as for suggestions for future research. For the reader's convenience, notation is made below of the sections, tables, and figures which best support each item.

Table 5.12. Load and End Shortening at Failure

Layup	Width, in.	$P_f$ , lbs.	$P_f/P_{cr}$	$\delta_f$ , in.	$\delta_f/\delta_{cr}$
[ $\pm 30/90$ ] <sub>5</sub>	4.0	8500	2.27	.129	3.9
	5.5	8570	3.12	.119	6.6
	7.0	9480	4.31	.112	9.7
[ $\pm 50/35$ ] <sub>5</sub>	4.0	6790	1.62	.225	2.7
	5.5	6740	2.17	.199	4.7
	7.0	7220	2.93	.195	7.4

Observations based on experiment behavior:

- The experimental setup is critical for laminates possessing anisotropy and/or bending-extensional coupling, in that mirror symmetry conditions cannot be used to ensure that a uniform axial load is applied. (Section 5.2.1.)
- Buckling loads tend to be slightly higher for the [ $\pm 50/35$ ]<sub>5</sub> panels, with the differences between results for the two layups being larger for the higher aspect ratio panels. (Table 5.6.)
- Transverse displacements and bending strains at buckling are not appreciable, indicating that the effect of bending-extensional coupling on prebuckling behavior is negligible for the laminates studied. (Figure 5.15, Table 5.10, Tables 5.6 and 5.7, Section 5.4.1.)
- According to end shortening results, there are two discernible regions in postbuckling. During the initial portion of postbuckling, the initial postbuckling stiffness of the panel is maintained. Then, about halfway through the postbuckling range, the stiffness of the panel begins to drop substantially. (Figure 5.8)
- Strain results indicate subtle changes in the buckle mode shape throughout postbuckling. The most noticeable changes are dramatic decreases in curvature in the central

portions of the  $[\pm 50/35]_5$  buckle patterns, as well as pronounced shifting of nodal lines for some panels. (Section 5.4.3.)

- Initiation of failure always occurs at or very close to a nodal line of the buckled shape. This lends credence to the observations advanced in [15]. (Figure 5.19.)
- Locations of failure initiation and final failure are not necessarily the same, probably due to redistribution of load after the initial damage. (Figure 5.19.)
- Postbuckling load carrying capability is much greater for the  $[\pm 30/90]_5$  panels than for the  $[\pm 50/35]_5$  panels. (Table 5.12.)
- Maximum observed transverse displacement ranges between one and four times the panel thickness and is inversely proportional to panel aspect ratio. (Figure 5.10.)
- Satisfaction of displacement symmetry conditions described in Chapter 2 is not consistent; the conditions are violated in both of the 7 inch-wide panels. (Section 5.4.2.)
- Twisting behavior is observed for both layups, but does not appear in all six panels. No pattern of absence or presence of twisting is discernible, since no twisting is observed, either analytically or experimentally, in the two higher aspect ratio,  $[\pm 30/90]_5$  panels. (Section 5.4.2.)

Observations based on finite element modeling efforts:

- Modeling of global response in the prebuckling range presents no problem, since the test and analysis end shortening results differed less than two percent within the prebuckling range. (Section 5.4.1.)
- Buckling loads estimated from a nonlinear finite element analysis are an average of 14.4% different from buckling loads estimated from test results. Predictions are better for lower aspect ratio panels, and are slightly better for  $[\pm 30/90]_5$  panels (13.1%

average difference) than for  $[\pm 50/35]_5$  panels (15.7% average difference). The most likely cause of the overall disparity is the presence of imperfections of the order of 1.5 times the panel thickness. (Table 5.6.)

- For the panels examined herein, linear bifurcation buckling analysis is as accurate as a nonlinear analysis in the prediction of buckling loads. This result again emphasizes that the prebuckling behavior of the panels studied was not appreciably nonlinear. Bifurcation analyses were also very helpful in determining expected mode shapes, as well as in pointing out the likelihood of a mode change during postbuckling. (Tables 5.6 and 5.7.)
- Linear bifurcation buckling analysis predicts nearly coincident eigenvalues, i.e., eigenvalues separated by less than .5%, for three of the six panels. Only in the case where separation of the eigenvalues was the smallest (.3%) was an obvious mode change observed. (Table 5.7.)
- In the initial portion of postbuckling, agreement between test and analysis end shortening results is good (2% to 8% difference in slope) except in the case of the  $[\pm 50/35]_5$ , 4 inch-wide panel, where the slopes differ by 13.5%. In all cases, slightly better agreement is obtained for the three  $[\pm 30/90]_5$  panels. (Table 5.8.)
- In the later portion of postbuckling, the stiffness degradation is always larger than that predicted by finite element analysis. Predictions of the drop in stiffness (as measured by percent difference between analysis and test) are much better for the  $[\pm 30/90]_5$  panels by factors of two to five, and are significantly worse for the 5.5 inch-wide panels of both layups. Possible causes for this disparity between analysis and test include the lack of transverse shear flexibility in STAGS and the possibility that matrix shearing occurs long before final failure. (Table 5.9, Section 5.4.1.)

- Finite element results indicate subtle changes in the buckling mode shape occurring throughout postbuckling. In all the  $[\pm 50/35]_5$  panels, the mode shape tends to flatten, causing decreases in curvature at points of maximum transverse displacement. This observation is confirmed by strain results, as described above. In some panels, pronounced shifting of nodal lines and inflection points also occurs, but no pattern is evident in this behavior, and such phenomena can be observed in orthotropic panels. (Section 5.4.3.)
- In all three cases, the  $[\pm 50/35]_5$  panels have proven more difficult to model in postbuckling than the  $[\pm 30/90]_5$  panels. In reviewing the results for the two sets of panels, the fact stands out that the largest differences between analysis and experimental results were usually seen for the  $[\pm 50/35]_5$  panels. In particular, difficulties arose in predicting the slope of the initial part of the postbuckling end shortening curve, and the stiffness degradation during the latter part of postbuckling. The only substantial difference between the two panels is that the  $[\pm 30/90]_5$  panel does not possess any extension-shear coupling; however, the evidence is not sufficient at this time to attribute the modeling difficulties to this distinguishing feature. (Throughout chapter.)
- The one panel which exhibited an observable mode change ( $[\pm 50/35]_5$ , 4 inch-wide) has proven very difficult to model. Apart from the current lack of a simple way to model the actual mode change, other seemingly unrelated aspects of the behavior were more difficult to model. For example, the percent difference in buckling load between analysis and experiment was 12.5% greater for this panel than for any of the others. Similarly, initial slope of the postbuckling curve was predicted 5.9% worse for this panel than for any other. (Throughout chapter.)
- Transverse displacements are well-predicted if adjustments are made to account for the error in predicting the buckling load. (Figure 5.10.)



- Although symmetry satisfaction is inconsistent in the experimental results, STAGS results behave precisely as predicted by the symmetry conditions of Chapter 2. (Table 5.11.)

## Chapter 6

### Observations and Recommendations

#### 6.1 Observations

Following is a summary of the observations derived from the present work. For the reader's convenience, notation is made of the section, tables, and figures which best support each statement. Also, each point is preceded by a short statement which categorizes it within the subsection.

##### 6.1.1 Observations Related to the Modified Rayleigh-Ritz Technique

###### 6.1.1.a Observations related to linear results

- Effect of boundary conditions on results: Accurate solution of problems involving the two axially loaded panels required the use of more functions per displacement degree of freedom than did similar problems involving transverse loading. This was due to the more complex boundary conditions used in the axial loading problems; in those problems, the in-plane displacement  $u_2$  was constrained along the loaded edges, causing a complicated stress state to be present in the corners of the panels. (Sections 4.2.3 and 4.2.4)
- Effect of anisotropy and bending-extensional coupling on results: Accurate solution of problems involving the anisotropic panel with bending-extensional coupling required the use of many more functions per displacement degree of freedom than did identical problems involving an orthotropic panel. (Section 4.2)
- Effectiveness of exterior penalty approach for enforcing boundary conditions:  
The external penalty function approach was effective in assuring satisfaction of boundary conditions for all problems, although in the case of the axially loaded panels, satisfaction of the constraint  $u_2 = 0$  constraint along the loaded edge was somewhat sensitive to variations in the penalty parameter. Overall, a broad range of four orders

of magnitude in the penalty parameter gives acceptable results for a linear problem; however, a narrower range of two orders of magnitude is recommended for nonlinear analysis due to observed convergence problems attributable to too high a penalty parameter. (Section 4.3)

- Performance of basis vectors:

- For the problems involving axial loading of anisotropic panels, the chosen basis vectors performed well. (Section 4.4.1)
- For the problems solved herein, the Grammian provides a good estimate of the number of basis vectors required to solve a given problem, thus alleviating the need to examine detailed results in order to select an appropriate reduced system size. (Section 4.4.2)

#### 6.1.1.b Observations related to nonlinear results

- Effect of anisotropy and bending-extensional coupling on results: Using the modified Rayleigh-Ritz technique, postbuckling response of the orthotropic panels studied can be accurately predicted; however, about twice as many functions are required in order to predict the postbuckling response of the nonorthotropic panels studied. A reasonable estimate of the postbuckling behavior of the nonorthotropic panels was obtained using the largest possible number of approximation functions (as defined by computer hardware limitations.) (Section 4.5)
- Effect of first order transverse shear deformation effects: Slight differences in overall postbuckling stiffness were seen which could definitely be attributed to transverse shear deformation, as in the case of the  $[0_4/90_4]_S$  panel; however, the addition of transverse shear deformation did not result in better prediction of postbuckling stiffness degradation in either of the other two cases studied. (Section 4.5)

### 6.1.2 Observations Based on Experiments

- Experimental setup: The experimental setup is critical for laminates possessing anisotropy and/or bending-extensional coupling, in that mirror symmetry conditions cannot be used to ensure that a uniform axial load is applied. (Section 5.2.1.)
- Prebuckling range: Transverse displacements and bending strains at buckling are not appreciable, indicating that the effect of bending-extensional coupling on prebuckling behavior is negligible for the laminates studied. (Figure 5.15, Table 5.10, Tables 5.6 and 5.7, Section 5.4.1.)
- Postbuckling:
  - According to end shortening results, there are two discernible regions in postbuckling. During the initial portion of postbuckling, the initial postbuckling stiffness of the panel is maintained. Then, about halfway through the postbuckling range, the stiffness of the panel gradually begins to drop. (Figure 5.8)
  - Strain results indicate subtle changes in the buckle mode shape throughout postbuckling. The most noticeable changes are dramatic decreases in curvature in the central portions of the  $[\pm 50/35]_5$  buckle patterns, as well as pronounced shifting of nodal lines for some panels. (Section 5.4.3.)
  - Experimental satisfaction of displacement symmetry conditions described in Chapter 2 is not consistent. (Section 5.4.2.)
  - Twisting behavior is observed for both layups, but does not appear in all six panels. No pattern of absence or presence of twisting is discernible. (Section 5.4.2.)
- Failure:
  - Initiation of failure always occurs at or very close to a nodal line of the buckled shape. This lends credence to the observations advanced in [15]. (Figure 5.19.)
  - Locations of failure initiation and final failure are not necessarily the same, probably due to redistribution of load after the initial damage. (Figure 5.19.)

### 6.1.3 Observations Based on Finite Element Modeling Efforts

- General observations:
  - In all three cases, the experimental postbuckling behavior of the  $[\pm 50/35]_5$  panels was more difficult to predict analytically than that of the  $[\pm 30/90]_5$  panels. In reviewing the results for the two sets of panels, the fact stands out that the largest differences between analysis and experimental results were usually seen for the  $[\pm 50/35]_5$  panels. In particular, difficulties arose in predicting the slope of the initial part of the postbuckling end shortening curve, and the stiffness degradation during the latter part of postbuckling. The only substantial difference between the two panels is that the  $[\pm 30/90]_5$  panel does not possess any extension-shear coupling; however, the evidence is not sufficient at this time to attribute the difficulties to this distinguishing feature. (Throughout chapter 5.)
  - The experimental behavior of the one panel which exhibited an observable mode change ( $[\pm 50/35]_5$ , 4 inch-wide panel) has proven very difficult to predict analytically. Apart from the current lack of a simple way to model the actual mode change, other seemingly unrelated aspects of the behavior were more difficult to model. For example, the percent difference in buckling load between analysis and experiment was 12.5% greater for this panel than for any of the others. Similarly, prediction of initial slope of the postbuckling curve was 5.9% worse for this panel than for any other. (Throughout Chapter 5.)
- Prebuckling range: Modeling of global response in the prebuckling range presents no problem, since the test and analysis end shortening results differed less than two percent within the prebuckling range for all panels. (Section 5.4.1.)
- Buckling:
  - Buckling loads estimated from a nonlinear finite element analysis are an average of 14.4% different from buckling loads estimated from test results. A likely cause of the

overall disparity is the presence of imperfections of the order of 1.5 times the panel thickness. (Table 5.6.)

- o For the panels examined herein, linear bifurcation buckling analysis as obtained from STAGSC-1 is as accurate as a nonlinear analysis in the prediction of buckling loads. Bifurcation analyses were also very helpful in determining expected mode shapes, as well as in pointing out the likelihood of a mode change during postbuckling. (Tables 5.6 and 5.7.)
- Postbuckling:
  - o In the initial portion of postbuckling, agreement between test and analysis end shortening results is good for five of the six panels. (Table 5.8.)
  - o In the later portion of postbuckling, the stiffness degradation is always larger than that predicted by finite element analysis. Predictions of the drop in stiffness (as measured by percent difference between analysis and test) are much better for the  $[\pm 30/90]_5$  panels by factors of two to five, and are significantly worse for the 5.5 inch-wide panels of both layups. Possible causes for this disparity between analysis and test include the lack of transverse shear flexibility in STAGS and the possibility that matrix shearing occurs long before final failure. (Table 5.9, Section 5.4.1.)
  - o Finite element results indicate subtle changes in the buckling mode shape occurring throughout postbuckling. In all the  $[\pm 50/35]_5$  panels, the mode shape tends to flatten, causing decreases in curvature at points of maximum transverse displacement. This observation is confirmed by strain results, as described in the previous section. In some panels, pronounced shifting of nodal lines and mode shape inflection points also occurs, but no pattern is evident in this behavior, and such phenomena can be observed in orthotropic panels. (Section 5.4.3.)

- o Satisfaction of displacement symmetry conditions described in Chapter 2 is consistent for the finite element results; the conditions are violated only for the two panels which exhibited antisymmetric buckle mode shapes. (Section 5.4.2.)

## 6.2 Recommendations

### 6.2.1 Recommendations Related to the Modified Rayleigh-Ritz Technique

- Work should be done to obtain a more suitable set of approximation functions for analysis of anisotropic panels, continuing to bear in mind the symmetry relations for such panels which could be utilized to simplify the selection process. Using the existing Rayleigh-Ritz code, new sets of functions can be easily investigated.
- A more efficient nonlinear solution technique such as an arc-length projection technique which would work in conjunction with the existing Newton-Raphson technique should be implemented in order to minimize program execution times.
- The reduced basis techniques discussed in Section 3.4.1.b should be implemented using the existing code. The code was written with an eye toward doing this, including organized generation of all the necessary partitioned arrays utilized in Section 3.4.1.b.

### 6.2.2 Recommendations Related to Experimental Work

- Additional studies should be conducted to determine the cause of the gradual degradation of stiffness late in the postbuckling range. Panels with mechanical couplings similar to those used by Jensen in [14] should be tested in the same way as those examined herein in order to isolate the cause of the phenomenon. In particular, laminates which are likely to display matrix shearing failures (e.g.,  $\pm 45$ -dominated laminates) should be carefully isolated, since matrix shearing is one possible cause of the observed stiffness degradation.
- Along a similar vein, additional attention should be focused on determining precisely why the  $[\pm 50/35]_5$  panels were generally more difficult to model than the  $[\pm 30/90]_5$

panels. Again, laminates which are likely to exhibit matrix shearing should be treated with care.

- More tests involving panels which exhibit mode changes should be performed, since this behavior appears to introduce seemingly unrelated modeling difficulties into the problem. Such tests should rely on the panel geometry to induce mode changes, rather than bringing in the unnecessary complications of anisotropy and bending-extensional coupling. Apparently, simple bifurcation buckling analyses using STAGS can provide some idea of which panels are likely to exhibit mode changes, since the panel which displayed a mode change also had eigenvalues spaced only 0.3% apart, the smallest spacing of any of the six panels.
- Additional tests involving anisotropic panels should be performed in which several DCDT's (perhaps 10) are placed down the centerline of the panels in order to further study the gradual flattening of the postbuckled shape with increases in load. Orthotropic panels should also be tested in this way as control specimens, to confirm that the phenomenon is due to anisotropy.



## References

1. Price, M.A.: HiMAT Structural Development Design Methodology. (Rockwell International Corporation; NASA Contract NAS4-2560.) NASA CR-144886, 1979.
2. Shirk, M.H.; Hertz, T.J.; Weishaar, T.A.: Aeroelastic tailoring: theory, practice, and promise. (Presented at the AIAA/ASME/ASCE/AHS 25th Structures, Structural Dynamics, and Materials Conference, Palm Springs, California, May 14-16, 1984), *Journal of Aircraft*, vol. 23, January 1986, 6-18, AIAA Paper No. 86-0982.
3. Dickson, J. N.; Biggers, S. B.; Wang, J. T. S.: A Preliminary Design Procedure for Composite Panels with Open-Section Stiffeners Loaded in the Post-Buckling Range. *Advances in Composite Materials* (Proceedings of the Third International Conference on Composite Materials, Paris, France, August 26-29, 1980, vol. 1), Oxford, Pergamon Press, 1980, 812-825.
4. Starnes, Jr., J.H.; Knight, Jr., N.F., Rouse, M.: Postbuckling Behavior of Selected Flat Stiffened Graphite-Epoxy Panels Loaded in Compression. *AIAA Journal*, vol. 23 (1985) 1236-1246. AIAA Paper No. A82-0777.
5. Leissa, A. W.: *Buckling of Laminated Composite Plates and Shells*, AFWAL-TR-85-3069, 1985.
6. Ashton, J.E.: Anisotropic plate analysis - boundary conditions. *Journal of Composite Materials*, vol. 4 (1970) 162-171.
7. Ashton, J.E.; Waddoups, M.E.: Analysis of anisotropic plates. *Journal of Composite Materials* 3 (1969) 148-165.
8. Jones, R.M.: *Mechanics of Composite Materials*. McGraw-Hill Book Company, 1975.
9. Whitney, J.M.: Fourier analysis of clamped anisotropic plates. *Transactions of the ASME, Applied Mechanics Review*, June 1971, 530-531.
10. Whitney, J.M.: Analysis of Anisotropic Rectangular Plates. *AIAA Journal*, vol. 10, October 1972, 1344-1345.
11. Craig, Jr., R. R.: *Structural Dynamics: An Introduction to Computer Methods*. John Wiley & Sons, Inc., 1981.
12. Noor, A.K.; Peters, J.M.: Reduced basis technique for nonlinear analysis of structures. *AIAA Journal*, vol. 18, 455-462 (1980).
13. Noor, A.K.; Camin, R.A.: Symmetry considerations for anisotropic shells. *Computer Methods in Applied Mechanics and Engineering*, vol. 9 (1976) 317-335.
14. Jensen, David W.: Buckling and Postbuckling Behavior of Unbalanced and Unsymmetric Laminated Graphite/Epoxy Plates. Ph.D. Thesis, Massachusetts Institute of Technology, 1986.
15. Starnes, Jr., J.H.; Rouse, M.: Postbuckling and Failure Characteristics of Selected Flat Rectangular Graphite-Epoxy Plates Loaded in Compression. Proceedings of the AIAA/ASME/ASCE/AHS 22nd Structures, Structural Dynamics and Materials Conference, Atlanta, GA, April 6-8, 1981. AIAA Paper No. 81-0543.
16. Stein, M.; Bains, N.J.C.: Postbuckling Behavior of Longitudinally Compressed Orthotropic Plates with Three-Dimensional Flexibility. (Presented at the AIAA/ASME/ASCE/AHS 27th Structures, Structural Dynamics, and Materials Conference, San Antonio, Texas, May 19-21, 1986), AIAA Paper No. 86-0976-CP.
17. Noor, A.K.; Mathers, M.D.; Anderson, M.S.: Exploiting symmetries for efficient postbuckling analysis of composite plates. *AIAA Journal*, vol. 15 (1977) 24-32.
18. Noor, A.K.: Reduction method for the nonlinear analysis of symmetric anisotropic panels. *Finite Element Methods for Nonlinear Problems* (Proceedings of the 3rd Europe-US Symposium, Trondheim, Norway, August 12-16, 1985), Springer, 1986, 389-407.

19. Barlow, J.: Constraint relationships in linear and nonlinear finite element analyses. *International Journal for Numerical Methods in Engineering*, vol. 18 (1982) 521-533.
20. Anderson, C.M.; Noor, A.K.: Use of group theoretic methods in the development of nonlinear shell finite elements. *Variational Methods in Engineering*, Department of Civil Engineering, University of Southampton, England, Southampton University Press (1972) 12/1-12/50.
21. Noor, A.K.: On making large nonlinear problems small. *Computer Methods in Applied Mechanics and Engineering*, vol. 34, North-Holland Publishing Company, 1982, 955-985.
22. Noor, A.K.; Peters, J.M.: Mixed models and reduced/selective integration displacement models for vibration analysis of shells. *Hybrid and Mixed Finite Element Methods*, ed. by S. N. Atluri, R. H. Gallagher, and O. C. Zienkiewicz, John Wiley and Sons, NY, 1983, pp. 537-564.
23. Hildebrand, F.B.: *Methods of Applied Mathematics, Second Edition*. Prentice Hall Inc., 1965.
24. Almroth, B.O.; Brogan, F.A.; Stanley, G.M.: *Structural Analysis of General Shells, Volumes I & II, User Instructions for STAGSC-1*. Applied Mechanics Laboratory, Lockheed Palo Alto Research Laboratory, Palo Alto, California, May 1983, LMSC-D633873.
25. Riks, E.: An Incremental Approach to Solution of Snapping and Buckling Problems. *International Journal of Solids and Structures*, vol. 15 (1979) 529-551.
26. Shuart, M. J.; Williams, J. G.: Compression Failure Characteristics of  $\pm 45^\circ$ -dominated Laminates with a Circular Hole or Impact Damage. *AIAA Journal*, vol. 24, no. 1, January 1986, pp. 115-122.

## Appendix A

### Array Symmetrization Using Only Quadratic Energy Terms

This appendix will outline briefly the steps which must be taken in order to "symmetrize" the stiffness array  $\overline{K}_{ij}$  arising from the quadratic strain energy term

$$U_2 = \frac{1}{2} \overline{K}_{IJ} \mathbf{X}_I \mathbf{X}_J \quad (\text{A.1})$$

Note that  $\overline{K}_{ij}$  is already symmetric; nevertheless, symmetrization can still be used, if only for illustration purposes.

In order to take the variation of  $U_2$ , differentiation must be carried out with respect to  $X_\alpha$ , where  $\alpha$  is a dummy index having the same range as  $I$  and  $J$ . Therefore,

$$\delta U_2 = \frac{\partial U_2}{\partial \mathbf{X}_\alpha} \delta \mathbf{X}_\alpha \quad (\text{A.2})$$

The product rule of differentiation is then applied, as follows:

$$\delta U_2 = \frac{1}{2} \overline{K}_{IJ} \left( \frac{\partial \mathbf{X}_I}{\partial \mathbf{X}_\alpha} \mathbf{X}_J + \mathbf{X}_I \frac{\partial \mathbf{X}_J}{\partial \mathbf{X}_\alpha} \right) \delta X_\alpha \quad (\text{A.3})$$

Since  $\partial \mathbf{X}_I / \partial \mathbf{X}_\alpha$  can be written as  $\delta_{I\alpha}$ , and similarly,  $\partial \mathbf{X}_J / \partial \mathbf{X}_\alpha = \delta_{J\alpha}$ , where

$$\delta_{ij} = \begin{cases} 1 & i = j \\ 0 & i \neq j \end{cases} \quad (\text{A.4})$$

the variation of  $U_2$  may be rewritten as

$$\begin{aligned} \delta U_2 &= \frac{1}{2} \overline{K}_{IJ} (\delta_{I\alpha} \mathbf{X}_J + \mathbf{X}_I \delta_{J\alpha}) \delta X_\alpha \\ &= \frac{1}{2} (\overline{K}_{\alpha J} \mathbf{X}_J + \overline{K}_{I\alpha} \mathbf{X}_I) \delta X_\alpha \\ &= \frac{1}{2} (\overline{K}_{IJ} + \overline{K}_{JI}) \mathbf{X}_J \delta X_I \end{aligned} \quad (\text{A.5})$$

Notice that the last equation involves the sum of a matrix and its transpose, divided by two, which is the definition of the symmetric part of the matrix  $\overline{K}_{IJ}$  and will be denoted by the unbarred symbol  $K_{IJ}$ . This same kind of "symmetrization" also occurs as

a natural consequence of the variational procedure for both of the nonlinear arrays  $\bar{F}_{IJK}$  and  $\bar{G}_{IJKL}$ . For  $\bar{F}_{IJK}$ , the symmetrized array  $F_{IJK}$  consists of a factor of  $\frac{1}{6}$  and the sum of six permutations of  $\bar{F}_{IJK}$ , while for  $G_{IJKL}$ , a factor of  $\frac{1}{24}$  and twenty-four permutations of  $\bar{G}_{IJKL}$  are required. Note that in the case of the three- and four-dimensional arrays  $F_{IJK}$  and  $G_{IJKL}$ , symmetry of these arrays means that interchanging any two indices does not change the array.

Finally, the incorporation of the symmetrized array  $K$  into the expression for  $\delta U_2$  gives

$$\delta U_2 = K_{IJ} \mathbf{X}_J \delta X_I \quad (\text{A.6})$$

The above result, without  $\delta \mathbf{X}_I$ , can be thought of as contributing to the right hand side of the Newton-Raphson equations. Obtaining the contribution to the left hand side is trivial; it is simply  $K$ .

Again note that this symmetrization procedure is not particularly important for the quadratic energy term since the matrix  $\bar{K}_{IJ}$  was symmetric to begin with; however, for the cubic and quartic energy terms which give the  $\bar{F}_{IJK}$  and  $\bar{G}_{IJKL}$  arrays, symmetrization is of paramount importance, since those two arrays are not symmetric before the variation is taken. In implementing a computerized nonlinear solution technique involving these arrays, a significant storage savings can be realized if the symmetry of the arrays is noted, since all three can become quite large.

## Appendix B

### Experimental Moiré Fringe Photographs

This appendix contains representative Moiré fringe photographs for each of the six tests discussed in Chapter 5. Each photograph includes the load meter, which displays the applied load in thousands of pounds.

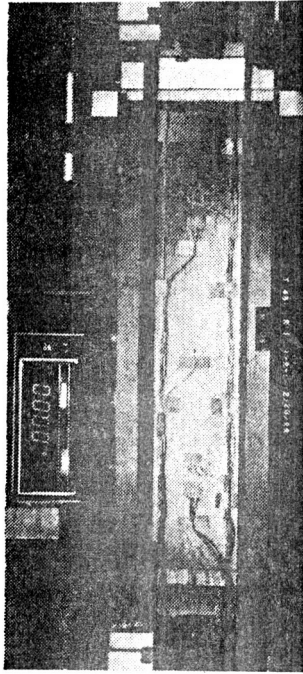
For each panel, four photographs are presented and are labeled as follows:

1. Before Test: photograph of the test setup prior to introduction of load. This photograph gives a qualitative indication of the initial imperfection present in the panel.
2. Buckling: photograph taken at a load as close as possible to the experimental buckling load as presented in Chapter 5.
3. Late Postbuckling: photograph taken at a load far into the postbuckling range.
4. Failure: photograph taken after the panel has failed. The load shown in this photograph will not correspond to the failure load reported in Chapter 5, since it was impossible to capture the panel at the precise moment of failure, before the panel's load carrying capability dropped dramatically.

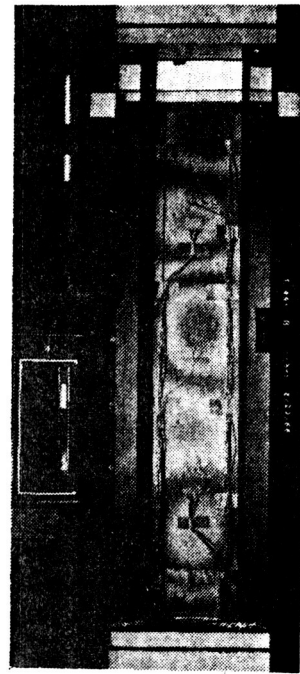
One additional set of two photographs is included for the  $[\pm 50/35]_5$ , 4 inch-wide panel to illustrate the mode change which occurred for that panel.

Recall that each panel was tested two times. The first test was only conducted up to the point of failure initiation, so that the location of failure initiation could be determined from C-scans, while during the second test, the panels were allowed to fail totally. The first three photographs shown for each panel were taken during the first test, while the photograph labeled "failure" was taken during the second test and will therefore appear slightly different from the other three photographs.

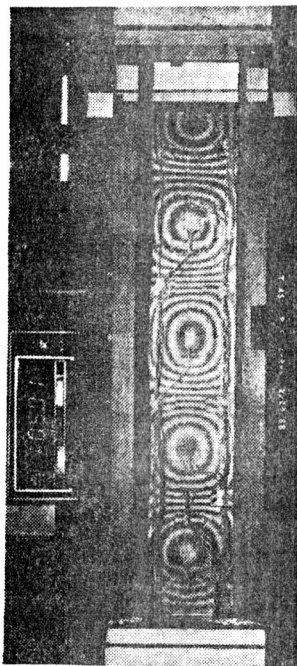
ORIGINAL PAGE IS  
OF POOR QUALITY



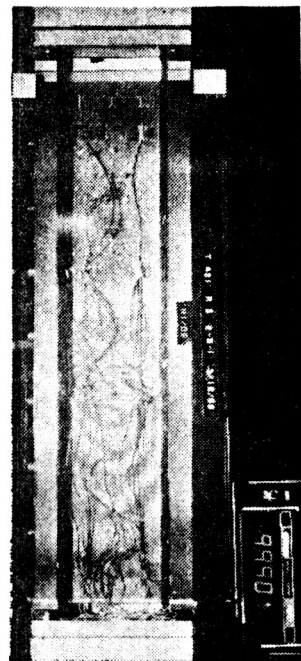
Before Test



Buckling

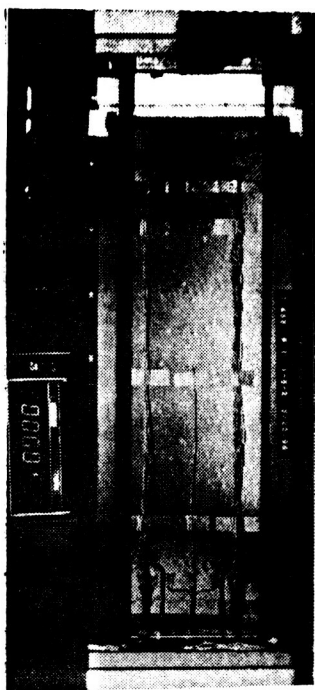


Late Postbuckling

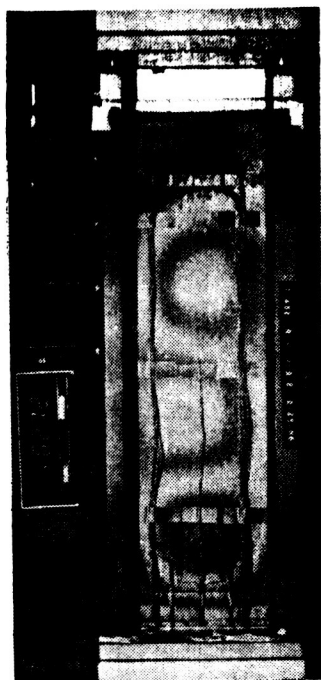


Failure

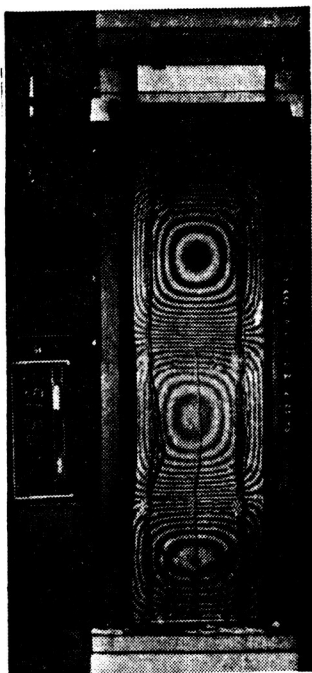
Figure B.1. Moire' Fringe Photographs for  $[\pm 30/90]_5$  4 Inch-Wide Panel



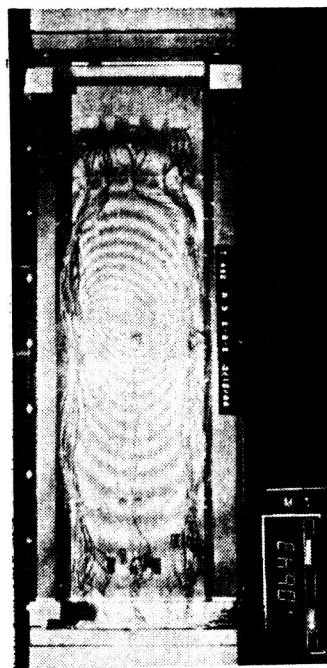
Before Test



Buckling



Late Postbuckling

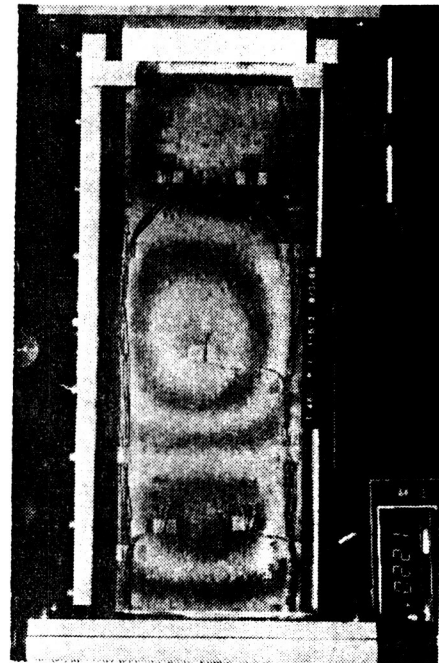


Failure

Figure B.2. Moire' Fringe Photographs for  $[\pm 30/90]_5$  5.5 Inch-Wide Panel

ORIGINAL PAGE IS  
OF POOR QUALITY

Initial Test Photo  
Unavailable



Buckling



Late Postbuckling

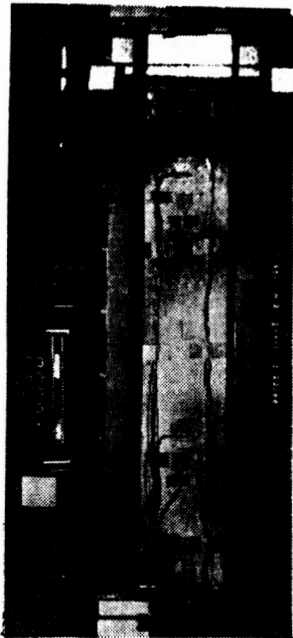


Failure

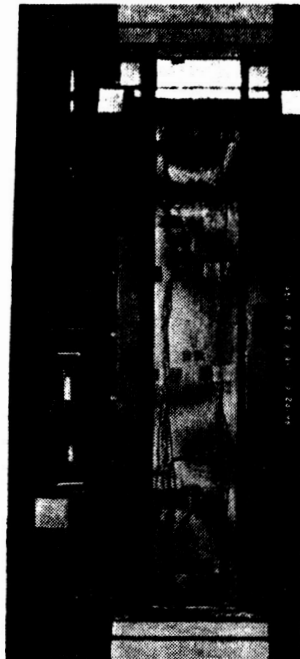
Figure B.3. Moire' Fringe Photographs for  $[\pm 30/90]_5$  7 Inch-Wide Panel



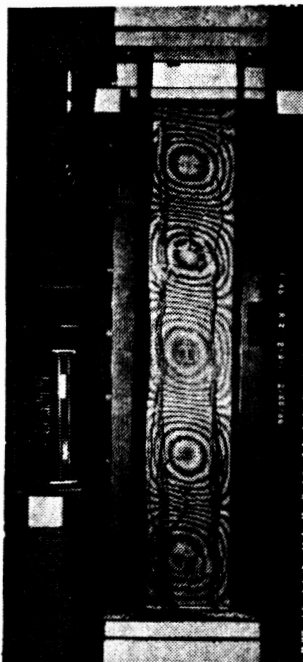
ORIGINAL PAGE IS  
OF POOR QUALITY



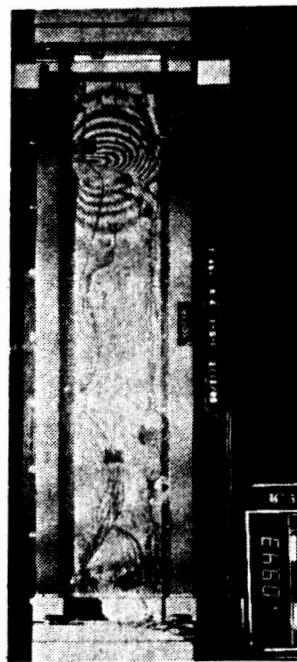
Before Test



Buckling



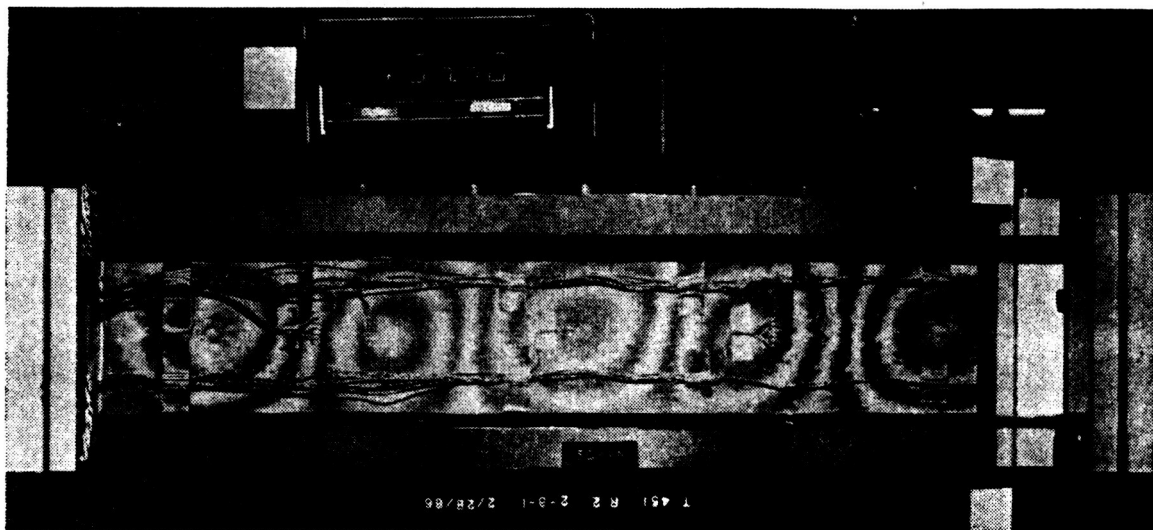
Late Postbuckling



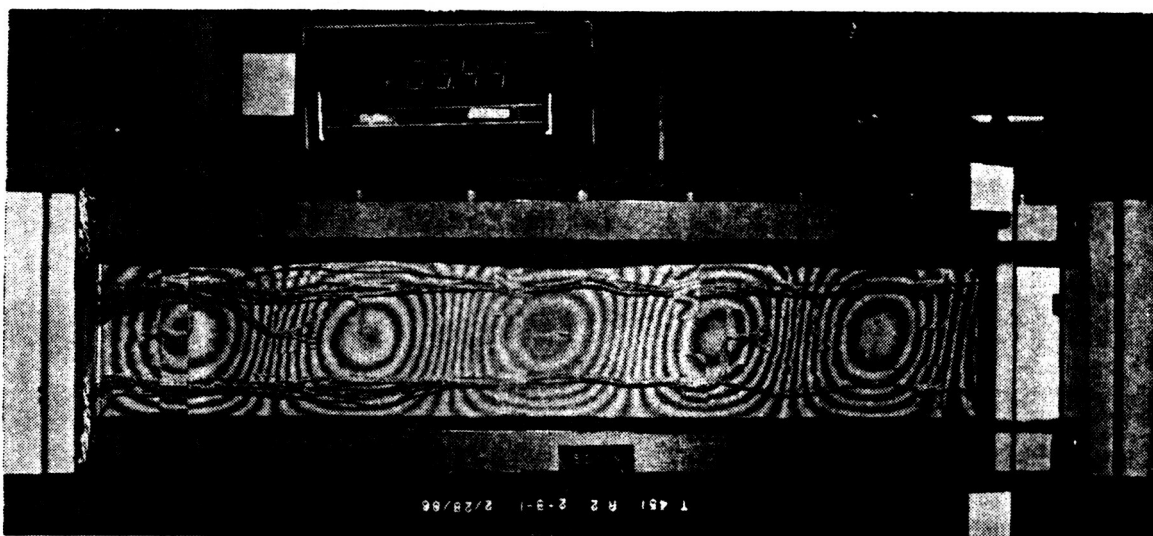
Failure

Figure B.4. Moire' Fringe Photographs for  $[\pm 50/35]_5$  4 Inch-Wide Panel

ORIGINAL PAGE IS  
OF POOR QUALITY.



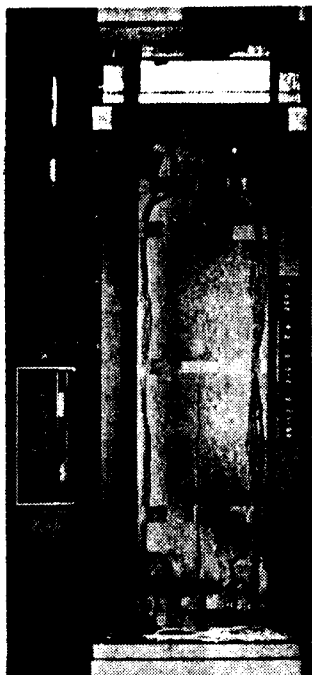
Five Half-Wave Mode Shape Observed Shortly After Buckling



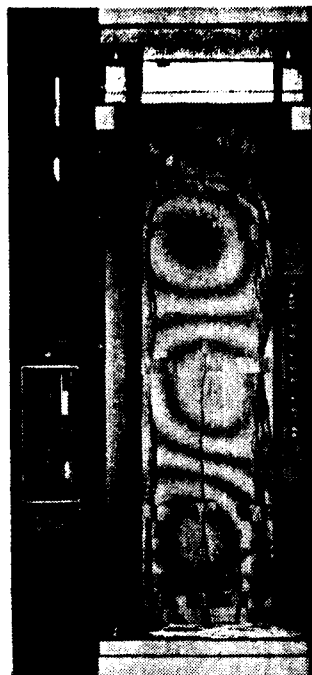
Six Half-Wave Mode Shape Observed 960 lb Later

Figure B.5.

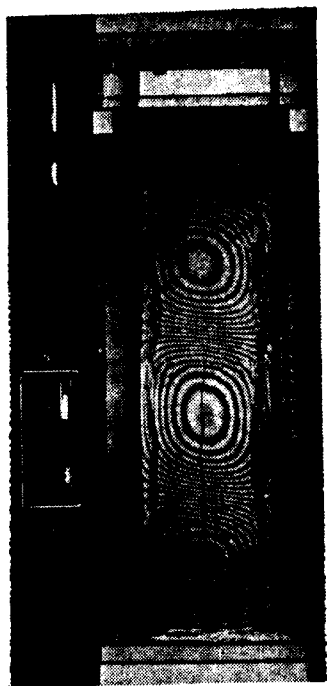
Moire' Fringe Photographs Illustrating  
Mode Change Exhibited by  $[\pm 50/35]_5$  4 Inch-Wide Panel



Before Test



Buckling



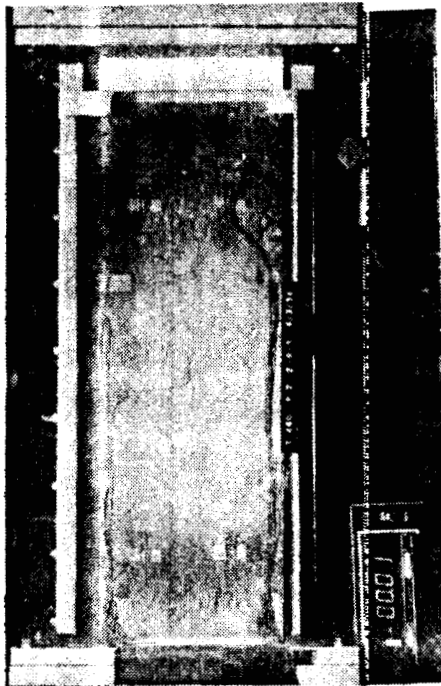
Late Postbuckling



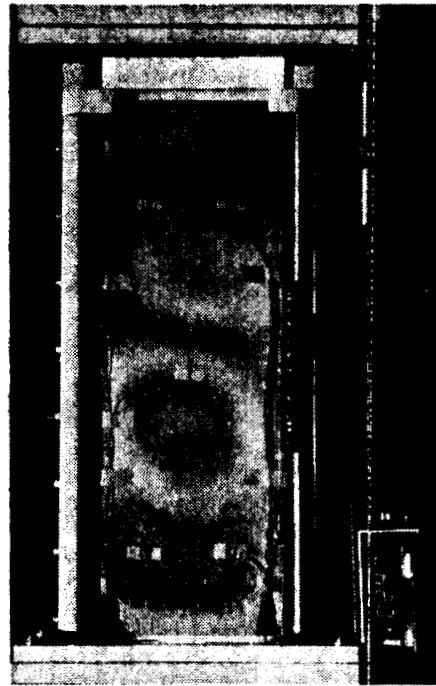
Failure

Figure B.6. Moire' Fringe Photographs for  $[\pm 50/35]_5$  5.5 Inch-Wide Panel

ORIGINAL PAGE IS  
OF POOR QUALITY



Before Test



Buckling



Late Postbuckling



Failure

Figure B.7. Moire' Fringe Photographs for  $[\pm 50/35]_5$  7 Inch-Wide Panel

## **Appendix C**

### **C-Scans of Experimental Panels**

This appendix contains C-scans for each of the six tests discussed in Chapter 5. Each C-scan is labeled with the location of failure initiation as reported in Figure 5.19, and some C-scans which included foreign objects easily confused with damage areas are labeled as such. Unfortunately, strain gages and associated wiring are visible on all C-scans, but these objects are easily identifiable. Recall that the white areas indicate damaged areas.

ORIGINAL PAGE IS  
OF POOR QUALITY

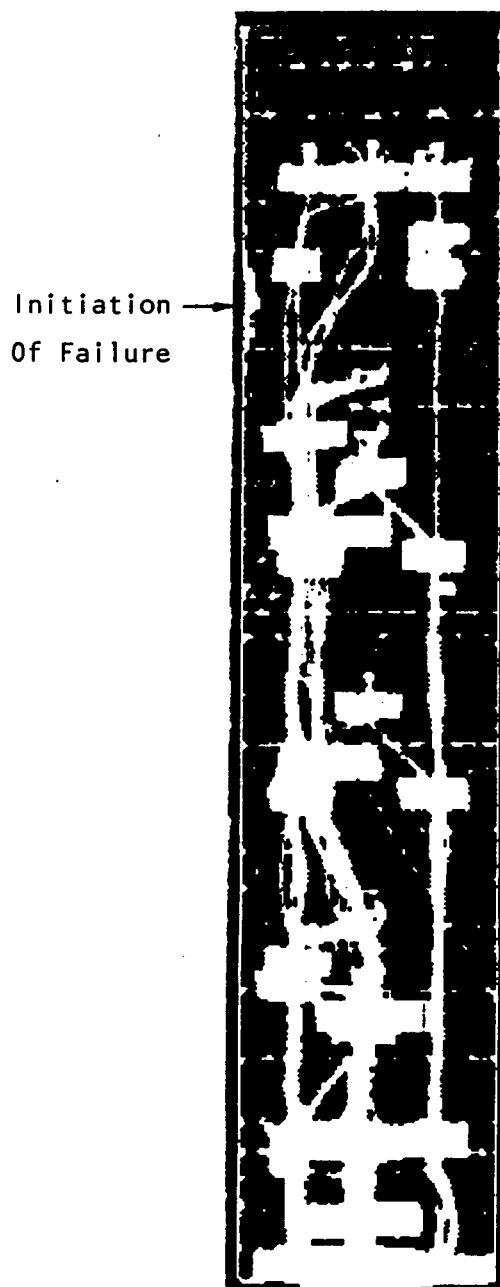


Figure C.1. C-Scan of  $[\pm 30/90]_5$  4 Inch-Wide Panel

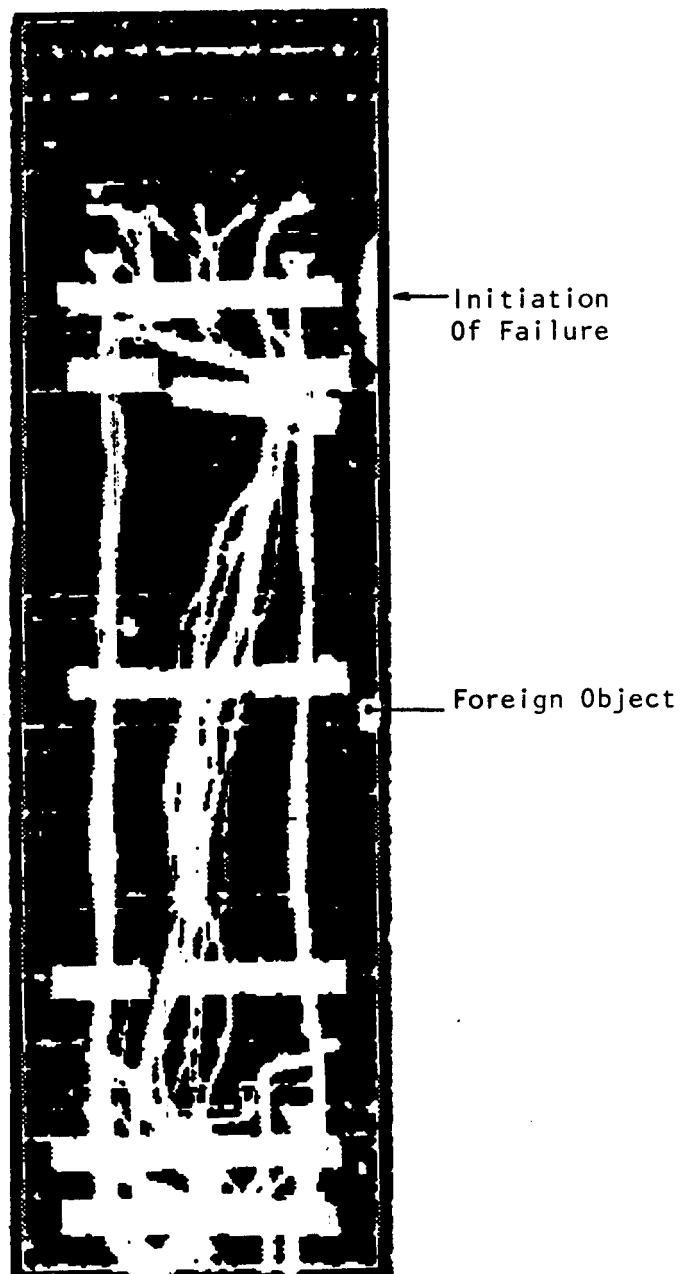


Figure C.2. C-Scan of  $[\pm 30/90]_5$  5.5 Inch-Wide Panel

ORIGINAL PAGE IS  
OF POOR QUALITY

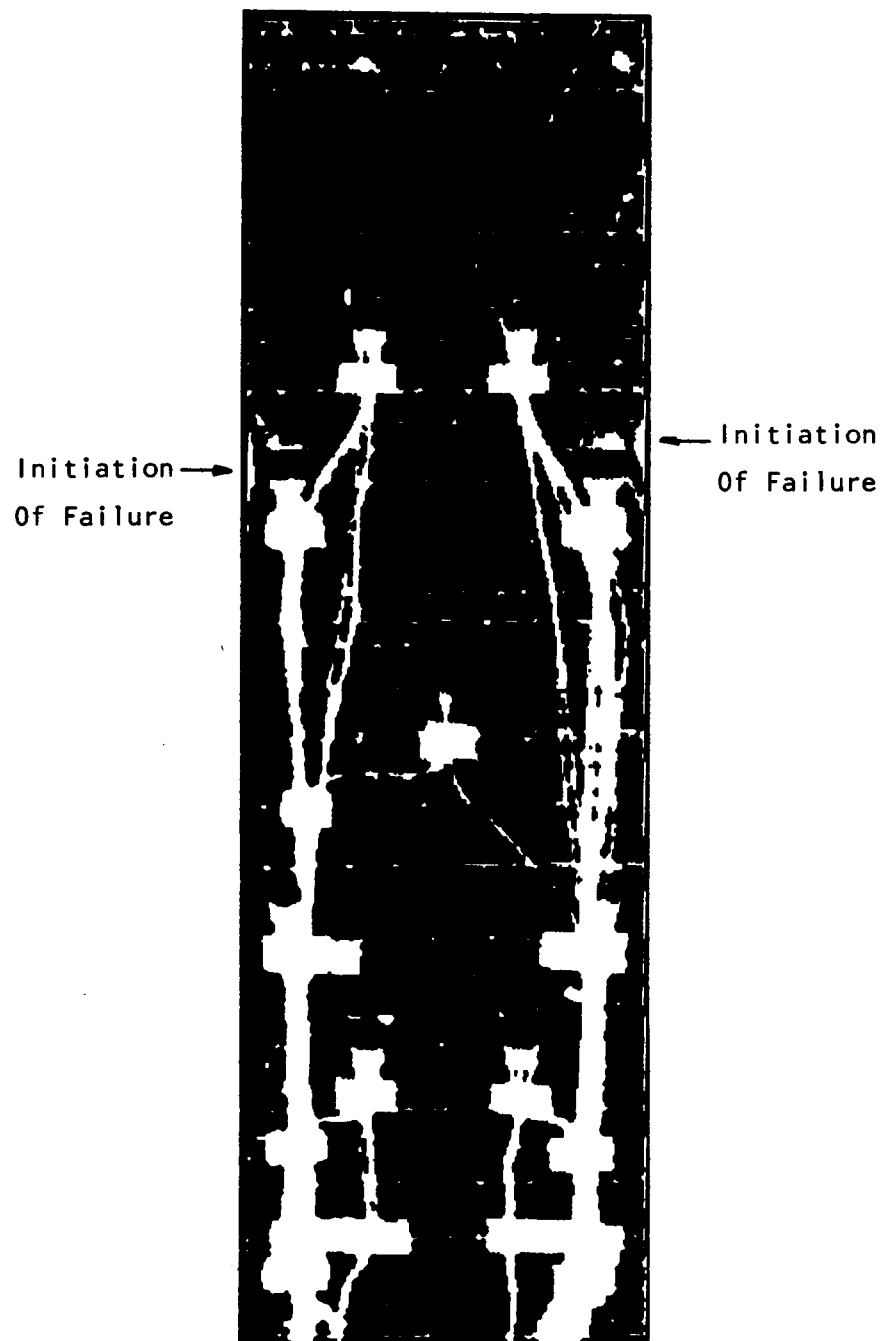


Figure C.3. C-Scan of  $[\pm 30/90]_5$  7 Inch-Wide Panel



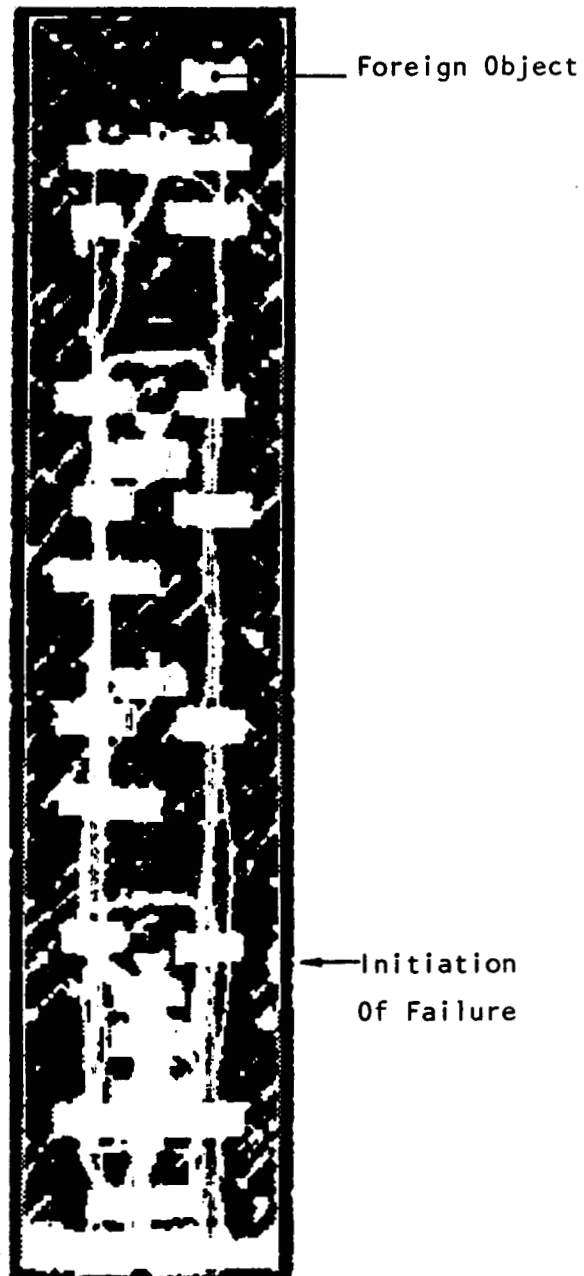


Figure C.4. C-Scan of  $[\pm 50/35]_5$  4 Inch-Wide Panel

ORIGINAL PAGE IS  
OF POOR QUALITY

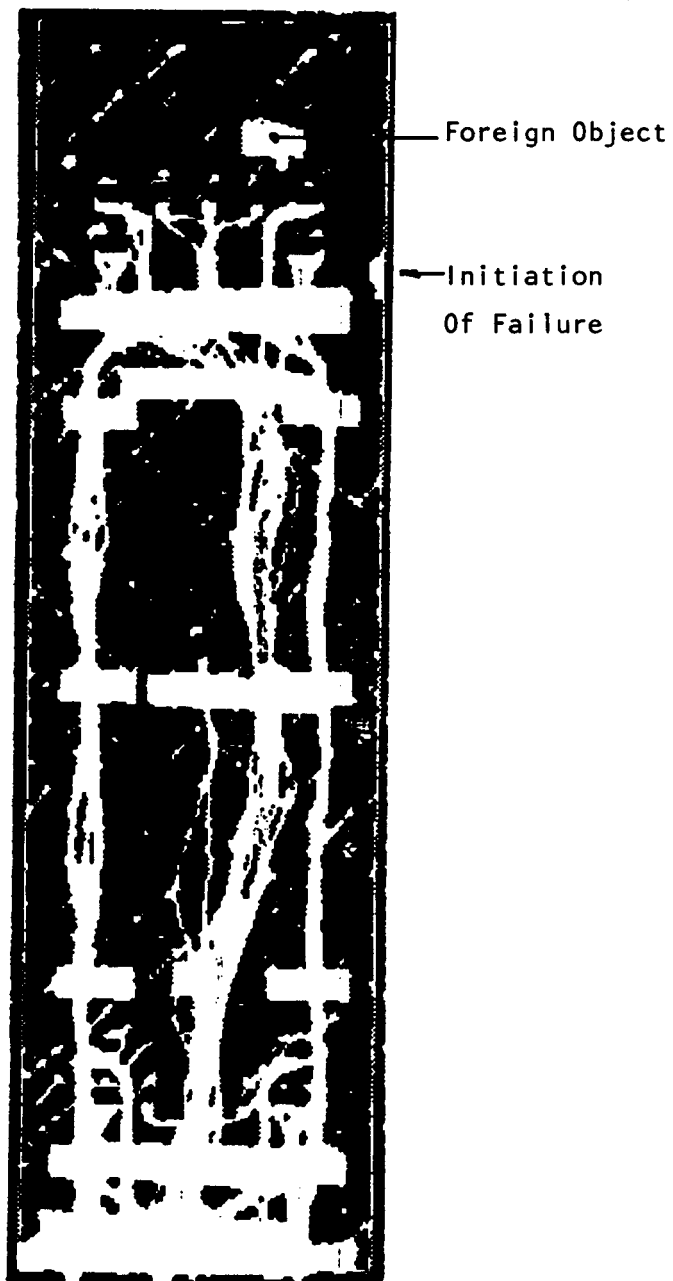


Figure C.5. C-Scan of  $[\pm 50/35]_5$  5.5 Inch-Wide Panel

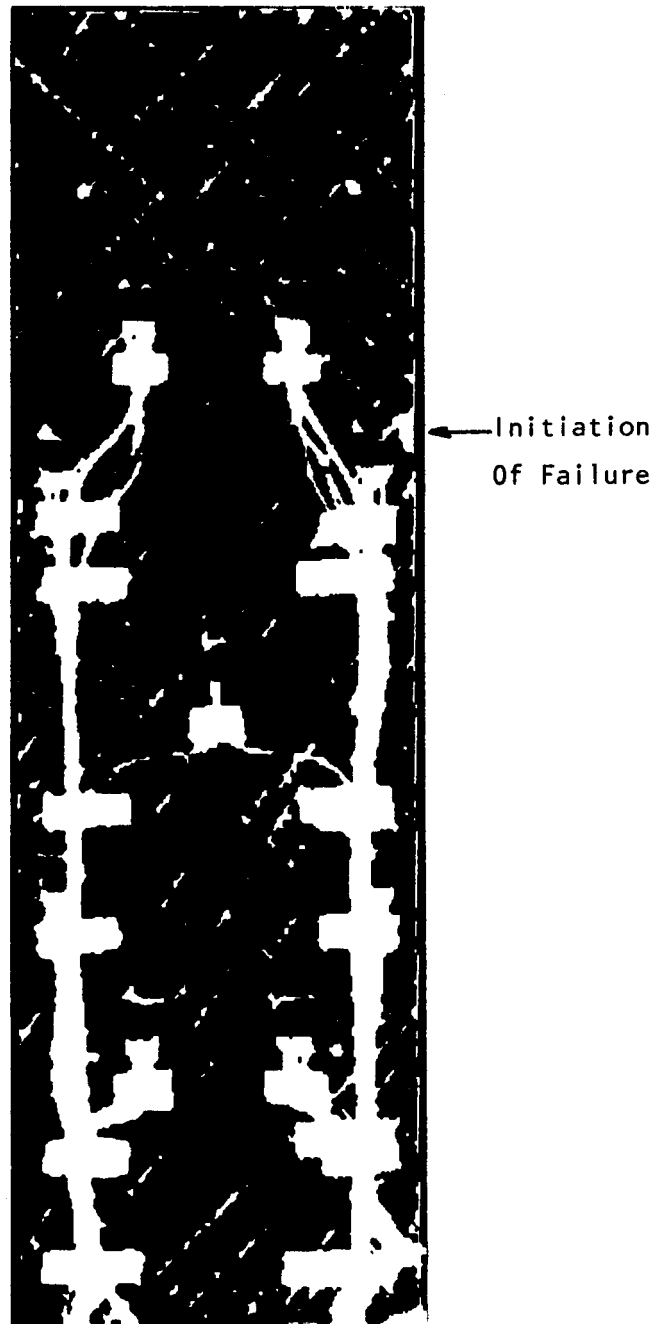


Figure C.6. C-Scan of  $[\pm 50/35]_5$  7 Inch-Wide Panel

## **Appendix D**

### **STAGSC-1 Runstreams**

This appendix contains the input data corresponding to the STAGSC-1 results presented in Chapter 5. The six runstreams differ primarily in the presence or absence of constraints (G cards) which force a certain symmetry to occur. Such constraints were necessary in order to obtain the postbuckled shape corresponding to the experimentally observed shape in cases where the first two eigenvalues were very closely spaced.

```

1 NONLINEAR RUN...[+30/-30/90]5 FLAT PLATE...4 in
2 3 1 1 0 0 0 1      $ B1:NONLINEAR RUN
3 1 0 0 0 1 -1 1      $ B2:1 DISPL PARTIAL COMPATIBILITY CARD
4 1 0 1 0              $ B3:1 MATERIAL TABLE; 1 SHELL WALL TYPE
5 -0.0008              $ B5:FACTOR MULTIPLYING MODE SHAPE USED AS IMPERF.
6 2000. 500. 8000.     $ C1:LOAD FACTOR
7 0 25000 7 -1 -1      $ D1:USE ARC LENGTH METHOD
8 63 11                $ F1:LEVEL OF DISCRETIZATION
9 1 1 3 1 1 1 0 1      $ G2:PARTIAL COMPATIBILITY IN U ALONG TOP EDGE
10 2                    $ G3: SET UP CONSTRAINT TO
11 1 31 5 3 1.E7 $ G4: FORCE SYMMETRIC BUCKLE
12 1 33 7 3 -1.E7 $ G4: PATTERN
13 1 0 $ I1:MATERIAL TABLE NUMBER
14 18.5E6 0.03027 0.832E6 1. 1. 1.6E6 0 $ I2:MATERIAL PROPERTIES
15 1 1 15 0 0          $ K1:15 LAYERED PLATE
16 1 5.11917e-3 -30.0 0 $ K2:LAYER 1
17 1 5.11917e-3 30.0 0 $ K2:LAYER 2
18 1 5.11917e-3 -90.0 0 $ K2:LAYER 3
19 1 5.11917e-3 -30.0 0 $ K2:LAYER 4
20 1 5.11917e-3 30.0 0 $ K2:LAYER 5
21 1 5.11917e-3 -90.0 0 $ K2:LAYER 6
22 1 5.11917e-3 -30.0 0 $ K2:LAYER 7
23 1 5.11917e-3 30.0 0 $ K2:LAYER 8
24 1 5.11917e-3 -90.0 0 $ K2:LAYER 9
25 1 5.11917e-3 -30.0 0 $ K2:LAYER 10
26 1 5.11917e-3 30.0 0 $ K2:LAYER 11
27 1 5.11917e-3 -90.0 0 $ K2:LAYER 12
28 1 5.11917e-3 -30.0 0 $ K2:LAYER 13
29 1 5.11917e-3 30.0 0 $ K2:LAYER 14
30 1 5.11917e-3 -90.0 0 $ K2:LAYER 15
31 2 0                  $ M1:SELECT RECTANGULAR GEOMETRY
32 0. 20. 0. 4.         $ M2A:CORNER COORDINATES
33 1 0 0. 0. 0 0        $ M5:SHELL WALL RECORD
34 411 8 5 0 0          $ N1:4-NODED QUAD ELEMENTS
35 .375 1.625 6.39 1.61 1.61 6.39 1.625 .375 $ N2:SEGMENTS IN X DIRECTION
36 1 6 18 6 6 18 6 1 $ N3:ELEMENTS PER SEGMENT
37 .25 .625 2.25 .625 .25 $ N5:3 SEGMENTS IN Y DIRECTION
38 1 2 4 2 1 $ N6:# ELEMENTS PER SEGMENT
39 0 3 2 3 0            $ P1:DEFND BELOW/UNCONSTR/CLAMPED/UNCONSTR
40 100 000               $ P2:U FREE ON TOP OF PLATE
41 1 0 0                 $ Q1:1 LOAD SYSTEM
42 1 5 0                 $ Q2:1 LOAD SYSTEM, 5 LOAD CARDS
43 1. 1 1 1 3 0         $ Q3:APPLIED LOAD ON TOP OF PLATE
44 0. -1 3 2 0          $ Q3:W=0 ON BOTTOM EDGE OF TOP CLAMPED SUPPORT
45 0. -1 3 0 10         $ Q3:W=0 ON INSIDE EDGE OF RIGHT SIMPLE SUPPORT
46 0. -1 3 62 0         $ Q3:W=0 ON TOP EDGE OF BOTTOM CLAMPED SUPPORT
47 0. -1 3 0 2          $ Q3:W=0 ON INSIDE EDGE OF LEFT SIMPLE SUPPORT
48 1 0 0                $ R1:PRINT DISPLACEMENTS

```

Figure D.1. STAGS Input Data for  $[\pm 30/90]_5$  4 Inch-Wide Panel

```

1 NONLINEAR RUN...[+30/-30/90]5 FLAT PLATE...5.5 in
2 3 1 1 0 0 1      $ B1:NONLINEAR RUN
3 1 0 0 0 1 -1 1    $ B2:1 DISPL PARTIAL COMPATIBILITY CARD
4 1 0 1 0           $ B3:1 MATERIAL TABLE; 1 SHELL WALL TYPE
5 -0.0008           $ B5:FACTOR MULTIPLYING MODE SHAPE USED AS IMPERF.
6 2000. 500. 8000.  $ C1:LOAD FACTOR
7 0 25000 10 -1 -1  $ D1:USE ARC LENGTH METHOD
8 45 13             $ F1:LEVEL OF DISCRETIZATION
9 1 1 5 1 1 1 0 1  $ G2:PARTIAL COMPATIBILITY IN U ALONG TOP EDGE
10 2                $ G3: SET UP CONSTRAINT TO FORCE
11 1 19 6 3 1.E7 $ G4: ANTISYMMETRIC BUCKLE
12 1 27 8 3 1.E7 $ G4: PATTERN
13 1 0 $ I1:MATERIAL TABLE NUMBER
14 18.5E6 0.03027 0.832E6 1. 1. 1.6E6 0 $ I2:MATERIAL PROPERTIES
15 1 1 15 0 0      $ K1:15 LAYERED PLATE
16 1 5.16583E-3 -30.0 0 $ K2:LAYER 1
17 1 5.16583E-3 30.0 0 $ K2:LAYER 2
18 1 5.16583E-3 -90.0 0 $ K2:LAYER 3
19 1 5.16583E-3 -30.0 0 $ K2:LAYER 4
20 1 5.16583E-3 30.0 0 $ K2:LAYER 5
21 1 5.16583E-3 -90.0 0 $ K2:LAYER 6
22 1 5.16583E-3 -30.0 0 $ K2:LAYER 7
23 1 5.16583E-3 30.0 0 $ K2:LAYER 8
24 1 5.16583E-3 -90.0 0 $ K2:LAYER 9
25 1 5.16583E-3 -30.0 0 $ K2:LAYER 10
26 1 5.16583E-3 30.0 0 $ K2:LAYER 11
27 1 5.16583E-3 -90.0 0 $ K2:LAYER 12
28 1 5.16583E-3 -30.0 0 $ K2:LAYER 13
29 1 5.16583E-3 30.0 0 $ K2:LAYER 14
30 1 5.16583E-3 -90.0 0 $ K2:LAYER 15
31 2 0              $ M1:SELECT RECTANGULAR GEOMETRY
32 0. 20. 0. 5.5    $ M2A:CORNER COORDINATES
33 1 0 0. 0. 0 0    $ M5:SHELL WALL RECORD
34 411 8 5 0 0      $ N1:4-NODED QUAD ELEMENTS
35 .375 2.805 4.41 2.41 2.41 4.41 2.805 .375 $ N2:SEGMENTS IN X DIRECTION
36 1 6 9 6 6 9 6 1 $ N3:ELEMENTS PER SEGMENT
37 .25 2. 1. 2. .25 $ N5:SEGMENTS IN Y DIRECTION
38 1 4 2 4 1 $ N6:ELEMENTS PER SEGMENT
39 0 3 2 3 0        $ P1:DEFND BELOW/UNCONSTR/CLAMPED/UNCONSTR
40 100 000           $ P2:U FREE ON TOP OF PLATE
41 1 0 0             $ Q1:1 LOAD SYSTEM
42 1 5 0             $ Q2:1 LOAD SYSTEM, 5 LOAD CARDS
43 1. 1 1 1 5 0     $ Q3:APPLIED LOAD ON TOP OF PLATE
44 0. -1 3 2 0      $ Q3:W=0 ON BOTTOM EDGE OF TOP CLAMPED SUPPORT
45 0. -1 3 0 12     $ Q3:W=0 ON INSIDE EDGE OF RIGHT SIMPLE SUPPORT
46 0. -1 3 44 0     $ Q3:W=0 ON TOP EDGE OF BOTTOM CLAMPED SUPPORT
47 0. -1 3 0 2      $ Q3:W=0 ON INSIDE EDGE OF LEFT SIMPLE SUPPORT
48 1 $ R1:PRINT DISPLACEMENTS ONLY

```

Figure D.2. STAGS Input Data for  $[\pm 30/90]_5$  5.5 Inch-Wide Panel

```

1 NONLINEAR RUN...[+30/-30/90]5 FLAT PLATE...7. IN
2 3 1 1 0 0 0 1 $ B1:NONLINEAR RUN
3 1 0 0 0 1 0 1 $ B2:1 DISPL PARTIAL COMPAT
4 1 0 1 0 $ B3:1 MATERIAL TABLE; 1 SHELL WALL TYPE
5 0.0008 $ B5:FACTOR MULTIPLYING MODE SHAPE USED AS IMPERF.
6 2000. 500. 8000. $ C1:LOAD FACTOR
7 0 99999 10 -1 -1 $ D1:USE ARC LENGTH METHOD
8 39 13 $ F1:LEVEL OF DISCRETIZATION
9 1 1 5 1 1 1 0 1 $ G2:PARTIAL COMPAT IN U ALONG TOP EDGE
10 1 0 $ I1:MATERIAL TABLE NUMBER
11 18.5E6 0.03027 0.832E6 1. 1. 1.6E6 0 $ I2:MATERIAL PROPERTIES
12 1 1 15 0 0 $ K1:15 LAYERED PLATE
13 1 5.25083E-3 -30.0 0 $ K2:LAYER 1
14 1 5.25083E-3 30.0 0 $ K2:LAYER 2
15 1 5.25083E-3 -90.0 0 $ K2:LAYER 3
16 1 5.25083E-3 -30.0 0 $ K2:LAYER 4
17 1 5.25083E-3 30.0 0 $ K2:LAYER 5
18 1 5.25083E-3 -90.0 0 $ K2:LAYER 6
19 1 5.25083E-3 -30.0 0 $ K2:LAYER 7
20 1 5.25083E-3 30.0 0 $ K2:LAYER 8
21 1 5.25083E-3 -90.0 0 $ K2:LAYER 9
22 1 5.25083E-3 -30.0 0 $ K2:LAYER 10
23 1 5.25083E-3 30.0 0 $ K2:LAYER 11
24 1 5.25083E-3 -90.0 0 $ K2:LAYER 12
25 1 5.25083E-3 -30.0 0 $ K2:LAYER 13
26 1 5.25083E-3 30.0 0 $ K2:LAYER 14
27 1 5.25083E-3 -90.0 0 $ K2:LAYER 15
28 2 0 $ M1:SELECT RECTANGULAR GEOMETRY
29 0. 20. 0. 7.0 $ M2A:CORNER COORDINATES
30 1 0 0. 0. 0 0 $ M5:SHELL WALL RECORD
31 411 8 8 0 0 $ N1:4-NODED QUAD ELEMENTS
32 .375 4.125 2.29 3.21 3.21 2.29 4.125 .375 $ N2:SEGMENTS IN X DIRECTION
33 1 8 4 6 6 4 8 1 $ N3:ELEMENTS PER SEGMENT
34 .25 .5 1.42 1.33 1.33 1.42 .5 .25 $ N5:SEGMENTS IN Y DIRECTION
35 1 1 2 2 2 2 1 1 $ N6:ELEMENTS PER SEGMENT
36 0 3 2 3 0 $ P1:DEFND BELOW/UNCONSTR/CLAMPED/UNCONSTR
37 100 000 $ P2:U FREE ON TOP OF PLATE
38 1 0 0 $ Q1:1 LOAD SYSTEM
39 1 5 0 $ Q2:1 LOAD SYSTEM, 5 LOAD CARDS
40 1. 1 1 1 5 0 $ Q3:APPLIED LOAD ON TOP OF PLATE
41 0. -1 3 2 0 $ Q3:W=0 ON BOTTOM EDGE OF TOP CLAMPED SUPPORT
42 0. -1 3 0 12 $ Q3:W=0 ON INSIDE EDGE OF RIGHT SIMPLE SUPPORT
43 0. -1 3 38 0 $ Q3:W=0 ON TOP EDGE OF BOTTOM CLAMPED SUPPORT
44 0. -1 3 0 2 $ Q3:W=0 ON INSIDE EDGE OF LEFT SIMPLE SUPPORT
45 1 $ R1:PRINT DISPLACEMENTS ONLY

```

Figure D.3. STAGS Input Data for  $[\pm 30/90]_5$  7 Inch-Wide Panel

```

1 NONLINEAR RUN...[+50/-50/35]5 FLAT PLATE...4 in
2 3 1 1 0 0 0 1      $ B1:NONLINEAR RUN
3 1 0 0 0 1 -1 2      $ B2:1 DISPL PARTIAL COMPAT
4 1 0 1 0              $ B3:1 MATERIAL TABLE; 1 SHELL WALL TYPE
5 0. 0.008             $ B5:FACTOR MULTIPLYING (2ND) MODE SHAPE USED A IMPERF.
6 2000. 500. 8000.     $ C1:LOAD FACTOR
7 0 25000 20 -1 -1     $ D1:USE ARC LENGTH METHOD
8 63 11                $ F1:LEVEL OF DISCRETIZATION
9 1 1 3 1 1 1 0 1      $ G2:PARTIAL COMPAT IN U ALONG TOP EDGE
10 2                   $ G3: SET UP CONSTRAINT TO
11 1 31 5 3 1.E7        $ G4: FORCE SYMMETRIC BUCKLE
12 1 33 7 3 -1.E7       $ G4: PATTERN
13 1 0 $ I1:MATERIAL TABLE NUMBER
14 18.5E6 0.03027 0.832E6 1. 1. 1.6E6 0 $ I2:MATERIAL PROPERTIES
15 1 1 15 0 0           $ K1:15 LAYERED PLATE
16 1 5.15417E-3 -50.0 0 $ K2:LAYER 1
17 1 5.15417E-3 50.0 0 $ K2:LAYER 2
18 1 5.15417E-3 -35.0 0 $ K2:LAYER 3
19 1 5.15417E-3 -50.0 0 $ K2:LAYER 4
20 1 5.15417E-3 50.0 0 $ K2:LAYER 5
21 1 5.15417E-3 -35.0 0 $ K2:LAYER 6
22 1 5.15417E-3 -50.0 0 $ K2:LAYER 7
23 1 5.15417E-3 50.0 0 $ K2:LAYER 8
24 1 5.15417E-3 -35.0 0 $ K2:LAYER 9
25 1 5.15417E-3 -50.0 0 $ K2:LAYER 10
26 1 5.15417E-3 50.0 0 $ K2:LAYER 11
27 1 5.15417E-3 -35.0 0 $ K2:LAYER 12
28 1 5.15417E-3 -50.0 0 $ K2:LAYER 13
29 1 5.15417E-3 50.0 0 $ K2:LAYER 14
30 1 5.15417E-3 -35.0 0 $ K2:LAYER 15
31 2 0                 $ M1:SELECT RECTANGULAR GEOMETRY
32 0. 20. 0. 4.         $ M2A:CORNER COORDINATES
33 1 0 0. 0. 0 0        $ M5:SHELL WALL RECORD
34 411 8 5 0 0          $ N1:4-NODED QUAD ELEMENTS
35 .375 1.625 6.39 1.61 1.61 6.39 1.625 .375 $ N2:SEGMENTS IN X DIRECTION
36 1 6 18 6 6 18 6 1 $ N3:ELEMENTS PER SEGMENT
37 .25 .625 2.25 .625 .25 $ N5:SEGMENTS IN Y DIRECTION
38 1 2 4 2 1 $ N6:ELEMENTS PER SEGMENT
39 0 3 2 3 0           $ P1:DEFND BELOW/UNCONSTR/CLAMPED/UNCONSTR
40 100 000              $ P2:U FREE ON TOP OF PLATE
41 1 0 0                $ Q1:1 LOAD SYSTEM
42 1 5 0                $ Q2:1 LOAD SYSTEM, 5 LOAD CARDS
43 1. 1 1 1 3 0         $ Q3:APPLIED LOAD ON TOP CENTER OF PLATE
44 0. -1 3 2 0          $ Q3:W=0 ON BOTTOM EDGE OF TOP CLAMPED SUPPORT
45 0. -1 3 0 10         $ Q3:W=0 ON INSIDE EDGE OF RIGHT SIMPLE SUPPORT
46 0. -1 3 62 0         $ Q3:W=0 ON TOP EDGE OF BOTTOM CLAMPED SUPPORT
47 0. -1 3 0 2          $ Q3:W=0 ON INSIDE EDGE OF LEFT SIMPLE SUPPORT
48 1 0 0                $ R1:PRINT DISPLACEMENTS

```

Figure D.4. STAGS Input Data for  $[\pm 50/35]_5$  4 Inch-Wide Panel



```

1 NONLINEAR RUN...[+50/-50/35]5 FLAT PLATE...5.5 IN
2 3 1 1 0 0 1 1      $ B1:NONLINEAR RUN
3 1 0 0 0 1 -1 1      $ B2:1 DISPL PARTIAL COMPAT
4 1 0 1 0              $ B3:1 MATERIAL TABLE; 1 SHELL WALL TYPE
5 0.008                $ B5:FACTOR MULTIPLYING MODE SHAPE USED AS IMPERF.
6 2000. 500. 8000.     $ C1:LOAD FACTOR
7 0 25000 10 -1 -1     $ D1:USE ARC LENGTH METHOD
8 45 13                $ F1:LEVEL OF DISCRETIZATION
9 1 1 5 1 1 1 0 1      $ G2:PARTIAL COMPAT IN U ALONG TOP EDGE
10 2                    $ G3: SET UP CONSTRAINT TO
11 1 19 6 3 1.E7 $ G4: FORCE ANTISYMMETRIC BUCKLE
12 1 27 8 3 1.E7 $ G4: PATTERN
13 1 0 $ I1:MATERIAL TABLE NUMBER
14 18.5E6 0.03027 0.832E6 1. 1. 1.6E6 0 $ I2:MATERIAL PROPERTIES
15 1 1 15 0 0          $ K1:15 LAYERED PLATE
16 1 5.14333E-3 -50.0 0 $ K2:LAYER 1
17 1 5.14333E-3 50.0 0 $ K2:LAYER 2
18 1 5.14333E-3 -35.0 0 $ K2:LAYER 3
19 1 5.14333E-3 -50.0 0 $ K2:LAYER 4
20 1 5.14333E-3 50.0 0 $ K2:LAYER 5
21 1 5.14333E-3 -35.0 0 $ K2:LAYER 6
22 1 5.14333E-3 -50.0 0 $ K2:LAYER 7
23 1 5.14333E-3 50.0 0 $ K2:LAYER 8
24 1 5.14333E-3 -35.0 0 $ K2:LAYER 9
25 1 5.14333E-3 -50.0 0 $ K2:LAYER 10
26 1 5.14333E-3 50.0 0 $ K2:LAYER 11
27 1 5.14333E-3 -35.0 0 $ K2:LAYER 12
28 1 5.14333E-3 -50.0 0 $ K2:LAYER 13
29 1 5.14333E-3 50.0 0 $ K2:LAYER 14
30 1 5.14333E-3 -35.0 0 $ K2:LAYER 15
31 2 0                  $ M1:SELECT RECTANGULAR GEOMETRY
32 0. 20. 0. 5.5        $ M2A:CORNER COORDINATES
33 1 0 0. 0. 0 0        $ M5:SHELL WALL RECORD
34 411 8 5 0 0          $ N1:4-NODED QUAD ELEMENTS
35 .375 2.805 4.41 2.41 2.41 4.41 2.805 .375 $ N2:SEGMENTS IN X DIRECTION
36 1 6 9 6 6 9 6 1     $ N3:ELEMENTS PER SEGMENT
37 .25 2. 1. 2. .25 $ N5:SEGMENTS IN Y DIRECTION
38 1 4 2 4 1 $ N6:ELEMENTS PER SEGMENT
39 0 3 2 3 0           $ P1:DEFND BELOW/UNCONSTR/CLAMPED/UNCONSTR
40 100 000              $ P2:U FREE ON TOP OF PLATE
41 1 0 0                $ Q1:1 LOAD SYSTEM
42 1 5 0                $ Q2:1 LOAD SYSTEM, 5 LOAD CARDS
43 1. 1 1 1 5 0         $ Q3:APPLIED LOAD ON TOP CENTER OF PLATE
44 0. -1 3 2 0          $ Q3:W=0 ON BOTTOM EDGE OF TOP CLAMPED SUPPORT
45 0. -1 3 0 12         $ Q3:W=0 ON INSIDE EDGE OF RIGHT SIMPLE SUPPORT
46 0. -1 3 44 0         $ Q3:W=0 ON TOP EDGE OF BOTTOM CLAMPED SUPPORT
47 0. -1 3 0 2          $ Q3:W=0 ON INSIDE EDGE OF LEFT SIMPLE SUPPORT
48 1 $ R1:PRINT DISPLACEMENTS ONLY

```

Figure D.5. STAGS Input Data for  $[\pm 50/35]_5$  5.5 Inch-Wide Panel

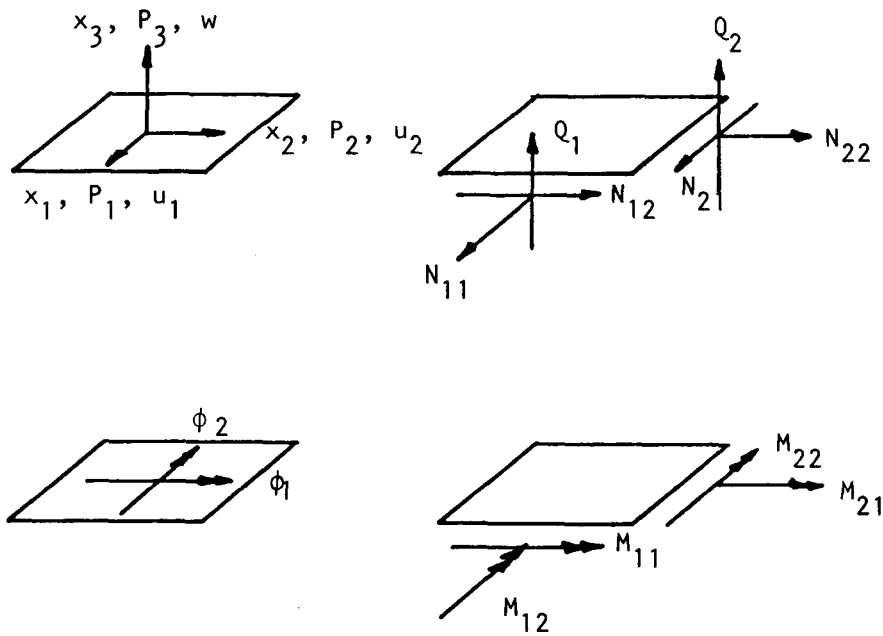
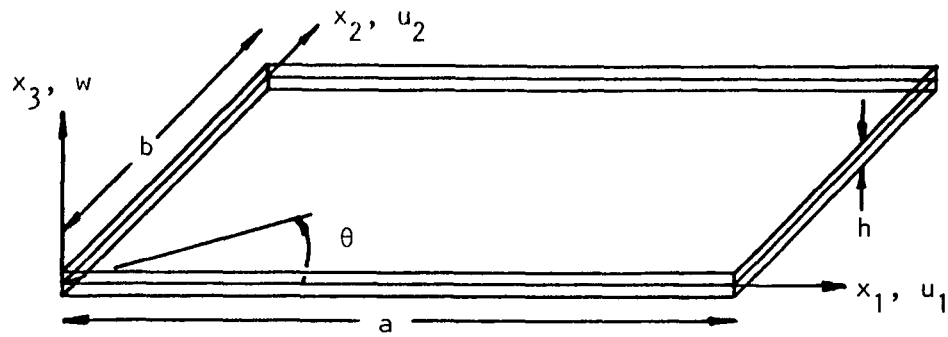
```

1 NONLINEAR RUN...[+50/-50/35]5 FLAT PLATE...7. IN
2 3 1 1 0 0 0 1      $ B1:NONLINEAR RUN
3 1 0 0 0 1 0 1      $ B2:1 DISPL PARTIAL COMPAT
4 1 0 1 0            $ B3:1 MATERIAL TABLE; 1 SHELL WALL TYPE
5 0.0008             $ B5:FACTOR MULTIPLYING MODE SHAPE USED AS IMPERF.
6 2000. 500. 8000.    $ C1:LOAD FACTOR
7 0 25000 10 -1 -1    $ D1:USE ARC LENGTH METHOD
8 39 13              $ F1:LEVEL OF DISCRETIZATION
9 1 1 5 1 1 1 0 1    $ G2:PARTIAL COMPAT IN U ALONG TOP EDGE
10 1 0 $ I1:MATERIAL TABLE NUMBER
11 18.5E6 0.03027 0.832E6 1. 1. 1.6E6 0 $ I2:MATERIAL PROPERTIES
12 1 1 15 0 0        $ K1:15 LAYERED PLATE
13 1 5.20083E-3 -50.0 0 $ K2:LAYER 1
14 1 5.20083E-3 50.0 0 $ K2:LAYER 2
15 1 5.20083E-3 -35.0 0 $ K2:LAYER 3
16 1 5.20083E-3 -50.0 0 $ K2:LAYER 4
17 1 5.20083E-3 50.0 0 $ K2:LAYER 5
18 1 5.20083E-3 -35.0 0 $ K2:LAYER 6
19 1 5.20083E-3 -50.0 0 $ K2:LAYER 7
20 1 5.20083E-3 50.0 0 $ K2:LAYER 8
21 1 5.20083E-3 -35.0 0 $ K2:LAYER 9
22 1 5.20083E-3 -50.0 0 $ K2:LAYER 10
23 1 5.20083E-3 50.0 0 $ K2:LAYER 11
24 1 5.20083E-3 -35.0 0 $ K2:LAYER 12
25 1 5.20083E-3 -50.0 0 $ K2:LAYER 13
26 1 5.20083E-3 50.0 0 $ K2:LAYER 14
27 1 5.20083E-3 -35.0 0 $ K2:LAYER 15
28 2 0              $ M1:SELECT RECTANGULAR GEOMETRY
29 0. 20. 0. 7.0    $ M2A:CORNER COORDINATES
30 1 0 0. 0. 0 0    $ M5:SHELL WALL RECORD
31 411 8 8 0 0      $ N1:4-NODED QUAD ELEMENTS
32 .375 4.125 2.29 3.21 3.21 2.29 4.125 .375 $ N2:SEGMENTS IN X DIRECTION
33 1 8 4 6 6 4 8 1 $ N3:ELEMENTS PER SEGMENT
34 .25 .5 1.42 1.33 1.33 1.42 .5 .25 $ N5:SEGMENTS IN Y DIRECTION
35 1 1 2 2 2 2 1 1 $ N6:ELEMENTS PER SEGMENT
36 0 3 2 3 0        $ P1:DEFND BELOW/UNCONSTR/CLAMPED/UNCONSTR
37 100 000           $ P2:U FREE ON TOP OF PLATE
38 1 0 0            $ Q1:1 LOAD SYSTEM
39 1 5 0            $ Q2:1 LOAD SYSTEM, 5 LOAD CARDS
40 1. 1 1 1 5 0      $ Q3:APPLIED LOAD ON TOP CENTER OF PLATE
41 0. -1 3 2 0        $ Q3:W=0 ON BOTTOM EDGE OF TOP CLAMPED SUPPORT
42 0. -1 3 0 12       $ Q3:W=0 ON INSIDE EDGE OF RIGHT SIMPLE SUPPORT
43 0. -1 3 38 0       $ Q3:W=0 ON TOP EDGE OF BOTTOM CLAMPED SUPPORT
44 0. -1 3 0 2        $ Q3:W=0 ON INSIDE EDGE OF LEFT SIMPLE SUPPORT
45 1 $ R1:PRINT DISPLACEMENTS ONLY

```

Figure D.6. STAGS Input Data for  $[\pm 50/35]_5$  7 Inch-Wide Panel

# Plate Geometry:



## Load, Displacement, Force, And Moment Resultant Conventions

Figure 2.1. Conventions Used In  
Theoretical Development

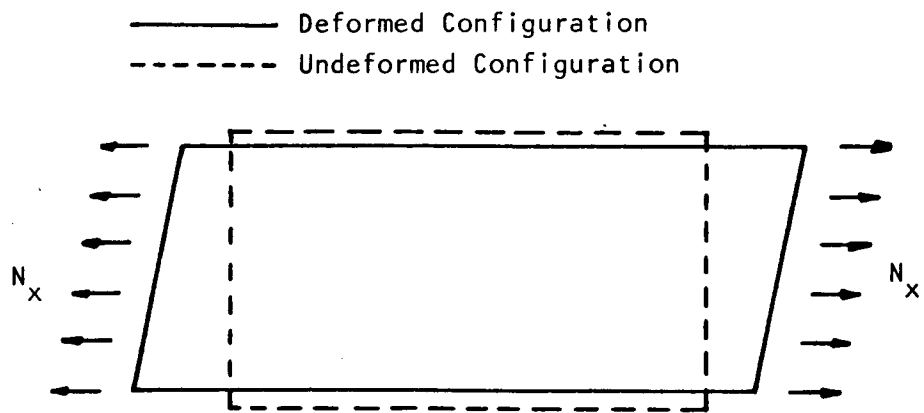


Figure 2.2. Effect of Shear-Extensional Coupling  
On Panel Subjected to Uniform Axial  
Loading

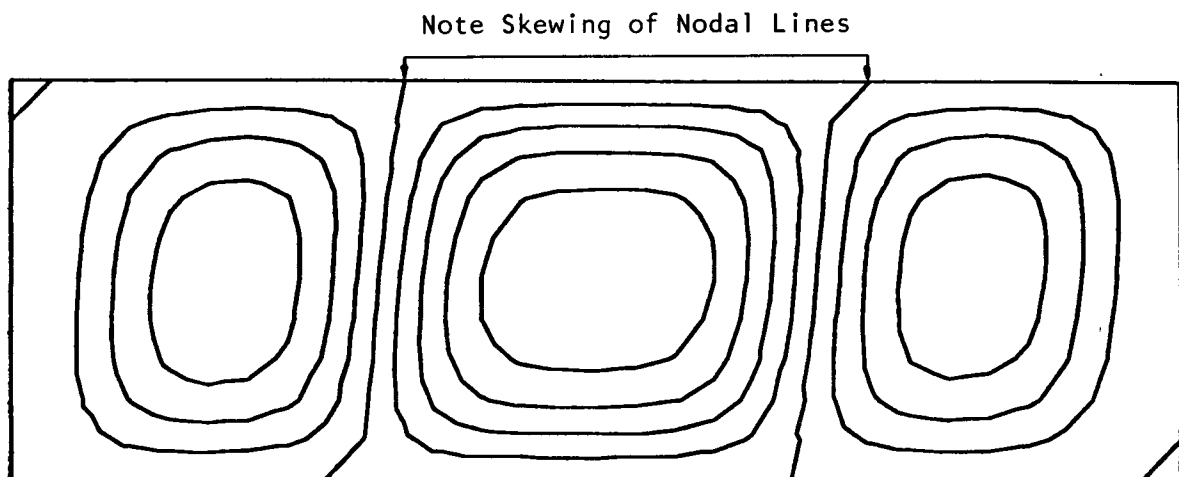
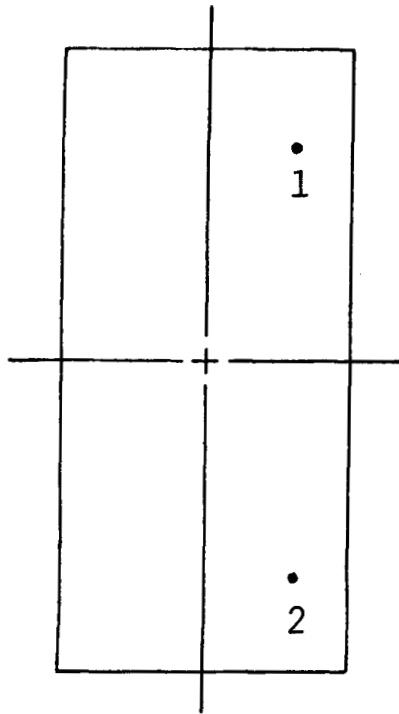
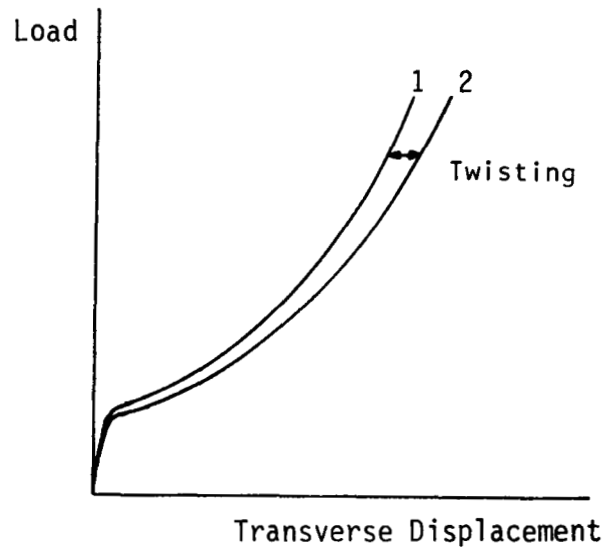


Figure 2.3. Effect of Shear-Extensional Coupling on Postbuckled Shape



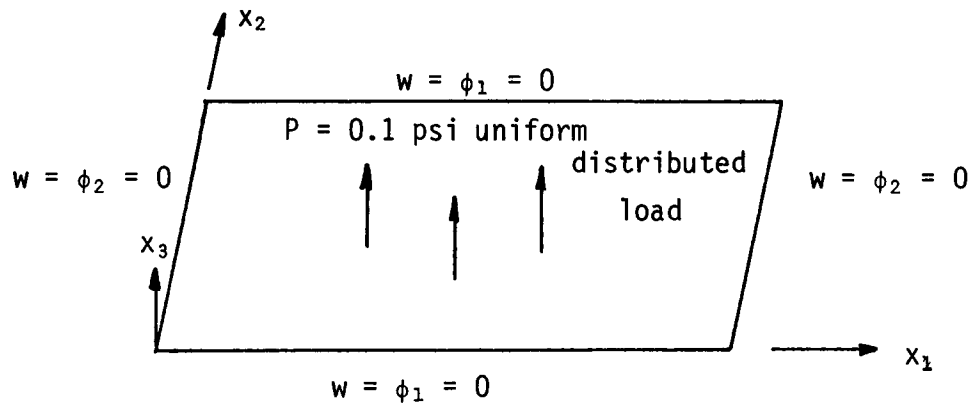
Location of Displacement  
Transducers in Reflectionally  
Symmetric Positions



Typical Results From Such  
Measurements

FIGURE 2.4. METHOD FOR OBSERVING TWISTING  
BEHAVIOR DURING AN EXPERIMENT

### TRANSVERSE LOADING PROBLEMS:



### AXIAL LOADING PROBLEMS:

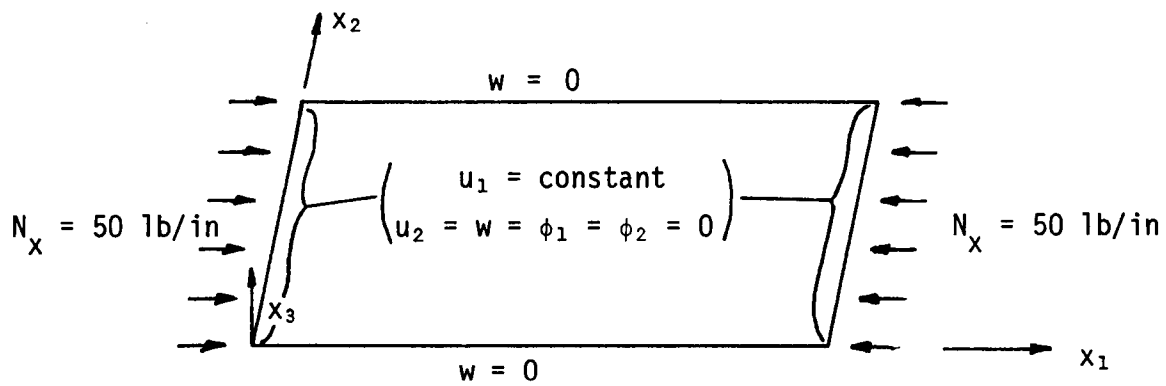
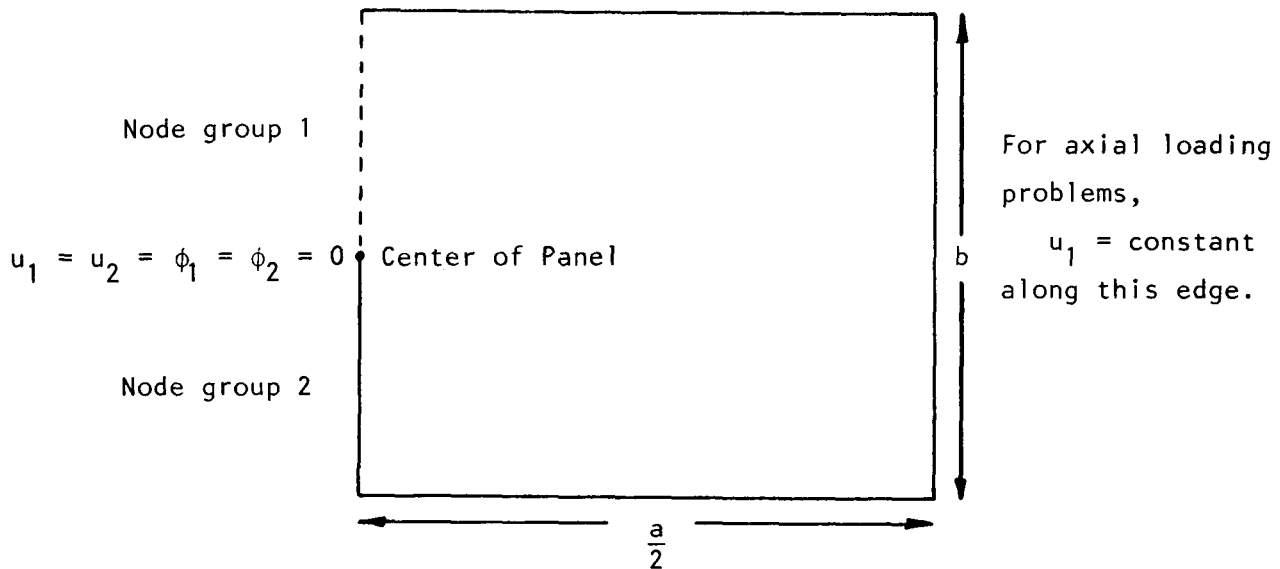


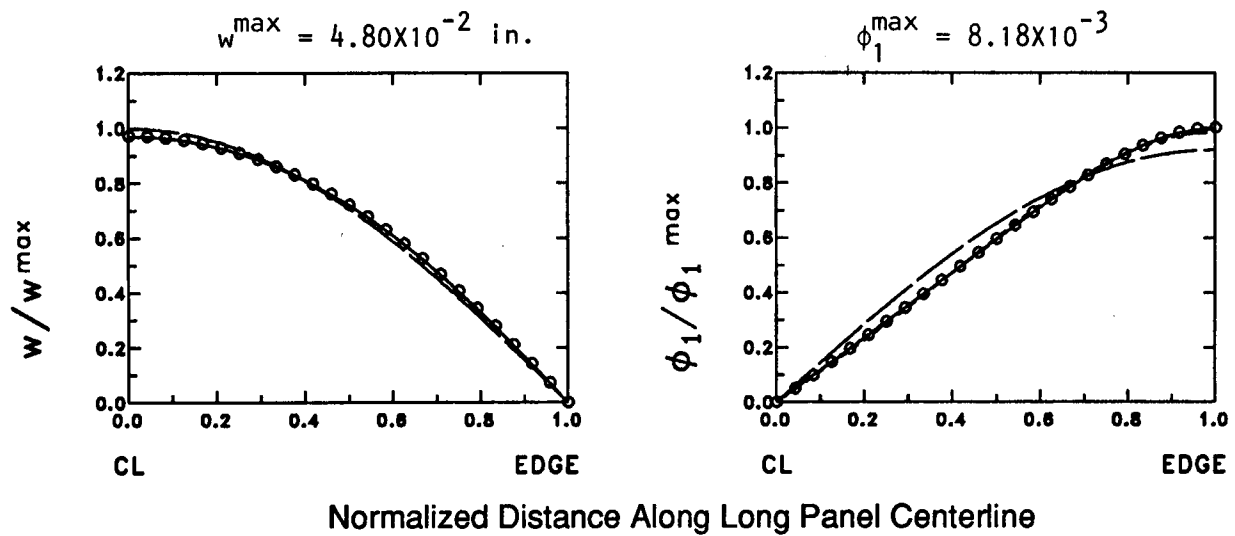
FIGURE 4.1. SCHEMATICS FOR LINEAR PROBLEMS

Half the panel is modeled:



1. Node group 1 is related to node group 2 by the symmetry relations of Chapter 2 and is therefore not modeled.
2. Left half of panel is related to right half by the symmetry relations of Chapter 2 and is not explicitly modeled.
3. Boundary conditions are imposed as described in the previous figure for the three exterior edges, except as noted in the above figure.

Figure 4.2. Schematic of Mixed Formulation Finite Element Models



LEGEND	
○	Mixed Formulation Finite Element Solution
— — —	Rayleigh Ritz Solution, 3 Terms
- - - - -	Rayleigh Ritz Solution, 9 Terms
- - - - -	Rayleigh Ritz Solution, 19 Terms
— — — — —	Rayleigh Ritz Solution, 33 Terms
— - - - -	Rayleigh Ritz Solution, 51 Terms
● Only $w$ and $\phi_1$ are shown since $u$ and $v$ are zero at all points, and $\phi_2$ is zero along the long centerline.	

**Figure 4.3. Linear Results for Simply Supported Transversely Loaded  $[0_4/90_4]_s$  Panel**



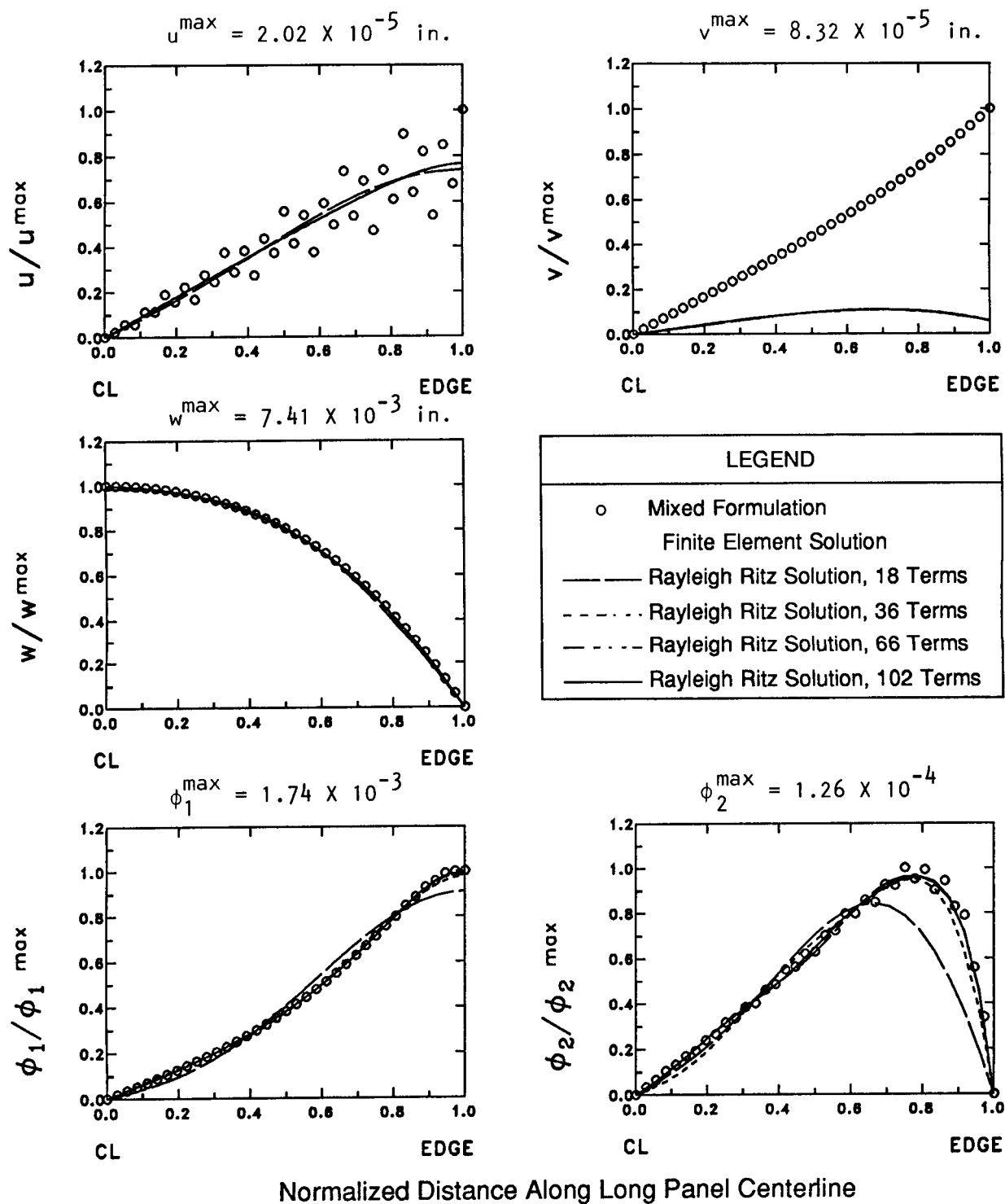
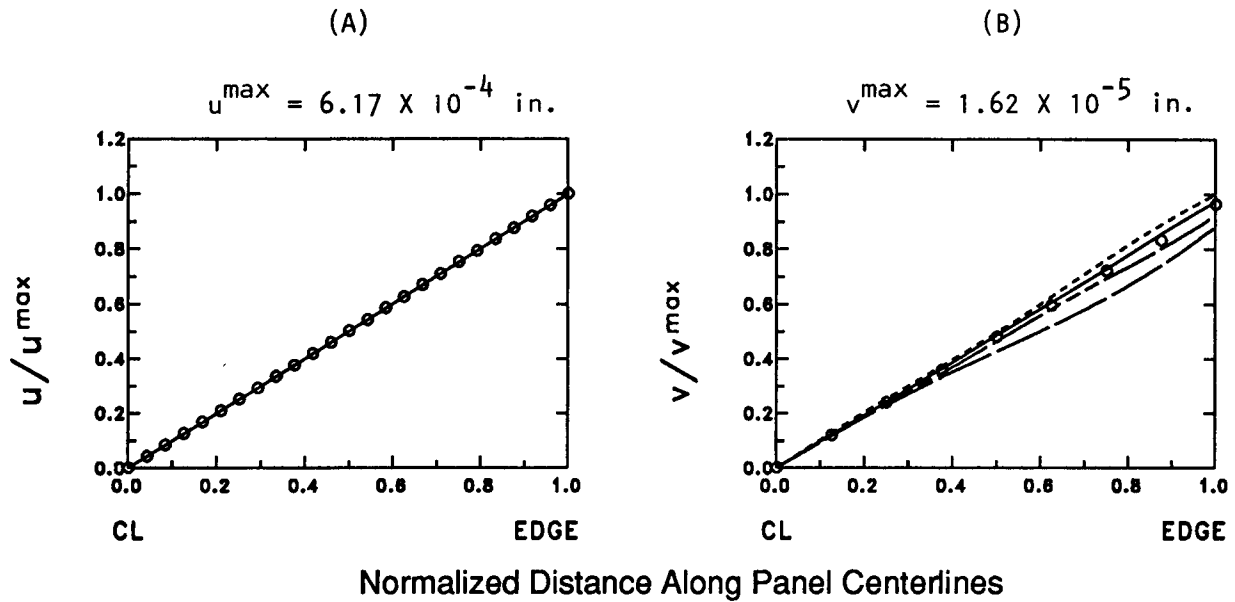


**Figure 4.4. Linear Results for Simply Supported Transversely Loaded  $[\pm 50/35]_5$  Panel**



LEGEND	
○	Mixed Formulation Finite Element Solution
—	Rayleigh Ritz Solution, 9 Terms
- - - -	Rayleigh Ritz Solution, 19 Terms
- . . . -	Rayleigh Ritz Solution, 33 Terms
—	Rayleigh Ritz Solution, 51 Terms
● $u$ is plotted down the long panel centerline, and $v$ is plotted down the short centerline.	
● Only $u$ and $v$ are shown since all other displacements are zero at all points.	

**Figure 4.5. Linear Results for Clamped/Simply Supported Axially Loaded  $[0_4/90_4]_s$  Panel**

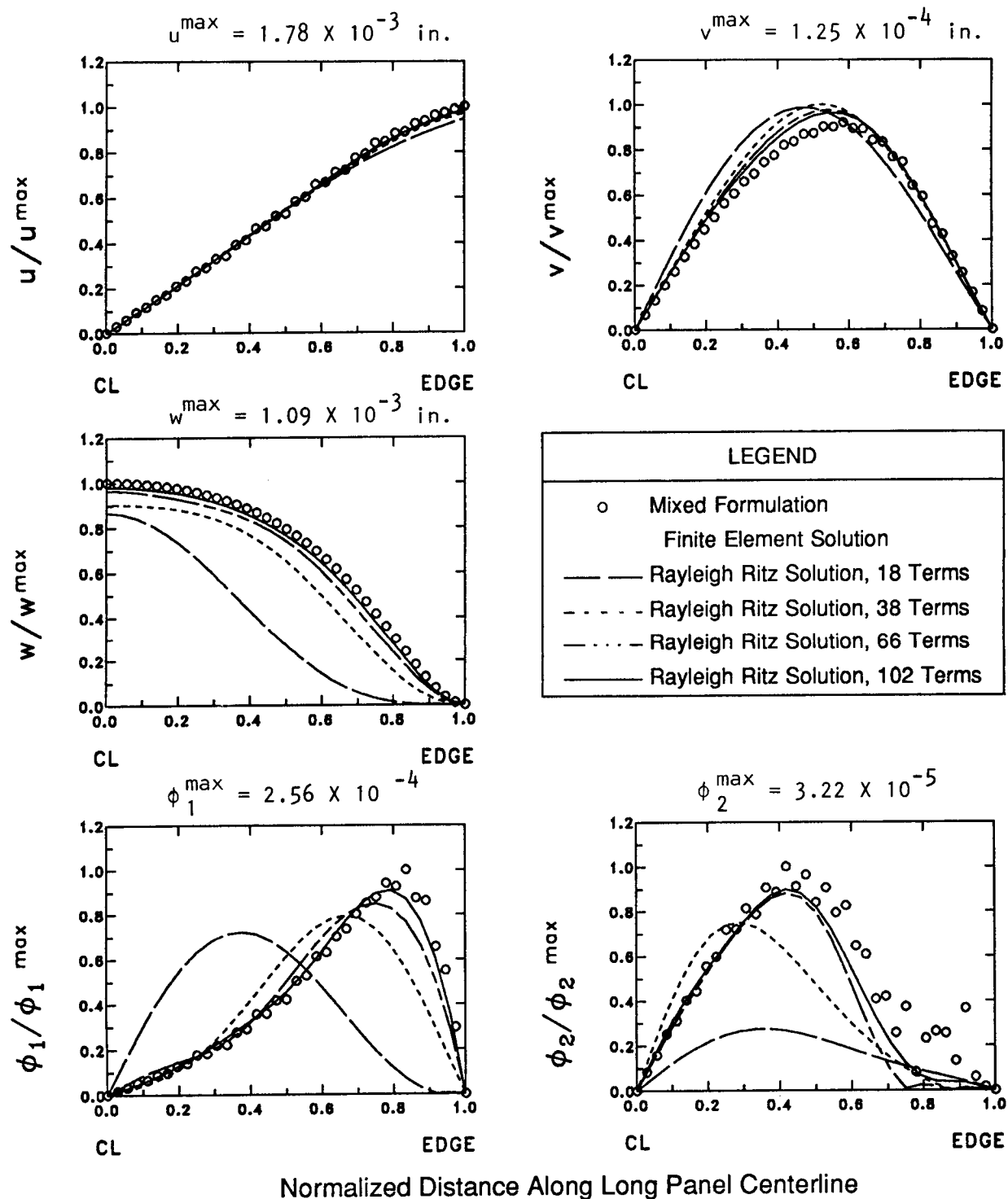
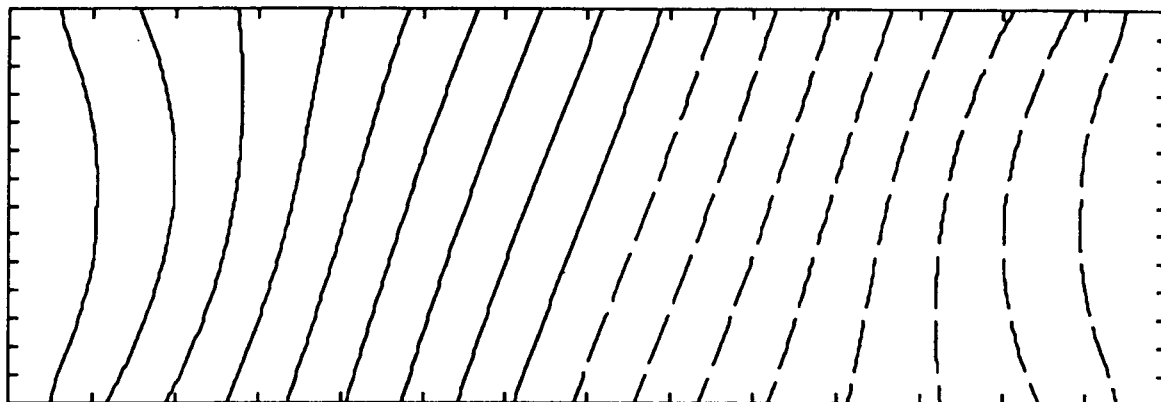
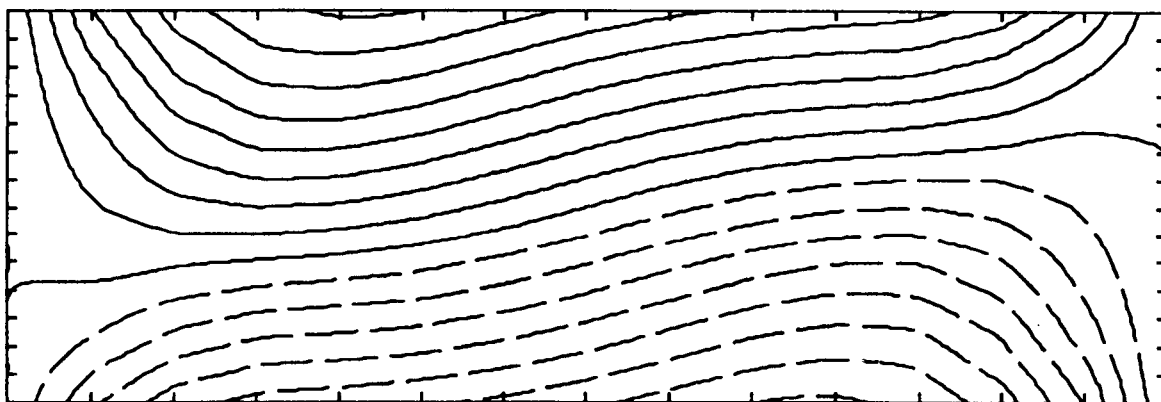


Figure 4.6. Linear Results for Clamped/Simply Supported  
 Axially Loaded  $[\pm 50/35]_5$  Panel

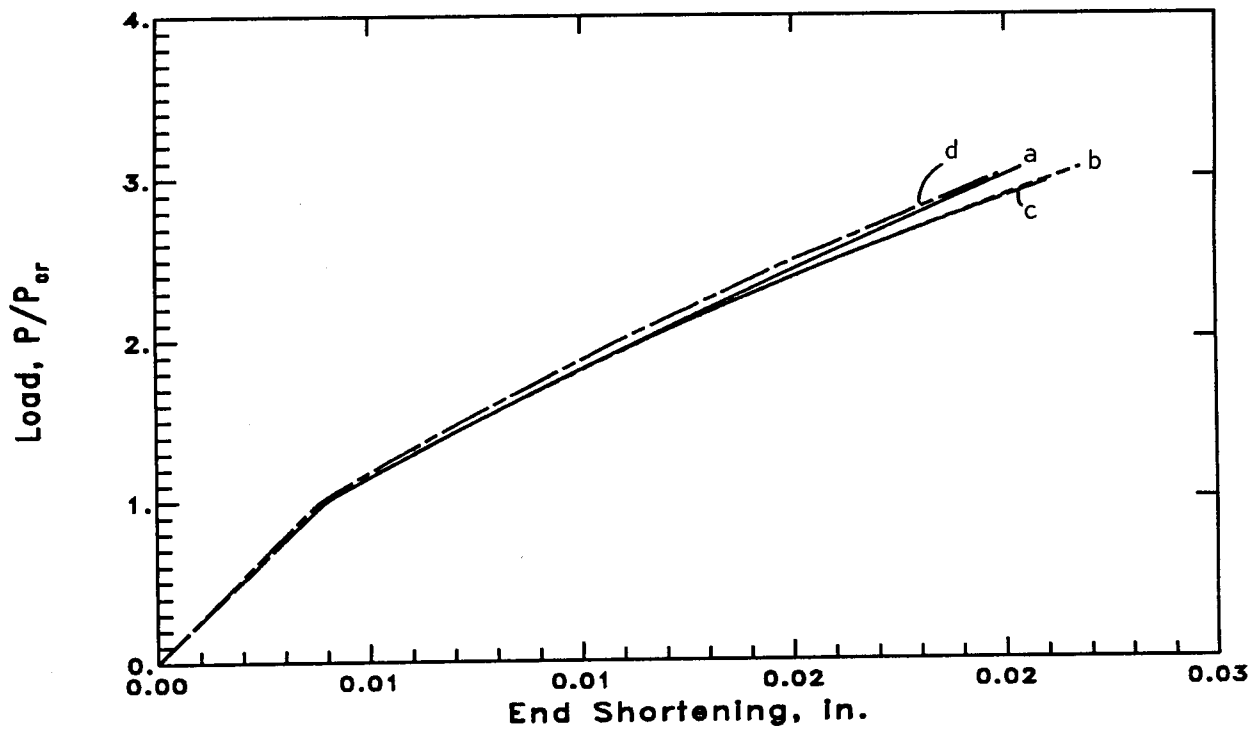


$u_1$  Displacement



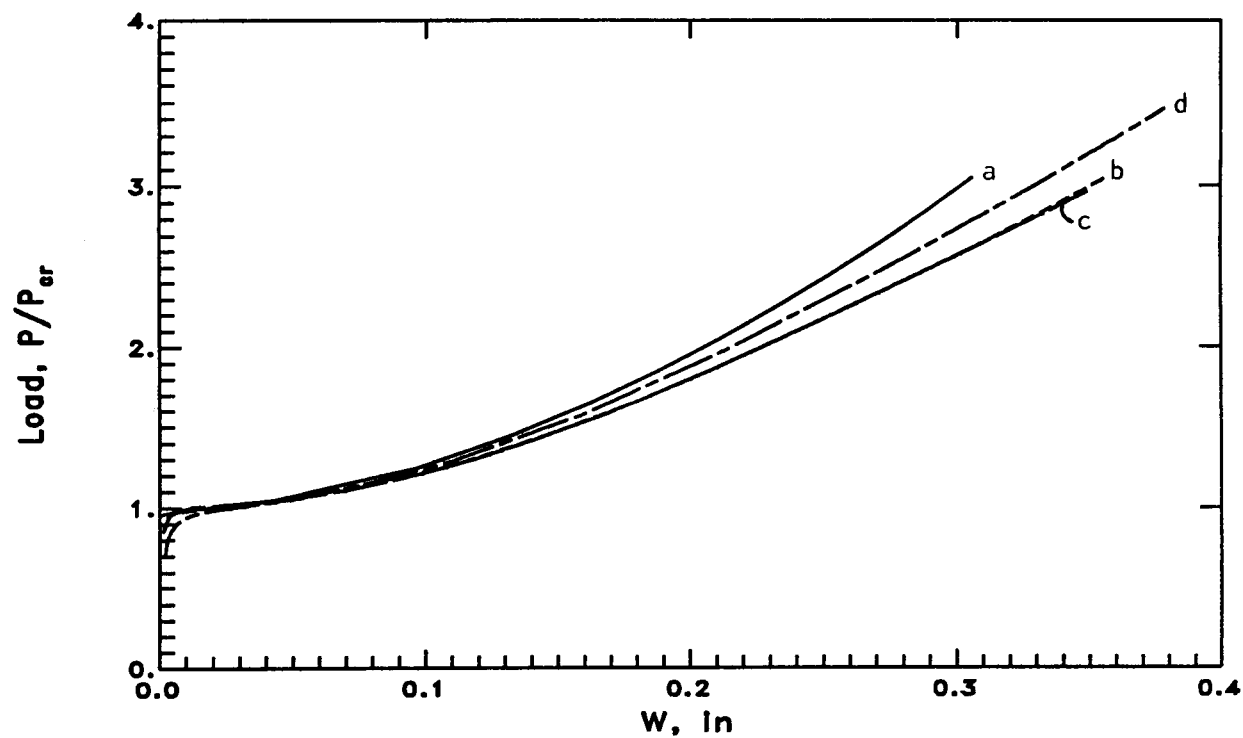
$u_2$  Displacement

**Figure 4.7. Contour Plots of Linear Solution For Axially Loaded Clamped/Simply Supported  $[\pm 50/35]_5$  Panel**



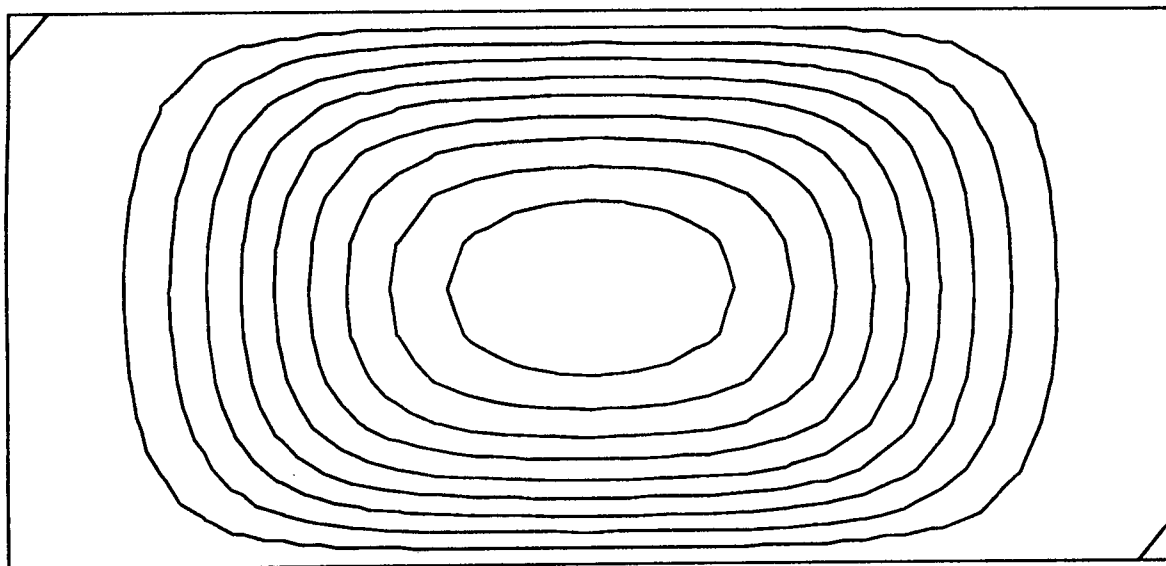
LEGEND	
a ———	Rayleigh Ritz Solution, 19 Terms
b - - - -	Rayleigh Ritz Solution, 33 Terms
c — — —	Mixed Formulation Finite Element Solution
d — - —	STAGS Solution

**Figure 4.8. End Shortening Behavior,  $[0_4/90_4]_s$  Panel**

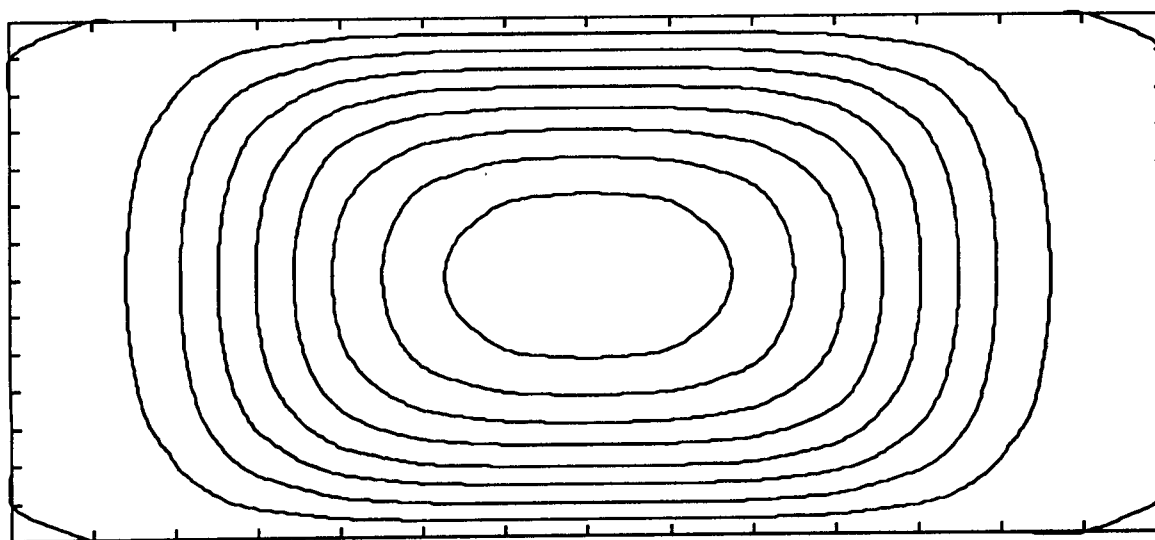


LEGEND	
a ———	Rayleigh Ritz Solution, 19 Terms
b - - - -	Rayleigh Ritz Solution, 33 Terms
c ———	Mixed Formulation Finite Element Solution
d - - - -	STAGS Solution

**Figure 4.9. Center Transverse Displacement Behavior,  $[0_4/90_4]_s$  Panel**

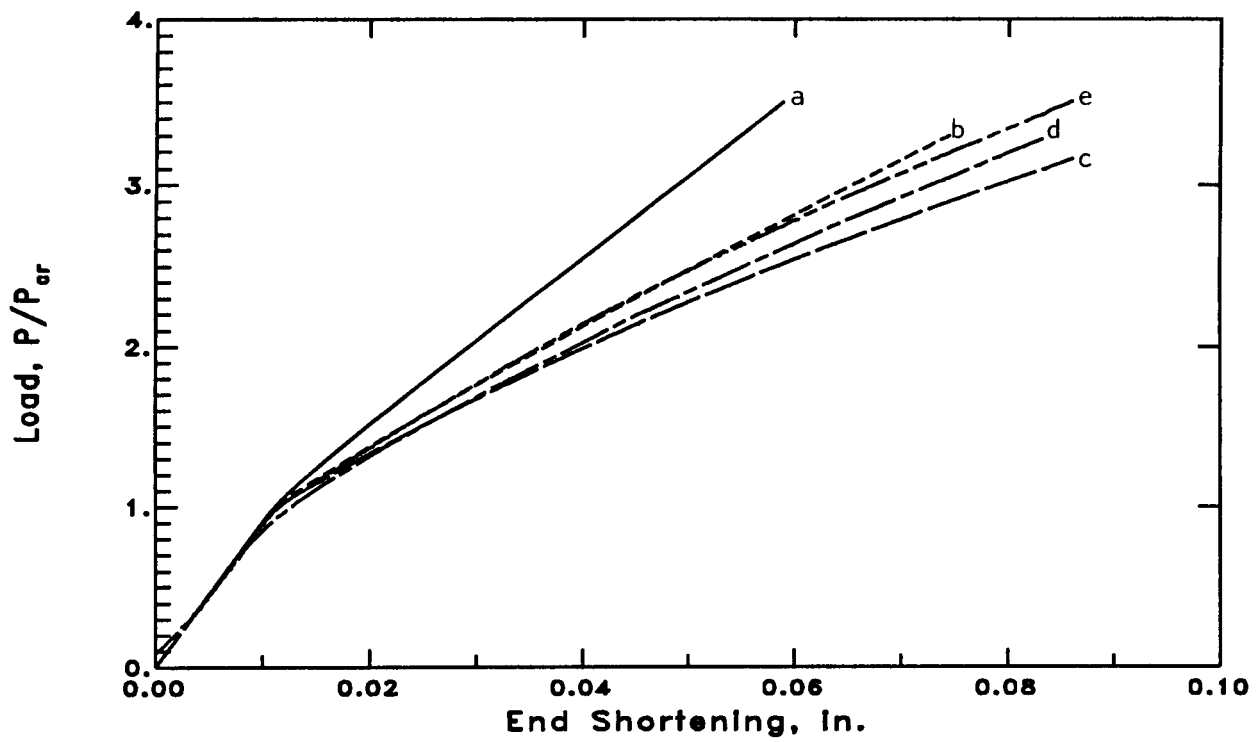


STAGS Results at  $P = 4347$  lb



Rayleigh-Ritz Results at  $P = 4407$  lb

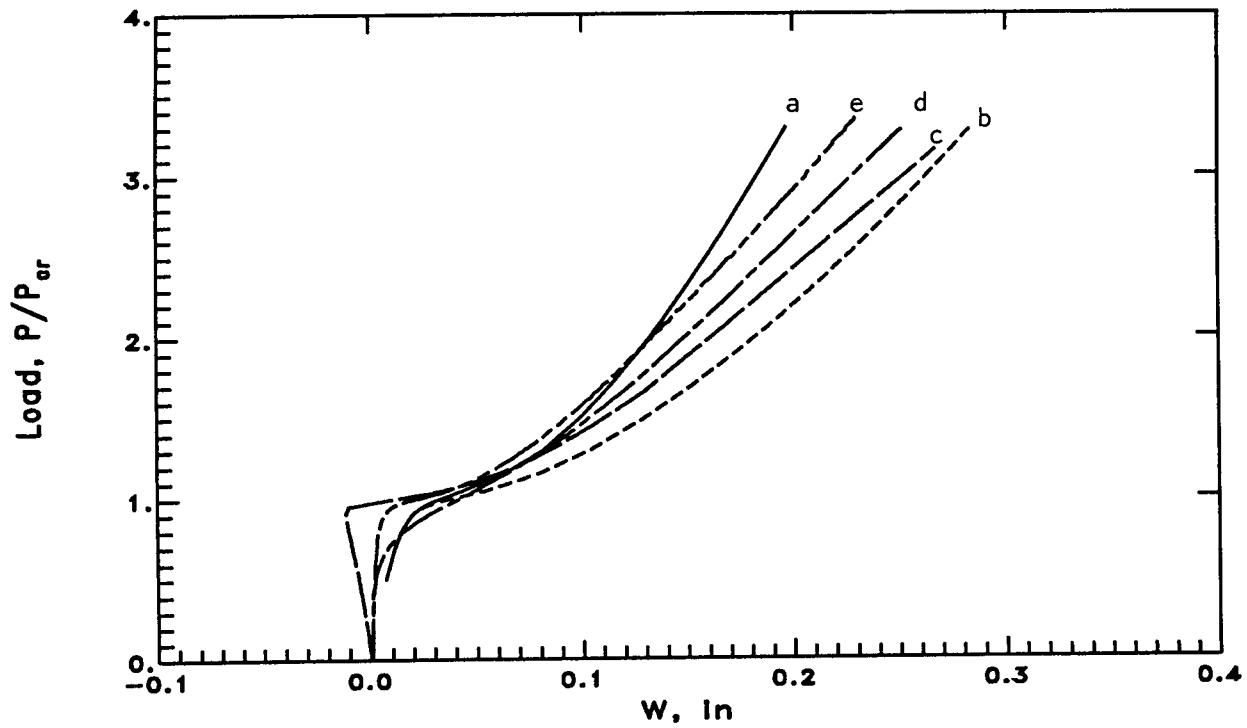
**Figure 4.10. Normalized Contour Plots of Transverse Displacement,  $[0_4/90_4]$  Panel**



LEGEND	
a ———	Rayleigh Ritz Solution, 38 Terms
b - - - - -	Rayleigh Ritz Solution, 66 Terms
c ———	Mixed Formulation Finite Element Solution
d — . — . —	STAGS Solution
e - - - - -	Experiment

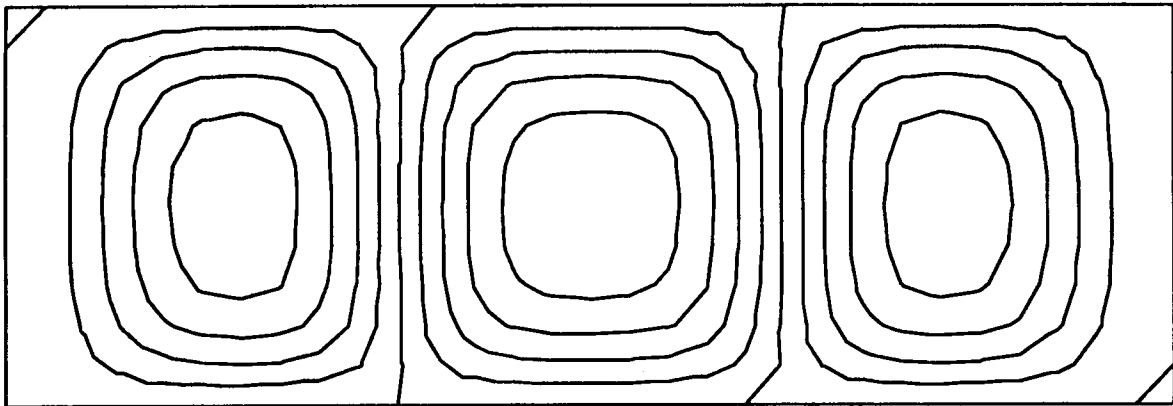
Figure 4.11. End Shortening Behavior,  $[\pm 30/90]_5$  Panel



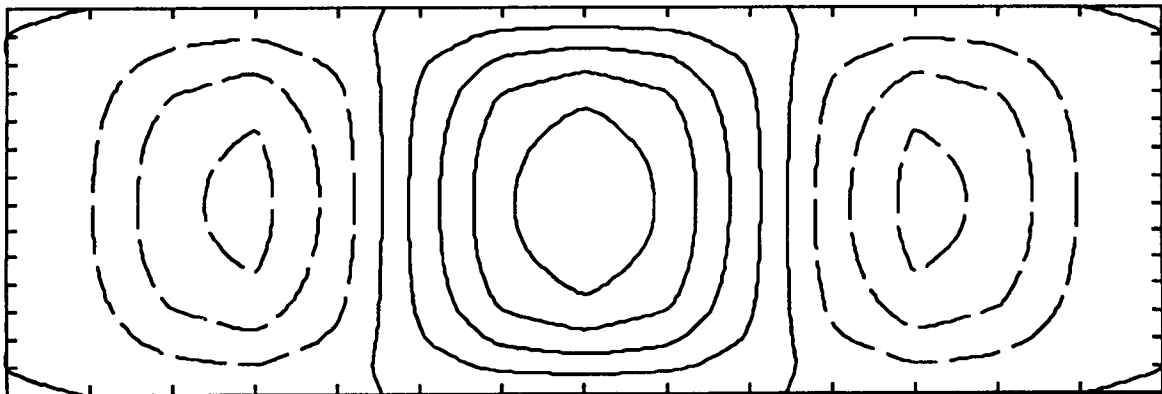


LEGEND	
a ———	Rayleigh Ritz Solution, 38 Terms
b - - - -	Rayleigh Ritz Solution, 66 Terms
c ———	Mixed Formulation Finite Element Solution
d - - -	STAGS Solution
e - - - -	Experiment

**Figure 4.12. Center Transverse Displacement Behavior,  $[\pm 30/90]_5$  Panel**

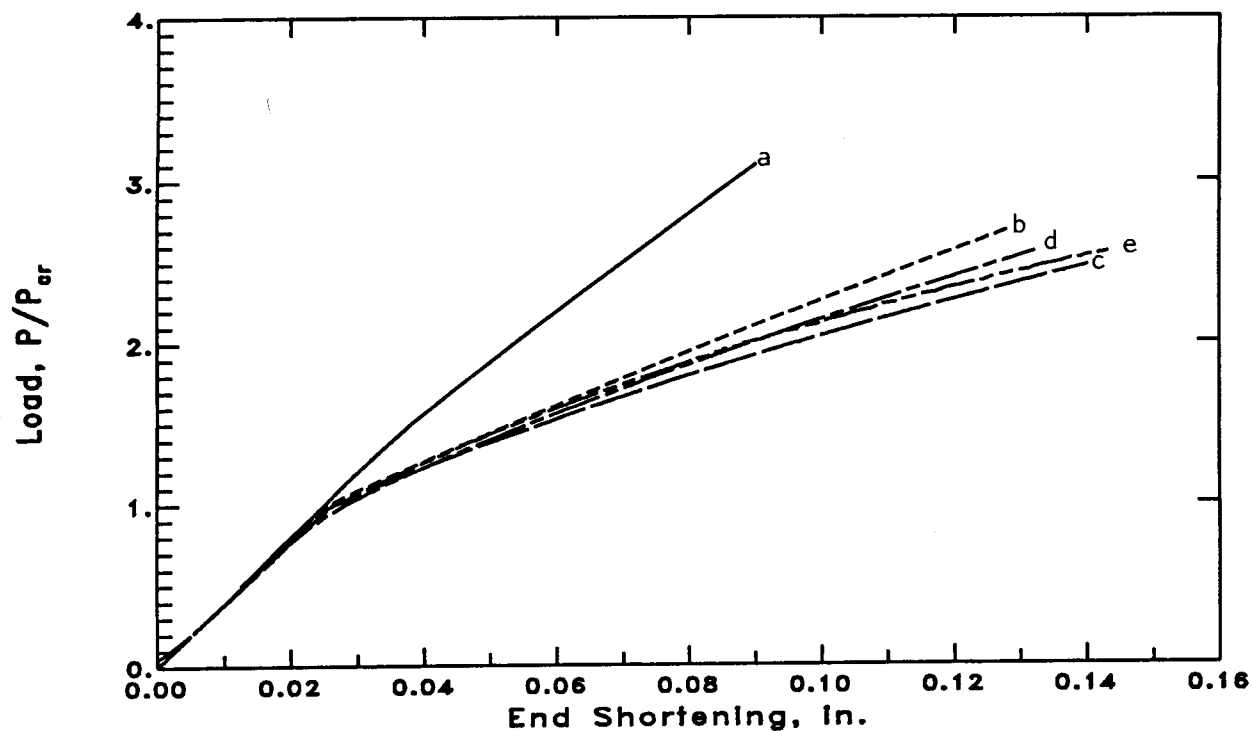


STAGS Results at  $P = 7100$  lb



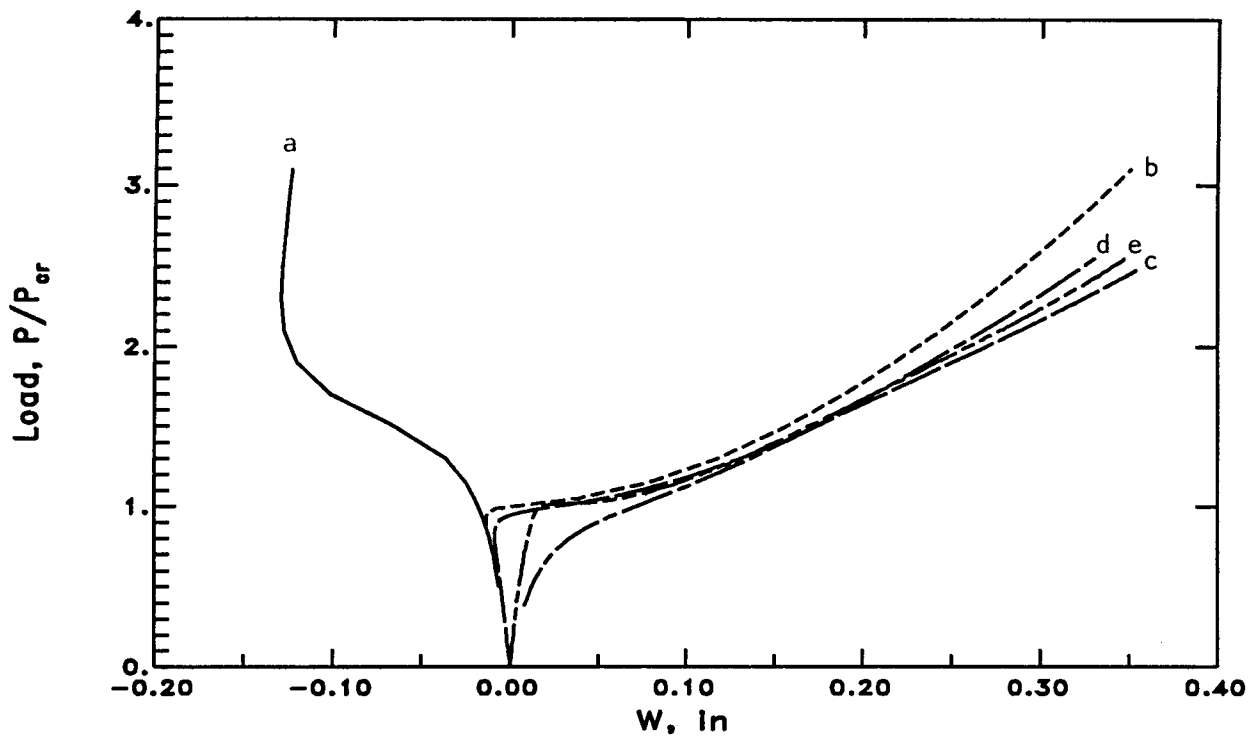
Rayleigh-Ritz Results at  $P = 7137$  lb

**Figure 4.13. Normalized Contour Plots of Transverse Displacement,  $[\pm 30/90]_5$  Panel**



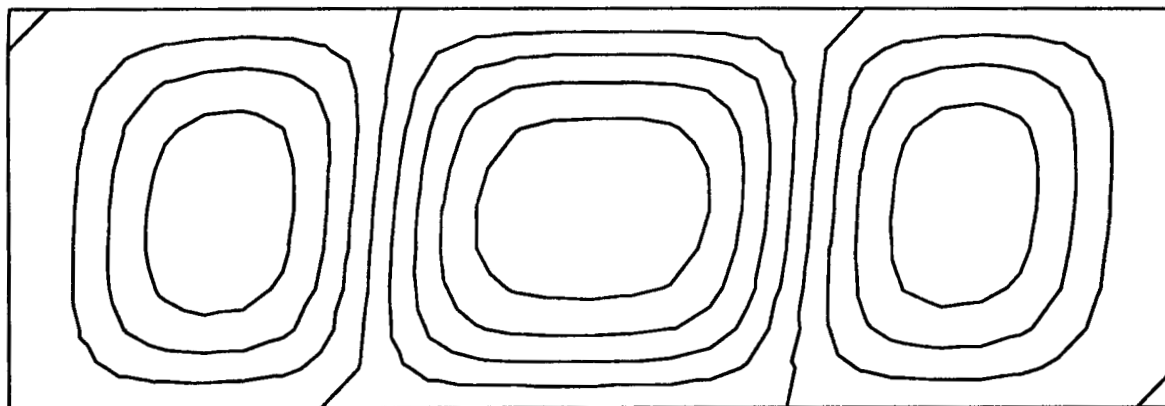
LEGEND	
a ———	Rayleigh Ritz Solution, 38 Terms
b - - - -	Rayleigh Ritz Solution, 66 Terms
c — — —	Mixed Formulation Finite Element Solution
d — - —	STAGS Solution
e — - -	Experiment

Figure 4.14. End Shortening Behavior,  $[\pm 50/35]_5$  Panel

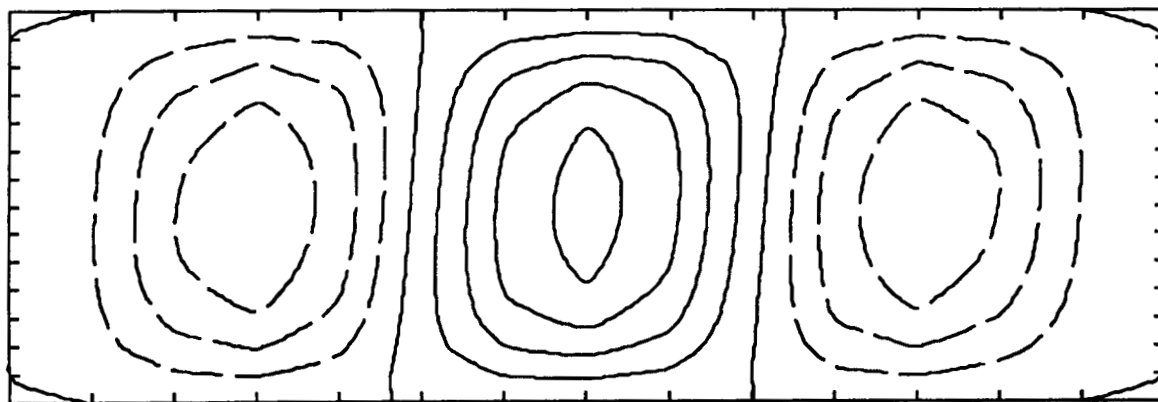


LEGEND	
a ———	Rayleigh Ritz Solution, 38 Terms
b - - - -	Rayleigh Ritz Solution, 66 Terms
c ———	Mixed Formulation Finite Element Solution
d - - - -	STAGS Solution
e - - - -	Experiment

**Figure 4.15. Center Transverse Displacement Behavior,  $[\pm 50/35]_5$  Panel**



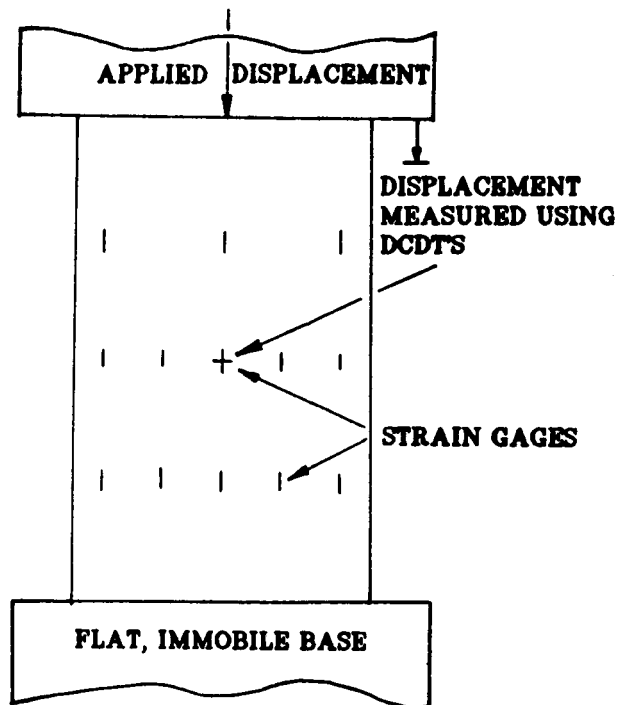
STAGS Results at  $P = 6000$  lb



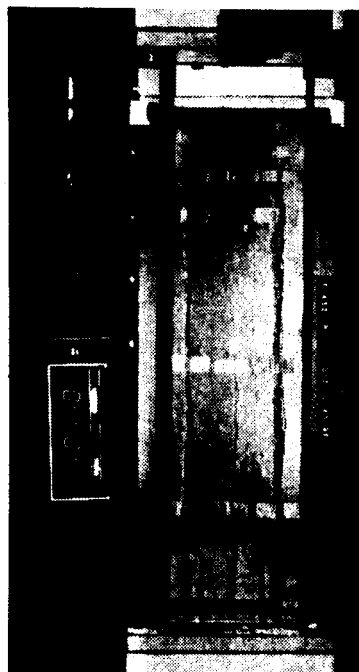
Rayleigh-Ritz Results at  $P = 6325$  lb

**Figure 4.16. Normalized Contour Plots of Transverse Displacement,  $[\pm 50/35]_5$  Panel**

ORIGINAL PAGE IS  
OF POOR QUALITY

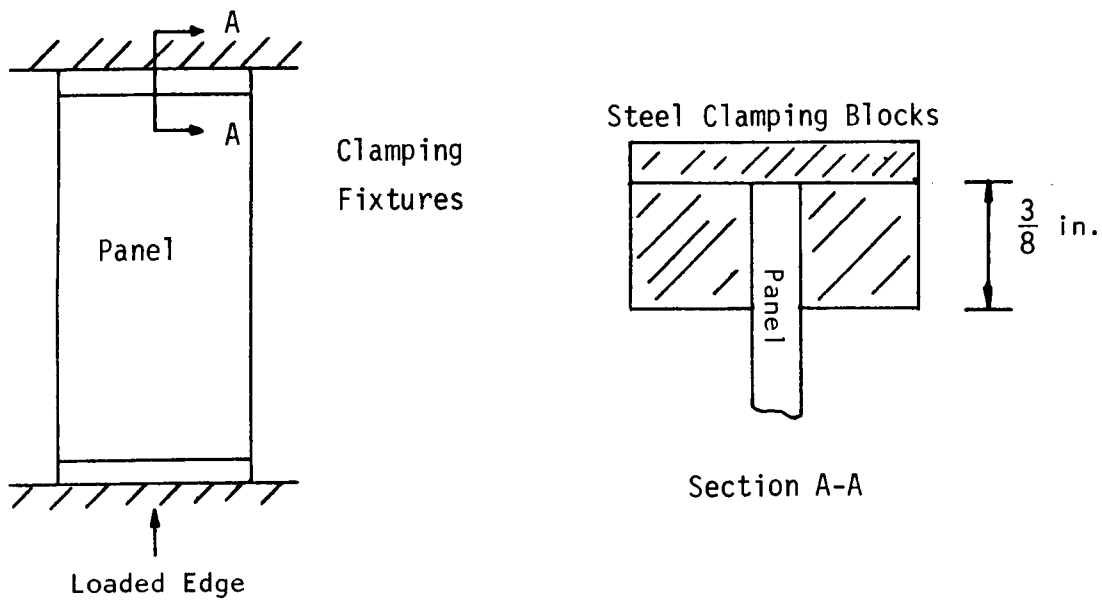


a. Schematic of Experiment Setup

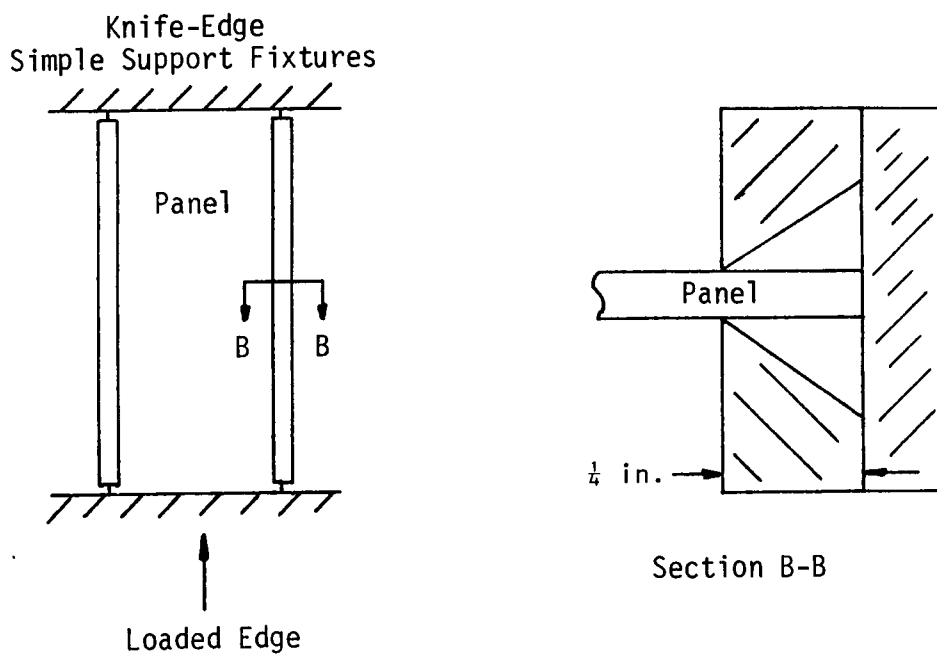


b. Photograph of Experiment Setup

Figure 5.1. Experiment Schematic and Photograph



A. SCHEMATIC OF CLAMPING FIXTURES



B. SCHEMATIC OF SIMPLE SUPPORT FIXTURES

FIGURE 5.2. SUPPORT FIXTURE SCHEMATIC

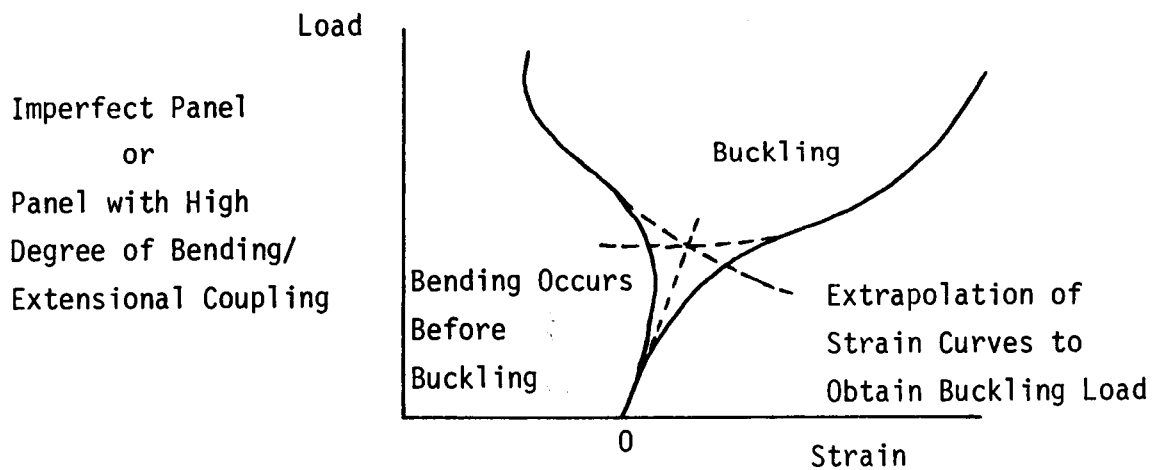
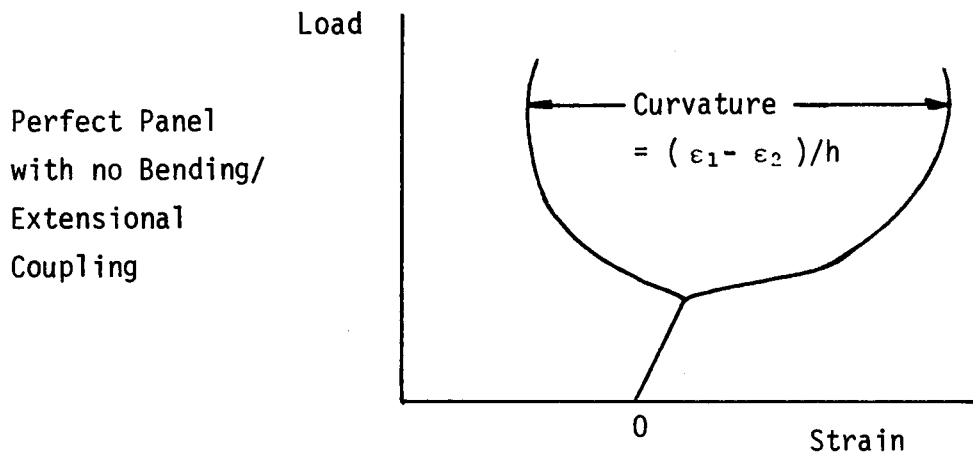
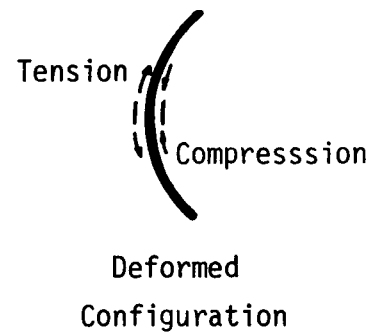
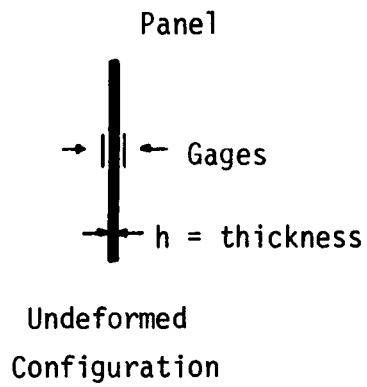


FIGURE 5.3. BENDING AS INDICATED BY BACK-TO-BACK STRAIN GAGE DATA



ORIGINAL PAGE IS  
OF POOR QUALITY

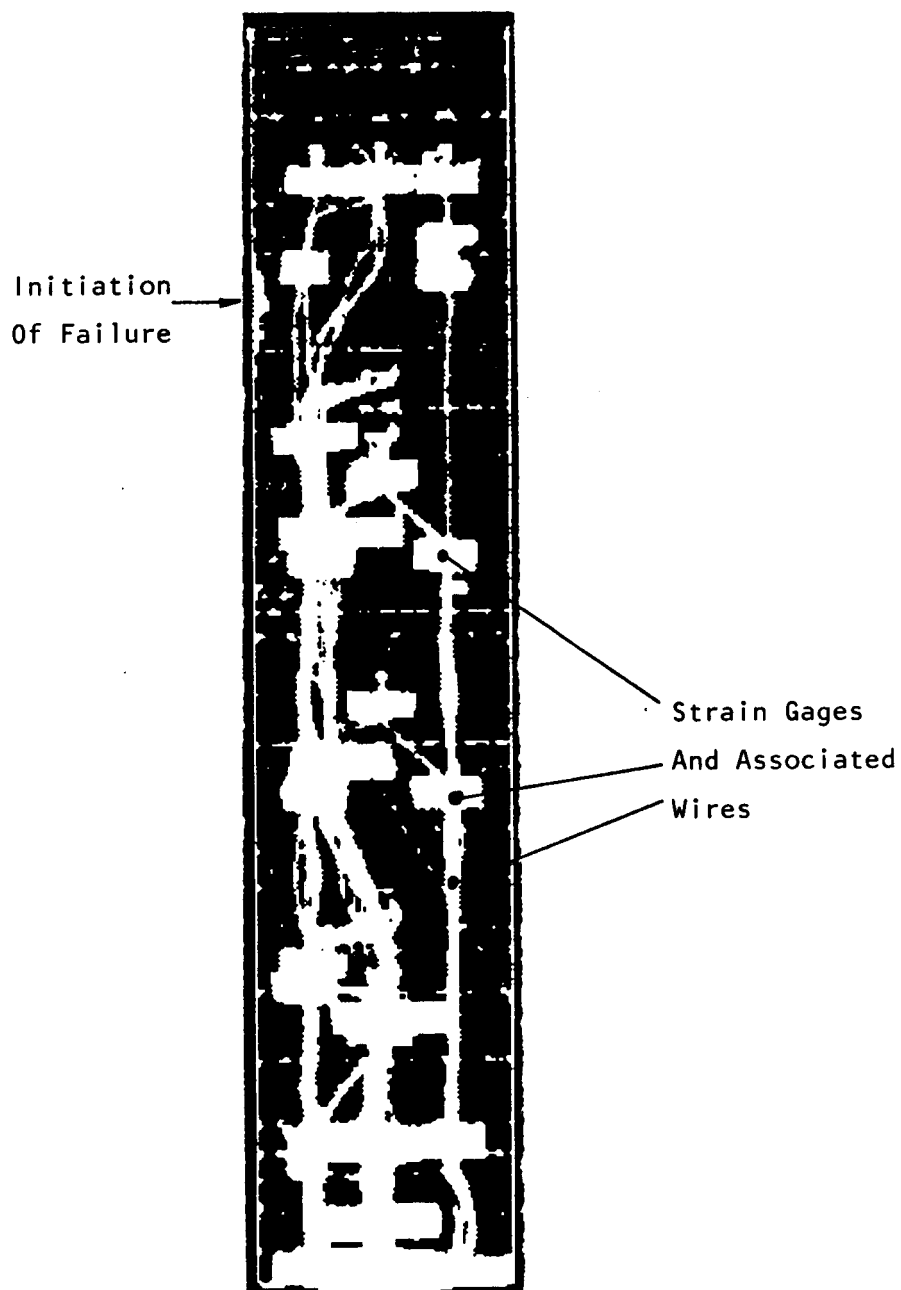
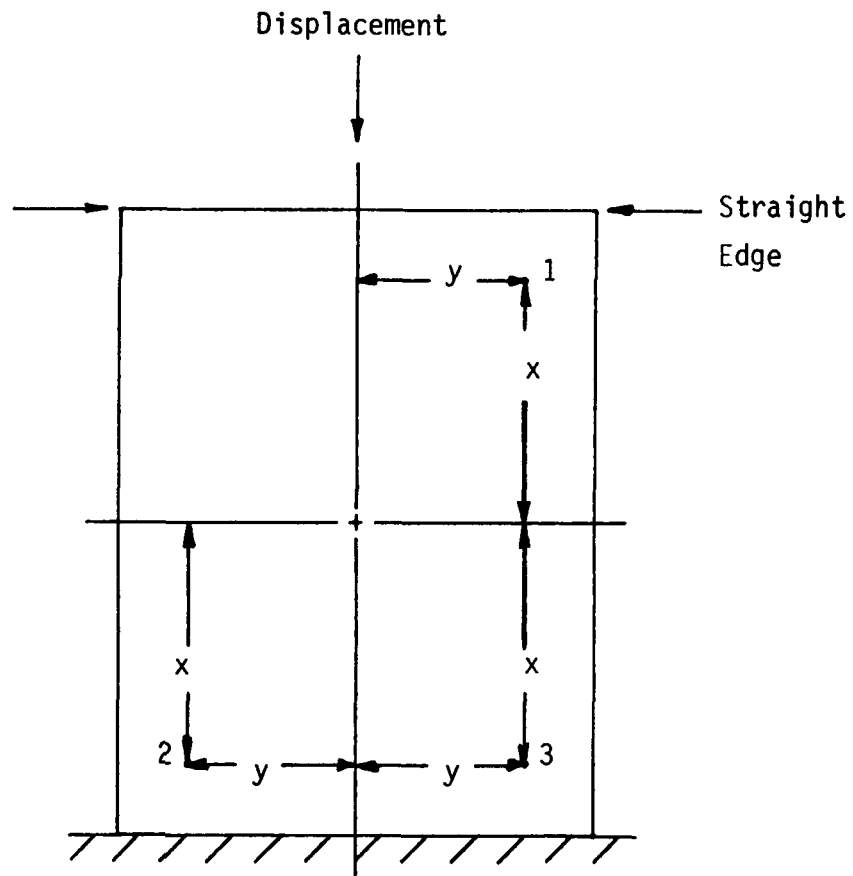


Figure 5.4. Sample C-Scan



To ensure that load is introduced parallel to the plane of the panel:

- Isotropic Panel: Points (1) and (3) must exhibit identical strain. (These points are reflectionally symmetric.)
- Anisotropic Panel: Points (1) and (2) must exhibit identical strain. (These points are inversionally symmetric.)

FIGURE 5.5. COMPARISON OF EXPERIMENTAL  
SETUP TECHNIQUE FOR ISOTROPIC  
AND ANISOTROPIC PANELS

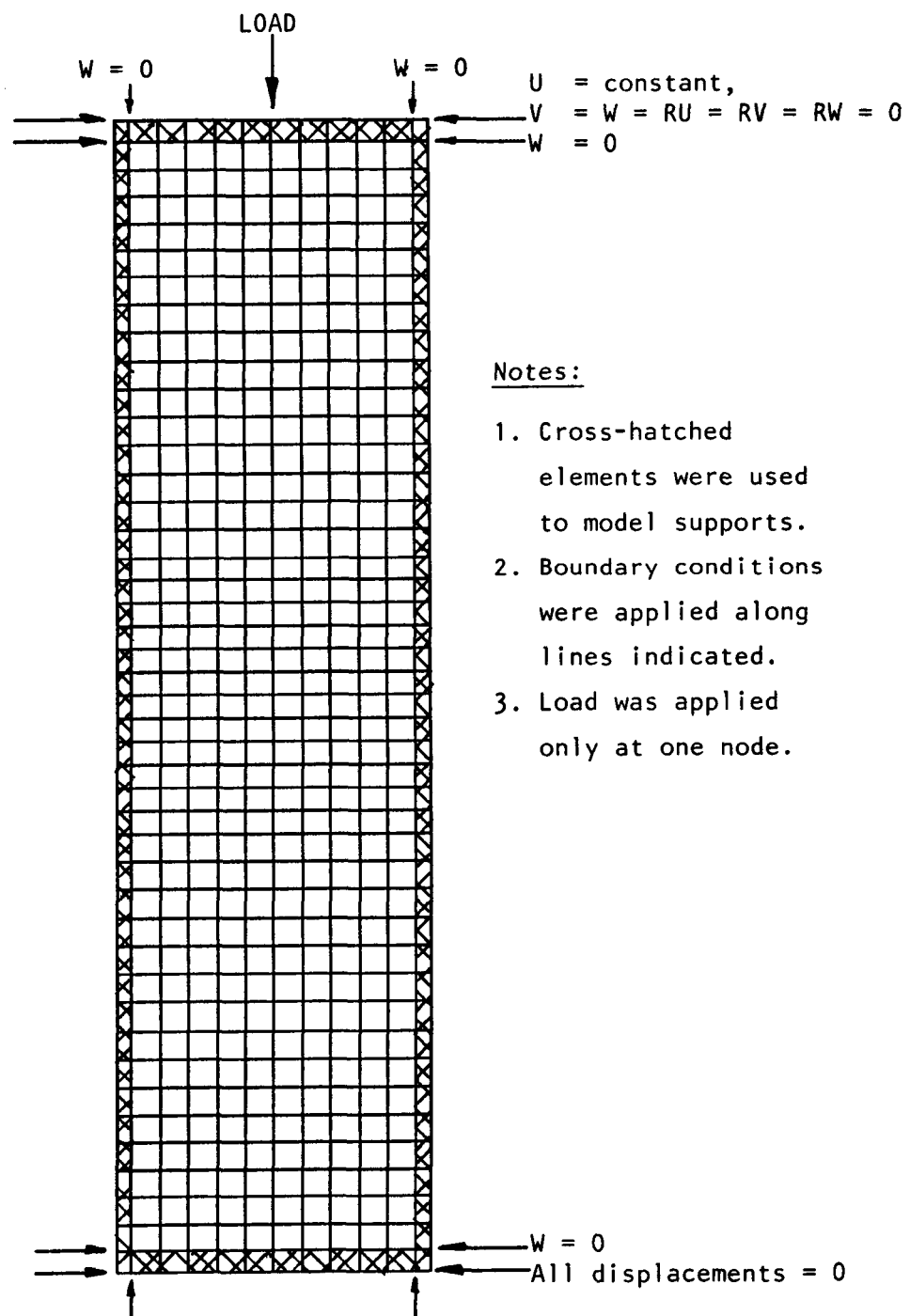


**Figure 5.6. Undeformed Geometry Plot of STAGSC-1 Finite Element Model for 5.5''  $[\pm 50/35]_5$  Panel**

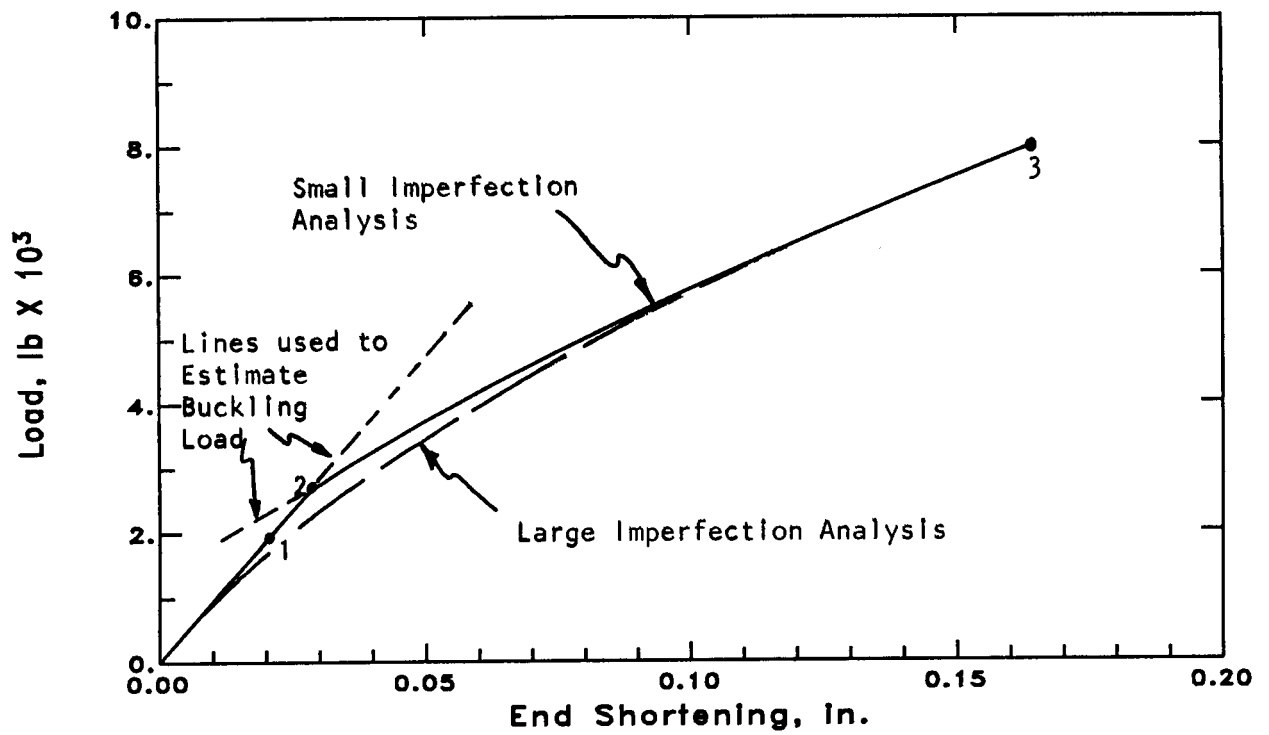
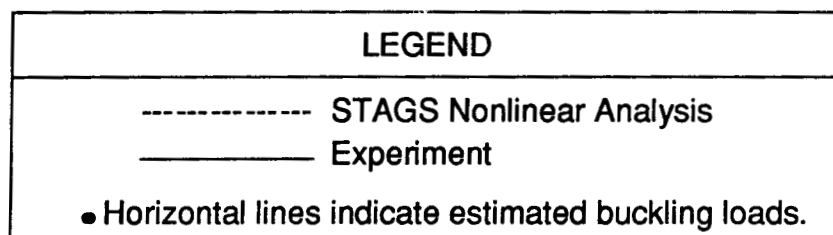
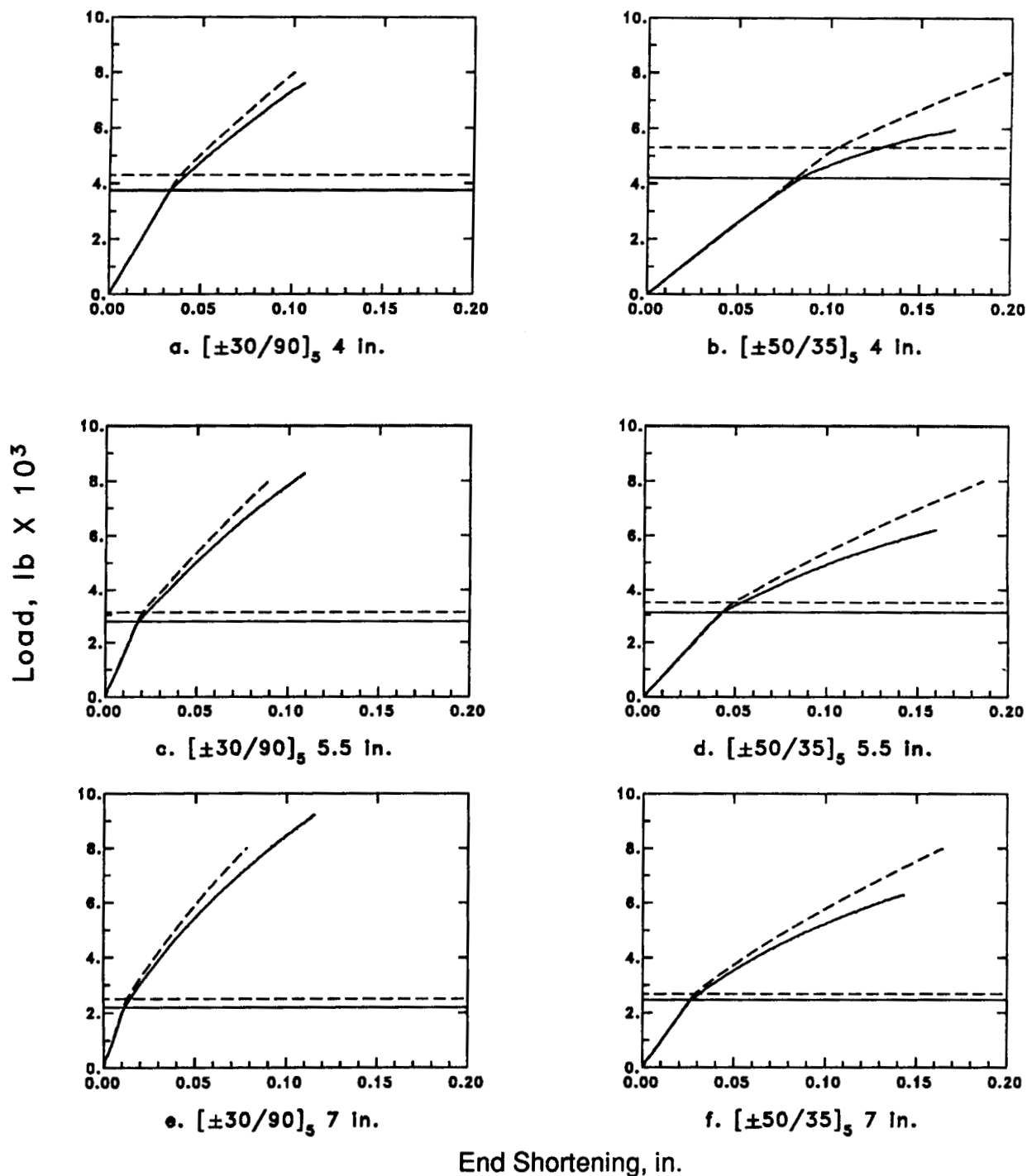
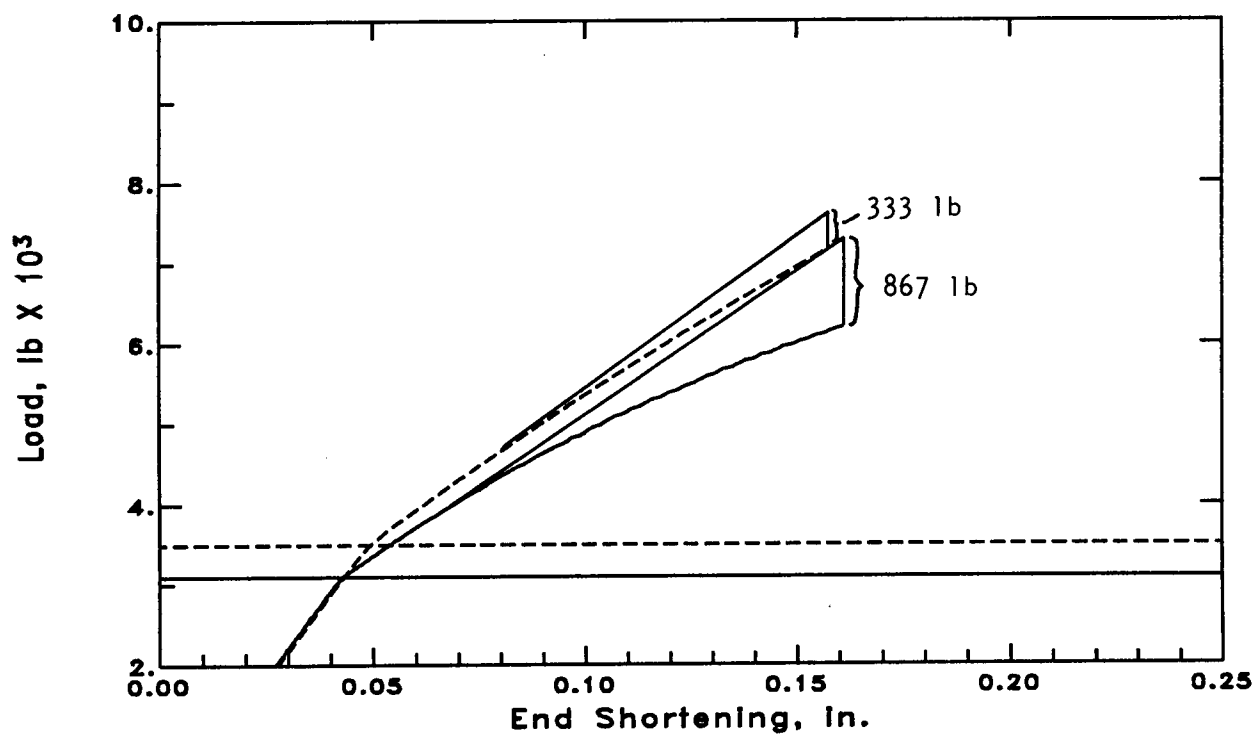


Figure 5.7. Typical Panel End Shortening Plot

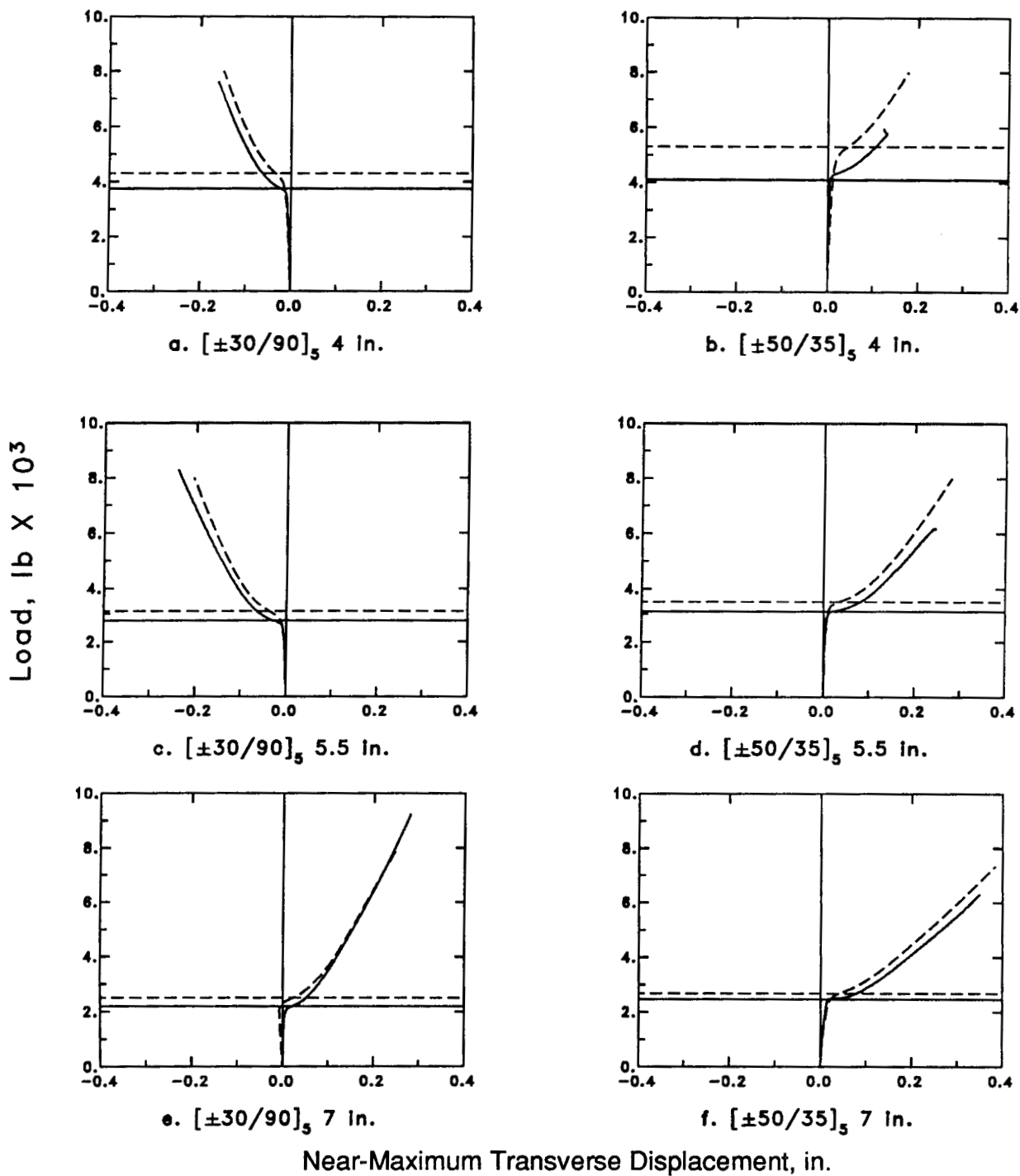


**Figure 5.8. End Shortening Results**



LEGEND	
-----	STAGS Nonlinear Analysis
————	Experiment
<ul style="list-style-type: none"> <li>• Calculation is made at loads of <math>2P_{cr}</math> for both curves.</li> <li>• Data shown is for <math>[\pm 50/35]_5</math> 5.5 inch-wide panel.</li> <li>• Horizontal lines indicate estimated buckling loads.</li> </ul>	

**Figure 5.9. Estimation of Stiffness Degradation**



LEGEND	
-----	STAGS Nonlinear Analysis
————	Experiment
• Horizontal lines indicate estimated buckling loads.	

**Figure 5.10. Near-Maximum Transverse Displacement Results**

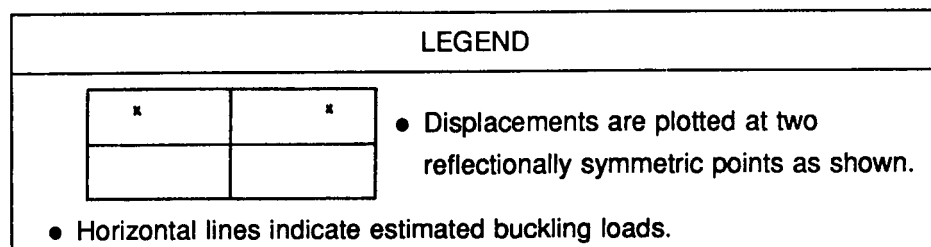
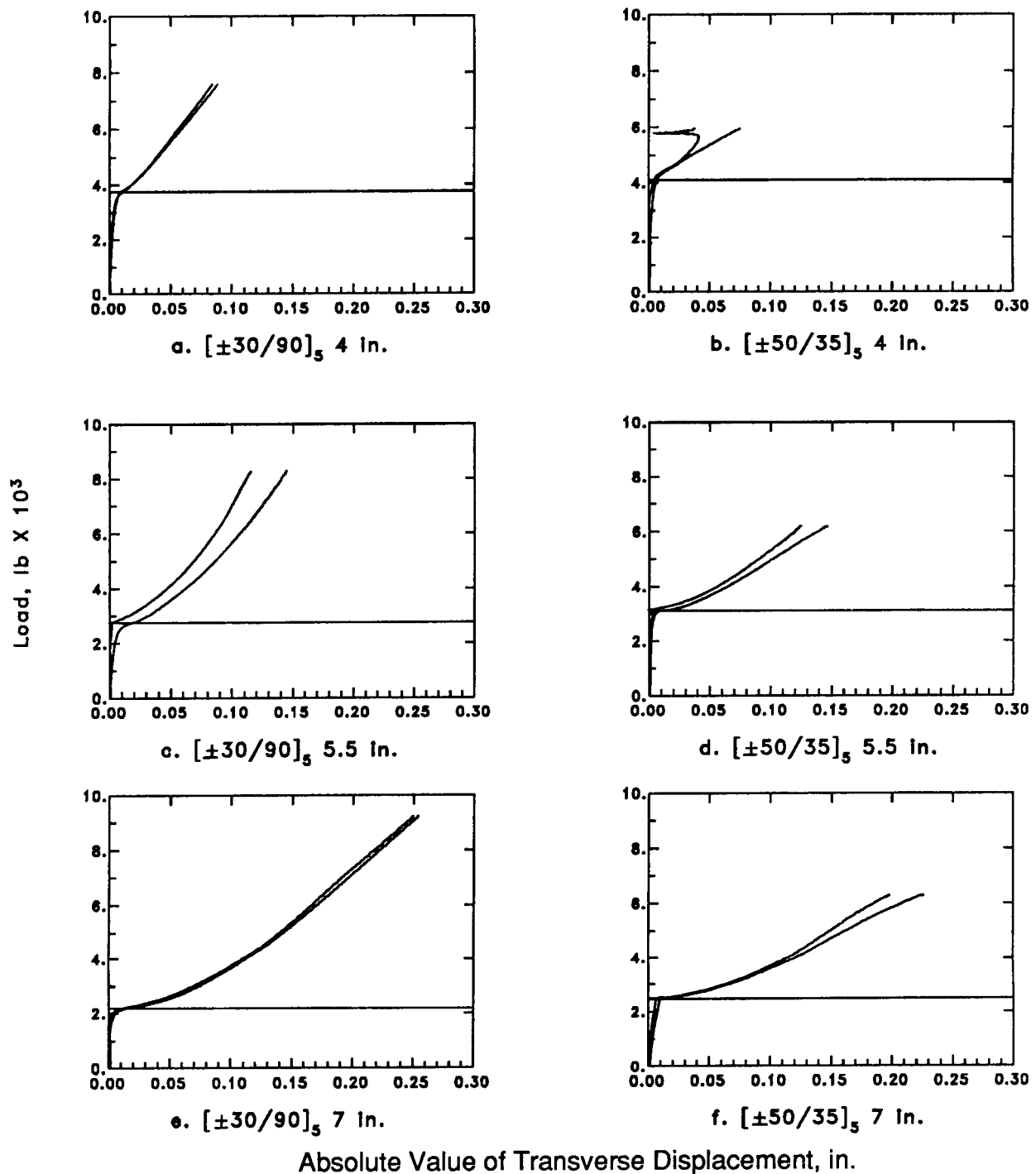


**Figure 5.11. Experimental Twisting Results**



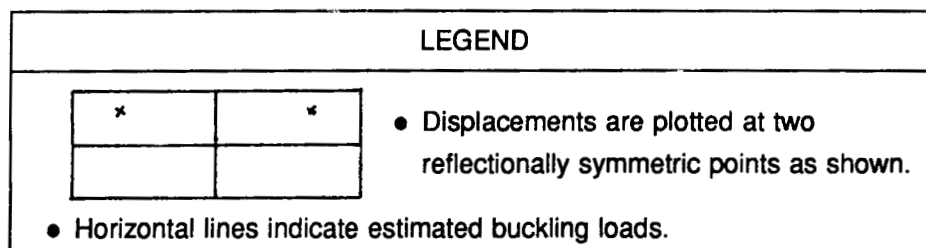
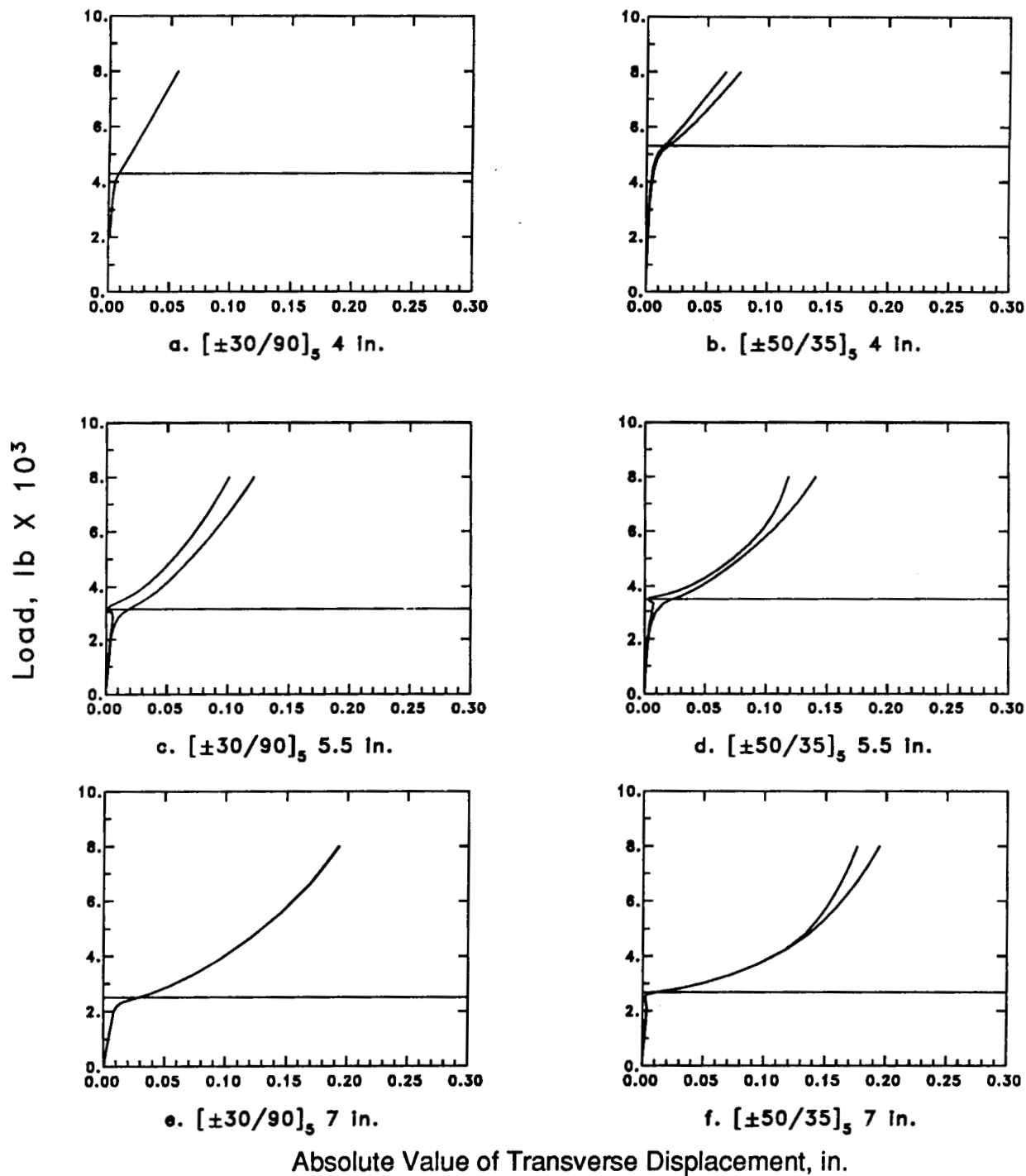
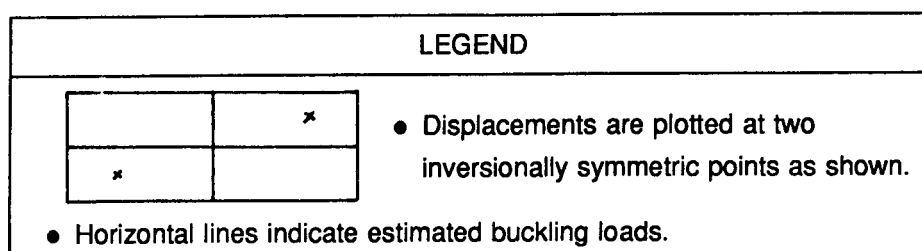
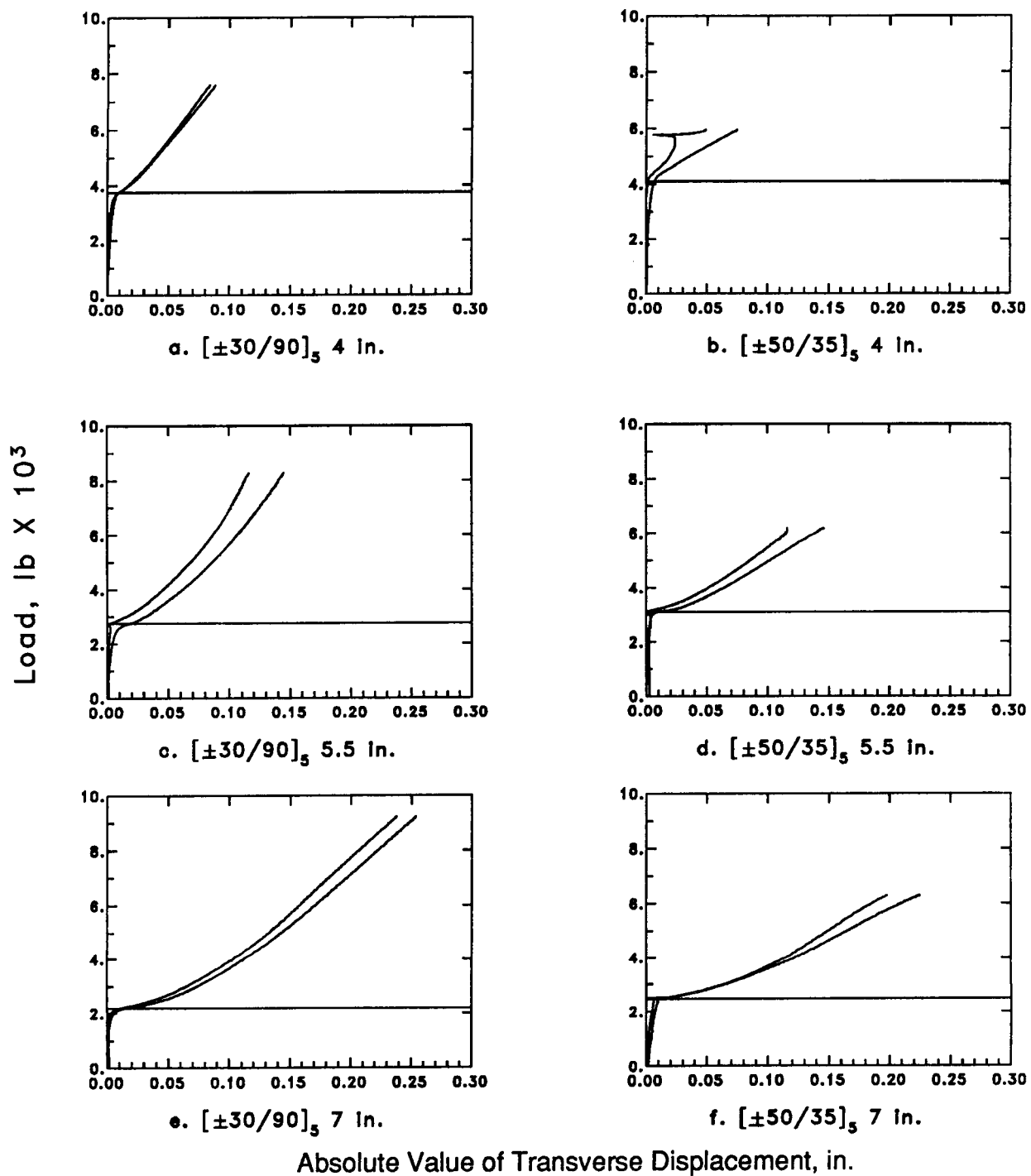
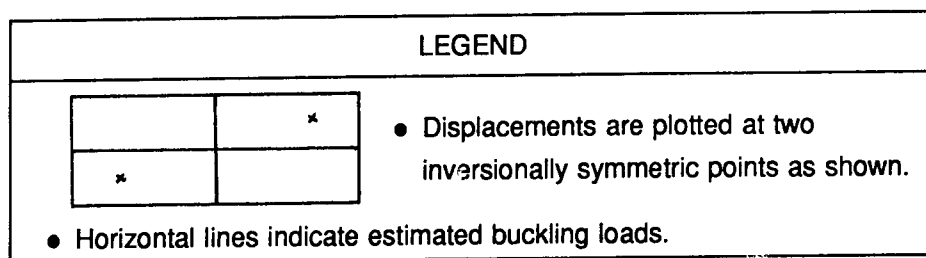
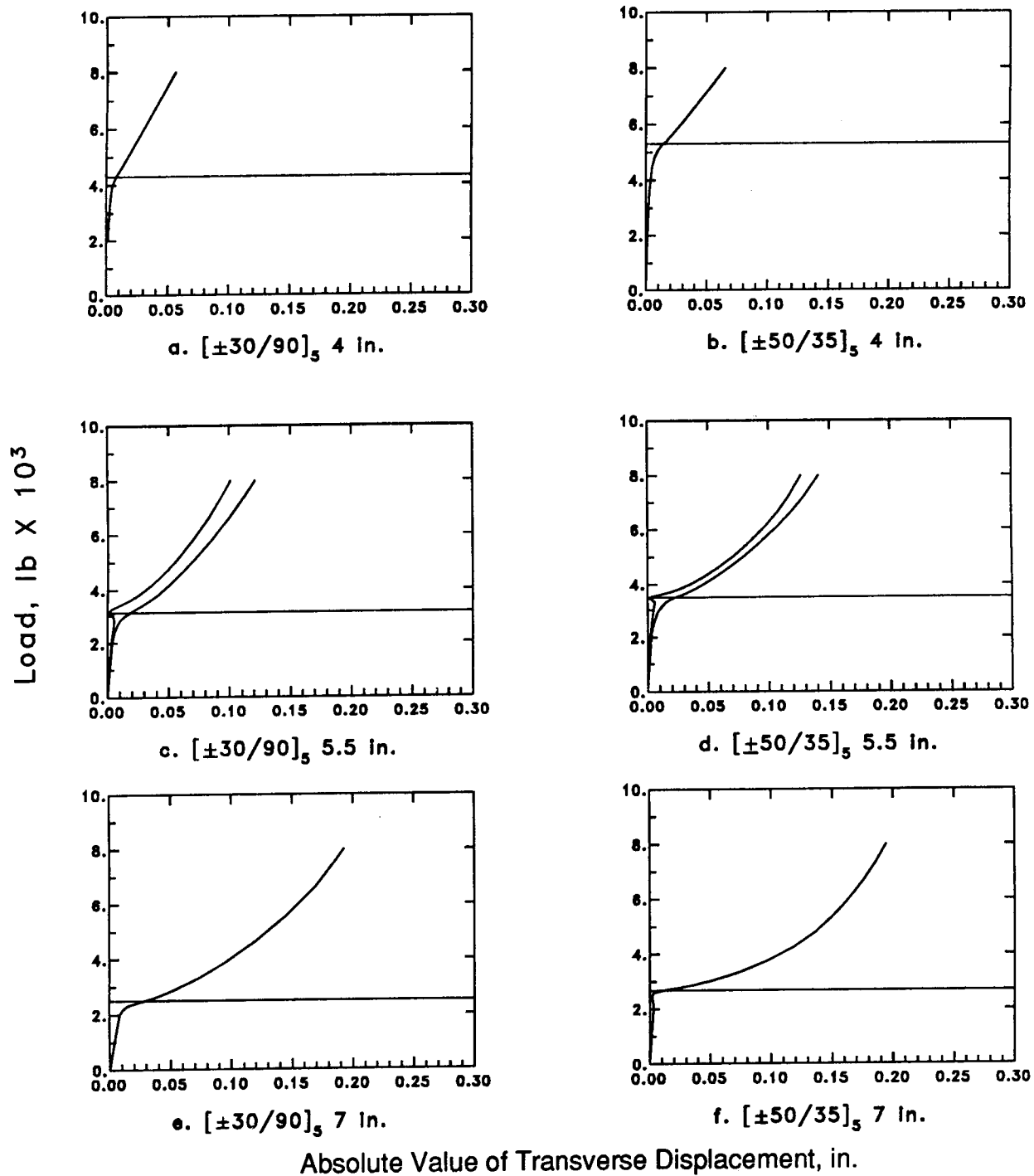


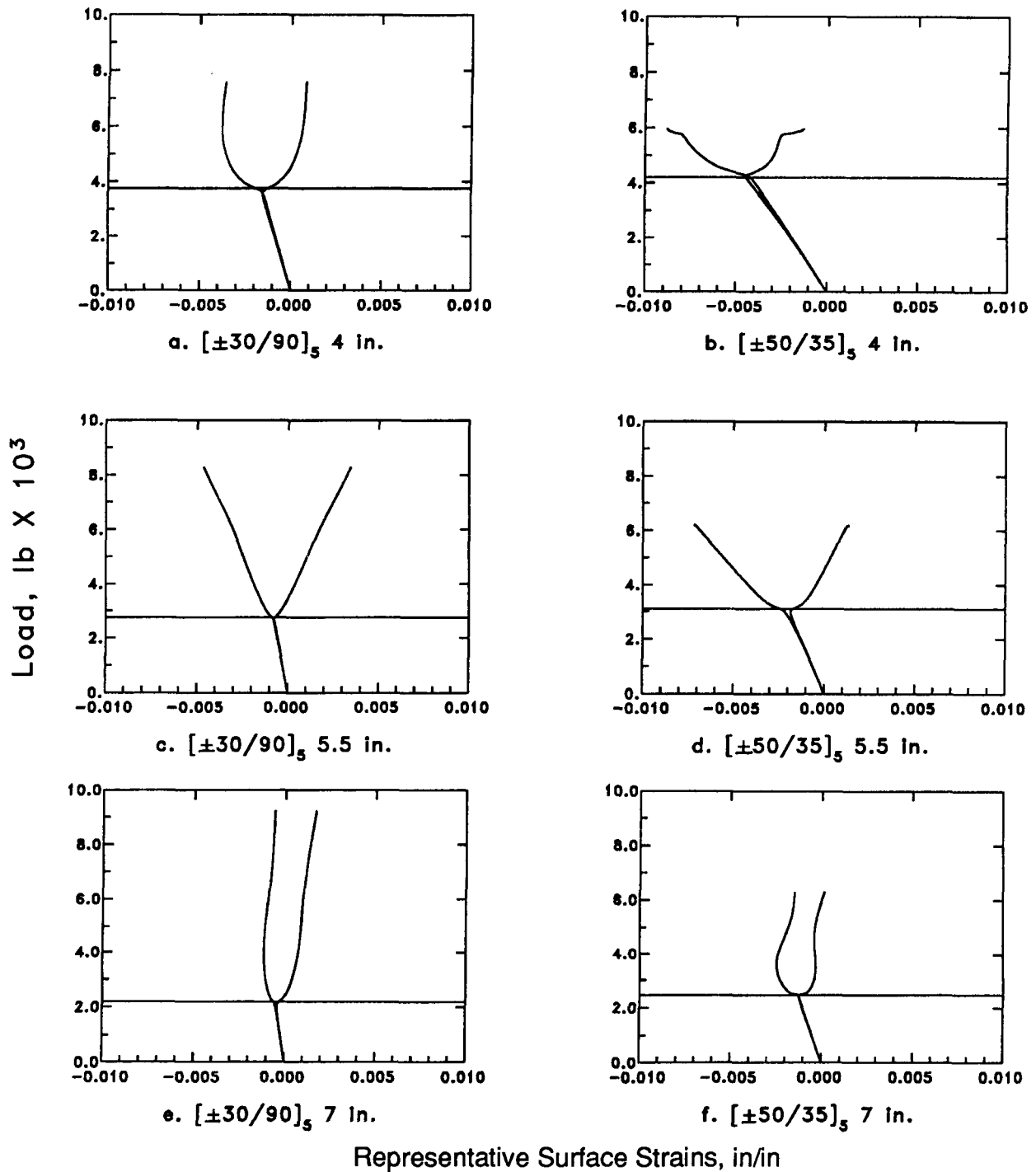
Figure 5.12. STAGSC-1 Twisting Results



**Figure 5.13. Experimental Symmetry Results**



**Figure 5.14. STAGSC-1 Symmetry Results**



LEGEND	
•	For 4 and 7 inch-wide panels, center panel strains are shown.
•	For 5 inch-wide panels, strains near top of panel in the center of the top half-wave are shown.
•	Horizontal lines indicate estimated buckling loads.

**Figure 5.15. Representative Experimental Surface Strain Results**

Back-to-Back Strains Corresponding to Points Noted Below

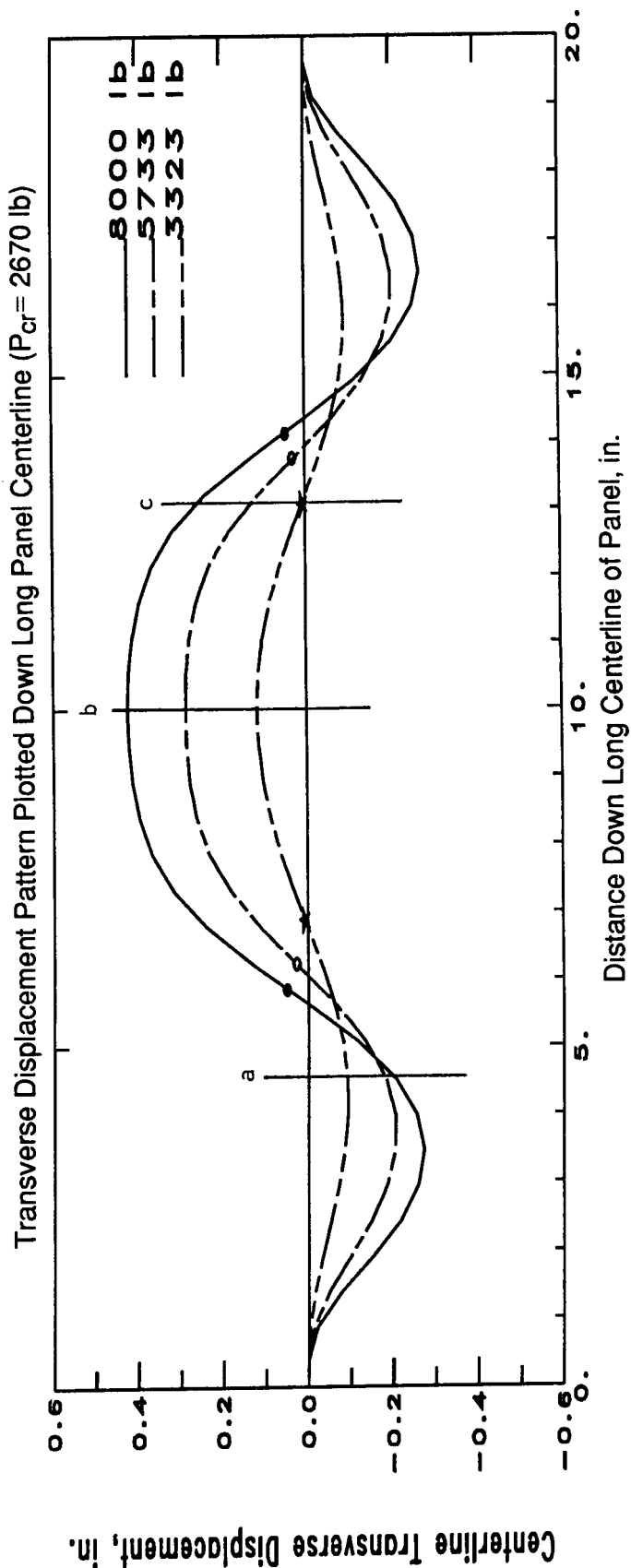
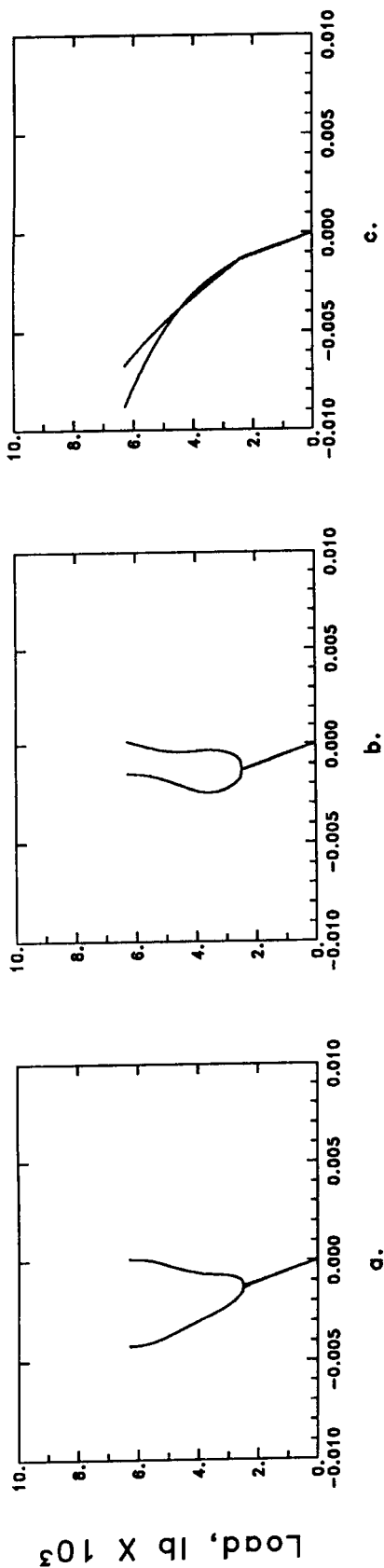
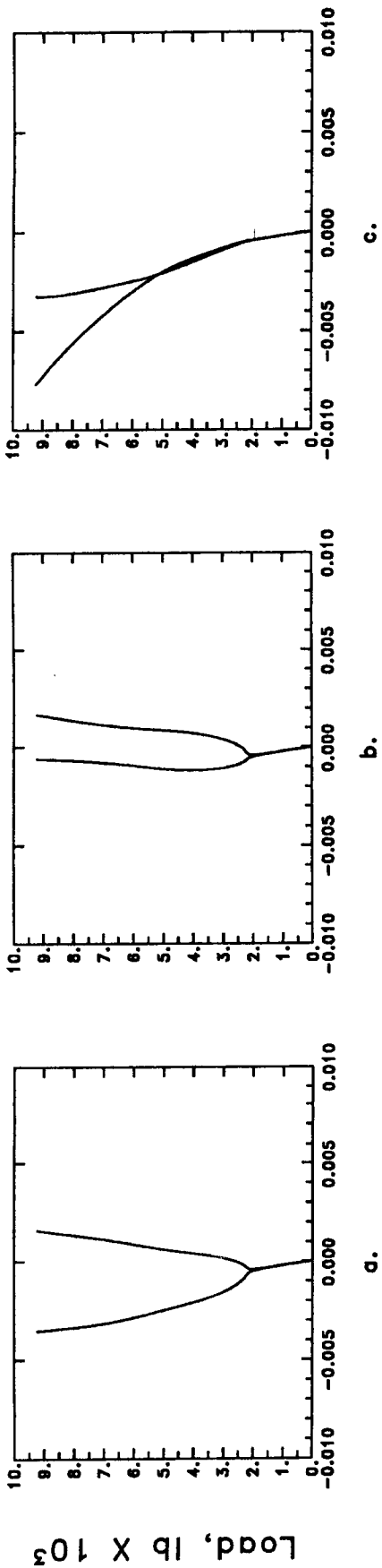


Figure 5.16. Progression of Transverse Displacement Pattern, [ $\pm 50/35$ ]<sub>5</sub> 7 Inch-Wide Panel

Back-to-Back Strains Corresponding to Points Noted Below



Transverse Displacement Pattern Plotted Down Long Panel Centerline ( $P_{cr} = 2500$  lb)

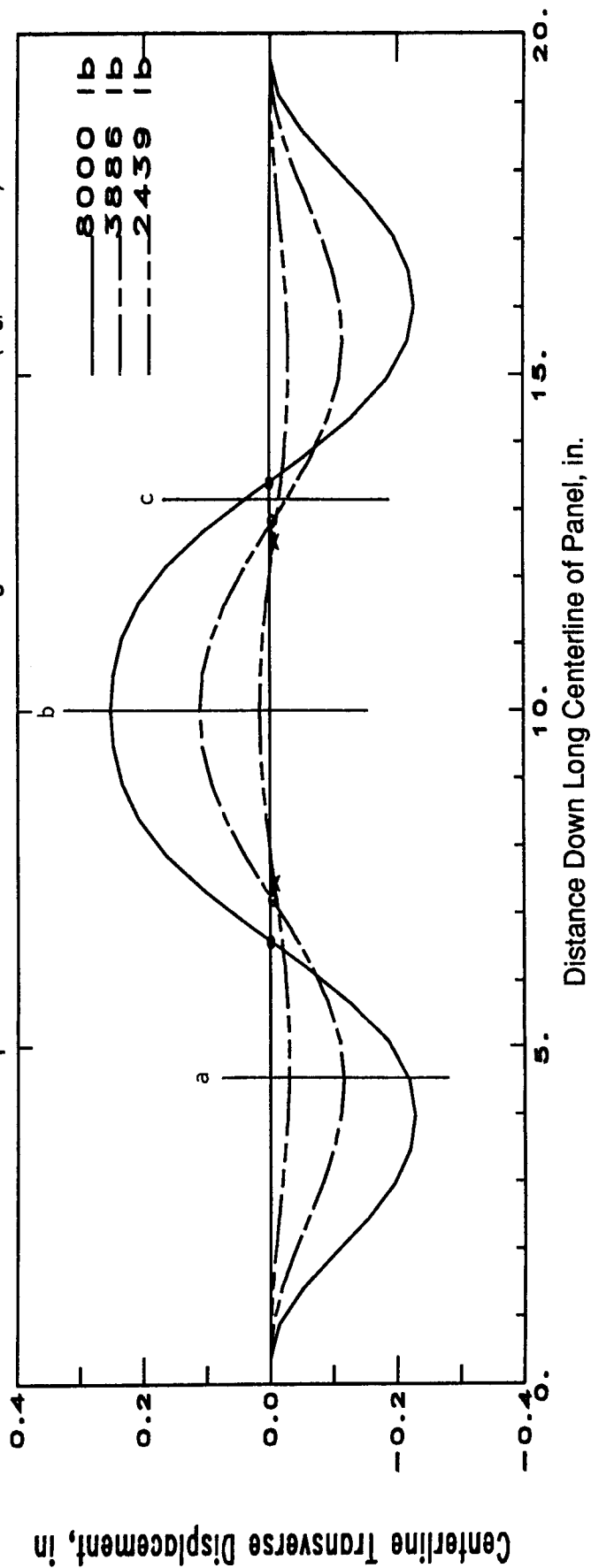
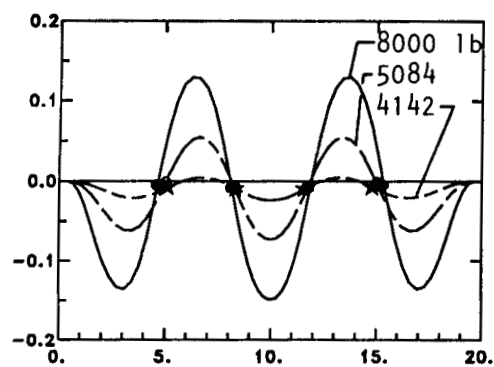
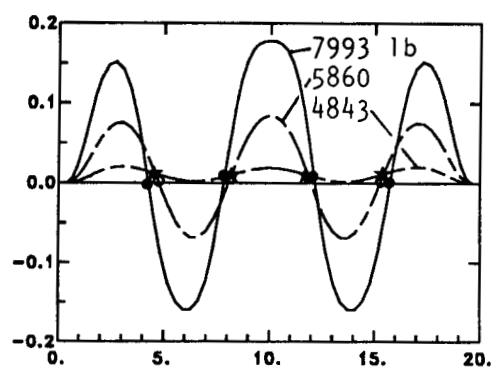


Figure 5.17. Progression of Transverse Displacement Pattern,  $[\pm 30/90]_5$  7 Inch-Wide Panel

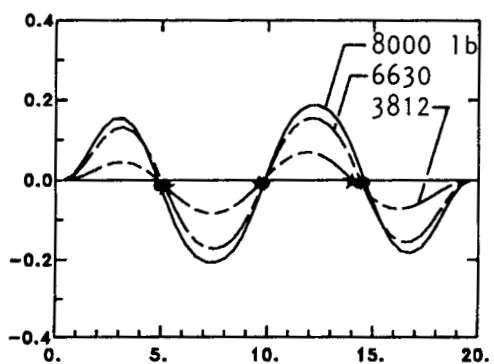
Transverse Displacement, in.



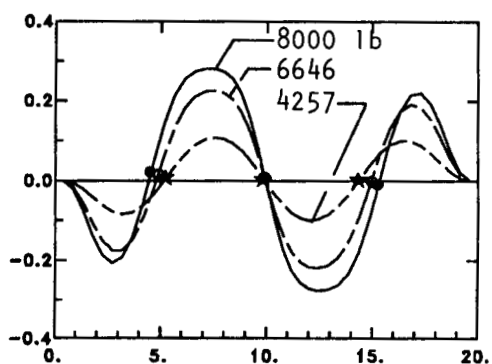
a.  $[\pm 30/90]_s$  4" ( $P_{cr} = 4300$  lb)



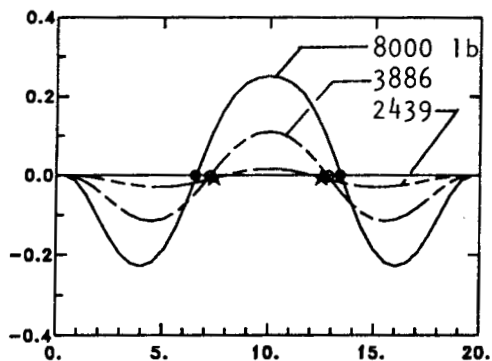
b.  $[\pm 50/35]_s$  4" ( $P_{cr} = 5300$  lb)



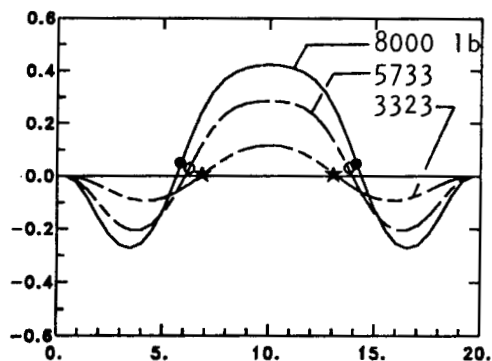
c.  $[\pm 30/90]_s$  5.5" ( $P_{cr} = 3100$  lb)



d.  $[\pm 50/35]_s$  5.5" ( $P_{cr} = 3500$  lb)



e.  $[\pm 30/90]_s$  7" ( $P_{cr} = 2500$  lb)



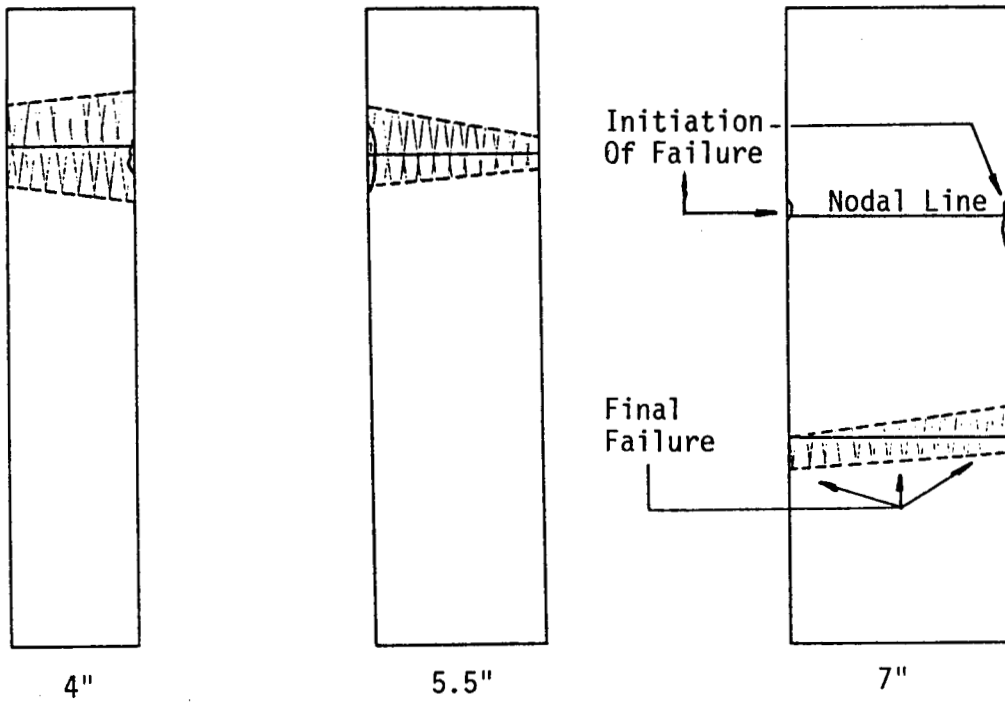
f.  $[\pm 50/35]_s$  7" ( $P_{cr} = 2670$  lb)

Distance Down Long Centerline of Panel, in.

LEGEND	
●	Symbols indicate the inflection points on each curve, as determined using cubic spline interpolation.

Figure 5.18. Progression of Transverse Displacement Pattern, All Panels

$[\pm 30/90]_5$  Panels



$[\pm 50/35]_5$  Panels

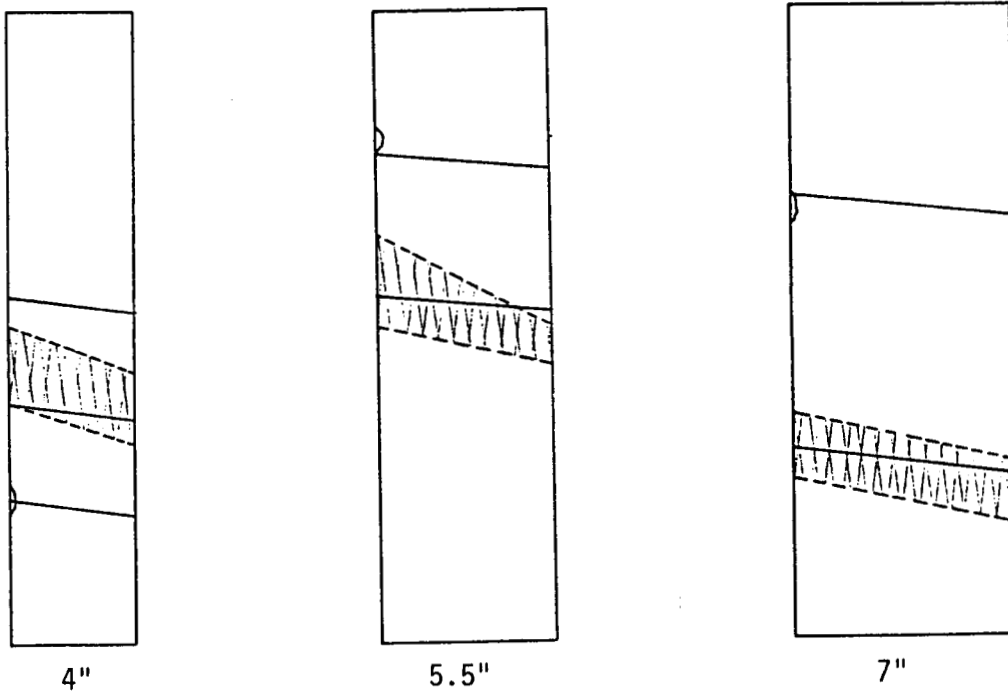
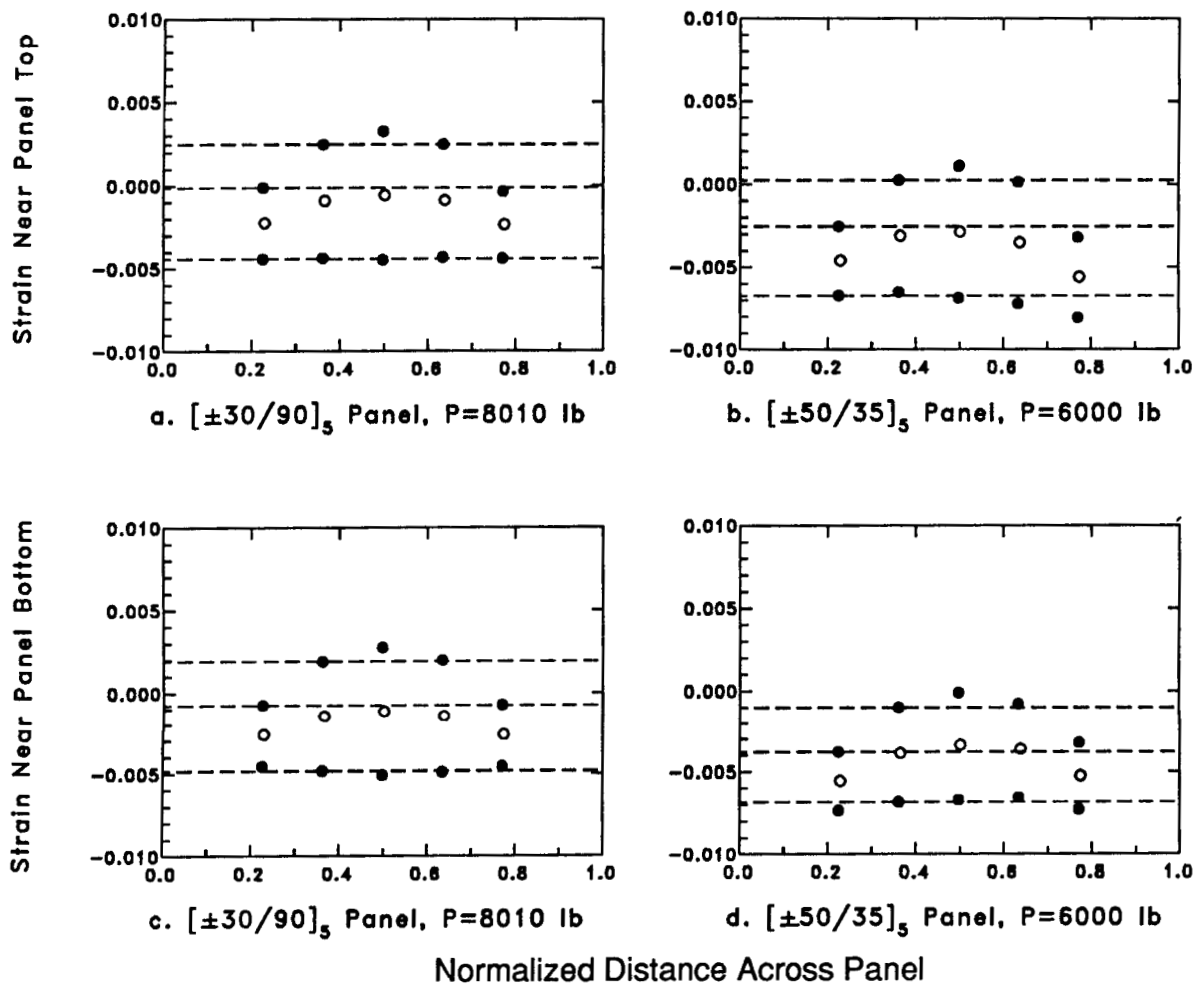


Figure 5.19. Failure Locations





LEGEND	
●	Experimental surface strain values
○	Calculated average strain values
----	Reference lines to aid in observing symmetry

**Figure 5.20. Strains Across 5.5 Inch-Wide Panels at Load Near Failure**

ORIGINAL PAGE IS  
OF POOR QUALITY



Figure 5.21. Photograph of Shear Failure,  $[\pm 50/35]_5$  7 Inch-Wide Panel

# Report Documentation Page

1. Report No. NASA TM-100509		2. Government Accession No.		3. Recipient's Catalog No.	
4. Title and Subtitle Postbuckling of Laminated Anisotropic Panels				5. Report Date October 1987	
				6. Performing Organization Code	
7. Author(s) G.L. Jeffrey				8. Performing Organization Report No.	
				10. Work Unit No. 585-01-21-02	
9. Performing Organization Name and Address NASA Langley Research Center Hampton, VA 23665-5225				11. Contract or Grant No.	
				13. Type of Report and Period Covered Technical Memorandum	
12. Sponsoring Agency Name and Address National Aeronautics and Space Administration Washington, DC 20546-0001				14. Sponsoring Agency Code	
15. Supplementary Notes					
16. Abstract <p>A two-part study of the buckling and postbuckling behavior of laminated anisotropic plates with bending-extensional coupling is presented. The first part involves the development and application of a modified Rayleigh-Ritz analysis technique. Modifications made to the classical technique can be grouped into three areas. First, known symmetries of anisotropic panels are exploited in the selection of approximation functions. Secondly, a reduced basis technique based on these same symmetries is applied in the linear range. Finally, geometric boundary conditions are enforced via an exterior penalty function approach, rather than relying on choice of approximation functions to satisfy these boundary conditions. Numerical results are presented for both the linear and nonlinear range, with additional studies made to determine the effect of variation in penalty parameter and number of basis vectors.</p> <p>In the second portion of the study, six panels possessing anisotropy and bending-extensional coupling are tested and detailed comparisons are made between experiment and finite element results in order to gain insight into the postbuckling and failure characteristics of such panels. The panels are constructed using two different lamination sequences, and panels with three different aspect ratios were constructed for each lamination sequence.</p>					
17. Key Words (Suggested by Authors(s)) Buckling Postbuckling Composite structures Anisotropy Rayleigh-Ritz method Finite element analysis Graphite-Epoxy composites Panels Computer programs Flat plates Laminates			18. Distribution Statement Unclassified—Unlimited		
			Subject Category 39		
19. Security Classif.(of this report) Unclassified		20. Security Classif.(of this page) Unclassified		21. No. of Pages 188	
				22. Price A09	